

Capillary-based microfluidic sample confinement for studying dynamic cell behaviour

Amin Hassanzadeh-Barforoushi

A thesis in fulfilment of the requirements for the degree of
Doctor of Philosophy



UNSW
SYDNEY

University of New South Wales

School of Mechanical and Manufacturing Engineering

March 2019

ORIGINALITY STATEMENT

'I hereby declare that this submission is my own work and to the best of my knowledge it contains no materials previously published or written by another person, or substantial proportions of material which have been accepted for the award of any other degree or diploma at UNSW or any other educational institution, except where due acknowledgement is made in the thesis. Any contribution made to the research by others, with whom I have worked at UNSW or elsewhere, is explicitly acknowledged in the thesis. I also declare that the intellectual content of this thesis is the product of my own work, except to the extent that assistance from others in the project's design and conception or in style, presentation and linguistic expression is acknowledged.'

Signed

Date

INCLUSION OF PUBLICATIONS STATEMENT

UNSW is supportive of candidates publishing their research results during their candidature as detailed in the UNSW Thesis Examination Procedure.

Publications can be used in their thesis in lieu of a Chapter if:

- The student contributed greater than 50% of the content in the publication and is the “primary author”, ie. the student was responsible primarily for the planning, execution and preparation of the work for publication
- The student has approval to include the publication in their thesis in lieu of a Chapter from their supervisor and Postgraduate Coordinator.
- The publication is not subject to any obligations or contractual agreements with a third party that would constrain its inclusion in the thesis

Please indicate whether this thesis contains published material or not.

This thesis contains no publications, either published or submitted for publication (if this box is checked, you may delete all the material on page 2)

Some of the work described in this thesis has been published and it has been documented in the relevant Chapters with acknowledgement (if this box is checked, you may delete all the material on page 2)

This thesis has publications (either published or submitted for publication) incorporated into it in lieu of a chapter and the details are presented below

CANDIDATE'S DECLARATION

I declare that:

- I have complied with the Thesis Examination Procedure
- where I have used a publication in lieu of a Chapter, the listed publication(s) below meet(s) the requirements to be included in the thesis.

Name	Signature	Date (dd/mm/yy)

COPYRIGHT STATEMENT

'I hereby grant the University of New South Wales or its agents the right to archive and to make available my thesis or dissertation in whole or part in the University libraries in all forms of media, now or here after known, subject to the provisions of the Copyright Act 1968. I retain all proprietary rights, such as patent rights. I also retain the right to use in future works (such as articles or books) all or part of this thesis or dissertation.

I also authorise University Microfilms to use the 350 word abstract of my thesis in Dissertation Abstract International (this is applicable to doctoral theses only).

I have either used no substantial portions of copyright material in my thesis or I have obtained permission to use copyright material; where permission has not been granted I have applied/will apply for a partial restriction of the digital copy of my thesis or dissertation.'

Signed

Date

AUTHENTICITY STATEMENT

'I certify that the Library deposit digital copy is a direct equivalent of the final officially approved version of my thesis. No emendation of content has occurred and if there are any minor variations in formatting, they are the result of the conversion to digital format.'

Signed

Date

Abstract

Cells in the body are in constant interaction with their surrounding environment. These interactions lead to creation of a variety of biophysical and biochemical events such as cell migration, neurite outgrowth and single cell protein secretion. In order to study these complex events, cells should be positioned in accurate spatial locations. This thesis is focused on application of microfluidics in studying cell dynamics based on a new capillary sample confinement approach. The main contributions of this thesis are the fundamentals of capillary-based trapping of biological samples (Chapter 3), microfluidic stamping method for studying cellular migration in patterned co-culture (Chapter 4), microfluidic cell and protein patterning for studying preferential neurite outgrowth dynamics (Chapter 5), and static droplet array for single cell trapping and long-term monitoring (Chapter 6). Using numerical simulation, liquid-air interface movement in a microchannel with different geometries is investigated. For hydrophobic channels, it is found that the slope of the channel geometry can be used to manipulate interface velocity and acceleration. Based on this understanding, microchannel junction geometry for liquid compartmentalization was proposed. The results revealed that the filling pressure and the relative dimensions of the channels at the junction are determinant factors in trapping liquid sample. Understanding of the mechanism of liquid-air interface stoppage in microchannels is used to develop a temporarily sealed microfluidic stamping device for patterning two adherent cell lines and biomolecules with well-defined interlacing configuration. Using this device, cell migratory patterns of endothelial cells co-cultured with cardiac stem cells are investigated. In addition, hippocampal neurons and inhibitory cue Nogo-66 are co-patterned revealing the axon outgrowth dynamics during CNS injury.

The stamping device is operated using only a lab pipet and uses very low reagent volumes of 20 μl with cell injection efficiency of $>70\%$. Based on the flow behaviour in junction geometry, a new sample trapping method is presented to easily and reliably generate an array of hundreds of dispersed nanoliter-volume semi-droplets for single-cells culture and analysis. The device isolates cells in droplet compartments and quantifies secretion profile of single or multiple cells over time period of hours up to days. The overall setup and injection procedure take less than 10 minutes, is insensitive to fabrication defects and supports cell recovery for downstream analysis.

Acknowledgements

Firstly, I would like to acknowledge my supervisors, Prof. Tracie Barber and A/Prof. Majid Ebrahimi Warkiani for all their support and guidance over the past four years. Tracie, thank you for granting me the freedom to do my research with peace of mind and for also ensuring that I never got too far off track. Majid, thank you for your motivation for hard work and for giving me the opportunity to step into the world of microfluidics.

Secondly, I would like to extend my deepest gratitude to Dr. David Gallego-Ortega and Prof. Thomas Fath for giving me the opportunity to work as part of their team. David, I should thank you for your wonderful encouragements and all of the enjoyable scientific debates we had in your office. Thomas, thanks for all of your support and opening my eyes to the world of neurons. Also, thanks for reminding me to be disciplined in a German way.

A huge appreciation goes to Andrew Law, Holly Stefen, Jonathan Shemesh, and Mehdi Rafeie. You were my first teachers in the laboratory since I started my PhD. Thanks for your patience and your continuous support. Andrew and Holly, thanks for your help with the biological protocols.

A huge appreciation goes to all the technical support at the School of Mechanical Engineering, Dr. Eldad Ben-Ishay, Dr. Tamsin Peters, School of Biomedical Engineering Lynn Ferris, Robert Nordon, Liyuan Wang, Jane Li and Neta Ben-Ishay. A big thank you to Garvan Institute of Medical Research Dr. William Hughes and UNSW Biomedical Imaging Facility Dr. Michael Carnell for their assistance with live-cell microscopy.

My regards to my fellow PhD colleagues Maira Syed, Mahdi Motamedi, Dr. Mahmoud Karimi for your advices and encouragement throughout this way. A special thank you

goes to my lovely friends Jing He and Abbas Hejri who were always there for support and without whom this would be too difficult to come into reality.

Finally, to my family who patiently encouraged me during this journey. To my dearest Sahar and Mostafa for being a source of happiness all the way during the PhD period. The ultimate gratitude is to my Mum and Dad for always believing in me and for their unlimited love, devotion and support.

List of publications

Journal papers

1. **A. Hassanzadeh-Barforoushi**, A. Law, A. Hejri, M. Asadnia, D. Gallego-Ortega, C. Ormandy, M. Warkiani, "Static droplet arrays for culturing single live adherent cells an isolated chemical microenvironment", *front cover Lab Chip* 18, 2156-2166.
2. **A. Hassanzadeh-Barforoushi**, J. Shemesh, N. Farbehi, M. Asadnia, G.H. Yeoh, R. Harvey, R. Nordon, M. Warkiani, "A rapid co-culture stamping device for studying intracellular communication", *Scientific reports* 6, 35618.
3. H. Stefen[#], **A. Hassanzadeh-Barforoushi**[#], M. Brettel, S. Fok, A. Suchowerska, N. Tedla, T. Barber, M. Warkiani, T. Fath, "A Novel Microfluidic Device-Based Neurite Outgrowth Inhibition Assay Reveals the Neurite Outgrowth-Promoting Activity of Tropomyosin Tpm3. 1 in Hippocampal Neurons", *Cellular and Molecular Neurobiology* 38, 1557-1563.
4. **A. Hassanzadeh-Barforoushi**, T. Barber, "Capillary microfluidics for live single cell monitoring in nanoliter droplet compartments", Under preparation for *Biosensors and Bioelectronics*.
5. B. Dang[#], **A. Hassanzadeh-Barforoushi**[#], M. Syed, D. Yang, G. Liu, J. Liu, R. Taylor, T. Barber, "Microfluidic actuation via 3D-printed molds towards multiplex biosensing of cell apoptosis", *ACS Sensors* 4, 8, 2181-2189 .
6. M. Rafeie, M. Welleweerd, **A. Hassanzadeh-Barforoushi**, M. Asadnia, W. Olthuis, M. Warkiani, "An easily fabricated three-dimensional threaded lemniscate-shaped micromixer for a wide range of flow rates", *Biomicrofluidics* 11(1), 014108.

Conference papers

1. **A. Hassanzadeh-Barforoushi**, J. Shemesh, N. Farbehi, M. Asadnia, G.H. Yeoh, R. Harvey, M. Warkiani, "A rapid microfluidic stamping device for studying cardiac stem cells and endothelial cells co-culture", *MicroTAS 2016, Dublin, Ireland*.
2. **A. Hassanzadeh-Barforoushi**, K. Chaudhry, M. Asadnia, M. Warkiani, "Rapid Tweezer-Shaped Static Droplet Array for Studying Cell-Cell Communication", *EMBS Micro and Nanotechnology in Medicine 2016, Waikoloa, Hawaii, USA*.
3. **A. Hassanzadeh-Barforoushi**, A. Law, A. Hejri, M. Asadnia, D. Gallego-Ortega, C. Ormandy, **M. Warkiani**, "Microfluidic droplet arrays for rapid single cell culture and analysis", *International MicroNanoConference 2017, Amsterdam, Netherlands*.
4. **A. Hassanzadeh-Barforoushi**, M. Li, T. Barber, M. Warkiani, "Manipulation of droplet content and gradient generation in microfluidic static droplet arrays" *ANZNMF 2017, Hobart, Tasmania, Australia*.

Table of Contents

Abstract.....	i
Acknowledgements.....	iii
List of publications	v
Table of figures.....	xi
Chapter 1. Introduction	1
1.1. Overview.....	2
1.2. Dynamic cell behaviour and cellular positioning.....	5
1.2.1. Cellular positioning.....	7
1.3. Microfluidic sample confinement	10
1.4. Thesis outline	13
Chapter 2. Cell dynamics via capillary-based geometrical sample confinement.....	16
2.1. Microfluidic sample confinement techniques	17
2.1.1. Sample patterning	17
2.1.2. Sample trapping	20
2.2. Capillary-based sample confinement	23
2.2.1. Capillary microfluidics	24
2.2.2. Capillary pumping.....	25
2.2.3. Capillary sequential systems	26
2.3. Capillary microfluidics sample confinement: mechanisms	27
2.3.1. Suspended microfluidics	27
2.3.2. Droplet metering	28
2.3.3. Capillary burst valve in centrifugal systems	28
2.3.4. Multilevel expansion valves.....	29
2.3.5. Trigger valves	30
2.3.6. Sample digitization	32
2.3.7. Capillary pinning at barriers	33
2.3.8. Droplet trapping	33
2.4. Capillary microfluidics cell confinement: application.....	34
2.4.1. Capillary pinning in 3D culture systems.....	34
2.4.2. Cell patterning capillary systems	37
2.4.3. Open microfluidics.....	38
2.4.4. Droplet trapping	39
2.5. Cell dynamics demanding microscale sample confinement	39

2.5.1. Cell migration	39
2.5.2. Single-cell migration.....	40
2.5.3. Collective cell migration.....	44
2.5.4. Neurite outgrowth	45
2.5.5. Single cell secretion	48
2.6. Summary	49
Chapter 3. Capillary-based sample confinement: Theory and numerical simulation	51
3.1. Fundamental concepts.....	52
3.1.1. Surface tension.....	52
3.1.2. Contact angle, hydrophobic and hydrophilic surfaces	52
3.1.3. Capillary pressure	53
3.2. Filling length and filling velocity.....	55
3.3. Confinement based on Capillary pressure	56
3.3.1. Air vents.....	57
3.3.2. Capillary flow resistance.....	57
3.4. Capillary-based liquid stoppage (stop valve).....	57
3.4.1. Theoretical analysis.....	57
3.4.2. Numerical simulation of the stop valve	60
3.4.3. Solution of the stop valve using Phase-field method	61
3.4.4. Results and discussion	63
3.4.5. Employing the stop-valve in liquid sample trapping mechanism	67
3.5. Capillary-based liquid movement in a microchannel.....	68
3.5.1. Analysis of meniscus advancing in the microchannel	68
3.5.2. Solution of the meniscus movement in the microchannel using Phase-field method	70
3.6. Liquid compartments via shearing	85
3.6.1. Numerical simulation of the liquid shearing and droplet formation	86
3.7. Conclusions.....	91
Chapter 4. A rapid co-culture patterning device for studying cellular migration	92
4.1. Introduction.....	93
4.2. Material and methods.....	95
4.2.1. Device design.....	95
4.2.2. Device fabrication	99
4.2.3. Cell isolation and culture	108
4.2.4. Viability assay of the patterned cells	112
4.2.5. Protein stamping	113

4.2.6. Microscopy	113
4.2.7. Image and data analysis	114
4.2.8. Microfluidic cell culture.....	115
4.3. Results and discussion	117
4.3.1. Device operation	117
4.3.2. Device characterization.....	118
4.3.3. Interaction of cardiac-derived mesenchymal SC and EC in patterned co-culture ..	126
4.4. Conclusions.....	133
Chapter 5. Microfluidic neuronal patterning for neurite's outgrowth and inhibition assay	136
5.1. Introduction.....	137
5.2. Material and methods.....	140
5.2.1. Device design.....	140
5.2.2. Device fabrication	145
5.2.3. Production of recombinant GST-Nogo-66 in <i>E. coli</i>	146
5.2.4. Primary cell preparation.....	146
5.2.5. Primary cell culture.....	147
5.2.6. Live imaging and axon growth rate	149
5.2.7. Immunocytochemistry	150
5.2.8. Imaging and data analysis	151
5.3. Results and discussion	152
5.3.1. Neuron and GST-Nogo66 coating	152
5.3.2. Neurite outgrowth dynamics.....	154
5.3.3. Neurite inhibition assay	156
5.4. Conclusion	158
Chapter 6. Single cell trapping and secretion assay.....	159
6.1. Introduction.....	160
6.2. Material and methods.....	163
6.2.1. Device design.....	163
6.2.2. Device fabrication	171
6.2.3. Device operation	177
6.2.4. Cell culture.....	188
6.2.5. Device preparation and set up.....	189
6.2.6. Cell loading and single cell monitoring	191
6.2.7. On-chip live/dead staining experiment	192
6.2.8. Cell viability and proliferation assay	192

6.2.9. Matrix metalloproteinase (MMP) assay	193
6.2.10. Microscopy	193
6.2.11. Image and data analysis	196
6.3. Results and discussion	197
6.3.1. Device fluidic performance.....	197
6.3.2. Cell distribution, single cell trapping	200
6.3.3. Device pressure test	204
6.3.4. Cell culture, viability, proliferation and on-chip staining	206
6.3.5. Post peeling cell access	208
6.3.6. Single cancer cell proteolytic assay	212
6.4. Concluding remarks	215
Chapter 7. Conclusions	217
7.1. Key findings.....	218
7.2. Future direction and limitations	222
Appendix A. UV exposure using mask aligner	226
Appendix B. MATLAB codes for analysing cell migration and proliferation.....	230
Appendix C. Cell counting in ImageJ	235
Appendix D. Production of recombinant GST-Nogo-66 in <i>E. coli</i>	237
Appendix E. Neurons antibody staining protocol	239
Appendix F. Cleanroom photolithography	244
References.....	252

Table of figures

Figure 1.1: Dynamic biophysical events. Cells migrate in two ways. (A) Collective migration of cells happens when several cells migrate together. [3]. (B) Each single cell may migrate individually due to exposure to chemical gradients in the environment in a process known as chemotaxis [4]..... 6

Figure 1.2: Images of the cell position in three fundamental tissues: (A) Squamous cell carcinoma and the surrounding stromal cells [5], (B) Patterned neurons of mice cortex [6] and (C) Embryonic bodies during development [7]. 8

Figure 1.3:(A) Heterogeneity exists in genetic and phenotypic characteristics of cells at the inter-tumour and intra-tumour levels [8]. (B) Average measurement can hide the cellular heterogeneity: Behaviours of cells in (i) at the ends of the distribution function (grey area) or (ii) Subpopulation (with a different mean value from the rest of the sample (μ : mean of the sample). (iii) The mean of two divided subpopulations may not be representative of the population [9]. 9

Figure 1.4:Methods for cell positioning at A) Multi-cellular level using surface chemistry [13] and B) Single cell level using cell dispensing [15]. 10

Figure 1.5: A) manipulation of single cells using surface acoustic waves, Bottom: Modes of operation [23] B) Control (a) and sonicated (b) yeast cells suspended in a 12% (v/v) water–ethanol mixture stained with fluorescence vacuole membrane dye [24]. 12

Figure 1.6: A) The concept of pressure-modulated passive cell positioning: Cells aggregate in hanging drop mode based on the surface tension between the liquid and the solid surface leading to formation of cell spheroid [25]. B) single cell are trapped in an array of cell traps due to difference in flow pressure in two paths [26]. 13

Figure 2.1: Sample patterning techniques: A) Chemical patterning: Schematic illustration of the process to generate micropattern of two cells in co-culture condition [30], (B) Soft lithographic patterning: Microcontact printing of fibronectin stamp with PLL-g-PEG as background; HeLa cells are patterned on the fluorescently labelled fibronectin patterns (in red) [32], (C) Active surface modification: Thermally responsive polymers are used for patterned co-culture of hepatocytes and endothelial cells [33], (D) Active cell patterning: SSAW-based sequential cell patterning by patterning cells in the nodes and anti-nodes of the acoustic field [34]. 18

Figure 2.2: Sample trapping techniques: (A) Sample sedimentation in microwell arrays. Single cells are isolated in microwells after multiple rounds of loading the cell suspension [43], (B) Dielectrophoretic trapping and lysing of single cells using DEP forces achieved via selective patterning of interdigitated ITO electrodes under the microwell arrays. A PDMS membrane is used to close and separate the microwells from each other [47], (C) Hydrodynamic trapping: Schematic illustration of sequential cell trapping, once a cell/spheroid fills one trap, the rest of the samples are guided to the next set of traps [50], (D) Acoustic trapping of single cells in a two dimensional domain created in microwells by application of surface acoustic waves [51], and (E) Droplet encapsulation: schematic illustration of single cell encapsulation in picoliter droplets followed by size-based sorting of the droplets containing single cells into a separate channel using DLD system [52]..... 21

Figure 2.3: Fundamental of capillary-controlled fluid flow in microchannels: (A) Using capillary pressure difference between two ports of the microchannel to control the flow direction and speed [76]. (B) Capillary pumping based on repeated patterns of microstructures: A serpentine capillary pump allows the liquid to be filled sequentially from one row to another [82]. (C) Capillary sequential system: A branched capillary pump is sucking a liquid sample placed at the inlet port due to hydrophilicity of the channel walls. When the liquid sample reaches the capillary retention

valve, the meniscus is pinned and the liquid flow is stopped until the next sample is injected into the system [83].	26
Figure 2.4: Mechanisms for capillary-based sample confinement: (A) Suspended microfluidics proposes liquid flow in an open channel. The aperture at the bottom of these channels can be used to create suspended membranes at predefined locations [86], (B) Droplet metering used for stopping the liquid at certain distance using hydrophobic path [88], (C) Centrifugal capillary burst valve: By controlling the centrifugal pressure at the entrance of burst valves sequential filling of a sample can be achieved, (D) multilevel expansion valves, an abrupt change in the channel height is used to stop the flow [92], (E) Trigger valves: the movement of a liquid at the junction is stopped until the liquid flow from another channel in the junction joins [98], (F) Sample digitization: Liquid sample can be trapped into side chambers of a microchannel under certain channel and chamber dimensions [100], (G) Capillary pinning at barriers: The liquid pinning in the capillary barriers based on the sudden expansion of the channel cross section in the pillar [101].	31
Figure 2.5: Application of capillary based geometrical confinement in studying cell dynamics: (A) Interaction between the human intestine Caco-2 cells cocultured with bacterial E.Coli cells under different flow conditions in the capillary pinning device [108], (B) Drug screening of Alzheimer disease by culturing neural progenitor cells in hydrogels pinned at the equally distanced micropillar arrays [110], (C) Evaluation of the behaviour of quorum sensing by patterning E.Coli in different shallow channels [112], (D) Measuring the invasiveness of prostate cancer (PC3-MM2) cells by imaging their migration through a membrane microgel formed via suspended microfluidics in open channels [86].	36
Figure 2.6: Directional migration: Cells that their path is closely following their displacement are more persistence in their migration.	42
Figure 2.7: Quantitative analysis of cell dynamics: (A) Migration of a single cell: migratory paths of IFN-DC cells towards SW620 colon carcinoma cells through capillary microchannels with and without drug treatments [118], (B) Collective migration of cells: Decrease in the blank surface area in wound healing assay of fibroblast cells with and without endothelial growth factor (EGF) [120], (D) Neurite outgrowth: Axon's growth length and direction in a zigzag microchannel geometry [122], (E) Single cell MMP secretion dynamics of PC-9 cancer cells in picoliter droplet over time [52].	46
Figure 3.1: Schematic illustration of the formation of the liquid-air interface on a solid surface and the formed contact angle.	52
Figure 3.2: Schematic illustration of the liquid in a hydrophilic (top) versus hydrophobic (bottom) channel.	53
Figure 3.3: Expansion of the liquid-air interface passing through a sudden expansion area. When the interface reaches the expansion area, it is pinned to the walls at both ends. At this moment, the interface has the highest radius of curvature. As the flow moves forward, the capillary pressure is built up while the radius of curvature is decreasing. R_2 is the minimum value of radius of curvature and corresponds to capillary burst pressure. After the burst pressure is overcome, the radius of curvature starts growing and the interface detaches from the sides and moves along the expansion.	58
Figure 3.4: Schematic illustration of the liquid-air interface movement/blockage while passing through a sudden geometrical expansion [29].	59
Figure 3.5: Schematics of the geometry of the microchannel with sudden expansion.	62
Figure 3.6: Mesh system used for solving the liquid-air interface passing through a sudden expansion microchannel with expansion ratio of 1:3.	63

Figure 3.7: Evolution of the liquid air interface over time in the sudden expansion region.....	64
Figure 3.8: Variation of the velocity magnitude in the expansion microchannel and across the liquid-air interface over time.	65
Figure 3.9: The air-liquid front as well as the velocity vectors in the domain over time.	65
Figure 3.10: Evolution of the pressure distribution over time in the expansion region.....	66
Figure 3.11: Variation of the contact point position along the horizontal contact line (Blue line) with time.	67
Figure 3.12: Implementation of liquid stoppage mechanism in the design of static droplet system: Liquid stops at the narrow restriction but moves through the main channel.	68
Figure 3.13: Device working mechanism: Tracking liquid-air interface in the channel; Theoretical analysis of liquid-air interface movement in the channel and through the traps[129].	69
Figure 3.14: Device working mechanism: Critical dimensions in the static droplet array device; Time-lapse images of liquid-air interface movement while entering the traps: Liquid filling the previous traps first and then moving toward the next set of traps; Liquid-air interface just before entering the traps demonstrating the entrance length to the traps and the main channel, Scale bar=100 μ m.....	70
Figure 3.15: Variations of channel design for investigating the capillary-based interface movement.....	71
Figure 3.16: Schematics of the geometries of a linear and nonlinear expansion microchannel.	72
Figure 3.17: Evolution of the liquid air interface over time in the A) linear versus B) nonlinear expansion geometries.....	73
Figure 3.18: Evolution of the velocity magnitude (A and B) and velocity vector (C and D) in the linear and nonlinear expansion channels over time, the scale factor for velocity vectors at C and D are 0.01 and 0.05 respectively.....	75
Figure 3.19: Evolution of the pressure distribution over time in the linear (top) and nonlinear (bottom) expansion geometries.....	76
Figure 3.20: Variation of the contact point position along the horizontal line with time in A) linear expansion geometry and B) non-linear expansion geometry.	77
Figure 3.21: Geometry of the microchannel junction.	78
Figure 3.22: Mesh system for solving the interface movement in the junction geometry.....	79
Figure 3.23: Evolution of the liquid air interface over time in the junction of the liquid trapping system.	80
Figure 3.24: Evolution of the velocity magnitude over time in the expansion region.	80
Figure 3.25: The air-liquid front as well as the velocity vectors in the domain over time.	81
Figure 3.26: Evolution of the pressure distribution over time in the gradual expansion geometry.	82
Figure 3.27: Evolution of the liquid air interface over time in the junction geometry at inlet pressures of 1 kPa and 1.3 kPa.....	83
Figure 3.28: Evolution of the pressure distribution over time in the junction geometry at inlet pressures of 1 kPa and 1.3 kPa.....	84
Figure 3.29: Evolution of the velocity vector over time in the junction geometry at inlet pressures of 1 kPa and 1.3 kPa.	85
Figure 3.30: Liquid shearing and droplet compartmentalization; Time-lapse image of liquid shearing in the main channel (Left) and critical dimensions in traps design (Right) (Scale bar=100 μ m).....	86
Figure 3.31: Geometry and the boundary conditions for the liquid shearing in static droplet array system.	87

Figure 3.32: Evolution of the liquid air interface over time in the gradual expansion region: red=air and blue=liquid.....	88
Figure 3.33: Evolution of the velocity magnitude over time in the expansion region.....	89
Figure 3.34: The air-liquid front as well as the velocity vectors at the liquid-air interface over time.	89
Figure 3.35: Evolution of the pressure distribution over time in the microfluidic junction.....	90
Figure 4.1: Microfluidic stamp structure. (A) PDMS device loaded with blue and red food dyes. (B) Device channel visualization by showing image of the device injected with blue and orange food colours. Zoomed image shows the restriction and air vent that limit liquid flow but allow air to escape. Scale bar, 1 mm and 200 μm ; (C) The stamping device in different sizes.....	96
Figure 4.2: Designing the photomask of the cell patterning device in AutoCAD software: (A) The photomask design is a 4 inch circle containing different chip designs. Different variations of the patterning device was positioned on a mask to investigate the effect of geometry on device operation (B) Each device's design has a number of features which includes: A number that differs the device from the nearby devices, small number carved near each branch of the patterning device for easy identification of each branch, a sufficient space from the nearby chip required for punching the access holes, and border lines (C) Critical dimensions of the microfluidic patterning chip; $w_{\text{wall}}=62.5\mu\text{m}$, $w_{\text{channel}}=150\mu\text{m}$, $w_{\text{gap}}=10\mu\text{m}$, $w_{\text{air}}=20\mu\text{m}$, (D) Chip dimensions: $W=6.7856\text{mm}$, $L=11.1150\text{mm}$	97
Figure 4.3: (A) Area of the chip design that needs to be dark for fabricating the devices (B) The fabricated mask is a bright-field mask with dark region made out of chrome.....	98
Figure 4.4: Materials and equipments for standard photolithography-based fabrication: (A) mask aligner (B) Transparency mask (C) negative photoresist (D) Silicon wafer and the spin coater.	100
Figure 4.5: Schematic illustration of the photolithography process. A layer of photoresistive is first spin coated on top of the silicon layer followed by alignment of the mask with the wafer and exposure. Depending on the type of photoresist used, the exposed area will either be removed or cross-linked after development. An additional step could be further etching or lift off of the silicon oxide layer using the photoresist as a protective layer.....	101
Figure 4.6: (A) Microfluidic patterning device fabricated on silicon wafer. (B) Sample leakage under a chip that is made on a silicon wafer.	102
Figure 4.7: The process flow of fabricating the microfluidic stamping device using photolithography on SOI wafer (I) SOI wafer is first coated with SU8 negative photoresist and exposed to UV light (B) The wafer is developed in SU8 developer (III) A thin layer of chrome is coated on the wafer which will be used to protect the underlying silicone-oxide layer. (IV) DRIE was performed in depth of $80\mu\text{m}$ (V) the thin chromium layer is removed using lift off.....	103
Figure 4.8: Spin coater used for coating photoresist (A) the spin coater is connected to vacuum from a hole at the middle of the sample holder (B) air gun is used for drying the surface of the silicon wafer after cleaning the surface with ethanol and acetone, (C) The spin coater controller.	104
Figure 4.9: The process of silanization: (A) Silane material trichloro (1H, 1H, 2H, 2H-perfluorooctyl) silane, (B) Silane is placed in a small container wrapped with aluminium, (C) The wafer was placed in vacuum chamber and the silane is vaporized (D) check valve to close and release the vacuum.	106
Figure 4.10: The process of soft lithography for making PDMS chips	107

Figure 4.11: (A) The autoclave machine use for sterilizing the devices and the tweezers. (B) The devices and tweezer in the autoclave bags. (C) Tweezers used for mounting the PDMS slab on the petri dish before sample injection.	108
Figure 4.12: Image of Endothelial cells EC (A) and stem cell SC (B) cultures in flasks and under the microscopes.....	111
Figure 4.13: Procedure of fibroblast cell culture	112
Figure 4.14: Double live/dead staining kit containing Calcein AM and propidium Iodide solutions.	112
Figure 4.15: Images acquired (A) before peel off (B) after cell doubling after 8 hours and (C) fluorescent image after device peel off.	115
Figure 4.16: Microfluidic stamp structure and patterning. (A) Stamping procedure: (a) The stamp is placed on a flat substrate such as a glass or a tissue-culture dish. (b) Cell suspension is injected to the first inlet using a standard lab pipet. The cell suspension fills the channels while allowing residual air to escape through the air vent. (c) In a similar manner, a second cell suspension is injected from a second inlet. (d) Following cell sedimentation and on-chip incubation, the PDMS stamp is removed while leaving cells attached to the substrate. (B) Fibroblasts L929 patterned on a TC plate. Scale bar 300 μm (C) Fluorescent-conjugated protein/peptide mixture patterning. Scale bar: 500 μm	119
Figure 4.17: Device Characterization: Comparing SOI (Silicone-On-Insulator) vs. Non-SOI wafer fabrication and the resultant leakage-proof performance. Scale bar 50 μm and 100 μm for the top and bottom images respectively.	120
Figure 4.18: Characterization of cell uniformity distribution in the channels by injecting L929 fibroblasts. (A) Each channel was divided to four zones (A, B, C, D) which were indexed based on the directionality of the flow. Scale bar, 200 μm (B) Boxplot of the normalized cell number in each of the zones for the injected bulk cell concentrations of 10^6 cells/ml, 2×10^6 cells/ml and 4×10^6 cells/ml (C) Linear curve fit between average number of cells in each zone and the inoculum concentration (cell suspension concentration).	122
Figure 4.19: Post-stamping cell viability: (A) Image of Fibroblast L929 Cell in stamp and after stamping peeling + Calcein/PI viability staining. (B) Quantification of post-stamp cell viability at $t = 4\text{hr}$, 24 hr and 48 hr . Viability was measured for both the case of counting/ignoring post-peeling washed cells.	124
Figure 4.20: Post-stamping cell proliferation: (A) Images of fibroblast proliferation over the course of 60 hours. Here $t=0\text{ h}$ is the time when the stamp was peeled. (B) Fibroblast proliferation (fold expansion), after stamp is peeled-off ($t= 0\text{ hr}$) tracked over the course of 96 hours.	125
Figure 4.21: Endothelial/Cardiac Stem Cells co-culture. Selected time lapse images of cardiac stem cells (SC) co-cultured with Endothelial Cells (EC) at time $t = 3\text{ h}$, 20 h , 60 h and their corresponding single-stamp culture of Endothelial Cells only (EC/EC) and Cardiac Stem Cells only (SC/SC). Scale bar: 200 μm	127
Figure 4.22: Endothelial/Cardiac Stem Cells co-culture. Overgrowth of Cardiac Stem cell clusters by neighboring Endothelial cells in a Co-culture experiment. Scale bar: 200 μm	127
Figure 4.23: (A) Proliferation of Endothelial cells and Stem cells in the single-culture versus co-culture reported as number of doublings versus time.	128
Figure 4.24: Kaplan-Meier and Cox regression analysis of time to division of SC in single-culture (SC SC) versus co-culture (SC EC) (A) Probability of division measured from the beginning of the experiment (B) Probability of division starting at $t=60\text{ hours}$ (risk factor= 0.34 ± 0.09 and $p=5.53 \times 10^{-6}$).	129

Figure 4.25: Single-cell tracking and collective cell migration analysis; The trajectory of multiple Endothelial Cells (EC) in the co-culture.	130
Figure 4.26: Single-cell tracking and collective cell migration analysis (B) Average migration speed of EC and SC in single culture and co-culture (n=30 for each condition) Scale bar: 200 μm	131
Figure 4.27: Single-cell tracking and collective cell migration analysis (A) Average migration velocity normal to channel direction for EC and SC in single-culture versus co-culture (n=100). (B) Average migration velocity distribution of Endothelial cells in single-culture versus co-culture (n=30).	131
Figure 4.28: Single-cell tracking and collective cell migration analysis (A) Variation of the relative distance of Cardiac Stem Cells from the symmetry line of their corresponding strip with time in the co-culture vs. single-culture, (B) Forward migration index (FMI) in the y-direction for EC and SC in single-culture and co-culture (n=30).	133
Figure 5.1: The concept of microfluidic neural patterning for generating a model of CNS injury in vitro.	140
Figure 5.2: Microfluidic neuronal patterning device. (A) Type 1: hatching device; in this device liquid containing cell samples is injected into a hatching area equipped with two in-built valving gaps as wells as narrow slots to trap single neurons (B) Type 2: PDMS device in which channels are visualized by showing image of the device injected with blue, green and orange food colours.	142
Figure 5.3: Designing the photomask of the neuronal patterning device in AutoCAD software: The photomask design is a 10 inch circle containing different chip designs. Different variations of the patterning device was positioned on a mask to investigate the effect of geometry on device operation. Each device is separated from nearby devices to accommodate punching the access holes, and border lines.	143
Figure 5.4: Critical dimensions of the neuronal patterning chip; $w_{\text{wall}}=62.5\mu\text{m}$, $w_{\text{channel}}=150\mu\text{m}$, $w_{\text{gap}}=10\mu\text{m}$, $w_{\text{air}}=20\mu\text{m}$, $w_{\text{slot}}=10\mu\text{m}$	144
Figure 5.5: (A) Area of the chip design that needs to be dark for fabricating the devices (B) The fabricated mask is a bright-field mask with dark region made out of chrome.	145
Figure 5.6: Cell extraction from mouse embryo: Embryos from day 16 mouse are obtained by sacrificing the mouse. Embryo's brain was removed and the meninges was isolated. The hippocampal part of the brain was first chopped into pieces and prepared for further digestion.	147
Figure 5.7: Primary cell culture in the neuronal patterning device: Devices are first placed on the coverslip coated with PDL-1. Hippocampal neurons were then injected into the device by adding 2 μl of cell solution to the inlet followed by pushing the sample into the channel using air blown via 1ml pipette. A cortical support was added to the culture on the tissue culture ring. Following cell attachment, the device was peeled off and fresh medium is added on top of the patterned neurons.	148
Figure 5.8: Cell culture in the neuronal patterning device before and after peeling.	149
Figure 5.9: (A) Images taken along the patterned substrate was stitched together divided into 6 equal size parts normal to the patterns using ImageJ. (B) Fluorescent image of the neurites and growth cones (C) corresponding analysis of the fluorescent image in which neurites expressing Tp8 are marked with green and the rest of neurites are in red. Scale bar: 150 μm	151
Figure 5.10: Design of microfluidic device. A Photo of microfluidic device for scale (top). Detailed schematic of microfluidic configuration with intercalating channels shown in yellow and green (middle) and enlarged image of area outlined showing device properties (bottom). Scale	

bars = 1 mm (middle) and 200 μm (bottom). B Schematic showing device being placed into live cell imaging dish B[1], loading of GST-Nogo-66 substrate (green) into channels on the right (B[2]), seeding of hippocampal cells into channels on the left (red) and cortical cells into a support ring (orange)(B[3]) and removal of the microfluidic device once cells are attached (B[4]). C Immunofluorescence image, displaying experimental loading of devices with GSTNogo- 66 inhibitory substrate coating on the right (green) and primary hippocampal cells on the left (orange). Scale bar = 1.5 mm. D Brightfield image of microfluidic device (white outline) with a schematic overlay showing channel dimensions and distances between intercalating channels. The schematic demonstrates how the lengths of neurites were measured 153

Figure 5.11: Validation of GST Nogo- 66 coating: (A-B)Fluorescence images of GST-Nogo-66 coating in channel pattern defined by microfluidic device at 1 day in vitro (DIV) and 7 DIV, scale bars = 150 μm . (C) Quantification of fluorescence intensity of GST-Nogo-66. Graph shows mean \pm SEM. Unpaired t test. n = 20. 154

Figure 5.12: (D-K) Fluorescence images of hippocampal neurons at 3 DIV, plated with (D, E, F, G) or without (H, I, J, K) a cortical support ring. Scale bars = 100 μm . (L) Quantification of cortical support ring experiments at 3 and 7 DIV. Graph depicts the mean percentage of alive cells per region of interest \pm SEM. Unpaired t tests. n = 10–11. P value ****P <0.0001. 155

Figure 5.13: (M-R) Immunofluorescence images of neurite outgrowth from 2 DIV to 7 DIV. (S) Quantification of neurite lengths from time points in (M–R). Graph shows mean \pm SEM. The distance between intercalating channels (175 μm) is indicated by the red line. The time point at which neurites reach the GST-Nogo-66-coated substrate is depicted by the black, dashed line. n = 23 (2 DIV), 120 (3 DIV), 119 (4 DIV), 125 (5 DIV), 95 (6 DIV), 43 (7 DIV). Scale bars = 200 μm 156

Figure 5.14: Neurite outgrowth promoting activity of Tpm3.1 in the presence of GST-Nogo-66. (A) Phase contrast image of hippocampal neurons at the completion of live recording. Grid overlay shows the division of cell culture area into regions of interest based on distance from GST-Nogo-66 substrate (pseudo-coloured green). Insert shows magnified region containing hTpm3.1 overexpressing and wt neurites circled in green and red, respectively. Scale bar = 50 μm . (B) Quantification of neurite growth rate within GST-Nogo-66-coated areas and non-coated areas. Tukey’s multiple comparisons test. Shown are mean \pm SEM. n \geq 12. P value *P = 0.016, **P < 0.01. 157

Figure 5.15: Quantification of the proportion of neurite tips within region – 1/1 and region 2/3 in the presence (+Nogo66) or absence (–Nogo66) of GSTNogo- 66. The graph depicts mean of proportions of total number of cells \pm SEM. Bonferroni’s multiple comparison test. n = 20. P value *P = 0.0475, ***P = 0.0003, ****P < 0.0001..... 158

Figure 6.1: Schematic illustration of the high-throughput static droplet device configuration and operation. (A) Image of a chip with (a) 500 \times 2.5nl droplet traps, (b) 600 \times 14nl droplet traps with close-up image of the traps. (B) 3D schematic of the device showing the traps, air plug sites and the main channel. (C) Chip components including traps, semi-droplets, main channel, air plug and trap indices. 163

Figure 6.2: Chemical isolation of the droplets throughout the experiment. The device is filled with different concentrations of fluorescein and the fluorescent intensity of droplet was measured over 48 hours experimental period. Each line belongs to a unique droplet. 164

Figure 6.3: (A) Critical dimensions in the static droplet array device (B) Dimensions in the L-shaped traps design. 166

Figure 6.4: Designing the photomask of the static droplet array in AutoCAD software: (A) The photomask design is a 10 inch circle containing different chip designs. Different variations of the

patterning device was positioned on a mask to investigate the effect of geometry on device operation (B) Two different geometries of the traps were designed namely the L-shaped device and the hexagonal device. The design is symmetrical. (C) The device has a serpentine structure and each device is separated from the nearby device with an island structure (D) The device design is a repetition of a pair of traps with corresponding numbers..... 168

Figure 6.5: (A) Schematic illustration of the geometrical parameters of each trap in which $w=150\mu\text{m}$, $h=300\mu\text{m}$, $l=100\mu\text{m}$, $d=400\mu\text{m}$ for device A and $w=300\mu\text{m}$, $h=620\mu\text{m}$, $l=300\mu\text{m}$, $d=750\mu\text{m}$ for device B. (B) Device dimensions, $x=6.39\text{mm}$, $y=32.8\text{mm}$ for device A and $x=14.29\text{mm}$, $y=27.85\text{mm}$ for device B. 170

Figure 6.6: (A) Area of the chip design that needs to be dark for fabricating the devices (B) The fabricated mask is a bright-field mask with the dark region made out of chrome. 171

Figure 6.7: Static droplet array device made out of silicon wafer: (A) Micrograph showing the device with the gaps between the traps and the wall is filled causing due to fabrication defects. (B) Range of chip operating pressures of the device for two different substrates (C) Leakage under the chip..... 172

Figure 6.8: Microscope images showing (A) the device pattern on the SOI wafer and (B) after fabrication out of PDMS..... 173

Figure 6.9: Bubbles trapped in the static trapping system during the soft lithography process. 174

Figure 6.10: Fabrication defect due to rapid PDMS demolding leads to blocked traps impairing the device operation. 174

Figure 6.11: Cracks on the surface of the SOI wafer which is caused either due to thermal stress induced by frequent change in temperature between the oven and room or physical stress during the PDMS de-moulding. 175

Figure 6.12: (A) Components of the oxygen plasma machine and (B) The chemistry behind plasma bonding. 175

Figure 6.13: The process of permanent bonding of the PDMS chips to coverslips: (A) PDMS chip and the glass slides were cleaned and mounted on the quartz platform facing up, (B, C) plasma formation in the chamber, (D) device and glass slide were removed out of the chamber and pressed together immediately to make permanent bond..... 176

Figure 6.14: Device loading steps: (I) Empty device (II) Cell-containing medium is injected into the channel (III) air pressure shears the continuous liquid into separate semi-droplets (IV and V) Fluorocarbon oil is introduced at the inlet and flows to sheath the stationary semi-droplets... 178

Figure 6.15: Formation of static droplets in SDA device; Particles are trapped in separate chambers, Scale bar= $300\mu\text{m}$ 178

Figure 6.16: A) The geometry of the narrow restriction, B) image sequence showing the liquid-air interface movement in the trap during the sample injection, C) liquid-air interface when moving towards a defective trap with blocked restriction at its end (Scale bar= $100\mu\text{m}$). 179

Figure 6.17: Experimental set up of fluidic experiment using syringe pump. 180

Figure 6.18: Setting up the syringe pump for injecting sample into the static droplet system at constant flow rate..... 181

Figure 6.19: Device operation with pipette injection..... 182

Figure 6.20: Device operation with pipette suction 182

Figure 6.21: Bubble generation in the static droplet array system: (A) A bubble that occupies a trap and is pushing the oil in the main channel, (B) Bubble extension in the system which pushes the FC oil out of the system. 184

Figure 6.22: Bubble generation in the static droplet array: (A) due to sharp geometry of the trap at the corners, (B) due to high flow rates which prevents the liquid from filling the trap before reaching the next pair of traps.....	185
Figure 6.23: Droplet evaporation over time in static droplet array.....	186
Figure 6.24: PMMA particles stock and diluted solutions used for the trapping assay.....	188
Figure 6.25: (A) Cells cultured in T-75 flask (B) Attached cells under the microscope.....	189
Figure 6.26: Experimental set-up of the sample injection under the cell culture hood.....	190
Figure 6.27: Cell culture in the device: Device setup by creating a humidity chamber.....	190
Figure 6.28: Cell attachment to the substrate; here two cells are located just adjacent to each other, Scale bar=200 μ m.....	191
Figure 6.29: Leica DMi8 live cell imaging microscope equipped with dedicated incubator and CO ₂ and temperature control.....	195
Figure 6.30: Fluorescent image of the MMP activity of single cells in the static droplet array device under different exposure times.....	195
Figure 6.31: Overlapped image of the transmitted and fluorescent microscopy. Magnified image also shows the cells in each droplet.....	196
Figure 6.32: Image showing the use of ImageJ for defining ROI and measuring the fluorescent intensity.....	197
Figure 6.33: Device working mechanism (A) Tracking liquid-air interface in the channel: Time-lapse images of liquid-air interface movement while entering the traps: Liquid filling the previous traps first and then moving toward the next set of traps; Liquid-air interface just before entering the traps demonstrating the entrance length to the traps and the main channel. (B) Liquid stops at the narrow restriction but moves through the main channel; (C) Liquid shearing and droplet compartmentalization; Time-lapse image of liquid shearing in the main channel (Scale bar=100 μ m).....	198
Figure 6.34: Device characterisation: (A) Trapping different concentration of particles inside droplets with regards to the solution concentration and particle size in static droplet arrays (n=9, (*): p<0.05; (**): p<0.01); N=500 droplets.....	201
Figure 6.35: single cell trapping efficiency versus flow rate.....	202
Figure 6.36: Device characterisation: Distribution of MDA-MB-231 breast cancer cells with a wide range of cell concentration in droplet arrays of different size (n=9, (*): p<0.05; (**): p<0.01); N=500 droplets.....	202
Figure 6.37: Poisson distribution function with λ values corresponding to MDA-MB-231 breast cancer cells with a wide range of cell concentration.....	203
Figure 6.38: Pressure test experimental set up; the pressure range applied at the inlet to drive the liquid into the traps during loading step with no leakage (n=5).....	205
Figure 6.39: Cell and solute treatment in the device. (A) On-chip cell viability assay in each droplet; cells were cultured in the droplets for 12 hrs, 18 hrs, 24 hrs, and 48 hrs after which Trypan blue was injected into the device; Dead cells uptake Trypan blue and can be distinguished from the live cell.....	207
Figure 6.40: Cell and solute treatment in the device. On-chip measurement of cell viability and proliferation over time in device A and B. (p<0.05, n=5); N=500 droplets.....	208
Figure 6.41: Device peel-off: (a) Peeling step using a pair of tweezers. (b) Cell retrieval following peeling from TC-substrate; the trace of traps as well as trap indices are clearly visible enabling cell retrieval and cell addressability with high accuracy. (c) Successful peeling of the device from a glass substrate, Scale bar=200 μ m in all images.....	209

Figure 6.42: Cell and solute treatment in the device. Left: On-chip solute dilution: the device was first filled with blue food dye followed by injection of a water plug. The droplet dilutes the solute in each trap; the size of the droplet defines the dilution factor. Right: Solute gradient formed in droplet array device: The device was first filled with pure water followed by shearing liquid from the main channel and injection of a plug of blue food dye. Shearing the food dye will leave the device with droplets containing gradient of food dye. 210

Figure 6.43: Multistep dilution and gradient generation in static droplet arrays A) Multistep dilution B) Two-colour gradient generation with two step addition of a 0.187 μ l plug of blue and red food colour respectively. C) Gradient generation with two step addition of a 0.187 μ l plug of blue food colour. (Note: This volume is calculated as the amount of sample filling the channel from the inlet up to the first trap). 211

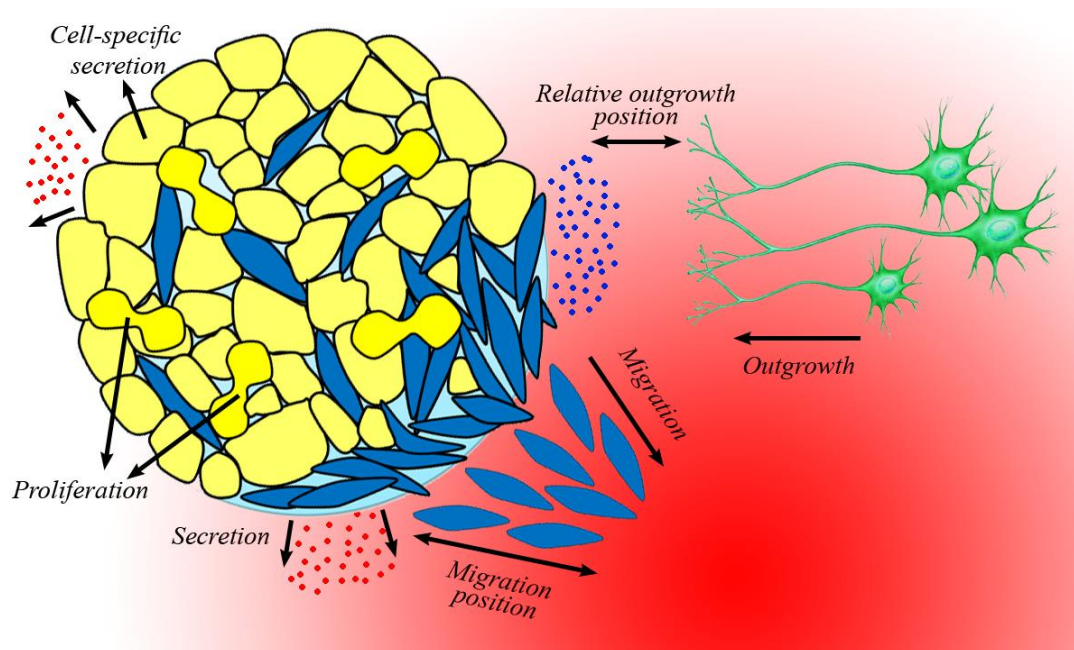
Figure 6.44: On-chip staining of cells by adding live/dead staining solution to the droplets content (calcein AM and propidium iodide) after 24 hours culturing period (Scale bar=300 μ m). 212

Figure 6.45: MMP assay at the single cell level of MDA-MB-231 cancer cell line. (A) Relative fluorescent intensity in semi-droplets (a) an array showing the fluorescent signal out of different semi-droplets, Scale bar: 1.5mm (b) zoomed view demonstrating droplets with no cell, high activity and low activity single cell with their corresponding fluorescent signal, Scale bar: 300 μ m, (c) A box plot demonstrating the relative fluorescent intensity of each chamber with no cell, one cell or two cells at a certain time point; as expected droplets containing one cell have higher fluorescent signal compared to empty droplets and droplets with two cells are brighter than those containing one cell (N=102 for cases with no cell, N=114 for cases with one cell and N=53 for cases with two cells), $P \leq 0.001$, n=3. 213

Figure 6.46: MMP assay at the single cell level of MDA-MB-231 cancer cell line. Single cell MMP activity over time (A) fluorescent intensity of droplets over time showing increase in MMP activity in droplets during the course of 14 hours in culture. (B), (C) Cellular heterogeneity and dynamic response; heat map presenting the relative fluorescent intensity in droplets containing one cell in (B) and different number of cells (0, 1, or 2 per droplet) in (C). Red color represents high MMP activity and blue color shows low MMP activity. 214

Figure 6.47: Cellular heterogeneity and dynamic response; heat map presenting the relative fluorescent intensity in droplets containing no cell, 1 cell and 2 cells (n=34, 45, and 35 respectively). Red color represents high MMP activity and blue color shows low MMP activity. Bottom: Image of 44 droplets containing different number of cells, Scale bar: 800 μ m. 215

Chapter 1. Introduction



1.1. Overview

Cells in the tissue and organs live in a dynamic microenvironment known as “niche”. This dynamic state is caused and controlled by several factors such as communication with the neighbouring cells, cell-matrix interactions and cellular secretion. Such events can be divided into two major categories: Biophysical events which take place (e.g. cell migration during tissue regeneration) and biochemical parameters involving cellular secretion and uptake. The capability to quantify these events can reveal hidden aspects of cell dynamics.

Capturing the dynamics of cells behaviour require specialized tools capable of tracking cells over extended period. Live-cell microscopy is the most prevalent equipment for imaging cells and providing time-lapse data. Depending on the cell type and the phenotype to be measured, the signal readout could be visualized with bright-field microscopy or through implementation of a fluorophore targeting a certain biomarker using fluorescent microscopy.

While live-cell microscopy can resolve the time of a dynamic cell event, a bigger challenge is the spatial resolution and accurate positioning of the cells in the cell culture chamber. The importance of cell positioning can be seen in phenomena such as collective cell migration, cell co-culture, cellular secretion/uptake. For example, studying cellular dynamics in co-culture requires positioning cells in a certain distance allowing free cell migration and proliferation.

In particular, two cell positioning modes are of high interest: bulk cell positioning and single cell positioning. Bulk cell positioning refers to methods for controlling the position of many cells (e.g. patterns of cells in collective cell migration) and single cell positioning refers to methods for separating single cells to be able to study their individual response.

Despite the importance of cell positioning, little attention has been dedicated to this topic either because positioning cells requires delicate manipulation via advanced engineering tools not present in medical research laboratories or because the available methods are costly, time-consuming and requiring engineering expertise.

The problem of cell positioning has different layers. First, the biological requirements: Depending on the phenomenon to be investigated the geometrical constraints of the culture environment needs to be modified. For bulk cell analysis this means cells should be spaced at certain distances and in certain shapes to mimic the physiological environment. In addition, there should be enough space for the cells to proliferate during the microscopy timespan. In some biological events such as migration or outgrowth, cells or cell parts should reach certain locations within a timeframe. Another important biological requirement is the volume of the culture environment. This is to make sure cells receive sufficient amounts of nutrition. Furthermore, in a phenomenon such as single cell secretion, the volume of the culture environment determines the time of the assay.

The second layer of the cell positioning problem is the positioning mechanisms and their corresponding interfaces. The available methods rely on surface chemistry, requiring surface treatment with chemical substances that may harm cells, or use of external acoustic, electrical, optical, and ultrasound forces to move the cells in the culture environment which can have adverse effect on cell behaviour. Both methods do not offer high throughput and are time consuming and laborious to perform. Microfluidics has been used to handle chemical and biological samples and can circumvent problems associated with the previous methods. It provides high throughput and uses a small volume of biological samples. However, even most of the microfluidic methods rely on external forces to operate. Standing acoustic waves [1], dielectrophoresis [2], and optical tweezers

[3] are among these methods. While providing positioning accuracy, these methods require bulky and specialized peripheral equipment, and may alter cell function through biophysical and biochemical interactions. The adoption of a passive, label-free microfluidics can therefore be an ultimate solution for sample positioning.

Passive sample positioning methods have some unique characteristics, the most important of which is using geometrical constraints to position a biological sample. Therefore, hereafter we refer to passive positioning techniques as passive confinement approaches. While previous researches have studied the fluid mechanics of the passive microfluidic confinement, the effect of capillary pressure as a determinant trapping factor and its relation to cell confinement for studying dynamic cell behaviour has not been investigated. Some of these aspects include the effect of the channel/trap geometry on the distribution of pressure in the liquid sample, systematic induction of regions of high and low pressures based on analysis of the flow field, and the effect of capillary pressure in microchannel's narrow spaces as a confinement tool. Particularly, leakage-free operation of passive microfluidic confinement systems bonded temporarily against a substrate of choice has not been considered. A temporary bond can offer many capabilities for studying cell dynamics including free migration of cells, and access to individual cells post assay.

This thesis will therefore focuses on the deep understanding of the microfluidic mechanisms in which capillary pressure can be used to confine cell samples and investigate their application for studying cellular growth, and migration dynamics, as well as time-dependent cell secretion/uptake.

1.2. Dynamic cell behaviour and cellular positioning

Cells receive physical and chemical signals in three modes of autocrine, paracrine and juxtacrine signalling. These signals then cause the cells to respond in the form of biophysical events such as growth, migration and morphology change as well as biochemical events such as secretion of proteins or uptake from their environment and subsequently signalling other cells. This cycle is an ongoing process and under normal condition is called homeostasis. Cells state such as its viability, proliferation (growth), migration, outgrowth and secretion can therefore be changed dynamically.

- Cell viability can change due to the adverse effect of the environment such as the presence of a drug. Measurement of the viability rate over time is therefore not only indicative of a biological phenomenon targeting the cell, but also a measure of the effectiveness of the biological assay to maintain cell viability over the course of the experiment.
- Cell proliferation is an event in which cells divide and their number increases over an extended period of time. Mammalian cells normally divide every 24 hours. However, this trend can be affected by a variety of events through different signalling pathways. In some event such as cancer, cells are dividing abnormally and without control. This fast proliferation can happen due to interaction with the stromal cells or from external stimulation disturbing the normal cell decision-making and replication process. Another important case where proliferation should be monitored as a cell dynamics characteristic is in cellular differentiation. One physical marker of cell differentiation is the growth arrest and reduced cell division [4, 5]. Neuron cell do not replicate and therefore proliferation does not exist with them.

- Cell migration is a complex phenomenon which takes place to develop or maintain the function of an organ (Fig. 1.1). It is an essential part of morphogenesis, tissue remodelling, wound healing and other regenerative and responsive events. Migration as a dynamic phenomenon can be seen in two aspects: First, the process of migration and the molecular aspects of cell stimulation for migration. This aspect includes cell adhesion, polarization and layered motility. The second aspect is the physical parameters of migration. These include directionality, persistence and directed migration, migration speed among others. Migration can be impaired or augmented through immune related issues which consequently lead to problems such as vascular and chronic diseases, and cancer.

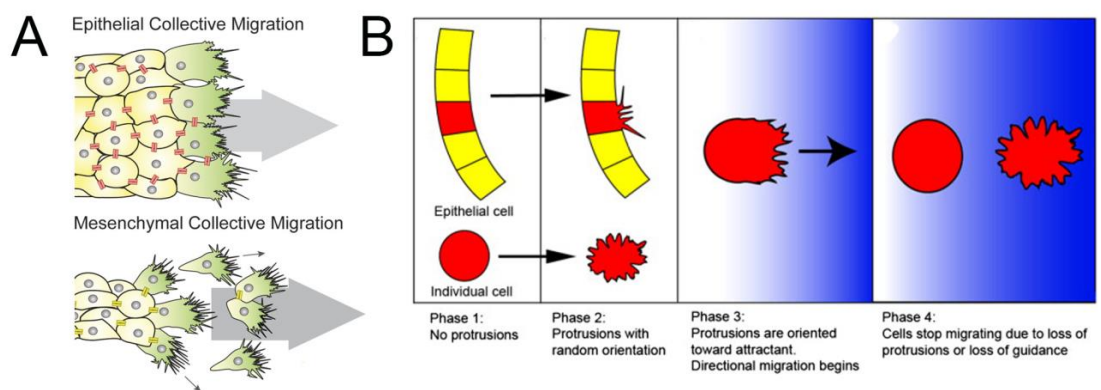


Figure 1.1: Dynamic biophysical events. Cells migrate in two ways. (A) Collective migration of cells happens when several cells migrate together. [6]. (B) Each single cell may migrate individually due to exposure to chemical gradients in the environment in a process known as chemotaxis [7].

- Neurons constantly explore their environment, taking up chemical signals and transmit them to the central nervous system for decision making. In order to understand nerves behaviour, it is crucial to monitor axons (the neurons exploring part) growth dynamics in response to external stimuli. An axon can be guided into certain direction, forced to stop growing in a harsh environment or bypassing the tissue's affected area to bind to the next nerve and transmit the message.

- Cells either receive or produce biomolecules including proteins, growth factors, and enzymes among many others. Depending on the type of study, there are different methods and biomarkers available for measuring cellular secretion or uptake. For example, in order to measure the amount of protein in biological samples western blotting and ELISA are being used. These methods are well practiced and characterized. However, the remaining question in studying cellular secretion and uptake is the contribution of single cells. This is proposed as the problem of cellular heterogeneity. Such measurements necessitate a method to separate a single cell, encapsulate it and using a biomarker that can bind to the secreted molecule or to the specific organelle and fluoresce to provide measurable signals.

1.2.1. Cellular positioning

Position of the cells is a determinant factor for studying dynamic cell behaviour. Firstly, in most of the physiological events, cells and the interacting component are communicating through paracrine signalling. This means that signalling molecules are travelling a distance between the interacting component and the cells. Hence, it is crucial to position the cells in a physiologically relevant distance (as shown in Fig. 1.2). Secondly, in order to be able to measure dynamic biophysical events, accurate cell spacing is required. For example, in order to measure the morphology and migratory behaviour of the cells during tissue regeneration, cells must have enough space to freely migrate in a limited space. This space is also important for successful measurement of the biophysical event with time-lapse microscopy.

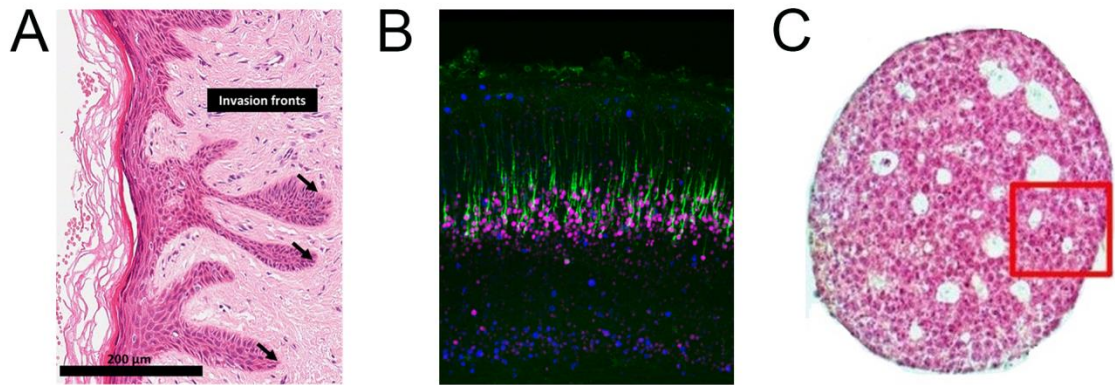


Figure 1.2: Images of the cell position in three fundamental tissues: (A) Squamous cell carcinoma and the surrounding stromal cells [8], (B) Patterned neurons of mice cortex [9] and (C) Embryonic bodies during development [10].

Thirdly, some of the cellular events happen at the single cell/single spheroid level. This includes biochemical events such as cellular secretion or biophysical events such as death rate in a tumour spheroid. Quantifying these dynamic events are needed to understand the cellular heterogeneity and in problems with multiple cell dynamics variants (Fig. 1.3). In order to monitor such events, one should be able to immobilize the biological sample in specific sometimes isolated environments so that each cell/spheroid can be monitored individually. Cell positioning can therefore take different forms depending on the dynamic event to be studied. This includes cell patterning, cell trapping and releasing, and cell encapsulation.

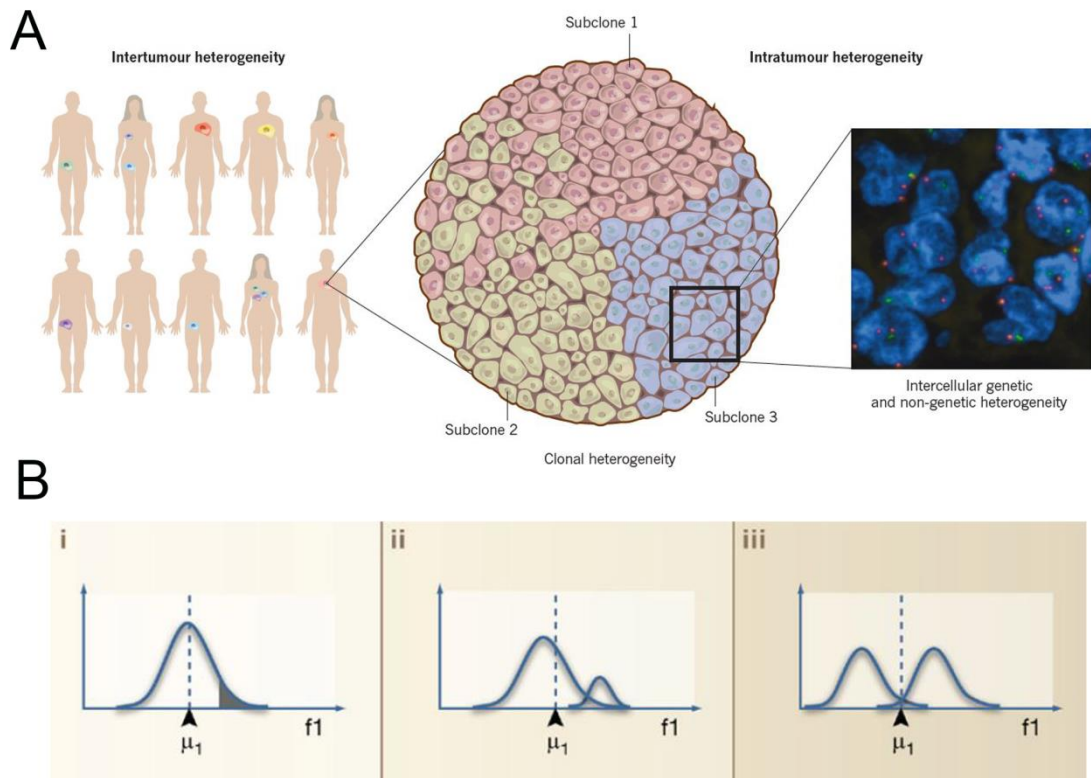


Figure 1.3:(A) Heterogeneity exists in genetic and phenotypic characteristics of cells at the inter-tumour and intra-tumour levels [11]. (B) Average measurement can hide the cellular heterogeneity: Behaviours of cells in (i) at the ends of the distribution function (grey area) or (ii) Subpopulation (with a different mean value from the rest of the sample (μ_1 : mean of the sample)). (iii) The mean of two divided subpopulations may not be representative of the population [12].

Studying each cell-dynamics problem demands a special positioning technique which meets the requirement of that specific problem. For example, in tracking neurite growth, neurites should be patterned in specific distance from each other. In the cancer invasion assays, cancer cells and stromal cells should be cultured in certain proximity. In addition, in measuring cellular secretion, it is essential to encapsulate the cells to maintain each cell chemical signature. To cover this wide spectrum of analyses, different positioning methods based on surface chemistry have been proposed (Fig. 1.4). These methods rely on pre-stamping a substrate with proteins [13, 14] or other chemical groups [15], followed by cell seeding and their selective attachment to the stamped regions [16]. In such methods the number of stamped molecules cannot be accurately controlled due to poor stamping repeatability. Patterning of two cell-types using this method is highly

challenging as it requires the pre-patterning of two cell-selective molecules, as well as aligning the pattern between subsequent steps while eliminating the cell-to-cell cross-contamination [17].

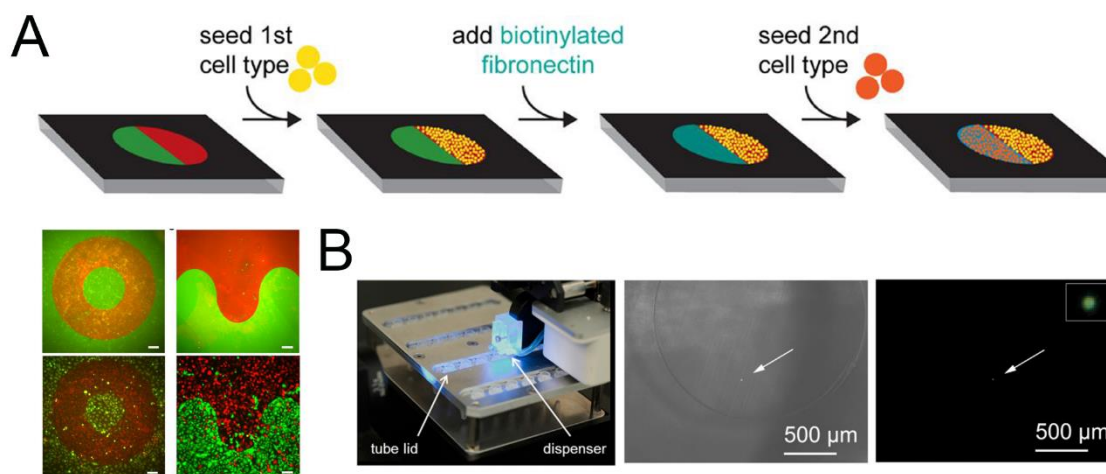


Figure 1.4: Methods for cell positioning at A) Multi-cellular level using surface chemistry [16] (further permissions related to the material excerpted should be directed to the American Chemical Society (ACS) <https://pubs.acs.org/doi/abs/10.1021/la404037s>) and B) Single cell level using cell dispensing [18].

Methods for single cell positioning are diverse and can be done with physical forces such as in single cell printing [19] and dispensing [18] methods, and use of magnetic forces [20], and laser and optical fibre based systems [3]. Though innovative, these methods have low throughput, may damage the cells, and require an external equipment to be operated. In addition, single cell seeding efficiency and viability is quite low. Most importantly, none of these methods can provide an environment to maintain the single cell's secretome and hence cannot give valid response for intercellular heterogeneity.

1.3. Microfluidic sample confinement

Over the past decade, microfluidic systems have been developed for a variety of cell-dynamics events based on cell positioning. The capabilities and advantages offered by microfluidic sample positioning such as high throughput, low sample consumption and

cells patterning, and single cell encapsulation accuracy makes it an ideal choice for cell-dynamics events (Table 1.1).

Table 1.1: Time and cost of the sample screening using robotic versus microfluidic methods [21].

	Robot	Microfluidic drops
Total reactions	5×10^7	5×10^7
Reaction volume	100 μ L	6 pL
Total volume	5000 L	150 μ L
Reaction/day	73000	1×10^8
Total time	~ 2 years	~ 7 hours
Number of plates/devices	260000	2
Cost of plates/devices	\$ 520000	\$ 1
Cost of tips	\$ 10 million	\$ 0.3
Amortized cost of instruments	\$ 280000	\$ 1.7
Substrate	\$ 4.75 million	\$ 0.25
Total cost	\$ 15.81 million	\$ 2.50

Several microfluidic sample trapping methods use external forces such as acoustic forces, dielectrophoretic forces or optical tweezers. These methods although accurate, need special engineering expertise and are both complicated to design and operate (Fig. 1.5). In addition, the presence of such forces signals the possibility of impaired cell function [22-24]. These complications demand passive methods which use only fluid flow for guiding cells and position them in predefined locations.

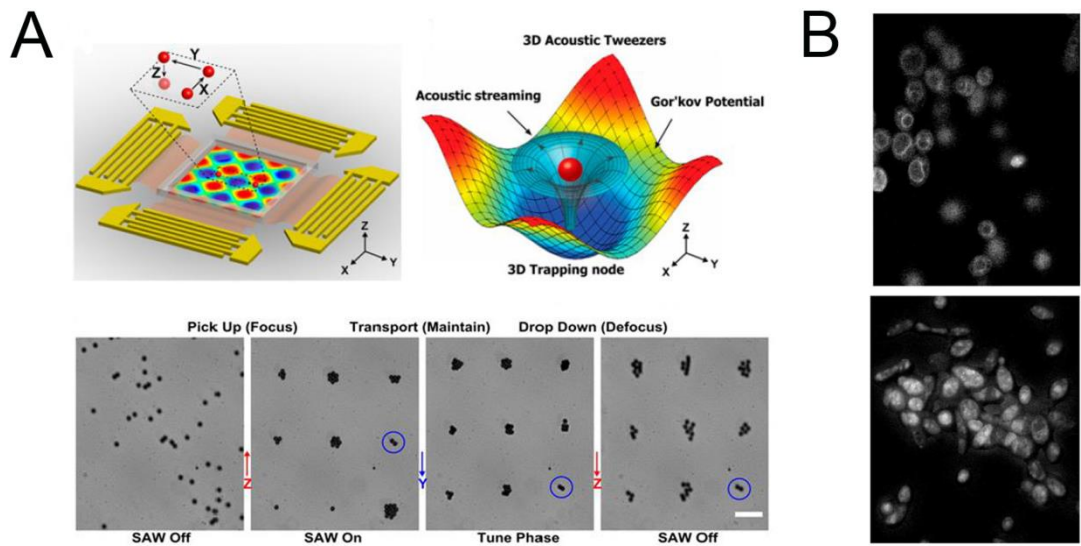


Figure 1.5: A) manipulation of single cells using surface acoustic waves, Bottom: Modes of operation [25] B) Control (a) and sonicated (b) yeast cells suspended in a 12% (v/v) water–ethanol mixture stained with fluorescence vacuole membrane dye [26].

Before thinking about passive mechanisms for cell sample confinement, it is crucial to take note that such mechanisms depend highly on the biological problem for which cells are being positioned. For example, if a bulk of cells is needed to be confined in one part of a microfluidic device, then the aim is to position the cells immersed in media. For the single cell confinement on the other hand, a single cell needs to be encapsulated in a droplet or trapped in a chamber. In these two cases the sample is a liquid containing cells (Fig. 1.6A). In contrast, for the other group, it is required to trap the cells one by one to study them separately. In such cases the sample is the cell or a spheroid and therefore the path through which the cell/spheroid moves in the flow is of special importance (Fig. 1.6B).

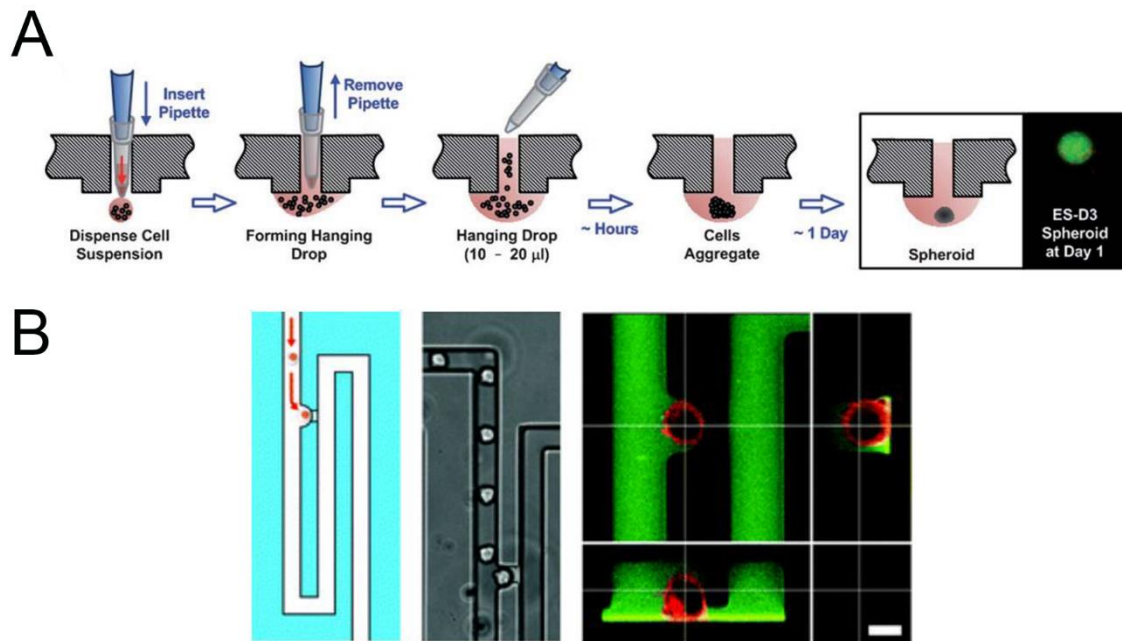


Figure 1.6: A) The concept of pressure-modulated passive cell positioning: Cells aggregate in hanging drop mode based on the surface tension between the liquid and the solid surface leading to formation of cell spheroid [27]. B) single cell are trapped in an array of cell traps due to difference in flow pressure in two paths [28].

1.4. Thesis outline

The goal of this project is to investigate the dynamic cell behaviour through novel cell positioning methods based on incorporation of capillary effects to confine cell samples in microfluidic systems. Depending on the phase of the cell samples i.e. liquid or solid samples, we assess potential cell immobilization mechanisms based on manipulation of flow pressure for patterning and trapping cell samples. The outcome will be led to new approaches for rapid and reliable performing of assays for studying cell migration, outgrowth and secretion dynamics.

Recent cell positioning methods based on microtechnology and microfluidics as well as microfluidic methods for performing cell dynamics assay are reviewed in Chapter 2. As will be shown, several approaches have been developed for a variety of cell positioning assays. However, little attention has been dedicated to understanding the role of flow

pressure as passive, label-free and non-invasive methods of cell trapping and the relationship between the microfluidic cell positioning and the dynamic cell event.

Chapter 3 provides analytical and numerical analyses of the microfluidic cell positioning mechanisms and explain the role of pressure as a determinant factor in cell positioning.

In chapter 4, a new microfluidic stamping method based on capillary pressure will be introduced as a method for patterning cells and proteins with any arbitrary geometry. The method is then used to study cell migration patterns in a co-culture of cardiac stem cells and endothelial cells as a mimic of the myocardial infarction. A thorough explanation of the experimental procedure including the cell culture, imaging and analysis will be provided. The experiment employs time-lapse microscope to track cells proliferation and migration behaviour over the course of 7 days culture in-vitro. The outcomes of this chapter is published in “A rapid co-culture stamping device for studying intracellular communication, Scientific reports 6, 35618” [29].

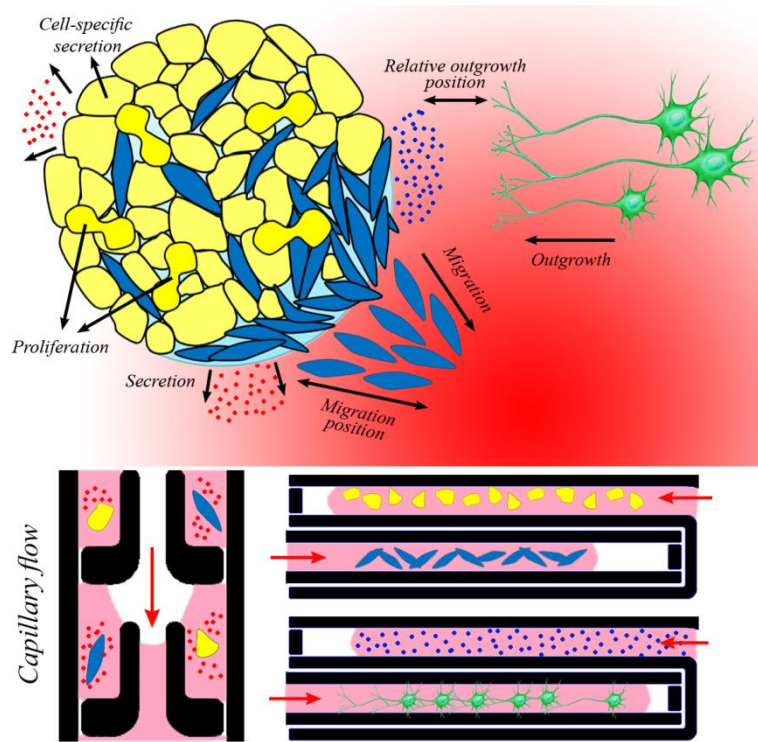
Chapter 5 presents a novel stamping assay for tracking neurite outgrowth dynamics in presence of inhibitory substrate. The results reveal that a family of actin cytoskeleton known as Tpm 3.1 are effective in maintaining the structural stability of neurite growth cone during central nervous system (CNS) injury. The results are presented in “A novel microfluidic device-based neurite outgrowth inhibition assay reveals the neurite outgrowth promoting activity of Tropomyosin Tpm3.1 in hippocampal neurons, Cellular and molecular neurobiology 38, 1557-1563” [30].

Chapter 6 introduces a novel static droplet array based on capillary pressure used for liquid sample compartmentalization into nanolitre droplets. It provides a new insight into how such system works and how it can be used to trap cell-laden samples into individual units with special application in single cell-analysis and secretion response. As an

example, MMP secretion of single breast cancer cells over 12 hours of culture is quantified and reported. The outcome of this chapter is published in “Static droplet array for culturing single live adherent cells in an isolated chemical microenvironment, Lab Chip 18, 2156-2166” [31].

Finally, Chapter 7 concludes the key findings of this thesis and summarises the methods through which effective patterning and trapping of cell samples can be done as a preliminary step for studying dynamic cell behaviour.

Chapter 2. Cell dynamics via capillary-based geometrical sample confinement



Cell dynamics takes place in a niche with micrometers of length scale. A necessity of studying cells at such small scales is a spatial control over their location. Almost all biological events are dependent on the location of the cells either through different cell patterns, cell-cell and cell-environment crosstalk. In this chapter, a detailed review of the microfluidic systems for cell sample micro-confinement is presented. The first part of this review presents the microfluidic techniques employed for positioning cells. These methods are compared based on their operation mechanism, challenges in operation, and suitability for studying cell dynamics event. In the second part, methods of employing capillary forces in microfluidic devices are briefly reviewed and the mechanisms for capillary-based geometrical confinement of cells are presented in detail. Next, cell-based assays performed using the capillary-based systems are reviewed to provide the reader with the latest application of these systems in understanding different aspects of cell dynamics. The final part of this review discusses the cell dynamics events at the microscales. We close this chapter with a brief overview of how our method of sample confinement is different from the presented literature as a transition step towards the next chapters.

2.1. Microfluidic sample confinement techniques

Depending on the spatial position of the cells in a dynamic cellular event, different sample confinement strategies can be adopted. Two major methods include sample patterning and sample trapping. Sample patterning is required in studying those events in which the arrangement of the cells and their relative position to the other cells/environmental factors is required. Therefore, this method is suitable for making microfluidic models of cell migration and intracellular signalling. Sample trapping on the other hand, can be used for studying single cell dynamics where separating single cells and maintaining them in culture during the event is required. Here we review the available methods of cell confinement and compare them together based on different criteria.

2.1.1. Sample patterning

Chemical patterning

This method is based on the fact that different cells express different levels of adhesion molecules such as cadherins and integrins which consequently lead to their preferential adhesion to certain substrates (Fig. 2.1A). To be able to pattern the cells, photolithography is used to make patterns of channels on a photoresist-coated surface. Once the pattern is made, the adhesive molecule is poured onto the surface, and fills the channels. The photoresist was then removed from the surface leaving the pattern of adhesive molecule on the surface. Next, cell suspension is poured onto the surface. Cells will preferentially adhere to the patterned area and the rest of the cells are washed away [32]. An alternative approach has been introduced in which the silicon surface is first modified with adhesive molecule (Type VI collagen) followed by spin coating of PVA photoresist, post exposure baking and development [33]. One of the main advantages of this system is the accuracy of the patterns offered by the photolithography process. However, this method has a number of drawbacks: 1) It relies on complex photolithography process and mask

fabrication, 2) It involves use of chemical compounds such as photoresist which may have negative impacts such as cytotoxicity, 3) to be used in patterning multiple cell types, it is dependent on relative adhesiveness of those cells to their corresponding substrate and the other cell type.

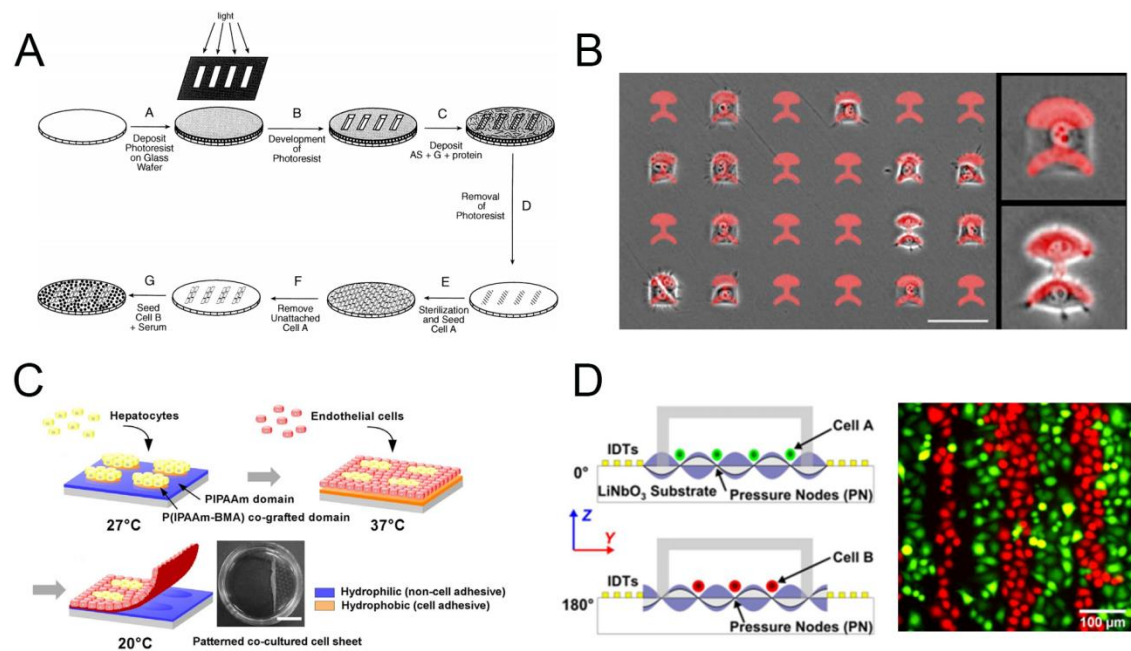


Figure 2.1: Sample patterning techniques: A) Chemical patterning: Schematic illustration of the process to generate micropattern of two cells in co-culture condition [32], (B) Soft lithographic patterning: Microcontact printing of fibronectin stamp with PLL-g-PEG as background; HeLa cells are patterned on the fluorescently labelled fibronectin patterns (in red) [34], (C) Active surface modification: Thermally responsive polymers are used for patterned co-culture of hepatocytes and endothelial cells [35], further permissions related to the material excerpted should be directed to the American Chemical Society (ACS) <https://pubs.acs.org/doi/abs/10.1021/ac502453z> (D) Active cell patterning: SSAW-based sequential cell patterning by patterning cells in the nodes and anti-nodes of the acoustic field [36].

Soft lithographic patterning

Microcontact printing is a well-known method based on soft lithographic fabrication of PDMS stamps which is used to print proteins and adhesive substrates on the surface. The PDMS stamp containing microstructures is made in contact with the solution of the adhesive substrate and pressed against the substrate to transfer the adhesive molecules onto the surface coated with a cell repellent molecule (Fig. 2.1B). Cells are then deposited on the substrate, let to attach and then the residual cells are washed away [34, 37, 38]. Microcontact printing offers a simple approach for cell patterning; however, there are

several drawback regarding the complete and uniform transfer of molecules to the surface, features buckling, lateral collapse and sagging [37].

PDMS based stencils use thin film membranes with different pore size to pattern cells. The membrane is first brought in contact with the substrate and the cell solution is transferred onto the membrane. Once attached the membrane is removed from the substrate [39, 40]. The main problems associated with PDMS stencils handling difficulty and low mechanical strength.

Active surface modification

The chemical interaction between the substrate molecules and the external forces such as electrodes, light and heat can be used to change the surface properties and lead to selective attachment of cells to the substrate. Mrksich et al. introduced a chemical coating of hydroquinone and penta(ethylene glycol) groups in a ratio of 1:99. By applying an electrical potential of 500mV for 10 seconds, hydroquinone was oxidized to quinone and RGD-Cp peptide enabling cell attachment on the surface [41]. Other mentionable switchable materials include thermally responsive polymers [35], and electrically oxidizing protein coated substrate [42]. Active surfaces open new windows to control cell attachment, spreading and even migration; however, they require delicate control of the substrate properties, involve several surface chemical treatment steps and application of an external force that may damage and perturb both the adhesive molecules and the cells.

Active cell patterning

The use of external force to manipulate cells rather than substrates is another method of cell patterning which can provide patterns with high spatial resolutions. Standing surface Acoustic Wave (SSAW) for example can be used to induce pressure fluctuation that moves the suspended cells to the pressure nodes or antinodes in the SSAW field [1, 36]. Magnetic field has also been used to pattern HUVEC cells labelled with magnetite

cationic liposomes (MCLs) and magnetic field gradient concentrator [43]. Although cell patterning is more repeatable with active methods, the use of external force can alter cell fate and impair the biological study for which the patterned cells are designed for.

2.1.2. Sample trapping

Sample traps are designed to study the cell dynamics in individual samples trapped into separate compartments. Depending on the requirement of the biological assay, these compartments need to be physically and chemically isolated or they can share their environment. Methods of sample trapping are diverse and depend on the sample size.

Sedimentation trapping

In this method, the sample is let to settle in a microwell based on gravitational force. The number of cells per well depends on several factors including the procedure of sample loading, initial concentration of the cell sample, settling time, and the shape and size of the wells. Samples of different size from single cells [44, 45] up to tumour spheroids [46, 47] have been trapped and cultured in microwells. Coating of the surface of microwells has enabled a variety of assays including cell secretion assays, gene expression analysis and enzymatic assays. The microwell systems are simple to operate however, the cell capture efficiency, the amount of cell sample used for loading the microwell system and the crosstalk between samples in different wells have been some of the problem associated with these systems.

Dielectrophoretic trapping

Dielectrophoresis is a force applied on a polarized cell or particle within an electric field with non-uniform spatial distribution. The manipulation mechanism is based on application of electric potential on the cell membrane which leads to formation of permeable pores [48]. Important features of DEP sample trapping are its short response

time, and fast and stable cell trapping and releasing of the cells. In addition the active system can be used for the cells with different size, adherence, and shape [49, 50]. However, there are some concerns regarding the effect of dielectrophoretic force on the cell's viability and fate, as well as membrane rupture due to application of high voltages. In addition, the need for implementation of electrical circuits makes it a tough choice for biologists with no engineering expertise.

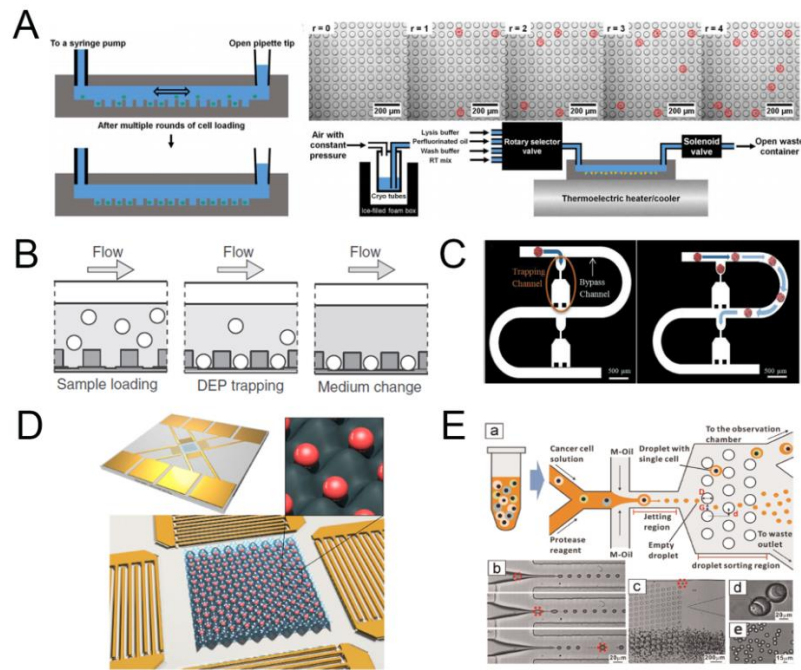


Figure 2.2: Sample trapping techniques: (A) Sample sedimentation in microwell arrays. Single cells are isolated in microwells after multiple rounds of loading the cell suspension [44], (B) Dielectrophoretic trapping and lysing of single cells using DEP forces achieved via selective patterning of interdigitated ITO electrodes under the microwell arrays. A PDMS membrane is used to close and separate the microwells from each other [48], (C) Hydrodynamic trapping: Schematic illustration of sequential cell trapping, once a cell/spheroid fills one trap, the rest of the samples are guided to the next set of traps [51], Published by Royal Society of Chemistry (D) Acoustic trapping of single cells in a two dimensional domain created in microwells by application of surface acoustic waves [52], and (E) Droplet encapsulation: schematic illustration of single cell encapsulation in Picoliter droplets followed by size-based sorting of the droplets containing single cells into a separate channel using DLD system [53].

Hydrodynamic trapping

This passive single cell trapping approach is based on the preferential flow of the cells towards the microchannels with lower flow resistance. The design of these channels includes a trapping channel and a bypass channel. Once a trap is filled, the rest of the cells

are guided towards the next trap. Geometrical dimensions of the trap channel and the bypass channel should be set to give the bypass channel higher flow resistance. The size of the trap is also adjusted based on the size of the cell sample [51, 54-56]. The chip made based on resistive trapping requires a big area for accommodating bypass channels and needs cell sample to have a uniform size. Most importantly, the cell media is shared among different traps impairing each cell's chemical signature.

Cell docking

Cell docking devices are basically comprised of several obstructions. The working mechanism is simple: Once a trap has been occupied, the flow around that trap guides the rest of the cells to the unoccupied traps [57, 58]. Docking arrays have simple designs; however, they also have the issue of shared media between the trapped cells. In addition, the possibility of cell clogging at high concentrations as well as losing high percentage of the initial cell sample reduces the reliability of these systems.

Active sample trapping

Besides dielectrophoresis, optical, magnetic and acoustic forces can also be used for single cell patterning and trapping. In optical trap for example a laser beam is used to accurately position a single cell [3, 59]. However, the focused power generated by the laser can lead to cell damage. Magnetic [60] and acoustic forces [52, 61] are non-contact methods of single cell manipulation. However, both methods require large amounts of sample and even with that there are concerns regarding the generation uneven magnetic/acoustic fields as well as exertion of extra force on single cells having adverse effect on their behavior.

Droplet microfluidics

Droplet microfluidics refers to dynamic production of monodispersed droplets using two immiscible liquids such as water and oil. In these systems, the stream of one liquid is cut and segmented leading to formation of droplets of different size and with different frequencies [62]. The size of the droplet is normally in femtoliter to nanoliter ranges [62, 63]. Encapsulation of cells in droplets has several advantages that do not exist in other trapping methods. These include isolation of droplets content, rapid mixing of reagents and possibility of recovering the cell samples after the experiment. In addition, cells are encapsulated at the rates of 1-10 kHz leading to fast and high throughput encapsulation of thousands of cells [64, 65]. One of the main drawbacks of droplet systems is the complexity of operation and instability in performing the assay which may lead to unwanted modes of droplet formation [66, 67]. In addition, the possibility of cell encapsulation is quite low. Most importantly, controlling the droplet logics such as droplet mixing, sorting and merging is challenging [68, 69]. This is obvious in performing long-term assays in which the generated droplets need to be maintained and monitored over time. Different methods of cell docking have been proposed which use bypass trapping and vertical posts [70, 71].

2.2. Capillary-based sample confinement

The motivation behind this thesis was to introduce a new approach of cell confinement which 1) is solely based on passive sample manipulation with no over-time flow control 2) is capable of providing different confinement techniques, i.e. both sample patterning and trapping. Besides active cell manipulation techniques which use an external force for sample confinement, other methods either need extensive efforts dedicated to operate peripheral systems (e.g. droplet encapsulation technique) which conflicts their promise as Lab on Chip systems or rely on the chemical and physical factors as in different methods of chemical patterning as well as mechanical sample trapping. Therefore, the

focus of this thesis is to find a technique that combines ease of operation, sample and reagent economy and lower cost. Capillary effects are dominant forces in microchannels as the size of the channel becomes smaller. Although capillary microfluidics has been adopted for performing diverse assays [72-76], the role of capillary forces in manipulating the liquid-air interface and the possibility of using this force as a tool for sample confinement has not been addressed. In this thesis we investigate the question on the role of capillary forces in confining samples in microfluidic systems and accordingly propose novel systems of cell patterning and cell trapping. Before reviewing the mechanism of capillary-based sample confinement, we present the fundamental aspects of capillary microfluidics as a preliminary tool for studying capillary-based confinement techniques.

2.2.1. Capillary microfluidics

Capillary microfluidics uses the surface tension effect to control the liquid flow based on the channel geometry and the channel's surface properties. One of the pioneering works to investigate the relationship between the capillary pressure (the pressure at the liquid-air interface) and the geometry was reported by Beebe's group [77]. In their work, they investigated the possibility of using the surface energy of small liquid drops to initiate a flow from one port of a microchannel to the other port. According to Young-Laplace equation the smaller droplets possess higher pressures. They used this fact to push the smaller droplet with higher positive energy towards bigger droplets enabling them to control the flow direction and speed. In their work, they reported calculations and experimental analysis of the flow rate in self-pumping capillary microchannels [78] and employed this principle to perform microfluidic logics on different samples [79]. Although offering operational simplicity, this method can produce only slow flows due to small pressure differences between the droplets at liquid ports and can suit only those

applications which require transferring samples from one side of the channel to the other side.

2.2.2. Capillary pumping

Capillary pumping is the phenomenon in which the capillary force is used to move the liquid sample in the microchannel. The principles of capillary pumping and liquid-air interface transport in a microchannel are described by the capillary induced potential at the convex and concave meniscus with increased potential at the convex meniscus and decreased potential at the concave meniscus. This theory has been used to explain the capillary-induced flows, flow halting in a microchannel, and electrocapillary and thermocapillary effects [80].

A broad range of capillary-based microfluidic pumping systems are dedicated to autonomous systems with hydrophilic walls enabling a negative pressure at the liquid-air interface and suction of the liquid sample into the device. For instance, a combined capillary/evaporation driven pumping of liquid samples with stable flow rates have been proposed. The driving force here was the pressure difference across a curved meniscus at the bottom corners of the outlet port [81]. Other means of capillary pumping and guiding has been introduced using different microstructure geometries [82, 83]. These methods are based on introducing repeated patterns of different shapes which increases the surface tension force at the hydrophilic surface and pulls the liquid from the upstream towards the downstream. Using the microstructure density, shape, position and continuity as the baseline design factors, different capillary pumps with controlled volumetric flow rate in the range of nanoliter per second were developed [82].

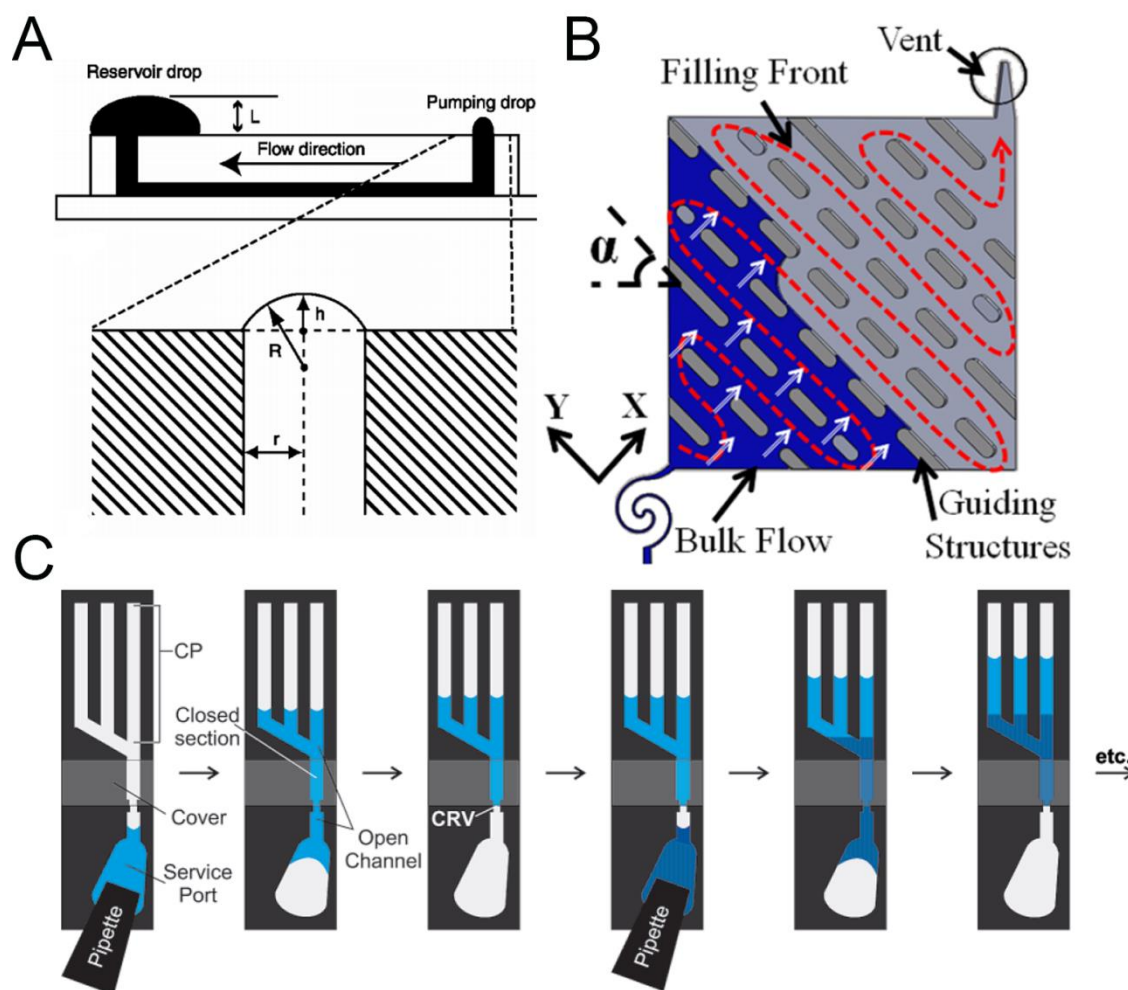


Figure 2.3: Fundamental of capillary-controlled fluid flow in microchannels: (A) Using capillary pressure difference between two ports of the microchannel to control the flow direction and speed [77]. (B) Capillary pumping based on repeated patterns of microstructures: A serpentine capillary pump allows the liquid to be filled sequentially from one row to another [83]. (C) Capillary sequential system: A branched capillary pump is sucking a liquid sample placed at the inlet port due to hydrophilicity of the channel walls. When the liquid sample reaches the capillary retention valve, the meniscus is pinned and the liquid flow is stopped until the next sample is injected into the system [84].

2.2.3. Capillary sequential systems

Since the magnitude of the capillary forces can be altered by the geometry of the microchannel, the primary application of this change is in sequential delivery of liquids in a microfluidic system. For instance, a combination of autonomous valving and pumping based on capillary phenomena has been reported which is able to transport liquids in sequence [84, 85]. The presented capillary device comprises of three functional parts: a service port for loading the sample, a capillary pump which sucks the liquid into

a branch of capillary microchannels, and a capillary retention valve mounted before a reaction chamber which stops the liquid from further movement (Fig. 2.3C). The liquid sample is first spontaneously moving into the capillary and fills the capillary pump area. The capillary pump uses the combined capillary forces at different branches to suck the liquid until there is no liquid remain in the inlet port and the liquid is pinned at the retention valve. This procedure is then repeated for sequential addition of the new samples. This method is used for performing a sequential immunoassay which requires multiple steps of liquid reaction and washing from the reaction chamber [84]. Based on the knowledge of sequential delivery of liquids and using the concept of Retention Burst Valves (RVBs), liquid samples were trapped in different reservoirs equipped with burst valves possessing different burst pressures. Simultaneous application of pressure to the system enabled opening them one by one and delivering the samples in a sequential manner and on demand. The assay has been used to deliver bacteria sample, detection antibody and fluorescent tags into a channel pre-coated with microbeads conjugated with capture antibodies [86].

2.3. Capillary microfluidics sample confinement: mechanisms

2.3.1. Suspended microfluidics

The concept of suspended microfluidics for open microfluidic platforms has been introduced which is capable of filling and maintaining liquids in microstructures with no ceiling and floor [87]. The authors use the term spontaneous capillary flow (SCF). In this mechanism, the liquid-air front moves in the open microchannel once the surface energy reduction at the liquid-solid interface is higher than its increase at the liquid-air interface (Fig. 2.4A). By designing apertures at the bottom of the flow channel, this device enabled creating arrays of collagen membranes known as micro Dots for multiplexed analysis of cellular invasion. In another research on this mechanism, spontaneous capillary flow in a

diverging open channel has been investigated. It is shown that in such channel geometry, the fluid does not flow indefinitely but rather stop at some location along the microchannel. For a linear diverging channel, this location has been analytical derived and reported [88].

2.3.2. Droplet metering

Burns et al., introduced a novel mechanism for metering nanolitre-size droplets using a hydrophobic patch patterned at specific locations in the microchannel (Fig. 2.4B). By blowing air through a splitter channel crossing the main channel, the device can produce nanolitre droplets with exact volume. This research also explains theoretically the mechanism of liquid stoppage at the hydrophobic patch area [89].

2.3.3. Capillary burst valve in centrifugal systems

The concept of capillary burst valve has been investigated in a number of researches related to centrifugal microfluidic platforms (Fig. 2.4C). In these systems, the pressure at the back of the liquid-air interface is controlled by the centrifugation parameters such as spinning rotational speed [90]. In order to let the liquid pass from one stage to another several strategies have been employed. Cho et al. presented a theoretical analysis of the pressure distribution in the geometry of a burst valve, explained the theoretical pressure drop across the valve and consequently calculated for the amount of angular velocity of the centrifugal system causing valve to burst. They also performed an experiment reporting for the variation of the bursting speed with channel width [91]. Similarly, Kazemzadeh et al. numerically investigated the flow in passive capillary microvalves in a centrifugal system with superhydrophilic and hydrophilic surfaces. Their investigation showed that burst frequencies depend on the channel width and is lower for wider capillaries [92].Based on the confinement of liquids behind burst valves in centrifugal

devices, a new sequential sweat testing device has been introduced. The system is a wearable device that is comprised of burst valves of different geometries each with different burst pressure. Using this device a time-varying chemical analysis of different ions concentration present in the sweat sample has been performed [93].

2.3.4. Multilevel expansion valves

A capillary stop valve based on the introduction of an expansion area in the channel design is known as a multilevel expansion valve and can be used to stop liquid flow in planar microfluidic systems (Fig. 2.4D). The numerical simulation of the flow in such geometry was performed by solving the free surface equilibrium equation using finite element method. The design comprises of a nozzle- shaped channel of height $15\mu\text{m}$ which opens into a wider channel with the height of $110\mu\text{m}$. The design's burst pressure was reported as a function of channels width and height ratios [94]. The multilevel expansion burst valve has also been used for stopping the liquids for an antigen-antibody assay. In this device first antibody is patterned at the bottom of the device using filling pressure followed by filling the channel with fluorescent tagged antigens. The ratio between the filling pressure and capillary pressure barrier has reported as a determinant factor of successful device operation. Success rate of 90% (the rate at which the liquid pinning at the stop valve and liquid filling in the open microchannels occurs) was reported for the device's operating pressure range [95]. In another work, Taher et al. performed a numerical and experimental analysis of a capillary flow in hydrophilic microchannel traversing a backward facing step with low capillary number. They reported the effect of contact angle on the capillary pressure and the change in capillary pressure across the step geometry [96]. Besides the reliance on the fixed channel geometries to create expansion valve, a new concept of capillary soft valves was reported which uses the same principle for stopping the liquid at the capillary barrier induced by abrupt expansion of the channel

cross-section. However, in this method the actuation of the valve happens by manually applying pressures in the order of few kPa using a tweezer or a pen on the soft cover of the valve which subsequently reduces the cross-sectional area and allows the liquid to pass [97, 98].

2.3.5. Trigger valves

Trigger valves comprise of a junction with two inlets and one outlet (Fig. 2.4E). The inlets are known as stop channel and trigger channels. The flow is passing by the junction towards the outlet only when the liquid in the stop valve channel is triggered by the fluid coming through the trigger channel. Indeed, once the two streams meet, the liquid contact with the channel wall is moved from each stop valves into the junction causing the streams to join. Melin et al. introduced this concept and analysed the problem based on the principle of surface energy minimization [99]. Zimmermann et al. investigated the effect of different inlet channel angles [100] and hagemeyer et al. [101] studied a time-varying phenomena of the joining of two liquids. They found that once the two liquids are joining, the pressure at the liquid front is build up but it suddenly jumps down after the merging took place. Trigger valves offer unique handling capabilities including performance of independent processes on one chip, mixing of liquids on demand, and removal of bubble in the microfluidic channels [99].

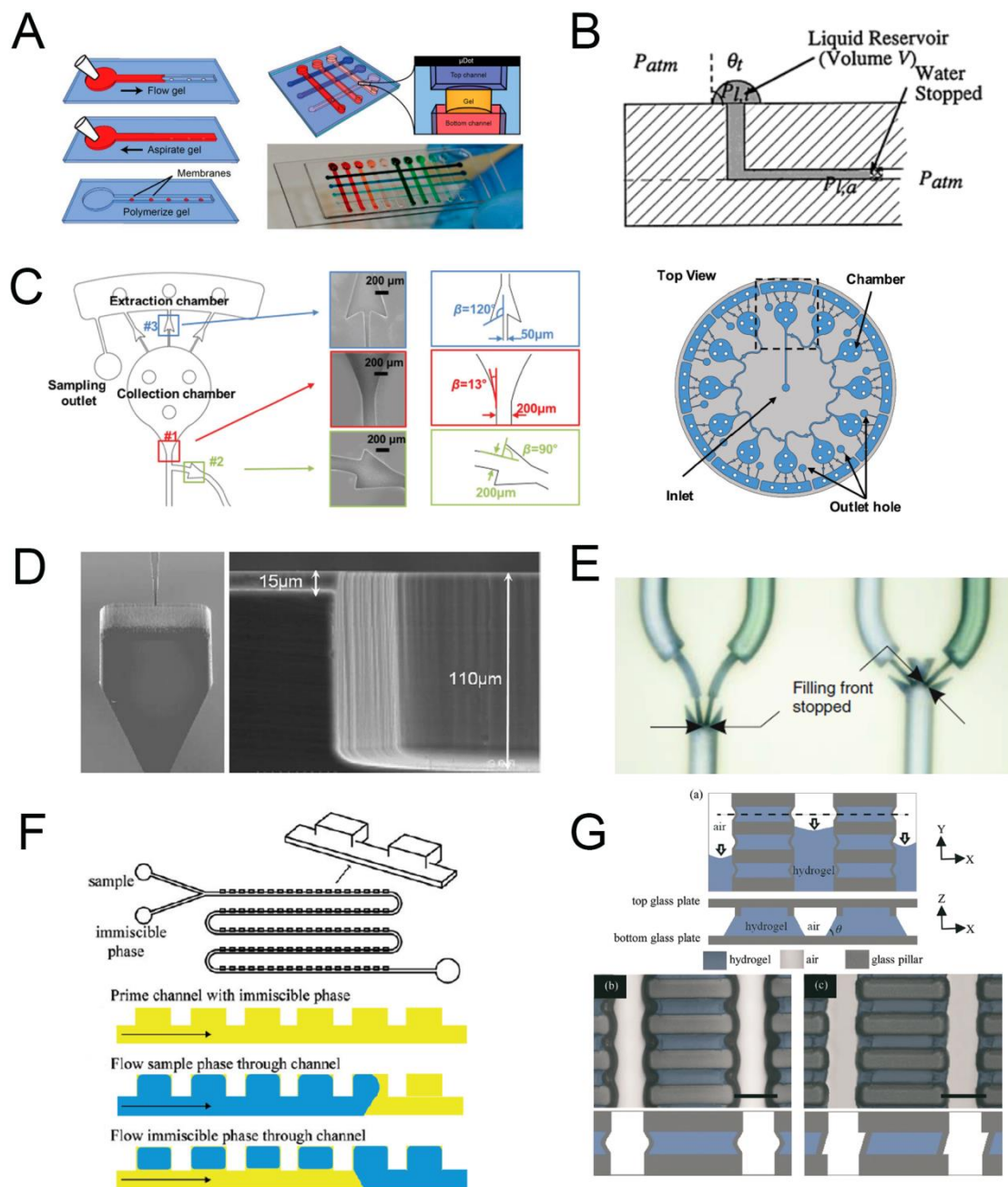


Figure 2.4: Mechanisms for capillary-based sample confinement: (A) Suspended microfluidics proposes liquid flow in an open channel. The aperture at the bottom of these channels can be used to create suspended membranes at predefined locations [87], (B) Droplet metering used for stopping the liquid at certain distance using hydrophobic path [89], (C) Centrifugal capillary burst valve: By controlling the centrifugal pressure at the entrance of burst valves sequential filling of a sample can be achieved [93], (D) multilevel expansion valves, an abrupt change in the channel height is used to stop the flow [94], (E) Trigger valves: the movement of a liquid at the junction is stopped until the liquid flow from another channel in the junction joins [100], (F) Sample digitization: Liquid sample can be trapped into side chambers of a microchannel under certain channel and chamber dimensions [102], (G) Capillary pinning at barriers: The liquid pinning in the capillary barriers based on the sudden expansion of the channel cross section in the pillar [103], published by The Royal Society of Chemistry.

2.3.6. Sample digitization

One of the concerns with capillary based flows is the air being trapped in the system which happens mostly due to the geometry of the device. Therefore, most of the capillary device designs consider an air venting component. In sample digitization method, a liquid sample is filling dead-end traps. However, the geometry of the trap can be designed to let the trap filling happen with successful air escape. This method of sample trapping is named sample digitization (Fig. 2.4F) and can be achieved through pressure-driven [102, 104], and centrifugal [105] actuation. An array of microwells has been introduced by Don Devoe's group which is designed to digitize liquid sample into nanoliter traps [106]. The device comprises of a set of traps located at the left and right of a fluidic path. The working mechanism of the device is based on the controlled pinning of the fluid at the geometric discontinuities. Three device designs with single row of traps, with symmetric traps or a staggered double row of traps were fabricated and tested. Device loading was performed by a capillary pump which is a porous PVDF membrane. The channel was made out of thermoplastic cyclin olefin polymer (COP) which is a polymer with weak hydrophobicity. However, the authors added a surfactant to reduce the contact angle and promote self-filling of the sample in the channel. First, an analytical approach was adopted to analyse the effect of trap aspect ratio (length to entrance width) on the filling success. Parametric study was performed by defining the geometrical models of the system and finding the relationship between different trap geometrical dimensions and constraints. For each trap design two parameters were evaluated: The filling ratio-FR (filling length: trap width) and channel ratio-CR (channel width: trap width). The results showed that maximum filling ratio is achieved at lower contact angle of 45° and when trap length to width ratio (L/w_t) is well below unity. In addition, both experimental

analysis and calculations demonstrated that a channel with staggered double trap has the highest possibility of complete trap filling among all designs [106].

2.3.7. Capillary pinning at barriers

Capillary pinning of a liquid-air meniscus can be used to confine liquid samples by stopping the liquid flow between arrays of capillary barriers. The concept was introduced for large scale patterning of hydrogel microarrays (Fig. 2.4G). The presented device contains an array of hundreds of glass pillars for trapping liquid hydrogel precursor sample. The sample was injected into the device and until it filled the whole chip. Next vacuum suction was applied to remove the residual sample from the channel while the pillars pin the underlying liquid. The liquid pinning happens because of the sudden expansion of the channel cross-section in the pillar area which locally increases the capillary pressure. The effect of angle of expansion, channel height and the capillary barrier height on the pinning efficiency was investigated. It is found that increase in capillary barrier to channel height ratio improves pinning of liquid sample and an optimal value of 1:4 was reported for experimental results [103].

2.3.8. Droplet trapping

Another mechanism for capillary-based geometrical confinement of samples is segmentation of a plug of liquid sample in a channel primed with oil [71, 107-109]. In these systems the sample is filling a junction which has two paths. The trap path comprises of channels of multiple width with a narrow trapping area at its end. The bypass path is made longer to have higher resistance compared to the trap path. Boukelal et al. performed a theoretical derivation of the condition by which the liquid can fill the trap and then move into the bypass channel to sequentially fill other traps. To achieve liquid confinement in the trap, they reported a critical plug velocity and claimed that below this

velocity, the pressure difference between the trap side and bypass side of the plug will be too small to let the plug move into the bypass channel [107].

2.4. Capillary microfluidics cell confinement: application

In this section, we review the applications of microfluidic systems that are designed based on capillary effect to geometrically confine cell samples. In addition, we explain how capillary-based microfluidic sample confinement mechanisms can be used for positioning cells samples.

2.4.1. Capillary pinning in 3D culture systems

Capillary pinning of hydrogel precursor has been investigated as a tool for generating compartmentalized 3D tissue culture arrays. In order to confine cells into separate patterned hydrogel compartments, collagen pre-gel and Caco-2 human intestine cells were mixed and then injected into the device (Fig. 2.5A). The compartments were then thermally cured, and the fresh media perfusion was performed to provide nutrients for the cells. Formation of cell clumps in each microgel was monitored over time to ensure the optimum perfusion flow rate in the system. It is found that cells show better spreading with the presence of perfusion culture. However, since the nutrient consumption increased over time, the cells proliferation was damped over the course of 21 days in vitro culture. An interesting capability of this compartmentalized device was co-culture of Caco-2 human intestine cells with intestinal bacteria *E.Coli* under static and perfusion culture. The result showed that 30% of the cells die under static condition while in the perfusion culture cell viability is maintained over the period of culture. The microgel co-culture compartments were then treated with an antibiotic drug Chloramphenicol at its inhibitory concentration which showed preventive effect on *E.Coli* proliferation [110].

The capillary pinning strategy has been used in a number of other devices known as 3D-microfluidic platforms to make co-culture of multiple cell types. In these systems an array of pillars are positioned between different compartments to be able to load samples separately into each compartment [111-113]. A hydrogel incorporating unit device was introduced for incorporation into well-known 24 and 96 well plates (Fig. 2.5B). The device is microchannel-free and cell-laden hydrogel is directly injected into a well which is confined by an array of pillars. In order for the gel to be efficiently loaded into the device, the authors made devices with different shapes and inter-pillar gap distances. In fact, the loading pressure can overcome the burst pressure of the inter-pillar gap geometry causing leakage in the system. In addition, to ensure that there is no air trapped between the gel side and the aqueous medium side, it was essential that gels protrude fully through the inter-pillar gaps. To achieve this goal, the authors reported optimal inter-pillar of 400-600 μm . They also reported that elliptical and trapezoidal pillars lead to higher gel protrusion due to decreased surface tension. The device has been successfully used for culturing and monitoring dynamic event in neurons-glia monoculture as well as neurons-glia vs endothelial cells co-culture. In addition, cell-laden hydrogels confined in each well were treated with Alzheimer drug β or γ -secretase inhibitors. Performance of ELISA on the medium collected from each culture proved suppressed levels of A β 40 and A β 42, pathogenic species produced during Alzheimer disease [112].

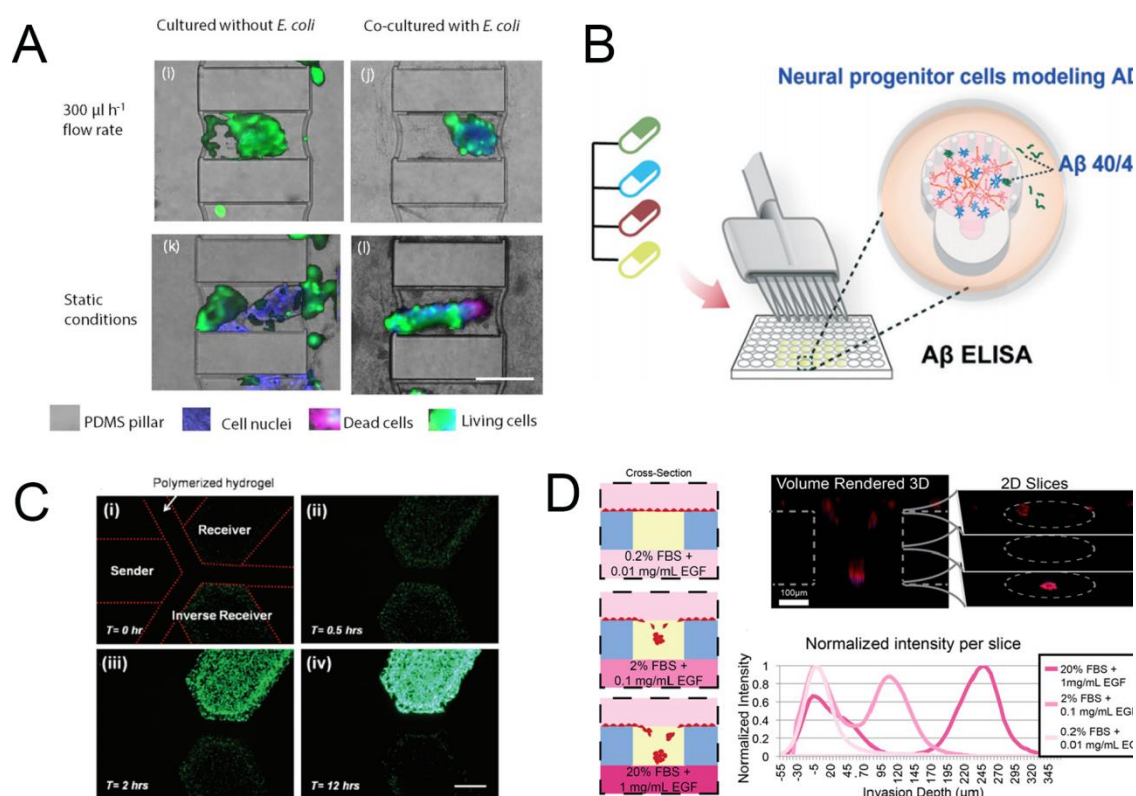


Figure 2.5: Application of capillary based geometrical confinement in studying cell dynamics: (A) Interaction between the human intestine Caco-2 cells cocultured with bacterial *E. coli* cells under different flow conditions in the capillary pinning device [110], (B) Drug screening of Alzheimer disease by culturing neural progenitor cells in hydrogels pinned at the equally distanced micropillar arrays [112], published by The Royal Society of Chemistry (C) Evaluation of the behaviour of quorum sensing by patterning *E. coli* in different shallow channels [114], (D) Measuring the invasiveness of prostate cancer (PC3-MM2) cells by imaging their migration through a membrane microgel formed via suspended microfluidics in open channels [87].

A stationary nanoliter well system based on liquid stoppage at the end of an array of symmetrical traps has been reported recently. In this system, liquid sample containing cells is injected into the trapping system using pressure-driven flow. The liquid is forced to stop in each trap due to presence of a narrow gap which builds up the pressure barrier. Although the device's operational steps were presented, the role of capillary pressure in liquid stoppage has poorly been addressed [115-117]. A few cell-based assays have been performed in this device with the focus on monitoring single cell response. These include metabolic activity of fibroblast cell and yeast cells over time [115, 116], *E. coli* bacterial aggregation and colony formation [115], and antimicrobial susceptibility testing [117].

For each assay a specific way of quantification was presented. The metabolic activities were measured by the fluorescent signal of each well using alamarBlue assay metabolic assay and measurement of YFP fluorescent signal induced by induction of GAL pathway at different galactose to glucose ratios. The bacterial activity was measured by counting the number of cells. The bacterial susceptibility was quantified by measuring the fluorescent intensity of the resazurin dye to resorufin reaction. This reaction takes place upon cell death; therefore, the resorufin signal can be used to measure the effectiveness of the antibiotic treatment.

2.4.2. Cell patterning using capillary systems

Patterning cells through capillary geometrical confinement was reported based on the liquid sample following the channels with controlled height and low capillary pressures [114, 118, 119]. Based on this principle a number of devices were designed and fabricated. An injection moulded plastic array compatible with the size of a 96 well-plates was reported for creating patterned 3D cultures. Since the channel is hydrophilic, the device operation is based on spontaneous capillary guided flow around the corner and then along a narrow gap under a beam named as rail structure. The corner-to-rail liquid capillary filling was set to work when the rail height is less than its width. The device has been used for co-cultured patterning of HUVEC (human umbilical endothelial cells) and LF (lung fibroblasts) embedded in 3D fibrin gels and monitoring formation of angiogenic sprouts [118]. A laterally open microchannel device with alternative shallow and deep channels for cell patterning has been proposed (Fig. 2.5C). The cell sample fills the shallow channel due to its higher surface tension and is prevented from entering the deep channel due to the forward pulling force. In order to operate device without flooding, the height and width of the shallow channel was designed to be smaller and bigger respectively. This cell patterning approach has been used to evaluate the behaviour of

quorum sensing by patterning *E. Coli* in different shallow channels that are connected with media present in the deep channels. The sensing mechanism was measured by the fluorescent signal activated on the GFP gene due to homoserine lactone (HSL) activation in the receiver cells [114].

2.4.3. Open microfluidics

The concept of suspended microfluidics in open microchannels has previously been introduced as a method of capillary-based liquid sample trapping by geometrical confinement [87]. This method is capable of creating an array of collagen membranes named as micro Dots separating two liquid chambers in a transwell format (Fig. 2.5D). The collagen arrays containing breast cancer cell line (T47D) were created by suspending the gel between two channels located at different heights. In order to assess the invasiveness of these cells, the cluster size was reported for cells in different gels (collagen, fibronectin and laminin) and exposed to matrix metalloproteinase (MMP) inhibitor. It was found that addition of MMP inhibitor drug significantly reduces the cluster size. In addition, since each of the top and bottom channel can be filled with different liquids, a gradient of Endothelial Growth factor (EGF) was induced across the gel array. Measurement of the fluorescent signal of the labelled cells at different depth in the gel revealed the effect of EGF gradient on tumour invasion through the gel. A variation of this device has been used to create membranes between two channels one of which seeded with the cells and the other one is filled with solvent. The metabolites generated in the cell compartment transferred into the solvent part and collected for metabolite analysis of Adrenal cells [87].

2.4.4. Droplet trapping

Droplet trapping based on segmentation of liquid plug into separate static compartments was shown in a number of researches. Since each droplet is separated from the adjacent droplets with an oil barrier, the content of each droplet is maintained. This capability makes droplet trapping systems suitable for culturing single or multiple cells. An application of such capability was shown in measuring the growth kinetics of algae cells over the period 15 days by reporting the number of cells in each droplet and their size distribution [107].

2.5. Cell dynamics demanding microscale sample confinement

In the previous sections, a review of the mechanisms of capillary-based sample confinement in microfluidic channels and some of the applications of this method were presented. In this section, we would like to introduce the reader the broader application of capillary-based sample confinement in cell positioning and studying different aspects of cell dynamics. Cell dynamics is defined herein as any cellular phenomenon that happens over time. Regardless of the source of the dynamic event, it is now evident that it happens at the microns scales. Most of the cells have a size that ranges between 5 to 100 μm . The cell niche in which the cell interacts with their surroundings can have the size of hundreds to thousands of microns. Considering the length scales of the space, microfluidic techniques can be used to confine the cells as in their native microenvironment, provide cell stimulations, and continuously monitor cellular response.

2.5.1. Cell migration

Cell migration is a key factor of homeostasis and regulation of organs functions in the body. The major causes of cell migration are cell-cell interactions through soluble and adhesive signalling cues or cell-environment interactions especially through generation

of gradients of biomolecules in the cell microenvironment. Cells migrate either as individual units or collectively as part of a tissue. In addition, cells can migrate from one environment to another by opening their way through epithelial cells (transmigration). Such conditions take place during the cancer extravasation and metastasis as well as migration of immune cells into the blood stream or lymphatic fluids. In order to understand each of these mechanisms it is essential to mimic the microscale environment in which such events occur and spatially locate the cells.

2.5.2. Single-cell migration

The migration of a single cell is characterised with the following factors,

Number of migrated cells

A cell migration assay has a start point and ends in an endpoint. In many migration phenomena, the number of cells that reached the endpoint is of significant importance. This endpoint can be a line or an area depending on the definition of cell migration. For instance, immune Dendritic Cells (DCs) and human colon carcinoma cells (SW 620) were cultured in two separated microfluidic compartment that were connected through capillary microchannels. The result of the number and fold increase of the migrated and infiltrated cells over 72 hours experiment time showed significant increase in the number of migrated DCs toward drug-treated carcinoma compared to the untreated cells [120].

Migratory patterns

The migratory path of each single cell can be tracked over time. This factor gives critical information for characterising the migration phenomenon. For example, Parlato et al. reported the migratory path of DCs moving towards carcinoma cells at 2 minutes time interval during the course of 72 hours revealing the migratory response of immune cells to the carcinoma [120].

Average migration speed

Speed is a scalar quantity and represents cell motility. Cell average and instantaneous speed is calculated as,

$$\bar{S} = \frac{P}{t} \quad (\text{Eq. 2.1})$$

$$S_i = \frac{\Delta P_i}{\Delta t} \quad (\text{Eq. 2.2})$$

In these equations, \bar{S} , S_i are the average and instantaneous migration speed, P and ΔP_i are the path length and instantaneous path length travelled by the cell and t and Δt are the time and time step of this migration respectively. Higher migration speed during cell migration shows higher cell motility which can be caused due to several intracellular crosstalk. In the example of immune-carcinoma interaction, time-lapse monitoring of the DC migration toward carcinoma cells demonstrated that DCs that are closer to the drug-treated carcinoma can sense the tumor-specific stimuli and therefore are more motile. However, once in contact with the carcinoma these cells reduce their motility and adapt their migration towards higher DC-carcinoma contact time [120]. In another example, time-lapse monitoring of neutrophils demonstrates that they are more motile in response to higher chemical gradients while this motility is decreasing over time [121].

Average velocity, directional migration, and persistence

Migration velocity is a vector and therefore depends on the direction of migration. It is defined in average and instantaneous forms as in Eq. 3 and Eq. 4 respectively,

$$\bar{\mathbf{v}} = \frac{\mathbf{d}}{t} \quad (\text{Eq. 2.3})$$

$$\mathbf{v}_i = \frac{\mathbf{d}_i}{\Delta t} \quad (\text{Eq. 2.4})$$

The directional migration explains the role of stimuli to attract or repel the cells. Therefore, higher cell velocity in the direction of stimuli is an expected outcome in many

studies. While cells may move into the direction of stimuli, their persistence to move on that direction is another factor which better captures and explains the directional migration phenomenon and is defined as,

$$DP = \frac{d}{s} \quad (\text{Eq. 2.5})$$

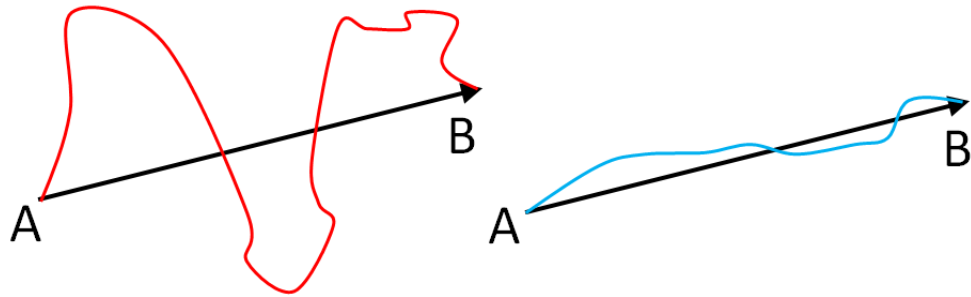


Figure 2.6: Directional migration: Cells that their path is closely following their displacement are more persistence in their migration.

As can be explained from Eq. 5 and Fig. 1, persistence depends on both the displacement and path length. Therefore, a cell with a high displacement in certain direction may have a big path length value leading to lower persistence values. In immune-carcinoma interaction, IFN-DC cells were shown to have higher DP values in migrating toward drug-treated cancer cells compared to the non-treated carcinoma [120].

Time of interaction

In the context of cell migration in the systems with intracellular interaction, the time of interaction is defined as a time period where two cells are in close proximity to each other after the migration took place. The criterion for cell proximity is defined based on the circular region of interaction around the target cell. Time of interaction is especially important in cell dynamics problems when cellular interaction is distance dependent. For instance, immune cells interaction time with cancer cells is a measure of the immune system's engagement. It is found that IFN-DCs have longer average interaction time with the drug treated cancer cells [120].

Chemotactic index (CI)

A key reason for single cell migration is the presence of chemical gradients in the microscale environment which attract the cells into certain direction. This type of cell migration is known as chemotaxis or chemotactic migration. Such migration is quantified by the chemotactic index (CI) which is defined as the ratio between the cell's migration along the gradient direction to the total migration path length. In order to track the cells migratory behavior over time, this index can be calculated for equal time intervals over the experimental period. As an example, chemotaxis of neutrophils in response to a chemoattractant fMLP has been characterized by measuring the CI. The results confirm neutrophil's higher chemo-attraction at higher gradients and shows that CI decreases over time [121]. Calculation of CI in this study also showed memory effect of neutrophil migration as well as synchronized migration due to cell-cell interaction.

Cell morphology during migration

During the single cell migration, the cell continuously goes through a process of contraction and expansion. Therefore, the cell morphology and structure undergo some changes. In order to quantify these changes, the cell's aspect ratio and surface area should be measured over time. The aspect ratio of the cell is identified by first contrasting the cell from its environment, followed by fitting the closest ellipse to the cells area. The aspect ratio is consequently defined as the ratio of the major and minor axis of the ellipse. For instance, measurement of neutrophils aspect ratio during chemotaxis revealed that at steep gradients (100nM), cell aspect ratio increases with time while it is decreasing with time at lower gradients (10nM). In addition cells area decreases consistently over time during the neutrophils chemotaxis [121].

2.5.3. Collective cell migration

Unlike single cell migration in which each cell is moving separately, in collective migration, cells are connected and move together. This phenomenon happens mostly in tissue regeneration, a prime example of which is in wound healing. Although parameters like velocity of migration are considered as trivial characterizing factors of collective migration, the definition of this velocity is different from single cell migration. Here we bring the quantities reported for collective cell migration.

Cell surface area

Since cells are moving collectively the area occupied by the cells is increasing over time. However, increased cell-occupied area could be contributed by both collective cell migration and cell proliferation.

An example of cell surface area measurement is presented in an in-vitro assay has been reported to study the collective migration of human gastric epithelial cells [122]. The cell-free regions were created by PDMS pillars in microfluidic device. Measurement of the area of the cell growth region over time has shown the effect of epithelial growth factor (EGF) in enhancing wound recovery. In another example, the effect of surface properties on collective migration of human bone marrow mesenchymal stem cell (hBMSC) has been studied using PDMS substrates with different mixing ratios. It was found that the maximum area covered with the migrating stem cells happens at intermediate levels of surface hydrophobicity, stiffness and roughness at 20:1 PDMS mixing ratio. Therefore, it was concluded that there exists a particular range of surface properties for which the optimal collective cell migration can be achieved [123].

Ki67 proliferative marker

Ki67 is a protein that is present in cells nuclei and is associated with cellular proliferation. Cell proliferation is a crucial event during the process of collective cell migration and therefore knowing the number of cells indicates the portion of the population which undergoes cell cycle. As an example, Zhang et al. reported that the number of Ki67 positive cells is significantly higher during collective migration of epithelial cells treated with 90ng/mL of EGF and is further increasing with increased concentration of EGF. In addition, most of the Ki67 positive cells were found near the edge of the migrating sheet which suggests that proliferation occurs at the front row of the migrating cells [122].

Cell migration index (CMI)

This index is aimed to capture the rate of migration and is defined as the rate of increase in the area occupied by the cells. Therefore, it can be found by calculating the absolute value of the slope of the area-time plot. Analysis of the epithelial cells collective migration revealed that the CMI value increases with increased value of the EGF growth factor [122].

Number of migrating cells

Another measure of the collective cell migration is presented by the number of cells migrated into a certain area or beyond a certain border line. For instance, when co-cultured with cancer cells versus epithelial cells, mesenchymal stem cells (MSCs) were found to be migrating at higher motility towards the cell-free area [122].

2.5.4. Neurite outgrowth

Neurons are physically different from other cells in the body. While most of the cells have just a cell body, neurons have a stretching organelle known as axon. Axon's responsibility is to receive information from the neurons microenvironment and transfer the data to the

cell body where decisions are made. In the normal condition, each axon is connected to the dendrites of the previous neuron forming the pathway for transferring data. However, in conditions such as CNS injury in which this connection is lost, the axon is responsible for inquire the environment and grow to re-establish the connection. To study a neuron's microenvironment, different approaches have been developed where most of them are focused on investigating axonal growth and guidance under the action of attractive and repulsive cues via an appropriate spatiotemporal control.

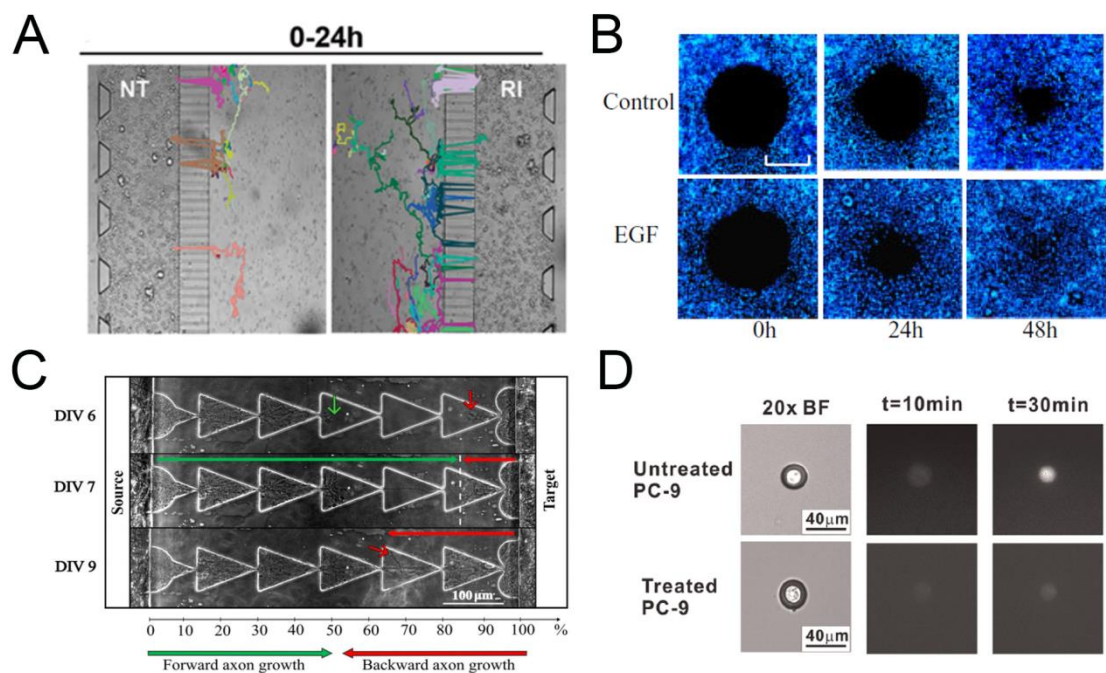


Figure 2.7: Quantitative analysis of cell dynamics: (A) Migration of a single cell: migratory paths of IFN-DC cells towards SW620 colon carcinoma cells through capillary microchannels with and without drug treatments [120], (B) Collective migration of cells: Decrease in the blank surface area in wound healing assay of fibroblast cells with and without endothelial growth factor (EGF) [122], (C) Neurite outgrowth: Axon's growth length and direction in a zigzag microchannel geometry [124], (D) Single cell MMP secretion dynamics of PC-9 cancer cells in picolitre droplet over time [53].

Neurite growth length and speed

As the first measurement criterion, neurite's outgrowth can be measured by their length. In fact, neurite's length indicates that the growth cone maintains its structural integrity over the course of the experiment. The rate of change in neurite length or growth speed is also reported as a measure of neurite dynamic response to chemical and physical cues.

As an example, an in vitro model of the neural network with different levels of complexity has been reported in a microfluidic device embedded with electrodes. It was shown that by controlling the electric field, it is possible to guide, accelerate, slow down and push up neurites in collagen scaffolds. To show this, the average growth speed of the axons was measured over time ($\mu\text{m}/\text{day}$) [125]. In another study, neurons were cultured in two microfluidic chambers that were connected to each other with the microchannels of different shapes including zigzag, and triangular channels [124]. In order to investigate the effect of geometry on outgrowth dynamics, the relative distance of axon outgrowth in the microchannels as well as the axon growth velocity ($\mu\text{m}/\text{h}$) was measured and reported.

Axon turning angle

Axons are constantly exploring their environment and respond to the chemical and physical cues. These cues could be growth factors, inhibitory barriers or physical signals from other parts of the nervous system. When an axon encounters such conditions, it may stop growing or change its growth direction. For example, Honegger et al. introduced an assay to study the axons response to different levels of electric voltage. It was found that axons are repelled by the increased electrical signal and show a sudden turning angle of $\sim 90^\circ$ [125]. Galdkov et al. demonstrated that axons will show different turning angle profiles in response to the channel geometrical changes [124]. The effect of different patterns of proteins on axon guidance was performed by compartmentalized microfluidic device. Turning of axons onto the strips of Ncad-fc and IgG patterns demonstrated the capability of Ncad-fc in aligning and guiding the neurite's outgrowth [126]. In order to investigate the effect of forces caused by localized fluid flow on the neural guidance, the turning angle of up to 90° parallel to the direction of the flow was reported [127]. In another example, the growth cone collapse in response to ephrin-A5 coating was reported in

microfluidic device. The result showed that growth cone collapse depends on the concentration of the guidance cue [128].

Number of neurites

Counting the number of fibres extending out of a primary culture area or entering another culturing area is indicative of the effectiveness of the neurite assay. For example, the number of axons that pass from a zig-zag and triangular microchannel was reported to measure the effect of geometry on axon path finding [124].

2.5.5. Single cell secretion

Single cells are secreting different levels of biomolecules over varying timescales. Once released, these biomolecules can perform as enzymes, growth factors, antibodies or other signalling pathways to other cells. The parameter to measure here is the amount of secreted protein which can be reported in the form of true concentration, the colour change, and the fluorescent intensity. This amount is regularly a small number and since unlike genomic molecules, proteins cannot be amplified, such assays demand sensitive detection methods. Common single cell secretion measurement in microfluidic systems are presented below.

T-cell cytokine secretion

T-cells are secreting a category of signalling biomolecules known as cytokines that are adjusting the immune system's response. In order to measure the level of secreted cytokines from each cell, several methods have been proposed. Single T-cells were co-encapsulated with microspheres coated with cytokine-specific (IL-10) capture antibodies and detection fluorescent-labelled antibodies (rat anti-human IL-10 FITC conjugated antibodies) within nanoliter size droplets. The concentration of IL-10 secretion over 2

hour time frame of the experiment was reported by measuring the fluorescent intensity and using the calibrated data intensity-concentration plots [129].

Matrix Metalloprotease (MMP) secretion

Proteolytic degradation of the extracellular matrix (ECM) is known to be a determinant factor in cancer invasion and metastasis. In this process, cancer cells release degrading enzymes that cleave the ECM protein. This highlights the importance of studying proteolytic activity of cells for development of novel protease targeting drugs. An established method for studying such an activity is based on observing the fluorescent intensity out of the reaction between the released enzyme and a protease-sensitive substrate known as fluorescence resonance energy transfer (FRET) substrate. Conventional proteolytic assays measure average activity of the cells masking the fact that cancer invasion due to proteolytic activity is driven by the heterogeneity between cancer cells. In addition, knowing the proteolytic activity of different subclones may lead to more effective treatment strategies. In order to measure the MMP activity of single cells, a dynamic droplet system has been introduced by which single cells were trapped inside picolitre droplets. To monitor the droplets containing single cells, a DLD system was employed to separate the cell-containing droplets from smaller empty droplet based on size. Using this approach and by monitoring the fluorescent signal produced out of cleavage of MMP substrate in each droplet, the activity of single PC-9 cancer cells were measured with and without the presence of anti-cancer drug doxycycline [53].

2.6. Summary

In this thesis, capillary-based sample confinement in microchannels will be introduced as a method for patterning and trapping cells. By detailed analysis of the flow behaviour in the microchannel and assessing the effect of geometry on capillary pressure, a simple, robust passive technique will be investigated. The developed method is applied to build

microfluidic devices for studying cell migration, neurite outgrowth dynamics and time-varying single cell secretion.

Chapter 3. Capillary-based sample confinement: Theory and numerical simulation

Microfluidic sample confinement is playing an important role in understanding different aspects of cell dynamics. These systems can immobilize cell-laden samples into different shapes. This immobilization can be used as a spatial control to decipher each cell's intrinsic behaviour as well as its interaction with other cells or environmental cues. While several active methods have been proposed to immobilize biological samples, the need for a simple passive approach which eliminates the need for complex active systems is an emergent need. In this chapter, we introduce the fundamentals of pressure-modulated trapping of biological samples based on the capillary pressure effect. We provide a deep analysis of the physics of sample trapping through geometrical confinement by applying theory, employing numerical simulation, and experiments. In brief, we show that how tracking the liquid-air interface in a confined microchannel can be used to manipulate liquid samples and sample immobilization.

3.1. Fundamental concepts

3.1.1. Surface tension

Surface tension is the tension at the surface of the liquid caused by the intermolecular forces. Under the liquid surface, the attraction of individual molecules pulls on each other in all directions. However, on the liquid surface, the molecules are pulled laterally and downward since there is a negligible intermolecular attraction above the molecules. Therefore, the net force on surface molecules is downward. The result of this downward force is that surface molecules are pulled down until counter-balanced by the compression resistance of the liquid. In other words, surface molecules are compressed more tightly together at the surface, forming a sheet with less distance between them compared to the molecules below.

3.1.2. Contact angle, hydrophobic and hydrophilic surfaces

Contact angle is the angle that is formed at the interface of three phases of liquid-gas-solid and is defined as the angle that the liquid-gas interface and the surface of the solid make at their contact point. Assuming that γ_{LV} , γ_{SL} , γ_{SV} and θ are the surface tension of the liquid, solid/liquid interfacial tension, surface free energy of solid and contact angle respectively, the balance of forces at the interface gives:

$$\gamma_{SV} = \gamma_{SL} + \gamma_{LV} \cos \theta \rightarrow \theta = \cos^{-1}((\gamma_{SV} - \gamma_{SL}) / \gamma_{LV}) \quad (\text{Eq. 3.1})$$

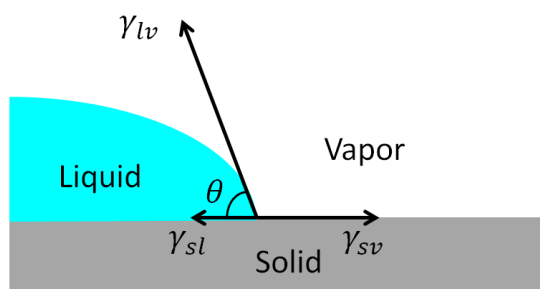


Figure 3.1: Schematic illustration of the formation of the liquid-air interface on a solid surface and the formed contact angle.

If the contact angle of the liquid on the surface is less than 90° ($\theta < 90^\circ$), the surface is called hydrophilic or wettable surface. In cases where the microchannel's wall is hydrophilic, the liquid-air interface will have a concave shape and the liquid will be drawn off in the channel. Conversely, if the contact angle of the liquid on the surface was larger than 90° ($\theta > 90^\circ$), the surface is called hydrophobic or non-wettable. A hydrophobic microchannel wall leads to a convex liquid-air interface shape in the microchannel which pushes the liquid out of the channel (Fig. 3.2).

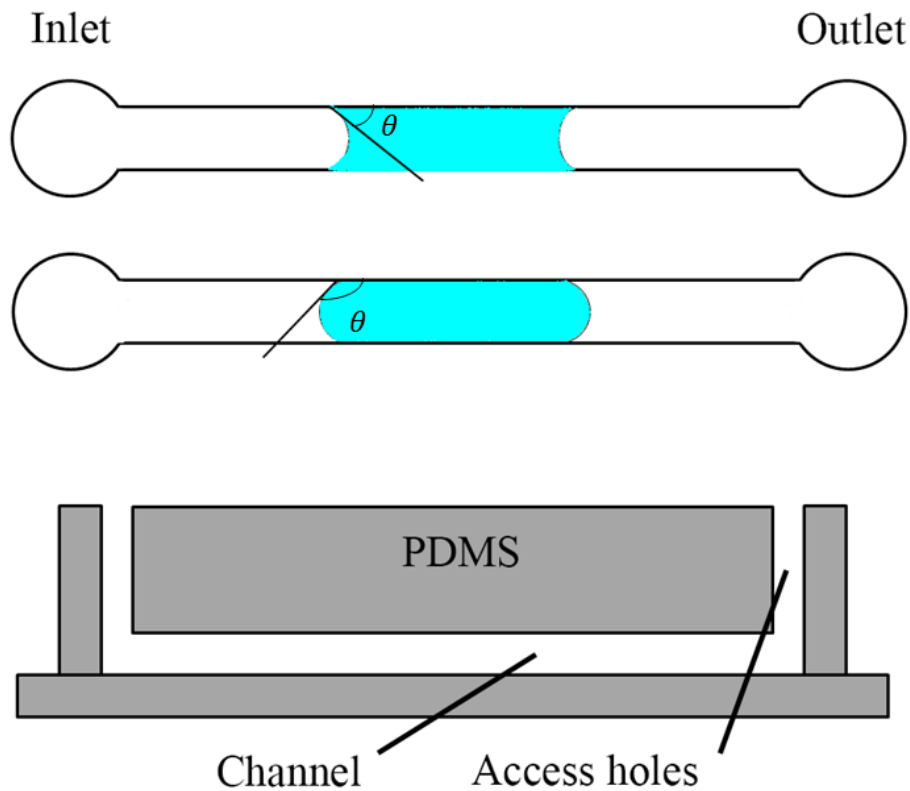


Figure 3.2: Schematic illustration of the liquid in a hydrophilic (top) versus hydrophobic (bottom) channel.

3.1.3. Capillary pressure

Capillary pressure is a pressure at the interface of the liquid and gas meniscus which is generated by the surface tension of the liquid and fixed contact angles at the interface. For a rectangular microchannel with the channel height and width of h and w , the Young-Laplace equation gives the capillary pressure as:

$$\Delta P = \gamma \left[\frac{\cos\theta_{top} + \cos\theta_{bottom}}{h} + \frac{\cos\theta_{left} + \cos\theta_{right}}{w} \right] \quad (Eq. 3.2)$$

In this equation, γ is the surface tension of the fluid, and θ are the contact angle between the fluid and the channel walls. If the channel walls are built from the same material, then θ will have one value. The PDMS chip is normally bonded against a glass substrate (hydrophilic, $\theta=25^\circ$) or PDMS substrate (hydrophobic, $\theta=107^\circ$) [130].

As can be seen, the capillary pressure depends on the surface properties of the microchannel's walls as well as the geometry of the channel. Based on this equation, smaller channels hold larger values for the capillary pressure. Therefore, by adjusting the geometry one can control the capillary pressure and the fluid flow. There are several important points that have been taken into account in design and operation of the devices proposed in this thesis:

1. The aspect ratio of the channel plays an important role in determining the capillary pressure and the fluid flow in the microchannel. The channel's aspect ratio is defined as the height to width ratio (h/w). If this ratio falls too small, the liquid surface tension force with the channel's upper and lower wall increases. Therefore, the first term in the Young-Laplace equation and consequently the capillary pressure will build up leading to flow stoppage. In the devices presented in this thesis, this aspect ratio is >1 and therefore, the effect of surface tension force caused by the upper and lower walls are negligible.
2. Depending on the application and the method of flow control, different capillary pressure modes can be obtained. For self-propelling microfluidic capillary channels, the contact angle should be much smaller than 90° preferably $\theta < 60^\circ$. However, whenever liquid stoppage or flow pacing is needed, this value can be larger ($\theta > 90^\circ$), i.e. a hydrophobic material for the microchannel needs to be chosen.

4. Any change in the channel geometry leads to a change in the capillary pressure. Such changes should be considered in controlling the fluid flow in a desired way.

5. If the channel walls were hydrophilic, there is a chance that the liquid-air interface takes a narrow shape at the corners and part of the liquid move faster than the other part. This may lead to formation of air bubbles as part of the flow proceeds the bulk flow and it may impair microfluidic device's function.

3.2. Filling length and filling velocity

In sample immobilization, either for patterning cells or trapping cells, having control over the flow rate is crucial for several reasons: First, the device's working mechanism is affected by the flow rate. If the flow rate is too high, the liquid sample is not trapped properly leading to formation of bubbles especially near the sharp corners. Second, the microchannel's filling flow rate not only affects the shear stress on the cells but also may affect the cell distribution in the channels. Finally, the flow rate may affect the timing and sensitivity of the assay. For example, in generating gradient of molecules in the static droplet system (Chapter 6- Fig.6.49), the faster the flow, the steeper will be the gradient of the molecules.

The filling velocity in a sample trapping system with rectangular cross-section of width w and height h can be calculated as,

$$Q = \frac{h^3 w \Delta P}{12 \mu L(t)} \left(1 - \sum_{n=1,3,5,\dots}^{\infty} \frac{1}{n^5} \frac{192}{\pi^5} \tanh\left(n\pi \frac{w}{2h}\right) \right) \quad (Eq. 3.3)$$

Where ΔP is the difference in capillary pressure across the microchannel, μ is the viscosity of the liquid, and L is the length of the liquid in the microchannel. In case $h \ll w$, $\tanh\left(n\pi \frac{w}{2h}\right) = \tanh(\infty) = 1$ the above equation is simplified into,

$$Q = \frac{h^3 w \Delta P}{12 \mu L(t)} \left(1 - 0.63 \frac{h}{w}\right) \quad (\text{Eq. 3.4})$$

The filling velocity is defined as the speed, at which the liquid-air interface moves in the channel and can be calculated as,

$$V = \frac{dL(t)}{dt} = \frac{Q}{wh} = \frac{h^2 w \Delta P}{12 \mu L(t)} \left(1 - 0.63 \frac{h}{w}\right) \quad (\text{Eq. 3.5})$$

Therefore, the expression for the location of the liquid-air interface and the filling time t can be found by integrating this equation over t :

$$\int \frac{dL(t)}{dt} = \int \frac{h^2 w \Delta P}{12 \mu L(t)} \left(1 - 0.63 \frac{h}{w}\right) \rightarrow \int L dL = \int \frac{h^2 w \Delta P}{12 \mu} \left(1 - 0.63 \frac{h}{w}\right) dt$$

$$\frac{L^2}{2} = \frac{h^2 w \Delta P}{12 \mu} \left(1 - 0.63 \frac{h}{w}\right) t \rightarrow L(t) = h \left(\frac{w \Delta P}{6 \mu} \left(1 - 0.63 \frac{h}{w}\right) t\right)^{0.5} \quad (\text{Eq. 3.6})$$

Using electrical analogies, the flow resistance, R , within a microchannel can be defined as:

$$R = \frac{\Delta P}{Q} = \frac{12 \mu L}{h^3 w} \left(1 - 0.63 \frac{h}{w}\right)^{-1} \quad (\text{Eq. 3.7})$$

This equation shows that channel filling is controlled by the resistance of the channel and the capillary pressure. Unlike regular microchannel flows in which the channel is prefilled with a liquid, here the liquid-air meniscus is moving along the channel. Therefore, the flow resistance is a variable quantity. As can be seen from the resistance equation, the fluidic resistance increases with L along the microchannel, and in a straight channel with varying shape, the section with smallest height has the lowest flow rate.

3.3. Confinement based on Capillary pressure

Capillary pressure can be used to immobilize and trap biological samples if the microfluidic device has some components that are governed by capillary pressure. Here,

we introduce these components and present an analysis of the capillary flow in the microchannels, leading to an efficient sample trapping and confinement.

3.3.1. Air vents

Since the sample is introduced into an empty microchannel, it pushes the existing air out while filling the channel. Therefore, it is crucial to be able to ensure that the air escapes the channel effectively. In the context of sample trapping, air vents can be a channel that is blocked by a cover but is opened upon flow requirement. However, a smarter design of the air vent is to increase the capillary pressure at certain points along the microchannel to stop the liquid from moving in the channel while letting the air escape. One way to achieve this is to increase the channel's walls hydrophobicity and generating positive capillary pressure. Therefore, channels made from hydrophobic materials are suitable choices for creating air vents. The alternative way for raising the capillary pressure is to design the channel geometry near the air vents for smooth air escaping while the liquid is stopped.

3.3.2. Capillary flow resistance

While the liquid samples move in the microchannel, the channel resistance slows down the flow. Although decreasing the channel length and increasing the channel width will decrease the overall flow resistance, it can also lead to a decrease in capillary pressure which may contradict the design goal.

3.4. Capillary-based liquid stoppage (stop valve)

3.4.1. Theoretical analysis

Sample confinement (with no surface modification) is only possible by blocking the liquid movement in the system at the desired locations. In order to achieve this, a sudden change in the channel geometry is necessary as it can pin the meniscus of the fluid at the

edges and stop flow. For a hydrophobic channel, this means decreasing the channel cross-section. This leads to an increase in the capillary pressure since the capillary pressure is acting against the filling pressure. On the other hand, for the hydrophilic channels, increasing the cross-section of the channel leads to decrease in the capillary pressure and stops the flow.

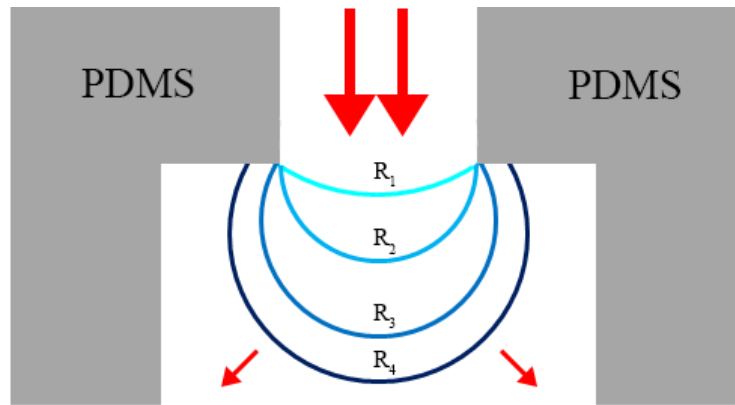


Figure 3.3: Expansion of the liquid-air interface passing through a sudden expansion area. When the interface reaches the expansion area, it is pinned to the walls at both ends. At this moment, the interface has the highest radius of curvature. As the flow moves forward, the capillary pressure is built up while the radius of curvature is decreasing. R_2 is the minimum value of radius of curvature and corresponds to capillary burst pressure. After the burst pressure is overcome, the radius of curvature starts growing and the interface detaches from the sides and moves along the expansion.

Here, the effect of abrupt change in the geometry is presented by the concept of "burst pressure" which is defined as the highest achievable capillary pressure at the liquid interface while moving through that geometry (Figure 3.3 and 3.4). Obviously, if the filling pressure continues to grow, it can overcome the burst pressure of the valve and break this preventive pressure. Designing capillary stop valves with desired burst pressure is therefore a determining factor in designing a sample confinement device. To achieve appropriate design, an analytical study of the burst pressure is presented.

Fig. 3.4 demonstrates a liquid-air interfacial line which is formed between the walls of a hydrophobic channel with expansion radius of r [31]. In this figure, α is the opening angle of the channel walls at the position of the meniscus, w is the width of the channel just

before the expansion, and θ is the contact angle of the liquid sample with the walls. Two new parameters are introduced here. w_α is defined as the channel width inside the expansion region. Moreover, $R(w)$ is defined as the radius of curvature of the advancing liquid.

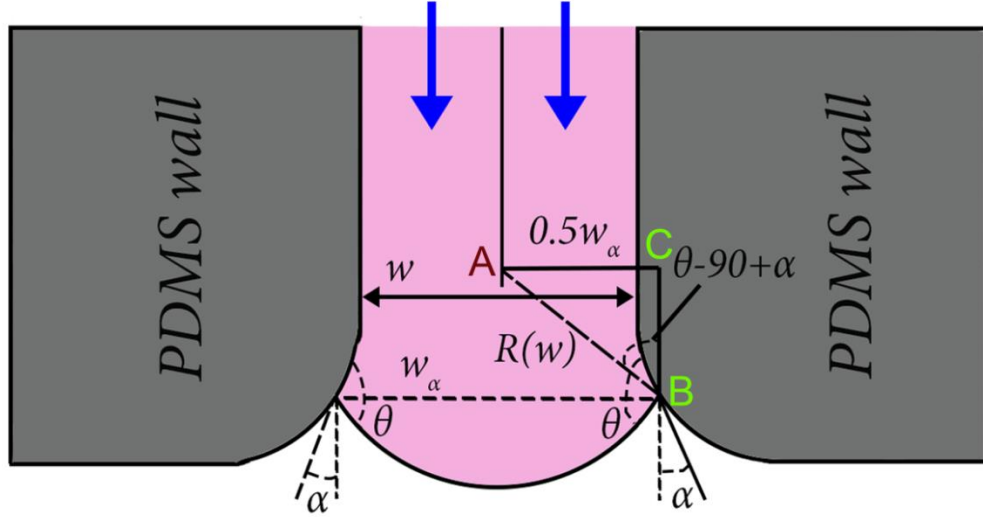


Figure 3.4: Schematic illustration of the liquid-air interface movement/blockage while passing through a sudden geometrical expansion [31].

From Eq. 3.1, a general expression for the capillary pressure at the interface of liquid-air in a rectangular cross-section microchannel:

$$\Delta P = \gamma \left[\frac{\cos\theta_{top} + \cos\theta_{bottom}}{h} + \frac{\cos\theta_{left} + \cos\theta_{right}}{w} \right]$$

Assuming that all of the channel walls are made up of homogeneous hydrophobic material, this equation can be re-written as,

$$\Delta P = \gamma \left[\frac{2 \cos \theta}{h} + \frac{2 \cos \theta}{w} \right] \quad (Eq. 3.8)$$

Looking into Fig. 3.5, we can write $w_\alpha = w + 2r - 2x$, $x = r \cdot \cos \alpha$. Looking into triangle ΔABC , one can write:

$$\sin(\theta - 90 + \alpha) = \frac{w_\alpha/2}{R(w)} \rightarrow R(w) = \frac{w_\alpha}{-2 \cos(\theta + \alpha)} \quad (\text{Eq. 3.9})$$

Combining Eq. 3.8 with Eq. 3.9, one can write the burst pressure as:

$$\Delta P_{burst} = \text{Max} \left(\gamma \left(\frac{2 \cos(\theta + \alpha)}{w_\alpha} + \frac{2 \cos \theta}{h} \right) \right), 0 \leq \alpha \leq 90^\circ \quad (\text{Eq. 3.10})$$

Therefore, for any given change in the channel geometry, there exists a burst pressure which occurs at the interface's minimum radius of curvature R_w .

3.4.2. Numerical simulation of the stop valve

In order to understand the effect of the geometry on the liquid blockage in the stop valves and to measure the burst pressure, a series of numerical simulations were performed using COMSOL multiphysics software.

Level Set versus Phase Field model for multiphase flow

In order to choose the suitable multiphase model, two interface tracking modules of COMSOL software were studied. These methods are designed to track the location of the interface between the two immiscible fluids. In both methods, first the Navier-Stokes and continuity equations are solved giving the velocity, pressure and mass distribution. Next, a phase function (φ) is defined to account for the transport of the fluid interface. The governing equation for the phase function for each method is as follows,

Level Set Method

$$\frac{\partial \varphi}{\partial t} + \mathbf{u} \cdot \nabla \varphi = \delta \nabla \cdot (\varepsilon \nabla \varphi - \varphi(1 - \varphi) \frac{\nabla \varphi}{|\nabla \varphi|}) \quad (\text{Eq. 3.11})$$

$$\rho = \rho_{air} + (\rho_{water} - \rho_{air})\varphi \quad (\text{Eq. 3.12})$$

$$\mu = \mu_{air} + (\mu_{water} - \mu_{air})\varphi \quad (\text{Eq. 3.13})$$

In this equation, \mathbf{u} is the velocity vector, δ is the re-initialization parameter, ϵ is interface thickness (which is normally set to half of the mesh size at the interface). $\varphi=0$ for air and $\varphi=1$ for the liquid. Therefore, the liquid-air interface is represented by $\varphi=0.5$.

Phase Field Method

The equation for phase function is known as Cahn-Hilliard equations,

$$\frac{\partial \varphi}{\partial t} + \mathbf{u} \cdot \nabla \varphi = \nabla \cdot \frac{\gamma \lambda}{\epsilon^2} \nabla \psi \quad (\text{Eq. 3.14})$$

$$\psi = -\nabla \cdot \epsilon^2 \nabla \varphi + (\varphi^2 - 1)\varphi \quad (\text{Eq. 3.15})$$

$$\sigma = \frac{2\sqrt{2} \lambda}{3 \epsilon} \quad (\text{Eq. 3.16})$$

In these equations, \mathbf{u} is the velocity vector, γ is the mobility and represents the interface diffusion time scale, λ is the mixing energy density, and ϵ is interface thickness (which is normally set to =mesh size at the interface/2). $\varphi=-1$ for air and $\varphi=1$ for the liquid. Therefore, the liquid-air interface is represented by $\varphi=0$. The volume fraction of each phase can be calculated after φ as,

$$VF_1 = \frac{1-\varphi}{2} \text{ and } VF_2 = \frac{1+\varphi}{2} \quad (\text{Eq. 3.17})$$

Where fluid 1 is air and fluid 2 is the liquid. The simulations performed here use Phase Field Method as it gives more accurate results for the interface tracking via controlling the mobility function. It is also developed based on the physical laws of energy minimization.

3.4.3. Solution of the stop valve using Phase-field method

In COMSOL multisphysics, the "Laminar Two-Phase Flow- Phase Field" was chosen as the physics with the Transient Phase Initialization as the solver mode. The geometry of

the sudden expansion in the microchannel is designed based on the dimensions of the channels for sample patterning and trapping. An expansion ratio of 1:3 with the lower channel width of 70 μm and upper channel width of 210 μm were used for this study (Fig. 3.5). In order to impose the liquid-air initial boundary, the geometry was designed by unifying two subsections of the wider channel and narrower channel.

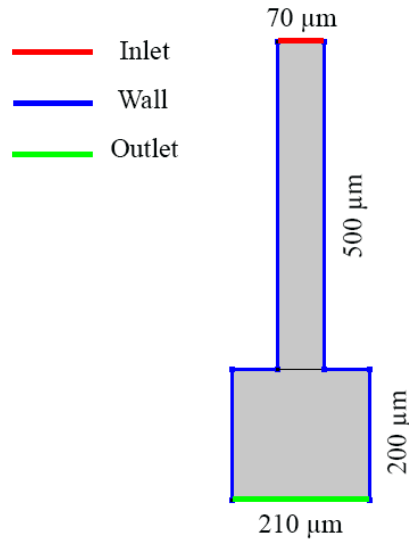


Figure 3.5: Schematics of the geometry of the microchannel with sudden expansion.

Water was chosen as the filling fluid with the properties of density $\rho=998 \text{ kg/m}^3$, dynamic viscosity $\mu=1.002 \times 10^{-3} \text{ kg/m.s}$ and surface tension of 0.0728 N/m. Air properties were density $\rho=1.1614 \text{ kg/m}^3$, and dynamic viscosity $\mu=1.846 \times 10^{-5} \text{ kg/m.s}$. For the Phase Field parameters, ϵ_{pf} (interface thickness parameter) was set to 6.5e-6 and χ (mobility tuning parameter) was set to 50. In order to set the initial position of the air and liquid in the channels, the initial values of each domain were defined. The lower bigger domain was set to have air at $t=0$ and the upper smaller domain was set to be filled with water. The boundary between the two domains was chosen to be the initial interface between the two phases.

Boundary conditions

The Inlet boundary condition was set to a constant pressure of 2 kPa and water was chosen as the liquid filling the inlet. The outlet boundary condition was set to $P=0$ kPa. The boundary condition at the walls was set to wetted wall boundary condition with the contact angle of $107^\circ = 1.8679$ radian for PDMS channels [130]. The mesh system is generated with the maximum element size=0.004mm, minimum element size= $7e-6$, maximum element growth of 1.1, and curvature factor of 0.2 leading to total number of 6000 mesh elements. The plot of maximum velocity against number of mesh elements is shown in the Fig. 3.6, indicating the results obtained using the mesh were independent of the mesh size.

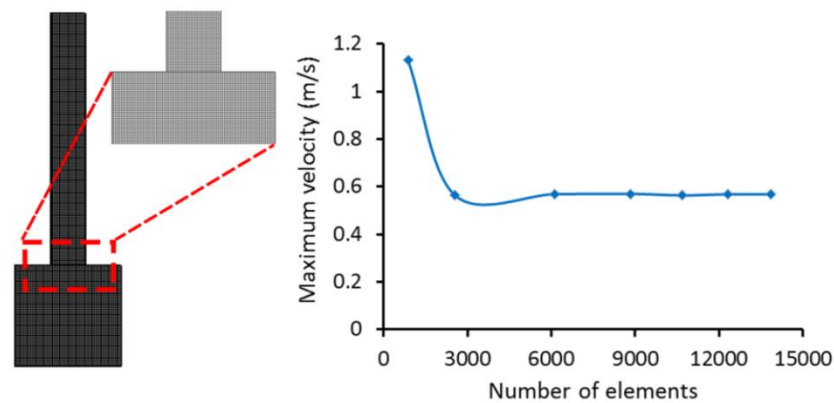


Figure 3.6: Mesh system used for solving the liquid-air interface passing through a sudden expansion microchannel with expansion ratio of 1:3.

Solver set up

The time dependent solver is set to be solved in the time span of [0-1e-3 seconds] with time step size of 0.25e-4. The time span and the time step were chosen by running the simulation for a number of times, tracking the interface movement through the geometry and choosing the time span/step which captures the total period of interface movement.

3.4.4. Results and discussion

Volume fraction

In order to track the liquid-air interface, the plot of volume fraction of each phase was obtained. In the plot of volume fraction of water for example, -1 means there is no liquid in that portion and 1 means the area that is fully filled with water. The interface is a diffuse layer through which the volume fraction of water changes from -1 to 1. Fig. 3.7 demonstrates the contour of the volume fraction of water through the expansion region.

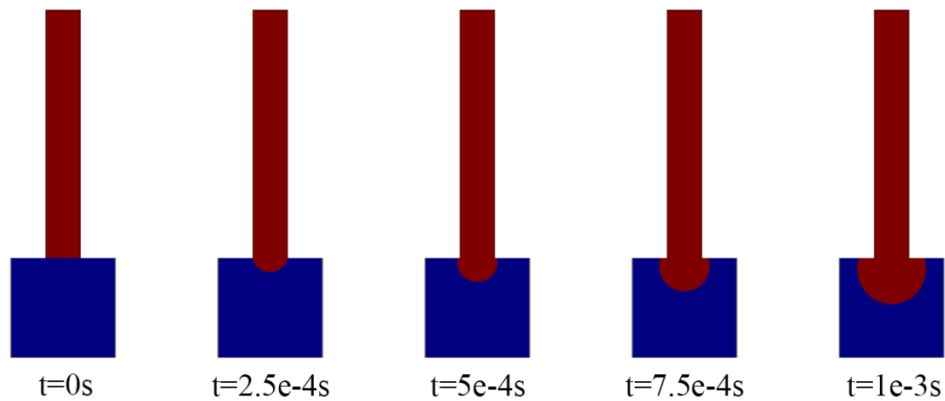


Figure 3.7: Evolution of the liquid air interface over time in the sudden expansion region.

Velocity

The velocity contour can explain how the liquid-air interface's movement is affected by the geometry. Fig. 3.8 presents the sequence of image showing the velocity magnitude in the sudden expansion channel at different time points. As can be seen, the liquid flow in the narrow channel has the parabolic profile with the maximum in the center and no slip at the walls. However, looking at the liquid velocity near the interface, a wider spectrum of velocity magnitudes can be seen which is changing radially and abruptly across the interface area. This behavior was expected as the capillary pressure acts as a resistive force against the filling pressure. One point that is clear from the velocity contour is that while the burst pressure is overcome and the interface passes the interface contact line, the velocity magnitude is constantly decreasing from the narrow channel up to the interface borders. Therefore, each liquid-air interface behaves as a barrier which stops the liquid at the expansion region.

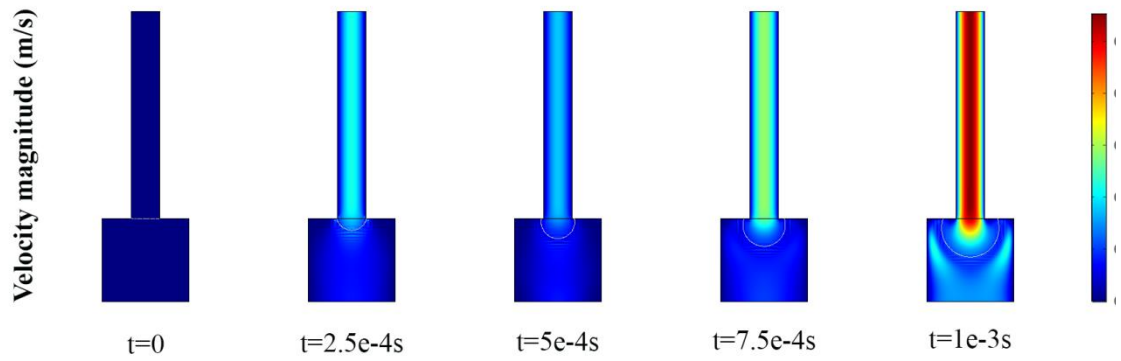


Figure 3.8: Variation of the velocity magnitude in the expansion microchannel and across the liquid-air interface over time.

In order to better visualize the velocity change in the domain, the velocity vectors at the expansion area was obtained. Fig. 3.9 demonstrates the air-liquid front as well as the velocity vectors in the fluid domain over time. A scale factor of 0.1 was applied on the vectors to be able to see the vectors throughout the period of $t=0$ to $t=1e-3s$.

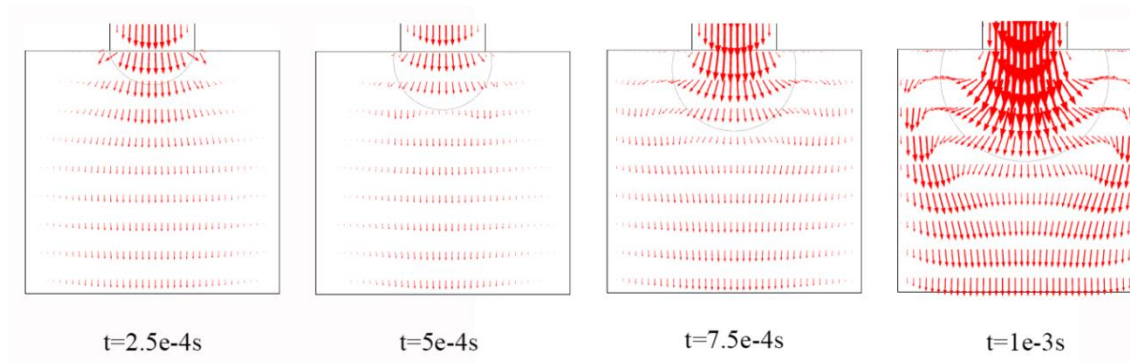


Figure 3.9: The air-liquid front as well as the velocity vectors in the domain over time.

Looking into Fig. 3.9, the velocity profile shows obvious decrease in magnitude both before reaching the interface and after the interface in the area which is occupied by air. At $t=5e-4s$ this decrease is even more clear. At $t=7.5e-4s$, when the burst pressure is overcome, the velocity increases behind the interface. An interesting phenomenon is the velocity magnitude and direction at the interface. Looking at the velocity profile at $1e-3s$, the velocity decreases drastically at the interface. Moving from the interface towards the air side however, the velocity is built up. It looks like that the distance between the

stagnant point at the interface and the expanded channel's wall behaves as a nozzle increasing the air velocity.

Pressure distribution

The pressure change across the liquid-air interface is the key factor which defines the device's performance in the sample trapping systems introduced in this thesis. Here, we are aiming to investigate this change. Fig. 3.10 presents the pressure distribution in the system.

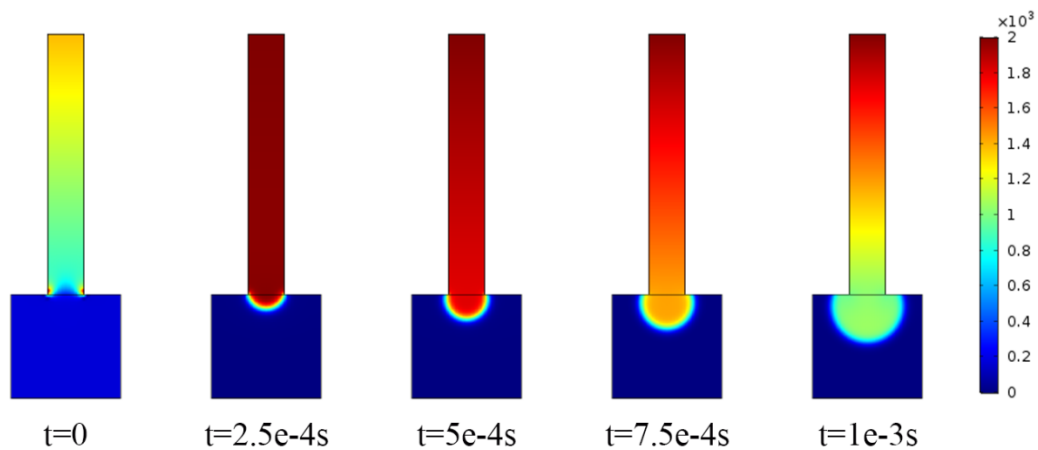


Figure 3.10: Evolution of the pressure distribution over time in the expansion region.

The pressure contour of Fig. 3.10 demonstrates the decrease in the pressure behind the liquid-air interface area over time. This decrease is initially abrupt until the capillary pressure rises to the geometry's burst pressure. For example, from $t=2.5e-4s$ to $t=5e-4s$, the pressure behind the interface changes from 2 kPa to ~ 1.8 kPa ($=-0.2$ kPa). However, from $t=5e-4s$ to $t=7.5e-4s$, this change is from 1.8 kPa to 1.4 kPa ($=-0.4$ kPa). After the burst pressure is overcome, the pressure decrease is either kept or decelerated as the interface movement now happens at a more stable rhythm.

Locating the position of the contact point can help understanding the motion of the liquid-gas interface in the channel. As can be seen in Fig. 3.11, the slope of the contact point

plot changes significantly at $\sim t=5e-4s$. This is the time when the capillary pressure reaches its maximum value known as "burst pressure". The contact point is then moving faster to let the liquid fill the expanded channel.

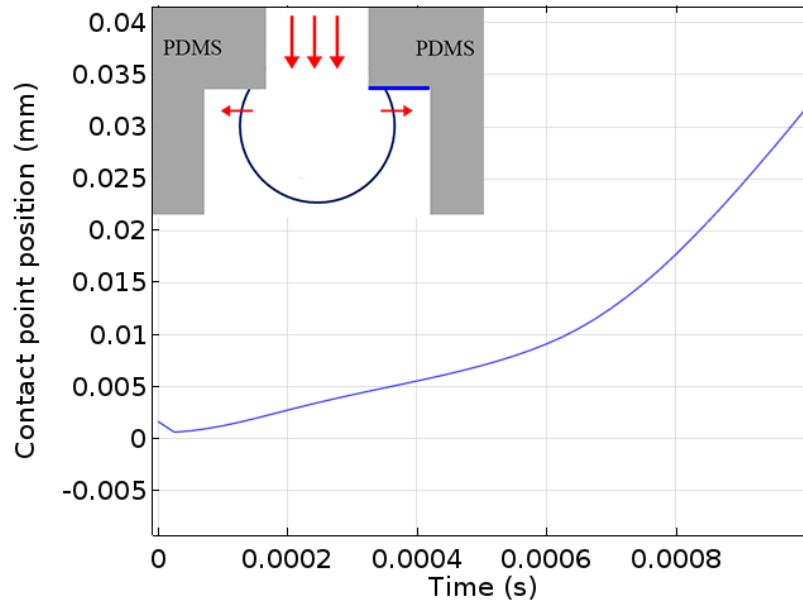


Figure 3.11: Variation of the contact point position along the horizontal contact line (Blue line) with time.

3.4.5. Employing the stop-valve in liquid sample trapping mechanism

The geometrical design of the cell confinement device of this thesis is presented in Figure 3.12A. In this design, we have two positions for stopping/decelerating the liquid: One when the liquid leaves the main channel and moves toward the traps, and the second one is at the narrow restriction site which functions as a stop valve (Fig. 3.12). We made sure that the burst pressure in the main channel is low enough to let the liquid pass with a wide range of filling pressures and is high enough in the restriction to stop the liquid from further movement ($w_{channel} = 70 \mu m$ vs $w_{gap} = 10 \mu m$). Based on equation 3.10, an approximate value for the burst pressure at these two locations are 2.06 kPa to 14.4 kPa respectively. Therefore, any number between these two values can potentially be used as a filling pressure. In addition, from Fig. 3.12, it is clear that comparing liquid movement

in the traps with the main channel, the interface moves faster in the trap which is wider ($w_{trap} > w_{channel}$).

The fact that the filling pressure needs to be bigger than the capillary pressure to force the liquid to move in the channel necessitates consideration of any geometrical change that may increase the capillary pressure. Although increased capillary pressure can be balanced with the increased filling pressure, since the device is made to be in a temporary bond with the substrate, the range of the operating pressure is limited.

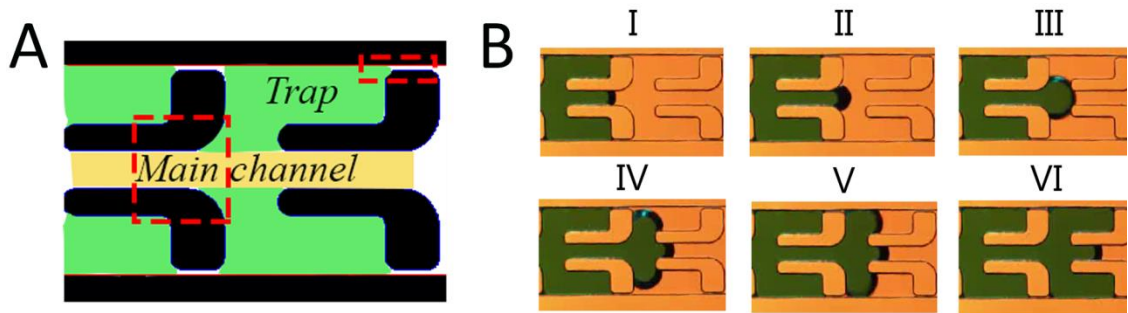


Figure 3.12: Implementation of liquid stoppage mechanism in the design of static droplet system: Liquid stops at the narrow restriction but moves through the main channel.

3.5. Capillary-based liquid movement in a microchannel

3.5.1. Analysis of meniscus advancing in the microchannel

In order to be able to design a functional sample trapping device and predict the traps filling behavior, the physics of the flow in the channel as well as its relation with the geometry of the traps and channel dimensions should be carefully considered. Capillary pressure opposes the injection pressure, and therefore to make sure that the interface reaches certain locations at certain time points, pressure's changes across the liquid-air interface needs to be calculated. The Young-Laplace equation can therefore be used to find the interface's capillary pressure which reads,

$$\Delta P = -\gamma \bar{\nabla} \cdot \hat{n} = 2\gamma H = \gamma \left(\frac{1}{R_1} + \frac{1}{R_2} \right) \quad (\text{Eq. 3.18})$$

Where ΔP is the pressure difference across the fluid interface called Laplace pressure, γ is the surface tension, \hat{n} is the unit normal pointing out of the surface, H is the mean curvature, and R_1 and R_2 are the principle radii of curvature. Assuming that the interface is part of a cylinder with radius r , Eq.3.18 becomes

$$\Delta P = \frac{\gamma}{r} \quad (\text{Eq. 3.19})$$

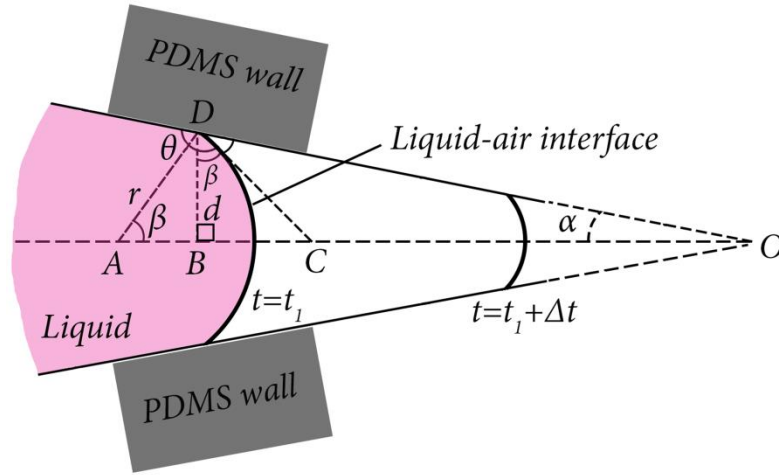


Figure 3.13: Device working mechanism: Tracking liquid-air interface in the channel; Theoretical analysis of liquid-air interface movement in the channel and through the traps[131].

To understand the effect of geometry on pressure, we will see how radius of curvature changes in the channel and through the traps. Fig. 3.13 demonstrates a schematic of fluid interface moving along PDMS channel walls. In this figure, θ is the liquid-PDMS contact angle, α is the half of the opening angle of the channels ($\beta=0$ for a straight channel), $r=AD$ is the radius of curvature of the liquid-air interface, and d is the half-distance between the channel walls.

$$\Delta COD: \theta = \alpha + (180^\circ - (90^\circ - \beta)) \rightarrow \beta = \theta - \alpha - 90^\circ \quad (\text{Eq. 3.20})$$

$$\Delta ABD: \sin(\beta) = d/r \quad (\text{Eq. 3.21})$$

From Eq. 3.20 and Eq. 3.21 we can write,

$$r = d/\sin(\beta) = d/\sin(\theta - \alpha - 90^\circ) \quad (\text{Eq. 3.22})$$

Combining (2) with (5),

$$P(x) = \gamma \cdot \sin (\theta- \alpha- 90^\circ)/d = \gamma \cdot \cos (\theta- \alpha)/d \quad (\text{Eq. 3.23})$$

To better understand this formula, we review the fluid movement along the channel. Looking at Eq. 3.23 and Fig. 3.13, when liquid-air interface moves from $t=t_1$ to $t= t_1+\Delta t$, the radius of curvature and consequently the value of d decreases leading to an increase in the capillary pressure value demanding higher injection pressure to fill the channel. Fig. 3.14 presents the geometry of a trap and the corresponding channel width in different locations. Fig. 3.14-II demonstrates the moment when the liquid-air interface reaches a trap's entrance. Based on the above explanations, in order to ensure that the liquid first enters the trap and only after it has fully filled the trap, it continues to fill the main channel (Fig. 3.14-VI), it is essential to have $w_{entr.} > w_{channel}$; In this design these values are $100 \mu\text{m}$ and $70 \mu\text{m}$ respectively.

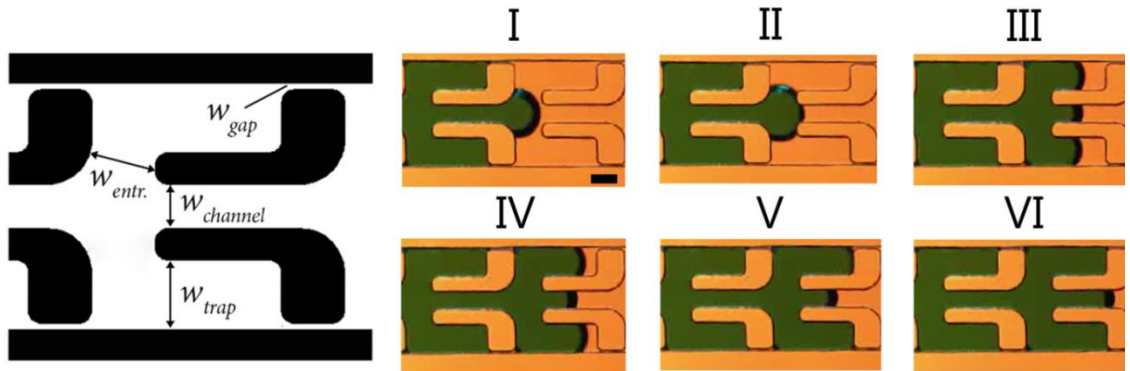


Figure 3.14: Device working mechanism: Critical dimensions in the static droplet array device; Time-lapse images of liquid-air interface movement while entering the traps: Liquid filling the previous traps first and then moving toward the next set of traps; Liquid-air interface just before entering the traps demonstrating the entrance length to the traps and the main channel, Scale bar= $100\mu\text{m}$.

3.5.2. Solution of the meniscus movement in the microchannel using Phase-field method

The aim of the following simulations is to provide a deeper understanding of the interface movement in the microchannel, with different geometrical structures. To achieve this

goal, three types of geometries are introduced (Fig. 3.15). Type 1 and 2 are gradual linear and non-linear channel expansion/contraction respectively. Type 3 presents the most general case which is the geometry of the microfluidic junction. Together, these geometries represent different variations of channel structures.

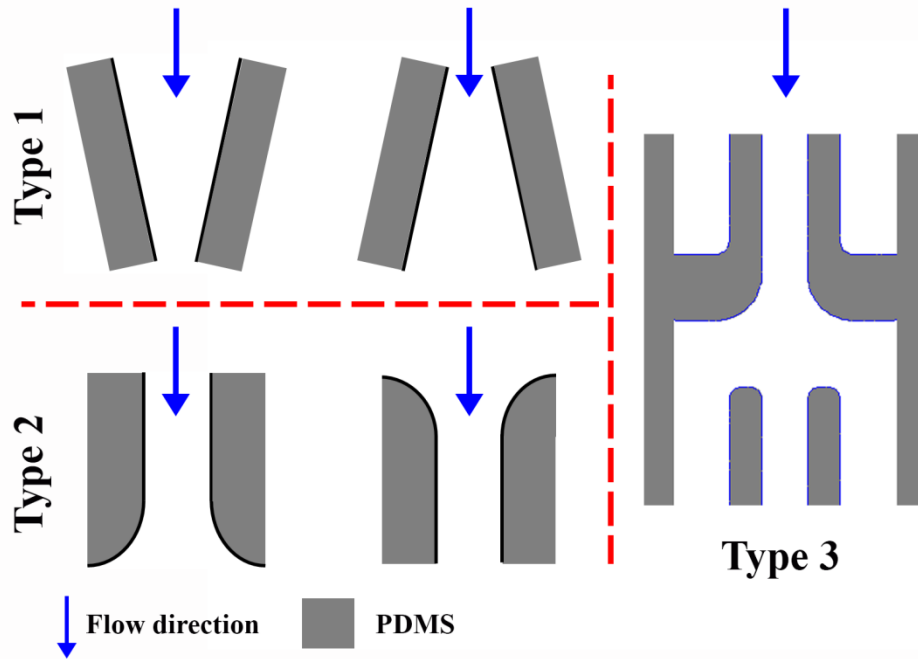


Figure 3.15: Variations of channel design for investigating the capillary-based interface movement.

Type 1 and 2: Solution of interface advancing in linear and nonlinear microchannels

In this section, a numerical simulation is held to understand the interface behavior in facing a gradual linear or nonlinear expansion in the channel geometry. The geometry of the expansion zones are designed based on the dimensions of the channels presented in this thesis, i.e. an expansion ratio of 1:3 with inlet size of $70\ \mu\text{m}$ and an outlet size of $210\ \mu\text{m}$. The dimensions of the expansion channels are shown in Fig. 3.16.

In COMSOL multiphysics, the Laminar Two-Phase Flow, Phase Field was chosen as the physics with the Transient with Phase Initialization as the solver mode. In order to impose the liquid-air initial boundary, the geometry was designed by unifying two subsections of

the channel. The lower bigger domain was set to have air at $t=0$ and the upper smaller domain was filled with water. The boundary between the two domains was chosen to be the initial interface between the two phases. The values of density, viscosity, surface tension, and Phase Field parameters were kept the same as presented before, i.e. $\rho_{water}=998 \text{ kg/m}^3$, $\rho_{air}=1.1614 \text{ kg/m}^3$, $\mu_{water}=1.002 \times 10^{-3} \text{ kg/m.s}$, $\mu_{air}=1.846 \times 10^{-5} \text{ kg/m.s}$ and water surface tension of 0.0728 N/m . The boundary conditions were set to 2 kPa , 0 kPa , and contact angle of 1.8679 rad for the inlet, outlet and the walls

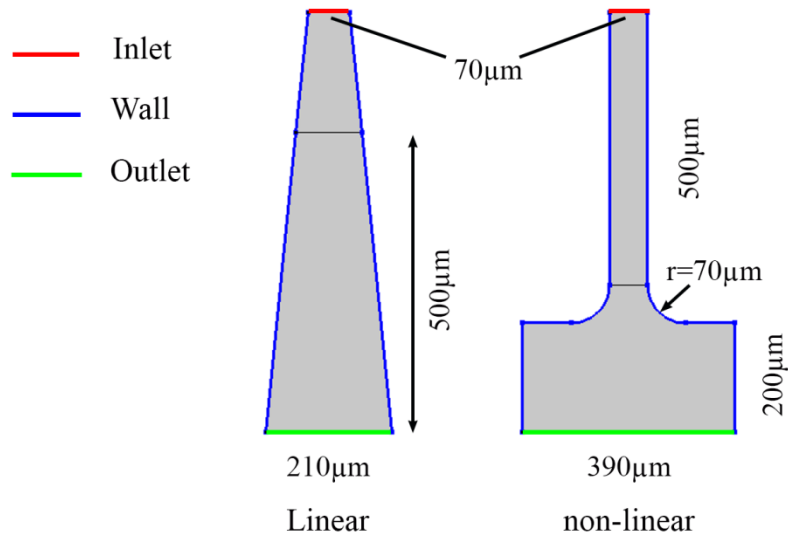


Figure 3.16: Schematics of the geometries of a linear and nonlinear expansion microchannel.

Mesh system is generated with the maximum element size= 0.007 mm , minimum element size= 1.4×10^{-5} , maximum element growth of 1.1 , and curvature factor of 0.2 . The time dependent solver is set to be solved in the time span of $[0-0.5 \times 10^{-3} \text{ seconds}]$ and $[0-1 \times 10^{-3} \text{ seconds}]$ for linear and nonlinear cases respectively with time step size of 0.25×10^{-4} . The time span and the time step were chosen by running the simulation for a number of times, tracking the interface movement through the geometry and choosing the time span/step which captures the total period of interface movement.

Results and discussion

Volume fraction

In order to compare the behavior of liquid-air interface over time between the linear and non-linear channels, the volume fraction of water is tracked over time (Fig. 3.17). As can be seen here, for the channel with linear expansion geometry, the interface movement accelerates along the channel. This is evident by comparing the change in the interface's front in equal time range of $1.25e-4s$ between consecutive images of Fig. 3.17A. From Fig. 3.18B, it is quite clear that nonlinear geometry introduces higher capillary pressure compared to the linear geometry and therefore is more successful in decelerating the interface's front. However, compared to the sudden expansion geometry, no visible difference is detected and further monitoring of the contact point is required.

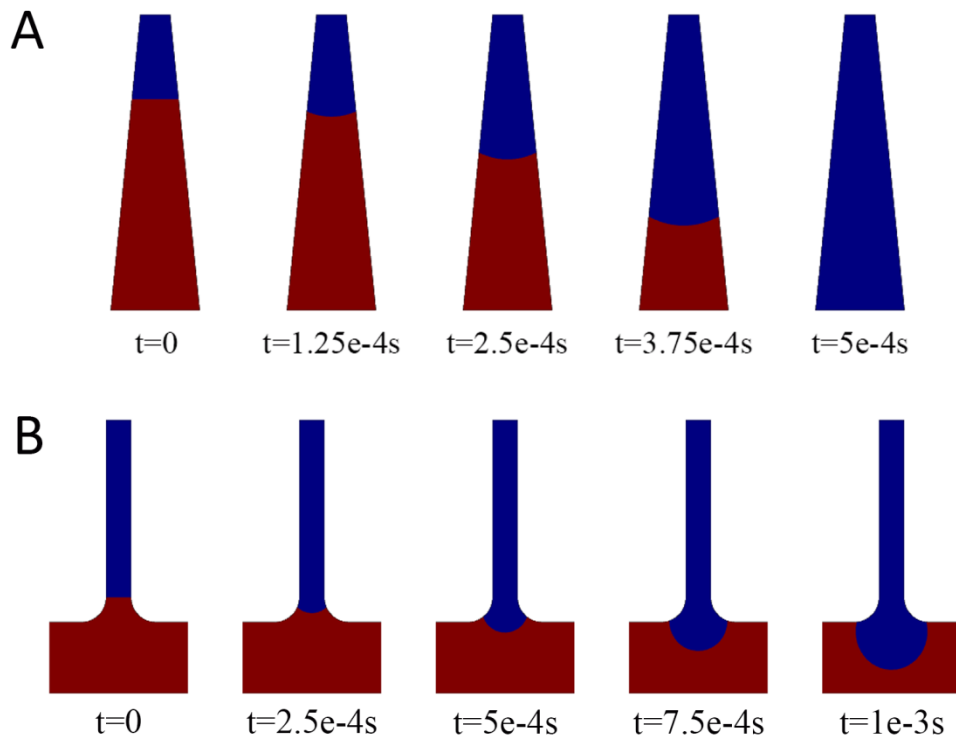


Figure 3.17: Evolution of the liquid air interface over time in the A) linear versus B) nonlinear expansion geometries.

Velocity

Fig. 3.18 presents the sequence of image showing the velocity magnitude and velocity profile at different time points. As demonstrated in Fig. 3.18A, due to the presence of capillary pressure, the interface behaves as a barrier and retards the flow. Therefore the velocity magnitude behind the interface is small. Compared to the sudden expansion case, the linear expansion geometry shows less resistance to the filling flow. In addition, in linear geometry, the interface is not stopped near the initial interface line and moves immediately after being pushed by the filling pressure. It can be concluded that the burst pressure for the linear expansion device is much smaller than the sudden expansion device. Fig. 3.18B demonstrated the velocity magnitude for the nonlinear expansion channel. Comparing the velocity magnitude between the nonlinear and sudden expansion geometry, it can be found that the nonlinear expansion is less resistive against the interface advancement in the channel. This means that the capillary burst pressure is lower in the nonlinear expansion geometry. The results of the velocity profile indicate that the nonlinear expansion shows smoother change across the interface compared to the sudden expansion geometry.

Fig. 3.18C and 3.18D demonstrate the air-liquid front as well as the velocity vectors in the fluid domain over time. As can be seen, the velocity magnitude experiences an abrupt decrease when facing the liquid-air interface. However, as the interface barrier proceeds further downstream, the velocity magnitude is built up over time. This trend is also present in the nonlinear channel geometry. However, the nonlinear channel shows a reverse flow in the regions of the interface near the walls. This confirms the fact that the nonlinear expansion is acting as a barrier and helps to stop the flow.

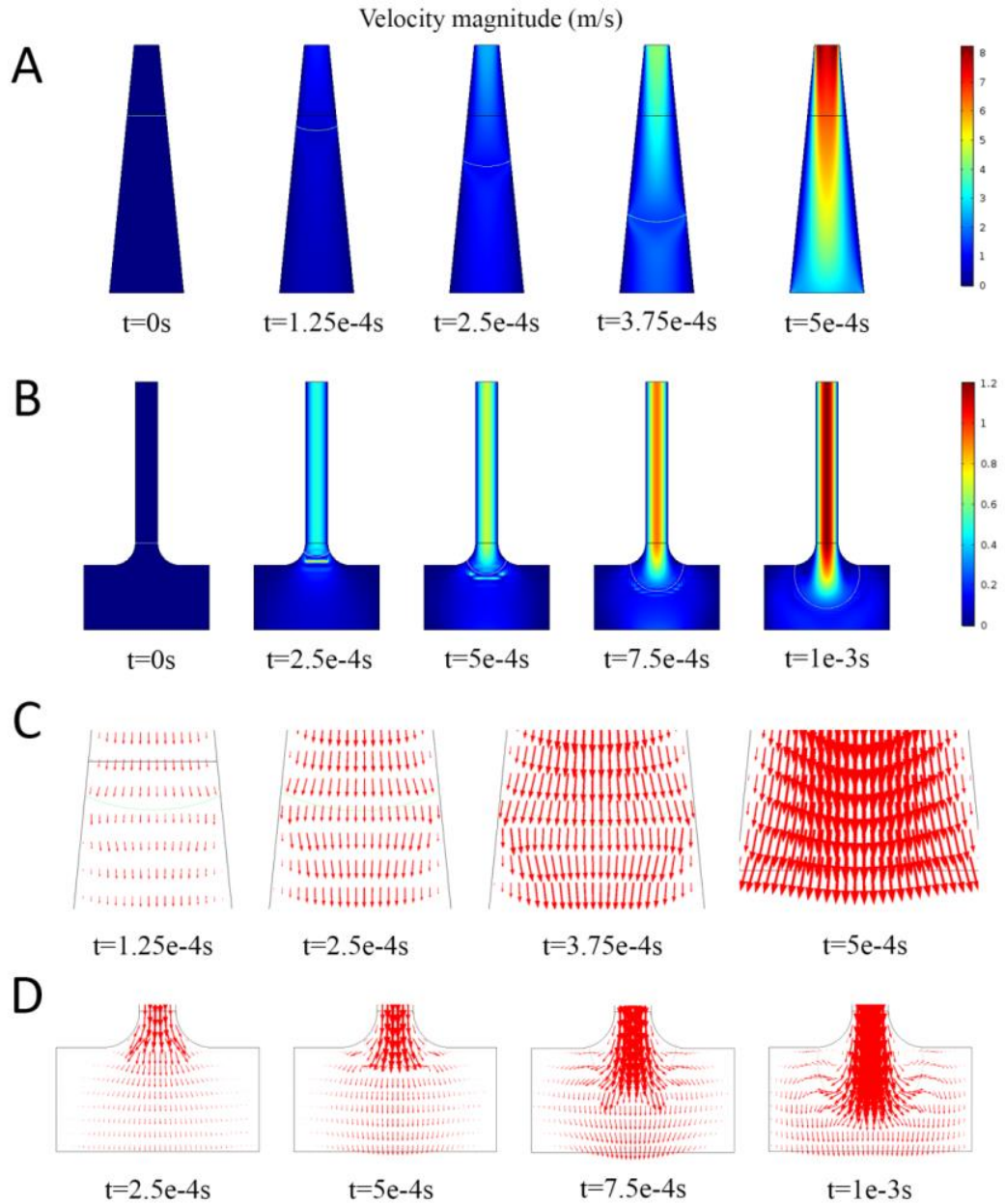


Figure 3.18: Evolution of the velocity magnitude (A and B) and velocity vector (C and D) in the linear and nonlinear expansion channels over time, the scale factor for velocity vectors at C and D are 0.01 and 0.05 respectively.

Pressure distribution

Fig. 3.19A presents the pressure distribution in the expansion geometries system. For the linear expansion geometry, the simulation results indicate that unlike the sudden expansion geometry, the pressure behind the interface is almost constant during its

movement. This can be interpreted as a constant force on the interface which is caused by the difference between the filling pressure and resistive capillary pressure.

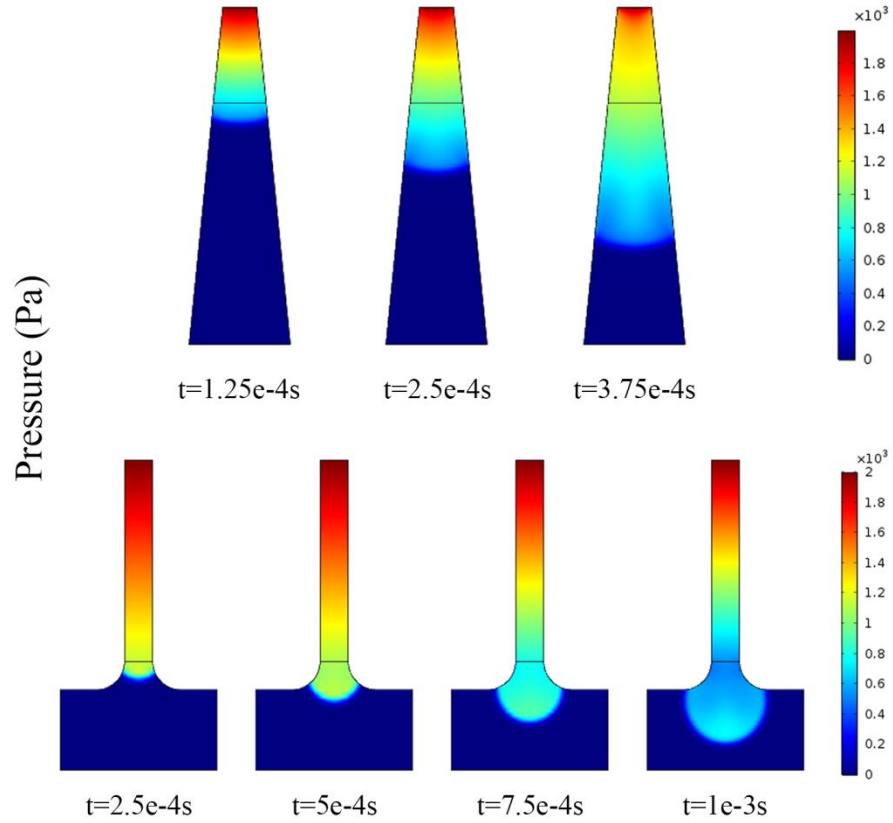


Figure 3.19: Evolution of the pressure distribution over time in the linear (top) and nonlinear (bottom) expansion geometries.

For the nonlinear expansion geometry however, the pressure behind the interface is much lower compared to the case of sudden expansion (Fig. 3.19B). This shows that a nonlinear expansion can be used to obtain lower burst pressures. Looking into Eq. 3.10 for the burst pressure this phenomenon can be easily explained. The cosine term in the nominator and the $w_a > w$ in the denominator both decrease the value of the burst pressure.

Locating the position of the contact point can help understanding the motion of the liquid-gas interface in the channel. As can be seen in Fig. 3.20A, the position of the contact point is continuously increasing. The increase however is happening gradually along the contact line and its rate gets bigger as can be seen from the slope of this plot. This

indicates that the interface movement is accelerating due to the presence of a constant force. A constant force with a constant mass leads to a constant acceleration which can be seen from the hyperbolic profile of the contact point. Fig. 3.20B demonstrates the position of the contact point while passing through the nonlinear expansion channel. As can be seen here, the position of the contact point is continuously increasing. However, comparing the result with the sudden expansion (Fig. 3.11), it is clear that the contact point displaces faster within the same time span (0-0.0008s). Looking into Fig. 3.20B, the contact point shows a decelerating profile.

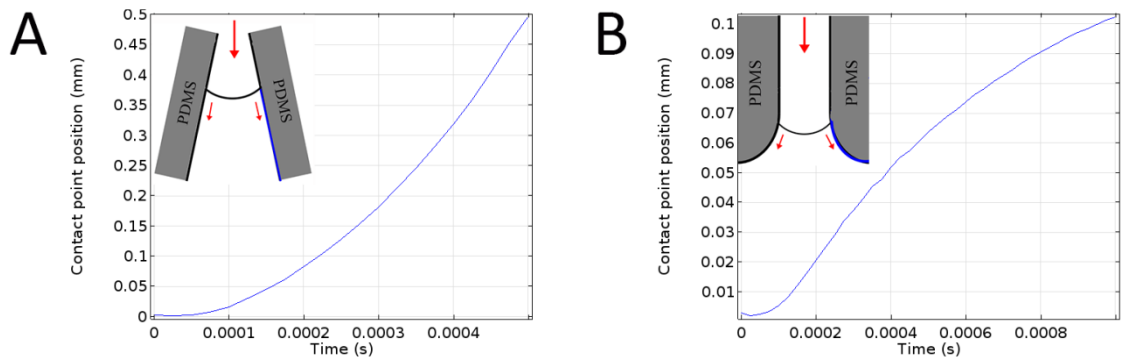


Figure 3.20: Variation of the contact point position along the horizontal line with time in A) linear expansion geometry and B) non-linear expansion geometry.

Type 3: Solution of interface advancing in a microchannel junction

Based on the behavior of the flow in facing expansion and contraction geometries, here we introduce and simulate the interface movement in microfluidic junction geometry. We seek a geometry that can enable trapping liquid samples into individual compartments. This requirement demands a more complex channel geometry in which the sample can be directed into each trap while redirecting the incoming samples into the other traps. Fig. 3.21 demonstrates the geometry of the trapping system. When the liquid-air interface reaches this junction, it has three ways to proceed. It can advance towards a pair of symmetrical traps and move in the middle channel between the traps.

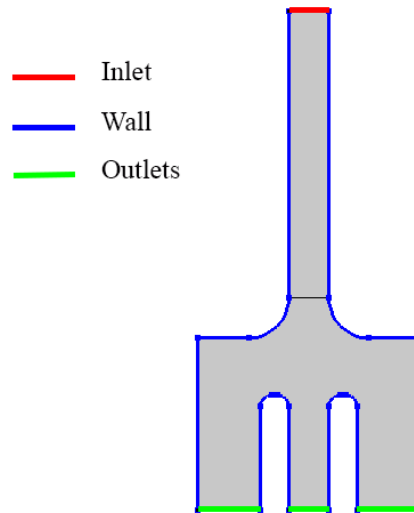


Figure 3.21: Geometry of the microchannel junction.

Since any geometrical change in the channel design can increase or decrease the capillary pressure, tracking the liquid-air interface front is required for understanding the mechanism of the separation of a liquid sample into individual compartments. Here we investigate the physics of the two-phase flow filling the junction geometry (Fig. 3.21). The width of each pair of side channels (traps) is set to be $110\ \mu\text{m}$. All liquid and air properties were kept the same as previous simulations. Boundary conditions were set at $P_{\text{inlet}}=2\ \text{kPa}$, $P_{\text{outlet}}=0\ \text{kPa}$, and contact angle $\theta=1.8679\ \text{rad}$. Free triangular mesh with maximum element size= $0.0087\ \text{mm}$, minimum element size= $1.74\text{e-}5$, maximum element growth of 1.1, and curvature factor of 0.2 was used (Fig. 3.22). The time dependent solver is set to be solved in the time span of $[0-1.2\text{e-}3\ \text{seconds}]$ with time step size of $0.25\text{e-}4$.

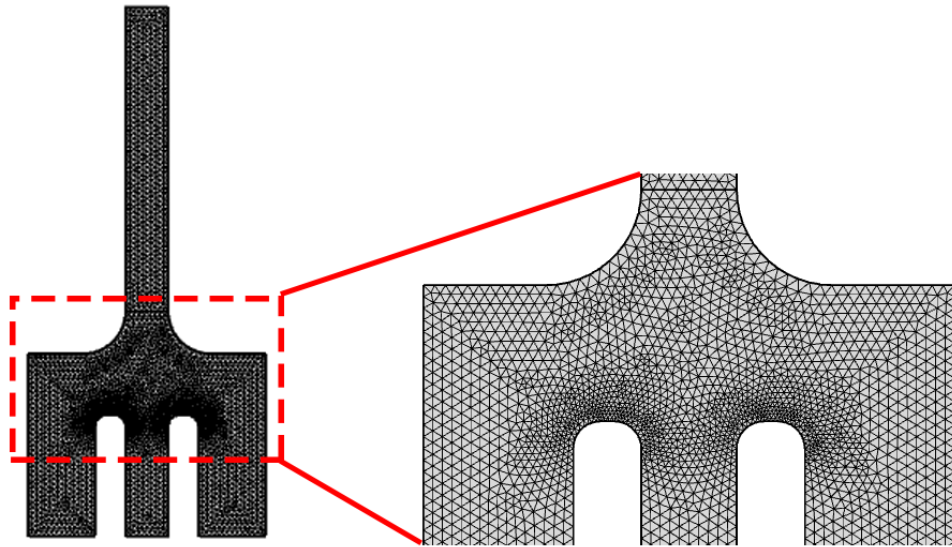


Figure 3.22: Mesh system for solving the interface movement in the junction geometry

Results and discussion

Volume fraction

Fig. 3.23 demonstrates the evolution of liquid-air interface in the junction geometry. At $t=9e-4s$, the interface is at the entrance of the main channel as well as the side traps. However, after this moment, the liquid front moves and fills the main channel while it is blocked from entering the side channel. Therefore, this geometry with the aforementioned filling pressure is not able to fill the traps.

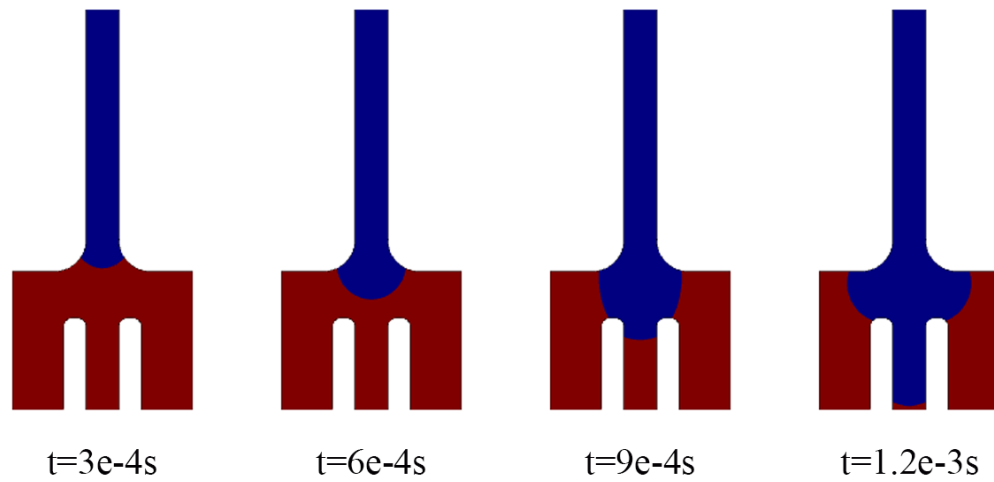


Figure 3.23: Evolution of the liquid air interface over time in the junction of the liquid trapping system.

Fig. 3.24 presents the velocity magnitude distribution in the junction geometry. When the liquid reaches the junction area at $t=6e-4s$, the flow has the well-known hyperbolic profile with the peak value in the middle of the channel. At $t=9e-4s$, the interface enters the main channel and the side channels. At this time point, the velocity magnitude behind the interface moving into the side channels drops drastically while the velocity in the main channel increases. This indicates that the capillary pressure is built up at the traps entrance while it is decreased in the main channel.

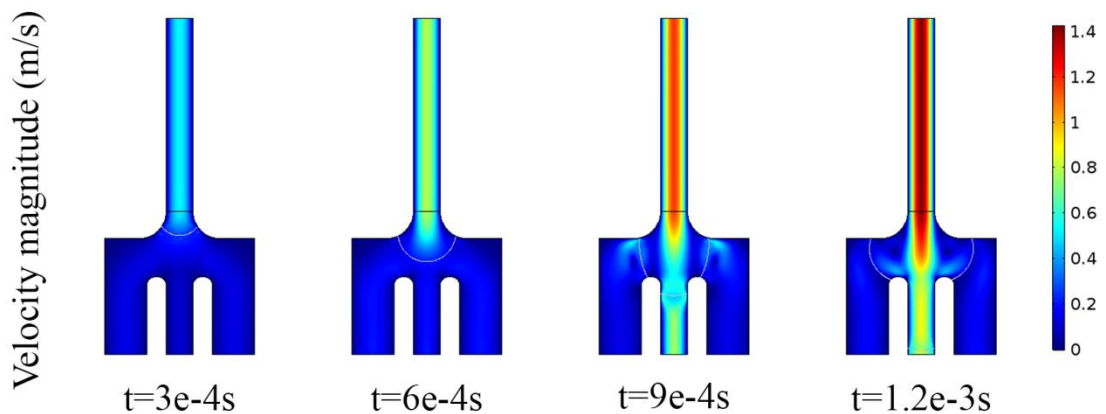


Figure 3.24: Evolution of the velocity magnitude over time in the expansion region.

In order to better understand the velocity change in the domain, the velocity vectors were found. Fig. 3.25 demonstrates the air-liquid front as well as the velocity vectors in the fluid domain over time. As can be seen here, at $t=9e-4s$ the direction of the flow at the traps entrance is nearly vertical and the component of the velocity vector normal to the trap's entrance is so small. At $t=1.2e-4s$, this trend changes and the liquid velocity at the interface pushes the interface into the traps.

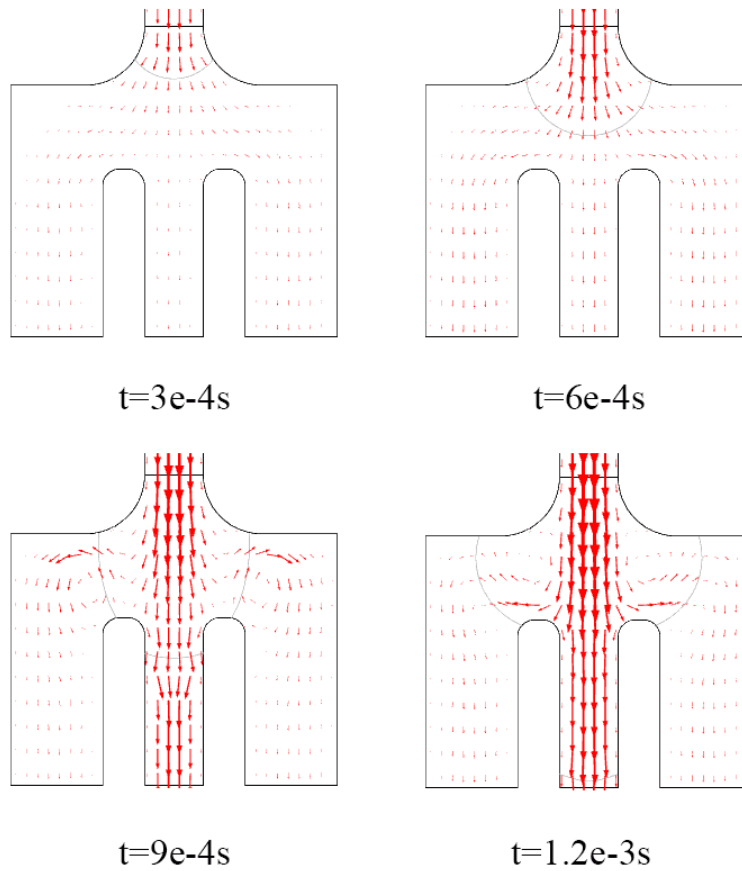


Figure 3.25: The air-liquid front as well as the velocity vectors in the domain over time.

Fig. 3.26 presents the pressure distribution in the system. Comparing the pressure change behind the interface explains the slow liquid movement in the traps and fast liquid movement in the main channel. This value decreases from 1 kPa to 0.5 kPa for the trap front while it decreases from 1 kPa to 0.8 kPa in the main channel. Therefore, the filling pressure is retarded in the traps' entrance.

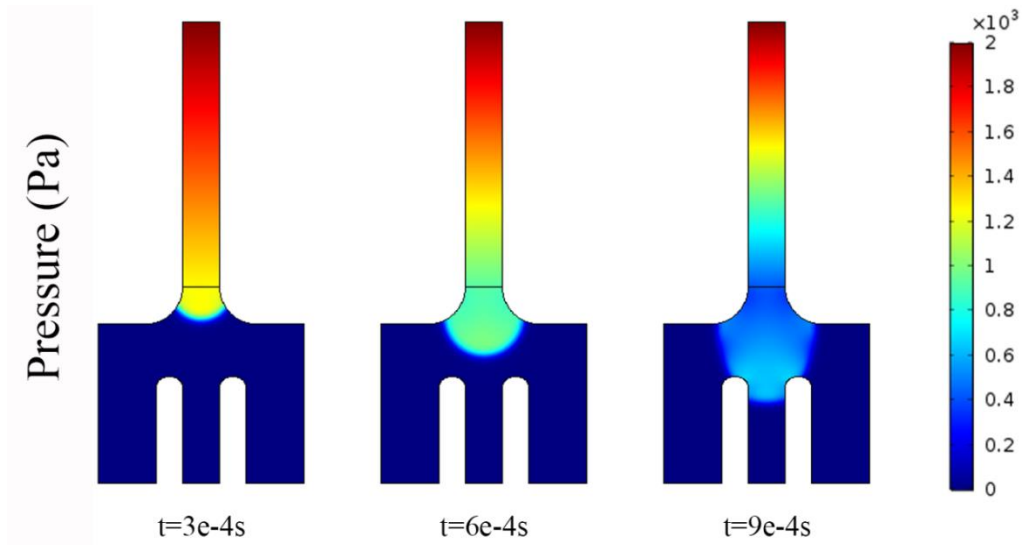


Figure 3.26: Evolution of the pressure distribution over time in the gradual expansion geometry.

As can be seen from the result of interface tracking in the channel, the liquid moves faster in the middle channel compared to the side channels. As we mention later in Chapter 6, when the liquid moves fast under high pressures, the filling pressure is much bigger than the capillary pressure and therefore the effect of capillary pressure in directing the liquid-air interface is hampered. This phenomenon is clearly shown in Fig. 3.25 where velocity vectors turn and make a small circulation area just at the entrance of the side channels. In order to let the liquid, move into the side channels before it fills the middle channel, a number of strategies can be adopted. For example, the main channel can be made narrower and main channel's length can be increased. In addition, the filling pressure can be decreased to make the liquid move into the traps.

Decreasing the inlet pressure

Decreasing the inlet pressure makes a balance between the filling pressure and the capillary pressure. At $P_{\text{inlet}}=2$ kPa, the inlet pressure is large and therefore undermines the effect of capillary pressure. Therefore, in the first step the inlet pressure is decreased to 1 Kpa. Fig. 3.27 demonstrates the liquid-air interface movement at different inlet pressures. As can be seen here, when the inlet pressure is 1kPa, the inlet pressure cannot overcome

the capillary pressure and therefore the interface stops before reaching the junction. In order to find the lowest pressure that leads to interface movement while filling the side channels, the pressure increased with pressure steps of 100Pa. At the inlet pressure of 1.3kPa, the interface moves through the junction and fills the side channels as well. However, comparing the interface movement at inlet pressure of 1.3 kPa with 2kPa (Fig. 3.27), it is clear that the interface is moving much slower compared to the case with higher inlet pressures.

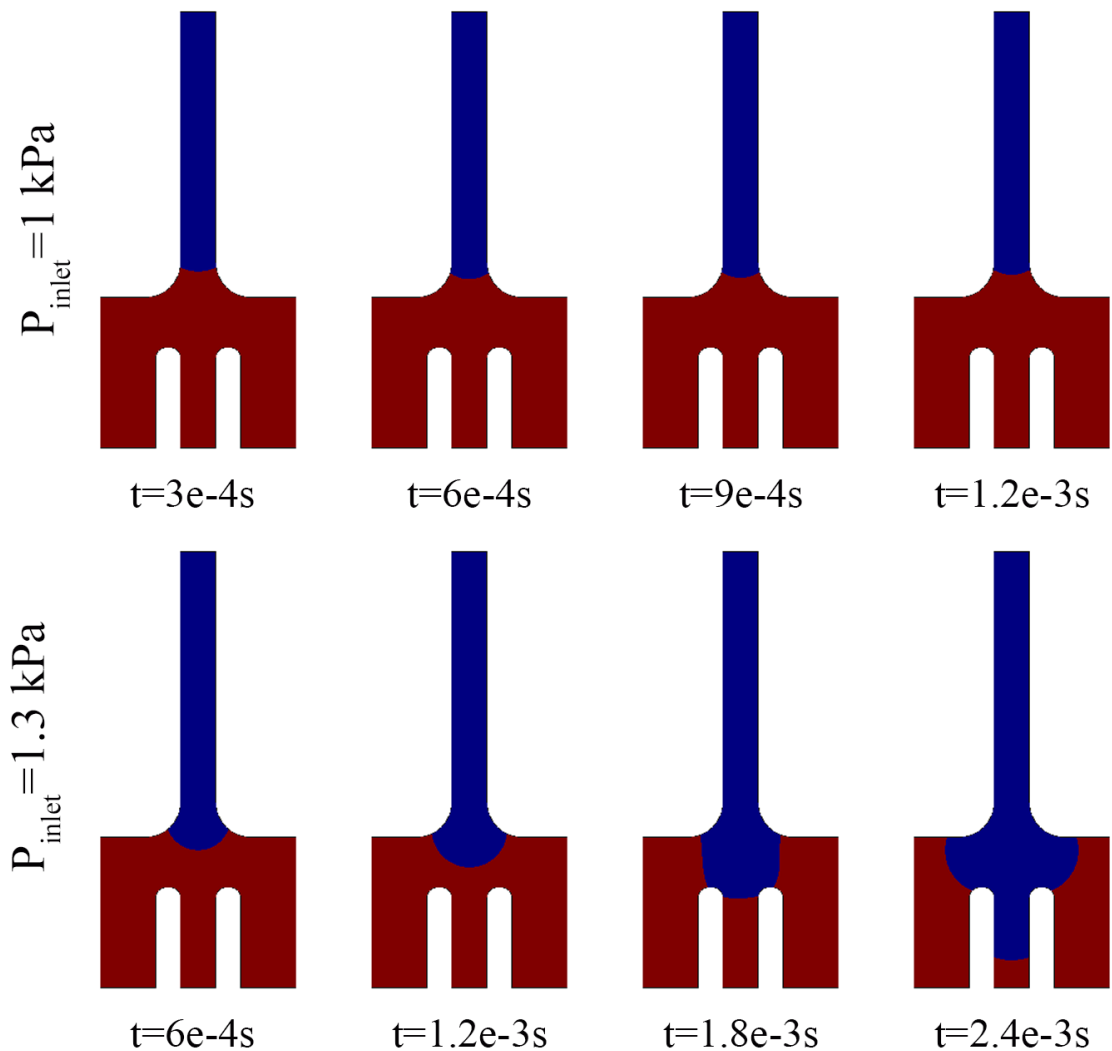


Figure 3.27: Evolution of the liquid air interface over time in the junction geometry at inlet pressures of 1 kPa and 1.3 kPa.

Figure 3.28 demonstrates the pressure distribution at different inlet pressures. At $P=1$ kPa, the pressure does not change in the liquid area since the liquid is stopped due to Laplace

pressure. However, looking into the pressure results at $P=1.3$ kPa, it is evident that the pressure at the liquid side initially reduces as the liquid passes through a gradual non-linear expansion (from $t=6e-4$ s to $1.2e-3$ s). This decrease continues until $t=1.8e-3$ s since there is no increase of the capillary pressure. Once the liquid-air interface moves into the traps, the filling pressure increases again as it encounters the capillary pressure dictated by the channel contraction.

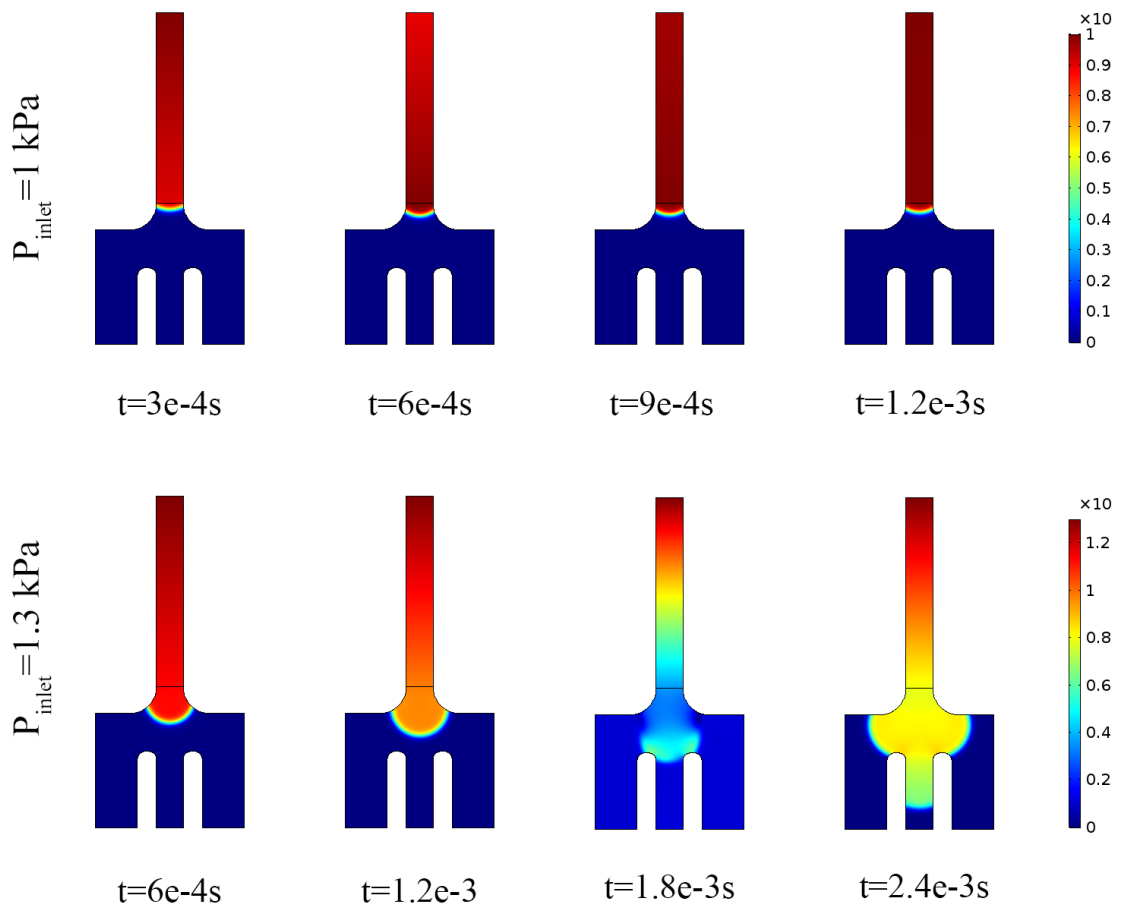


Figure 3.28: Evolution of the pressure distribution over time in the junction geometry at inlet pressures of 1 kPa and 1.3 kPa.

Fig. 3.29 demonstrates the velocity vector at different inlet pressures. It can be seen that the velocity vector is against the direction of the liquid movement at certain locations. For $P=1$ kPa, this happens before the junction. However, at $P=1.3$ kPa, preventive velocity happens when the liquid is at the entrance of the side channels.

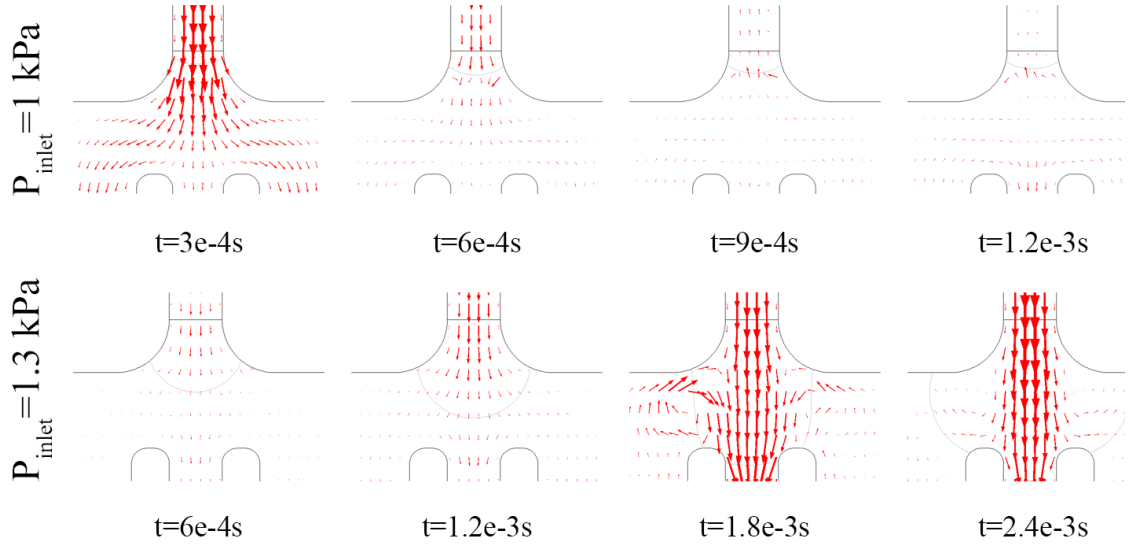


Figure 3.29: Evolution of the velocity vector over time in the junction geometry at inlet pressures of 1 kPa and 1.3 kPa.

3.6. Liquid compartments via shearing

In order to shear the liquid from the main channel and segment the liquid into semi-droplets in separate traps, the principle of surface energy minimization was considered. One such phenomenon takes place in splitting a sessile drop of radius a which is squeezed between parallel plates of distance δ . Assuming that γ_{SL} and γ_{LG} are the surface-liquid and liquid-gas interfacial tensions, the division of the drop requires an increase in surface energy of $\Delta E/E \approx (\sqrt{2} - 1)/\sqrt{2} \left(1 + \frac{\gamma_{SL} \cdot a}{\gamma_{LG} \cdot \delta}\right)$. If $a \gg \delta$ and $\gamma_{SL} > \gamma_{LG}$ this equation simplifies to $\Delta E/E \approx \frac{\gamma_{LG} \cdot \delta}{\gamma_{SL} \cdot a}$. This equation shows that to have droplet splitting, the liquid surface contact area should be maximized while liquid-air contact area should be minimized.

Looking at Fig. 3.30, this means that the trap's length and width should be maximized (the liquid-surface interfacial area) and its height and entrance width ($w_{entr.}$) should be minimized (the liquid-air interfacial area). However, decreasing the device height increases the capillary pressure limiting the range of operational filling pressure. In

addition, increasing the trap length may impair device filling during the sample injection step. Keeping these design considerations in mind, the device dimensions were chosen as shown in Fig. 3.30 which demonstrates liquid shearing from the main channel over time.

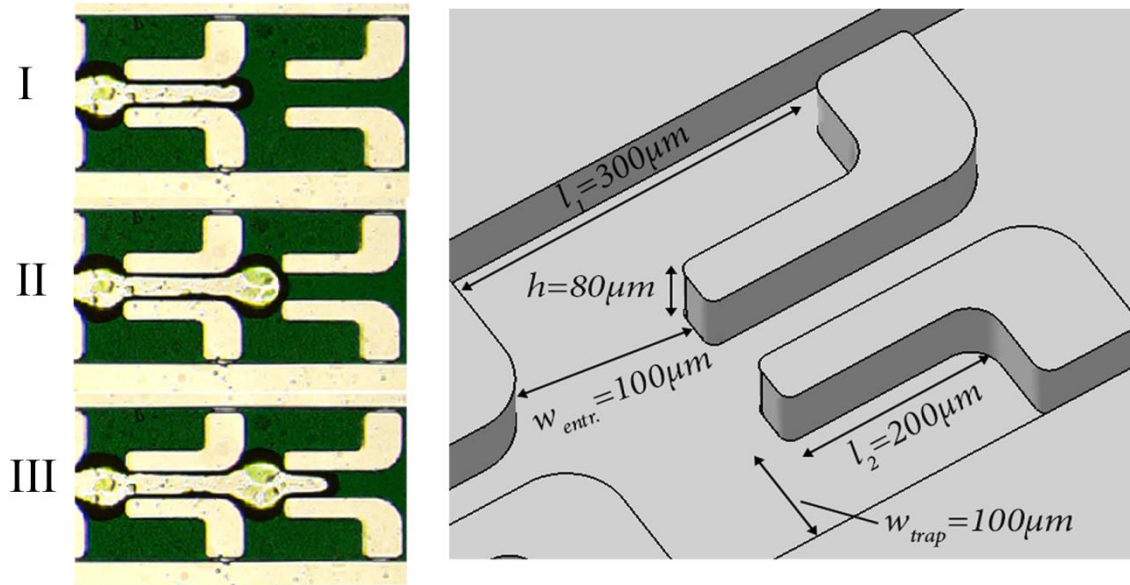


Figure 3.30: Liquid shearing and droplet compartmentalization; Time-lapse image of liquid shearing in the main channel (Left) and critical dimensions in traps design (Right) (Scale bar=100 μm).

3.6.1. Numerical simulation of the liquid shearing and droplet formation

In order to understand the physics of the flow during the liquid shearing step in the microfluidic junction geometry, two-phase flow simulation has been performed. Here, unlike the previous parts that liquid filled the channels, the liquid is pushed out of the channel using air pressure at the inlet leading to the formation of nanoliter sample compartments. In this problem, the initial state, the two side traps and the whole system is filled with liquid. The air is then blown into the system pushing the liquid out of the system. Fig. 3.31 demonstrates the geometry, boundary conditions, and the mesh system used for solving the problem.

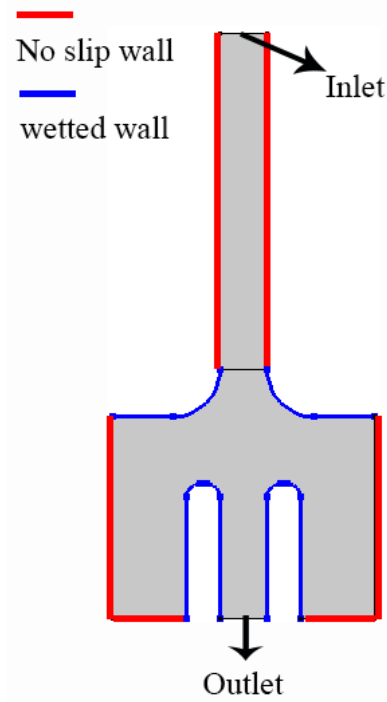


Figure 3.31: Geometry and the boundary conditions for the liquid shearing in static droplet array system.

The properties of air and water were set the same values used in the previous simulations. In order to set the initial position of the air and liquid in the channels, the initial values of each domain were defined. The lower bigger domain was set to have water at $t=0$ and the upper smaller domain was set to be filled with air. The boundary between the two domains was chosen to be the initial interface between the two phases. The time dependent solver was set to be solved in the time span of $[0-0.6e-3 \text{ seconds}]$ with time step size of $0.25e-4$.

Results and discussion

In order to track the liquid-air interface, the plot of volume fraction of each phase was obtained. Fig. 3.32 demonstrates the evolution of interface movement over time in the system.

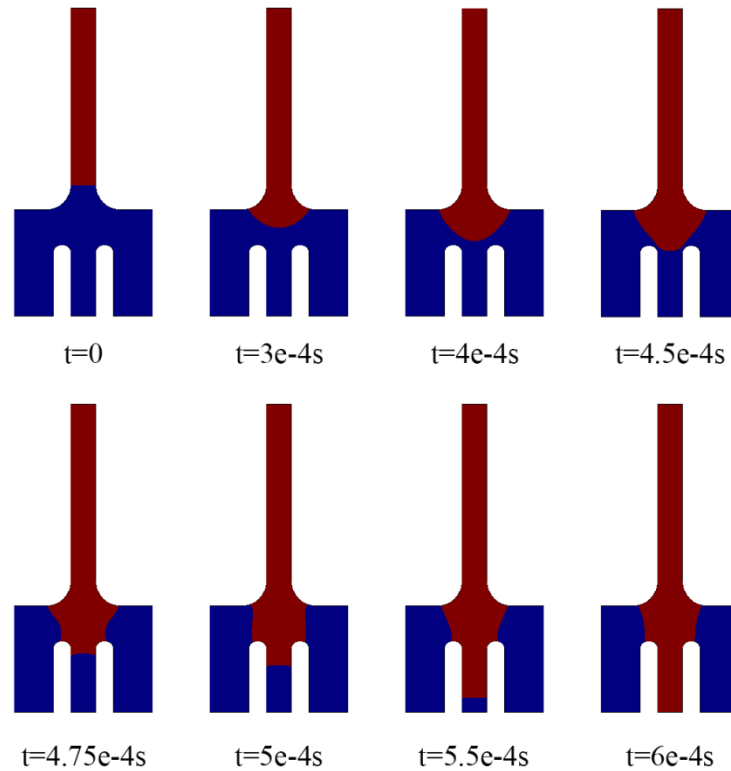


Figure 3.32: Evolution of the liquid air interface over time in the gradual expansion region: red=air and blue=liquid.

Looking into Fig. 3.32, at $t=4.5e-4s$, the interface is in contact with the entrance of both the middle channel and the side channels. Then within a short period of time, the air shears the liquid and separates it into the two compartments surrounded by the walls in the side channels and the liquid which remained in the channel. At $t=6e-4s$, the liquid is pushed out from the main channel and the liquid compartments get a stable shape at the liquid-air interface. Fig. 3.33 presents the sequence of image showing the velocity magnitude in the junction geometry during the shearing period. As can be seen, when the air-liquid interface passes the junction between $t=4.5e-4s$ and $t=4.75e-4s$, part of the pressure was trying to push the liquid in the traps is released and now only faces the main channel. Therefore, a region of high velocity is generated at the middle of the junction as can be seen from the velocity distribution at $t=4.75e-4s$. After this moment, the liquid in the traps shows a quite stable zero velocity and the air pressure is trying to push the remainder of

the liquid out of the channel. As the amount of remaining liquid in the main channel decreases, the air velocity increases. At $t=5.5e-4s$, there is an increase in the velocity magnitude showing fast air flow which now faces no liquid barrier. This behaviour is also demonstrated in Fig. 3.34 which depicts the velocity profile over time.

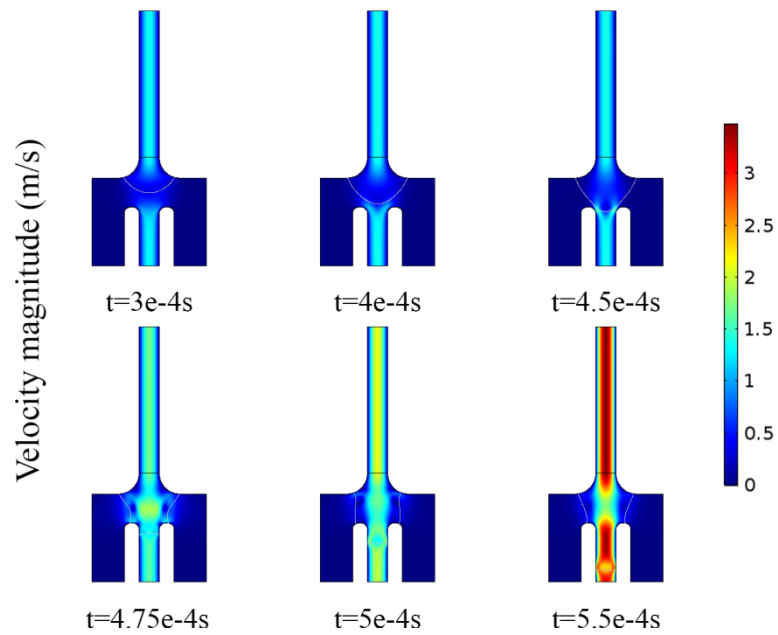


Figure 3.33: Evolution of the velocity magnitude over time in the expansion region.

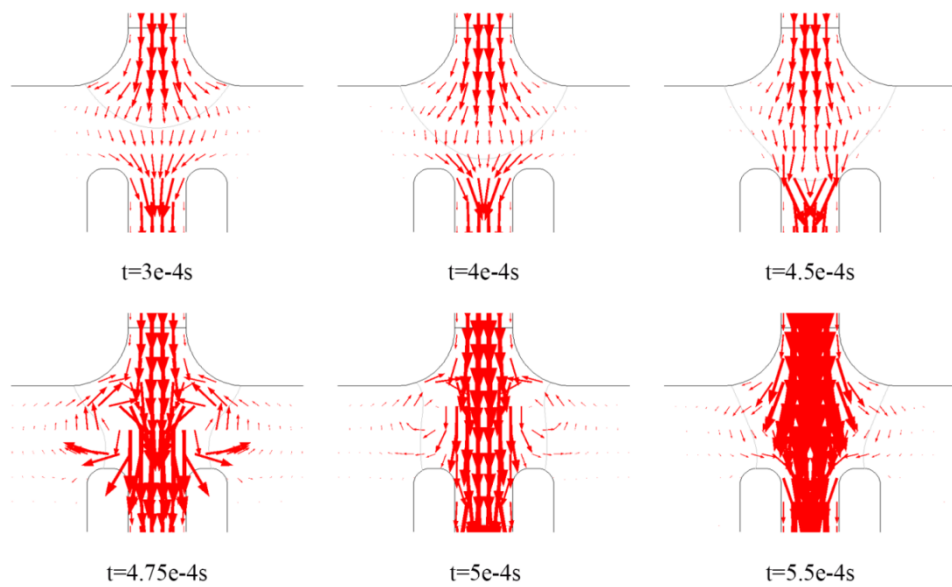


Figure 3.34: The air-liquid front as well as the velocity vectors at the liquid-air interface over time.

Finally, Fig. 3.35 demonstrates the pressure change in the liquid and air compartments. The result shows that as the air interface moves in the junction, initially the pressure is increased in the trap area but is released in the main channel that is connected to the outlet. However, after the interface passes the junction, a steep pressure gradient is formed in the main channel under the junction area. This steepness is caused due to the fact that the pressure is now translated into the remaining liquid in the main channel, an incompressible fluid which is connected to the outlet within a short channel length. During the liquid shearing experiment, this phenomenon can be seen by increased acceleration of liquid removal from the main channel during the shearing period. After the liquid is removed from the main channel ($t=5.5e-4s$), the pressure loss in the main channel gets into a normal condition with a much smoother gradient along the main channel.

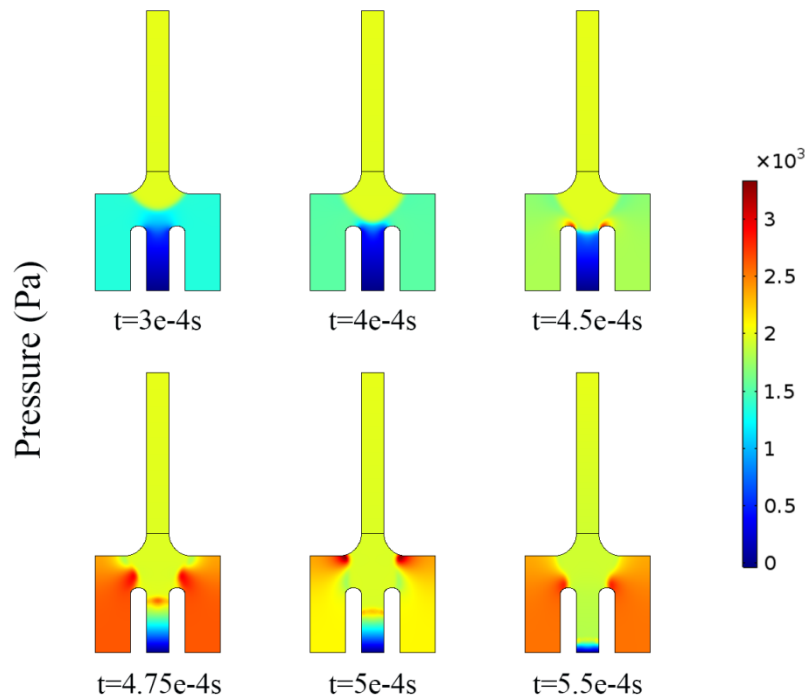
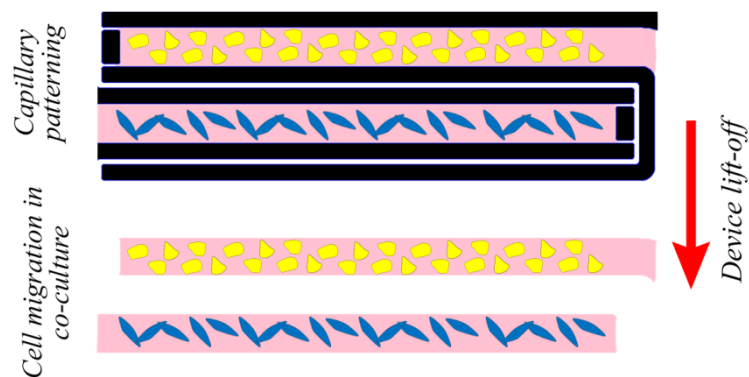


Figure 3.35: Evolution of the pressure distribution over time in the microfluidic junction.

3.7. Conclusions

In this chapter, numerical simulation of the two-phase flow of a liquid in microchannels with expansion, (non)linear expansion, and junction geometries was performed. The velocity magnitude, velocity vector and pressure distribution in the system have been used as tools for investigating the interface movement in different geometries. In addition, monitoring the location of the contact point over time provided valuable information regarding the rate at which the interface proceeds in the microchannel.

Chapter 4. A rapid co-culture patterning device for studying cellular migration*



Regulation of tissue development and repair depends on communication between neighbouring cell types. Recent advances in cell micro-contact printing and microfluidics have facilitated the in-vitro study of homotypic and heterotypic cell-cell interaction. Nonetheless, these techniques are still complicated to perform and as a result, are seldom used by biologists. Here, development of a temporarily sealed microfluidic stamping device is reported which utilizes a novel valve design for patterning two adherent cell lines with well-defined interlacing configurations to study cellular migration due to cell-cell spatial interactions. Post-stamping cell viability of > 95%, the stamping of multiple adherent cell types, and the ability to control the seeded cell density is demonstrated. Viability, proliferation and migration of cultured cells are explained enabling analysis of co-culture boundary conditions on cell fate. Collectively, an in-vitro model of endothelial and cardiac stem cell interactions as regulators of coronary repair after myocardial injury is developed. The stamp is fabricated using RIE etching, is operated with a lab pipettor and uses very low reagent volumes of 20 μ l with cell injection efficiency > 70%. This easy-to-use device provides a general strategy for micro-patterning of multiple cell types and will be important for studying cell-cell interactions in a multitude of applications.

* The outcome of this chapter has been published in "A rapid co-culture stamping device for studying intracellular communication", Scientific reports 6, 35618.

4.1. Introduction

The emergence of microfluidic organ-on-a-chip systems and the ongoing efforts to mimic live organ physiology on a smaller scale has led to renewed interest in the optimal conditions needed to support a cell's culture in an artificially designed microenvironment [132-134]. The sub-micrometer feature resolution and accurate geometries that can be readily manufactured using soft lithography opened new frontiers towards the identification of optimal conditions to support such conditions [135, 136].

These advances can be used to study cell-cell modulation in organ formation and the *in-vitro* reconstruction of tissues for tissue replacement. For example, the interaction between stem cells and their niche regulate tissue regeneration [137], co-culturing of HUVEC and fibroblasts assist in functional capillary formation [138] and activated stromal fibroblasts assist in cancer initiation and progression [139-141]. These findings further stimulated a search for new methods to easily characterize the complex interactions between various cell types *in-vitro*; the simple form of which is 2D cell patterning.

Cell patterning approaches are common and broadly categorized into active versus passive patterning. Active patterning involves the application of an external force such as optical [142], acoustic [1, 143, 144] or fluidic [145-147] forces to confine or transport cells to desired spatial positions. While they offer an on-demand capability, they generally require a skilled operator, complicated chip fabrication and specialized peripheral equipment such as lasers, pumps and waveform generators. More importantly, they are not well adjusted to the patterning of more than one cell type due to the incremental differences in the physical properties of different cell types.

Alternatively, passive patterning methods rely on the pre-stamping of a substrate with proteins or other hydrophilic chemical groups, followed by cell seeding and their selective attachment to the stamped regions [14, 148]. In such methods the number of stamped molecules cannot be accurately controlled due to poor stamping repeatability [149]. Moreover, patterning of two cell-types using passive patterning is highly challenging as it requires the pre-patterning of two cell-selective molecules, as well as aligning the pattern between subsequent steps while eliminating the cell-to-cell cross-contamination [17, 150]. Commercially available nano-drop printing system can solve some of these problems by depositing accurate nanoliter volumes of proteins in a high spatial resolution [151]. However, this method has its own drawbacks, such as high costs and low throughput.

Stencil-based patterning approaches have shown great promise for removing technical barriers required for engineering the cellular microenvironment [152]. In this approach, elastomeric stencils (i.e., made from Silicon, Polydimethylsiloxane (PDMS) or parylene) can be used to pattern cells or biomolecules to specific regions of a substrate [153, 154]. This approach allows easy control of the patterned cell density by directly adjusting the injected cell suspension concentration. However, the attachment of stencil over the substrates and residual of the cells or biomolecules that remain on non-perforated areas can cause trouble in large-scale applications. Cell patterning using switchable surfaces that can be turned from being cell repulsive to adhesive by specific stimuli such as electrical potential or temperature has also been demonstrated [155, 156]. Nonetheless, these approaches are still complicated to perform and as a result, are seldom used by biologists.

A platform that circumvents most of these problems in patterning cells in an open configuration using spatial confinement, was presented by Chiu *et al.* using multilayer soft lithography [157]. In spite of its multiple advantages, its fabrication involves complicated multilayer soft lithography and is operated by an external pump, which limits its widespread adoption. Therefore, although desirable, to date there is no simple method to easily stamp two types of adherent cells in a desired pattern on a 2D substrate.

Here, a new microfluidic stamp is introduced which utilizes a novel valve design to rapidly and accurately pattern two arbitrary live adherent cell types on a flat substrate in an interlaced configuration. The method does not require multilayer device fabrication; it is compatible with conventional soft-lithography and can be operated with a standard hand-held pipette by non-expert personnel.

4.2. Material and methods

4.2.1. Device design

In this work, a simple method for creating protein and cell patterns on a variety of substrates, using a novel microfluidic stamp, is introduced. The device design is depicted in Fig. 4.1. In this device, a liquid, such as cell medium, is loaded into the main channel that is sequentially branched to multiple dead-end microchannels (Fig. 4.1B). Air freely passes through narrow restrictions positioned at the end of each channel, while the liquid stops due to Laplace pressure. Unlike common microfluidic devices where the Polydimethylsiloxane (PDMS) slab is hermetically sealed against a substrate using plasma bonding, here the PDMS stamp is temporarily attached to a substrate, thus facilitating cell loading without any leakage.

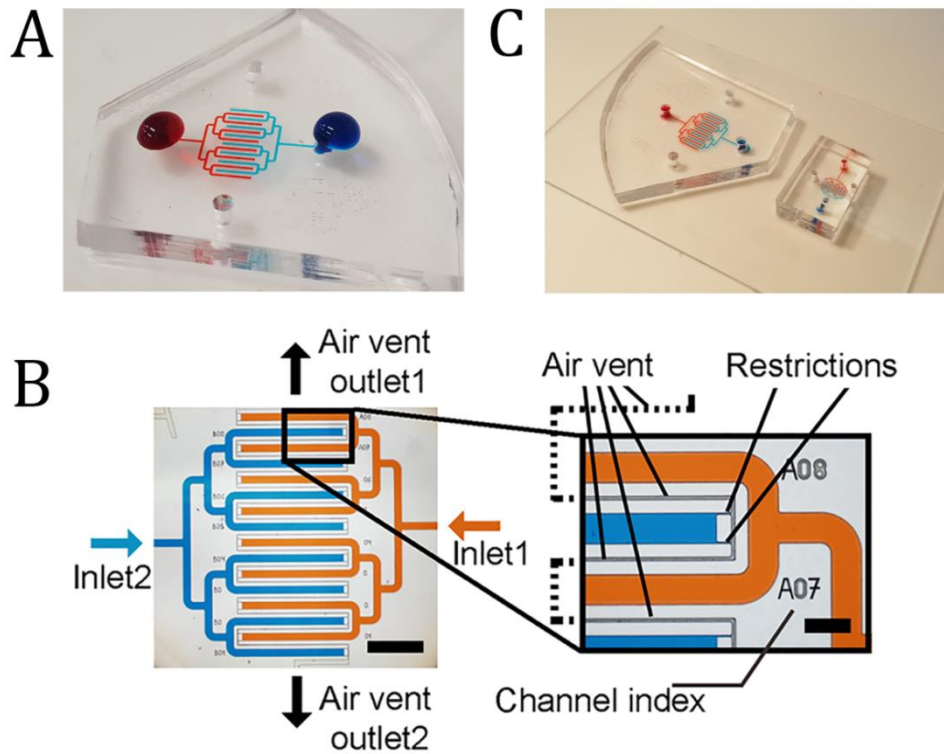


Figure 4.1: Microfluidic stamp structure. (A) PDMS device loaded with blue and red food dyes. (B) Device channel visualization by showing image of the device injected with blue and orange food colours. Zoomed image shows the restriction and air vent that limit liquid flow but allow air to escape. Scale bar, 1 mm and 200 μm ; (C) The stamping device in different sizes.

Assuming that (1) the contact angle between the liquid and PDMS walls is constant (2) the channel's depth is much smaller than its width and (3) the channel's cross section and the restrictions' cross section are both uniform along the channel's length, the failure-free injection pressure in the PDMS stamping device is determined only by the Laplace pressure caused by the air/liquid interface curvature at the restriction. Therefore, the allowed injection pressure depends only on the restriction width, regardless of channel dimensions. This makes manufacturing PDMS stamping device with different channel size (Fig. 4.1C) possible, as long as the restriction width is well designed to prevent leakage. In practice, the strength of these assumptions depends on the fabrication uniformity/quality and is complicated by the fact that there are two different contact angles: one between the liquid and the stamp PDMS walls, and another between the liquid and the cell-stamped substrate.

AutoCAD software was used to draft the design of the photomask (Fig. 4.2). The photomask is a plate or a film with transparent and dark areas. Light can pass through the transparent area while the dark area blocks the light; therefore, the pattern on the photomask can be transferred onto a substrate through optical exposure (e.g. a silicon wafer). Since the photomask will be used in the microfabrication process and needs to be mounted on the mask aligner's stage, a standard 4-inch circle was designed to accommodate different device designs. As shown in figure 4.2A, in order to investigate the effect of different geometries on the device's operation and also reduce the trial and error in device's fabrication, several variations of the devices were implemented in the design.

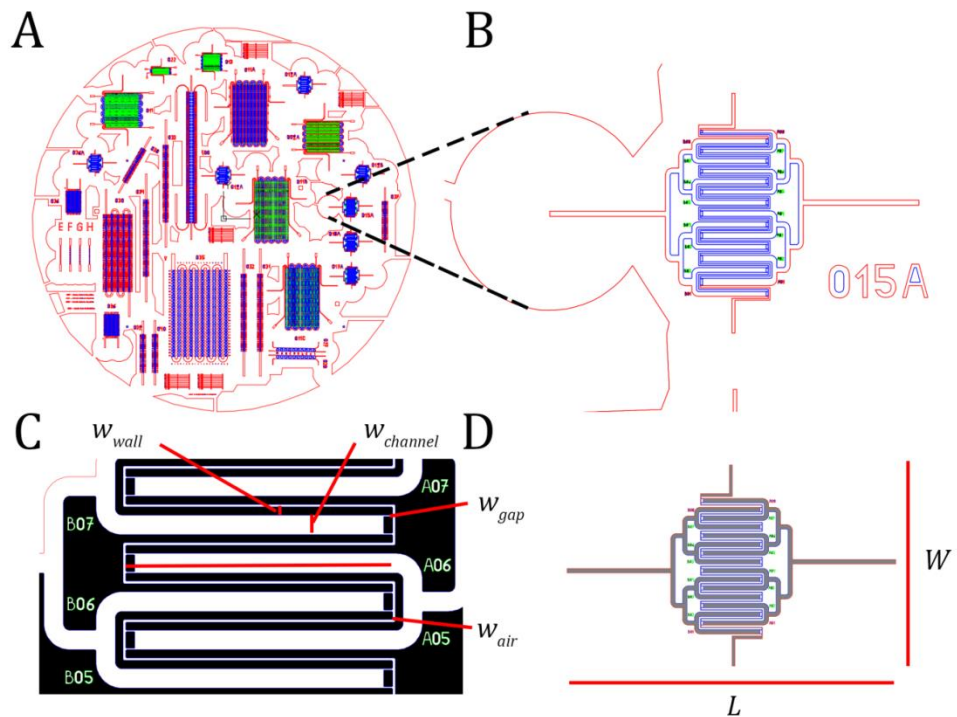


Figure 4.2: Designing the photomask of the cell patterning device in AutoCAD software: (A) The photomask design is a 4 inch circle containing different chip designs. Different variations of the patterning device was positioned on a mask to investigate the effect of geometry on device operation (B) Each device's design has a number of features which includes: A number that differs the device from the nearby devices, small number carved near each branch of the patterning device for easy identification of each branch, a sufficient space from the nearby chip required for punching the access holes, and border lines (C) Critical dimensions of the microfluidic patterning chip; $w_{wall}=62.5\mu\text{m}$, $w_{channel}=150\mu\text{m}$, $w_{gap}=10\mu\text{m}$, $w_{air}=20\mu\text{m}$, (D) Chip dimensions: $W=6.7856\text{mm}$, $L=11.1150\text{mm}$.

There are several points that need to be considered in designing the photomask. First, the dimensions of the channels; this parameter will determine the amount of reagent required for each assay. This is especially important in assays with primary cells. In addition, the dimensions of the device will determine the cells' seeding density in each branch of the device. Since different cells have different sizes, it will be crucial to design the channel's size to accommodate larger cells and control the number and distribution of the cells in each branch of the device. Therefore, the channel width is chosen to be $150\mu m$. Second, the location of the air traps; the air traps should be designed such that they pass through all air gaps. The operation of the device depends on successful air escape from the branched channels. Third, the distance between the nearby designs should be enough to punch the inlet and outlet access holes. In fabricating the devices, 1.5mm biopsy punches are used. Moreover, there should be some safe distance between the designs to be able to cut the PDMS slab using cutting blades. The critical geometrical dimensions of the chip are shown in Fig. 4.2C, D.

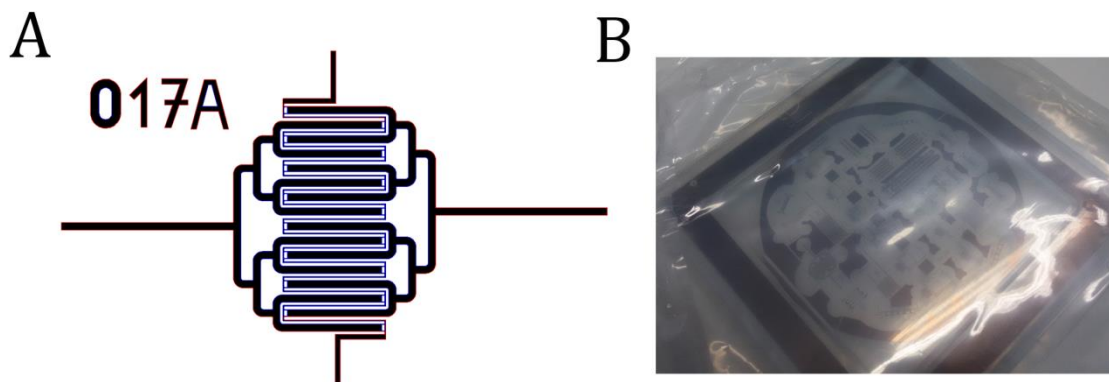


Figure 4.3: (A) Area of the chip design that needs to be dark for fabricating the devices (B) The fabricated mask is a bright-field mask with dark region made out of chrome.

The mask designed here is a bright-field mask (Fig. 4.3). This means that the area of the mask which belongs to the microfluidic channels is dark and the rest of the mask area is transparent. This is a requirement for microfabrication stage and depends on the type of

photoresist that is used for fabricating the device (and is explained in detail under in explanation of Fig. 4.7).

There are three types of materials available to fabricate the photomask (Table 4.1). Since the features in this design are quite small (the minimum size of the patterns is 10 μ m) and the devices' operation depends on accurate fabrication, the patterns were made on a glass mask which gives the highest resolution among available options (Fig. 4.3B).

Table 4.1: Different materials for the photolithography mask

Photomask material	Quartz	Soda lime	Plastic
Description	Expensive, High resolution, Very stable, Can break, Wavelength >180nm	Good price/quality ratio, High resolution, Easy to clean, Stable, Can break, Wavelength >350nm	Low price, Low resolution, Weak stability, Easy to handle, Wavelength >350nm

4.2.2. Device fabrication

The device was initially fabricated using photolithography on silicon wafer. Here first a short explanation of the materials used is presented and then the process of fabrication is explained in detail.

Silicon wafer: This wafer contains two layers of silicone and silicon dioxide and is used as a substrate to make a mould for fabrication of microfluidic devices.

Photoresists: Photoresist is a light-sensitive material that is either degraded or cross-linked upon exposure to light. The exposure energy and wavelength depend on the chemical properties of the photoresist. Based on this criterion, these chemicals are classified into negative or positive tone photoresists.

Positive tone photoresist: In this type of photoresist, exposure to UV light degrades the chemical structure of the photoresist and makes it more soluble. Therefore, the exposed

region of the resist will be washed away using developing solution. Positive photoresist reflects a copy of the photomask on the substrate.

Negative tone photoresist: In this type of photoresist, exposure to UV light cross-links the chemical structure of the photoresist and makes it harder. Therefore, the exposed region of the resist will remain on the substrate and the unexposed area will be removed by the developer solution. Negative photoresist reflects an inverse copy of the photomask on the substrate.

Spin coater: Spin coater is a device that can be used to coat a uniform layer of a liquid on a flat substrate by adjusting the spin time and spin rotational speed.

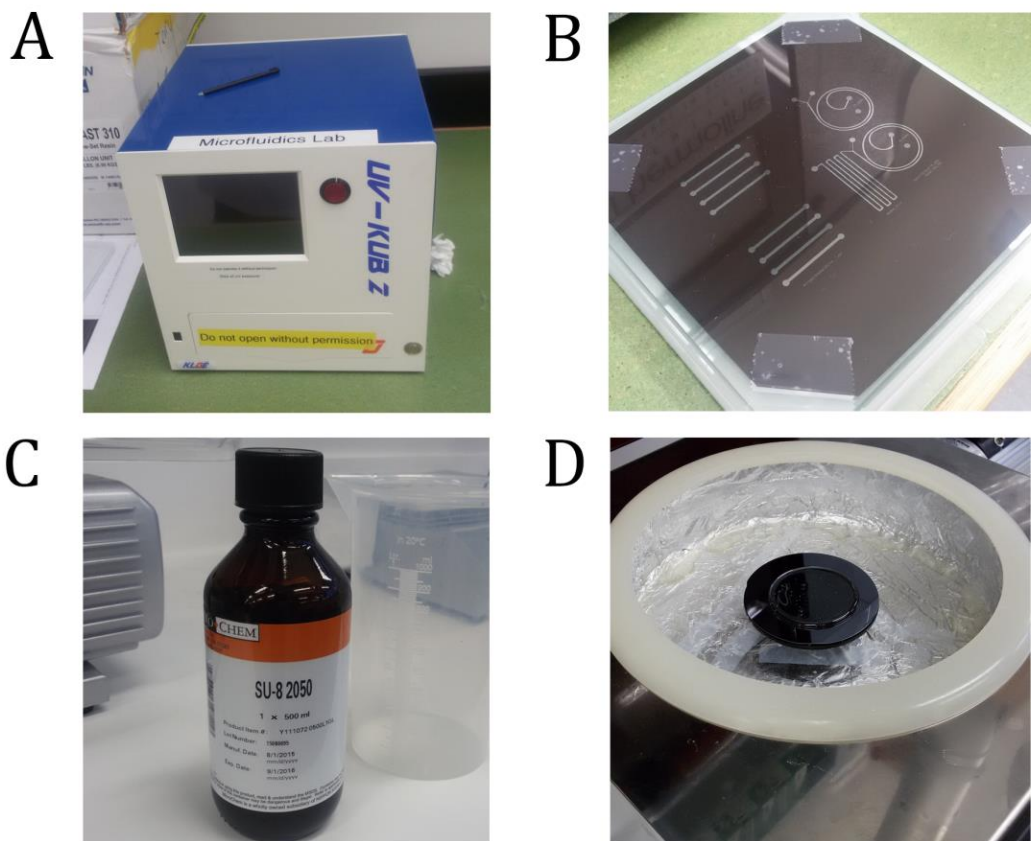


Figure 4.4: Materials and equipments for standard photolithography-based fabrication: (A) mask aligner (B) Transparency mask (C) negative photoresist (D) Silicon wafer and the spin coater.

Photolithography on silicon wafer was used to fabricate mould for cell patterning device. The procedure is shown in Fig. 4.5.

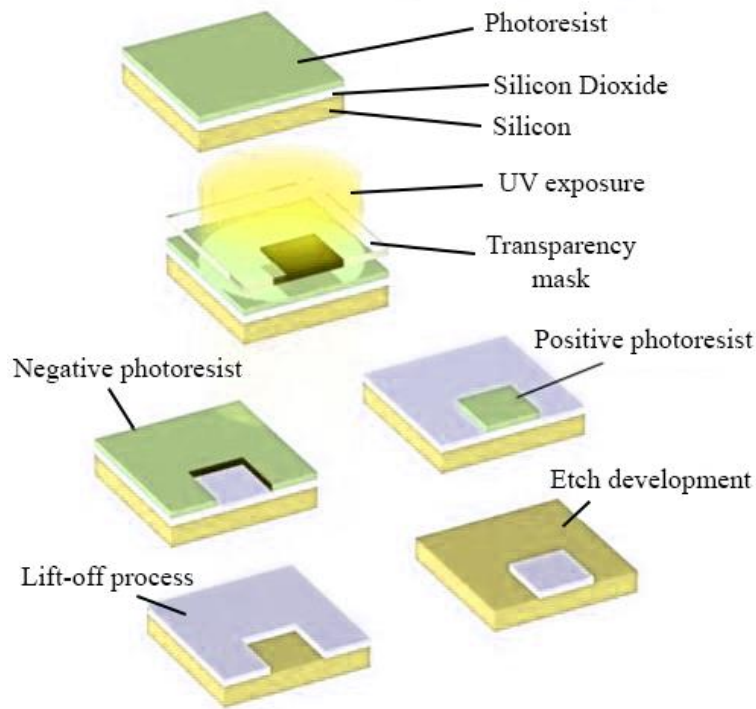


Figure 4.5: Schematic illustration of the photolithography process. A layer of photoresistive is first spin coated on top of the silicon layer followed by alignment of the mask with the wafer and exposure. Depending on the type of photoresist used, the exposed area will either be removed or cross-linked after development. An additional step could be further etching or lift off of the silicon oxide layer using the photoresist as a protective layer.

The microfluidic patterning device designed in this study acts as a stamp. Therefore, it is temporarily sealed against the substrate and can be lifted off from the patterning substrate following sample loading. This capability is central to the operation of this device as it allows free cell migration after device peel off. Since sealing to the substrate is temporary, the attachment force between the PDMS slab and the substrate is weaker compared to the standard bonded chips using oxygen plasma machine. Therefore, it is crucial to test the device leakage and its resistance under different filling pressures. Fig 4.6 demonstrates the pattern of microfluidic stamping device on standard silicon wafer and the leakage under the PDMS slab which occurs even at low pressures of $\sim 5\text{kPa}$.

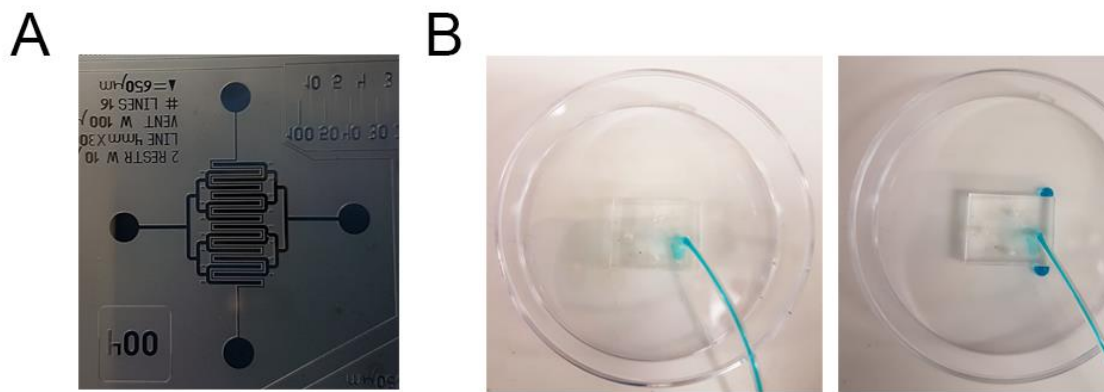


Figure 4.6: (A) Microfluidic patterning device fabricated on silicon wafer. (B) Sample leakage under a chip that is made on a silicon wafer.

To solve the problem of leakage under different pressures, fabrication using photolithography on silicon on insulator (SOI) wafer was investigated. In SOI wafers, a layer of insulator is sandwiched between the silicone layer and the top silicon dioxide layer. Since the surface of the insulator is well-polished, part of the PDMS that is in contact with the insulator surface will have a flat surface. Moreover, in fabricating the silicon mould using standard lithography method, it was seen that gaps with the size of $\sim 10\mu\text{m}$ are not fabricated precisely and therefore the standard photolithography does not provide the fabrication precision required for making narrow features as small as $\sim 10\mu\text{m}$. Based on this observation, a new approach based on Deep Reactive Ion Etching (DRIE) was adopted to make sharp and high-resolution features. The process flow of the fabrication procedure is shown in Fig. 4.7.

Standard microfabrication techniques to make silicon master moulds using SOI (Silicon on Insulator) wafers was employed with the following specifications: 100 mm wafer diameter, $80 \pm 1 \mu\text{m}$ device layer, $2 \mu\text{m}$ buried oxide layer, $500 \pm 15 \mu\text{m}$ handle layer.

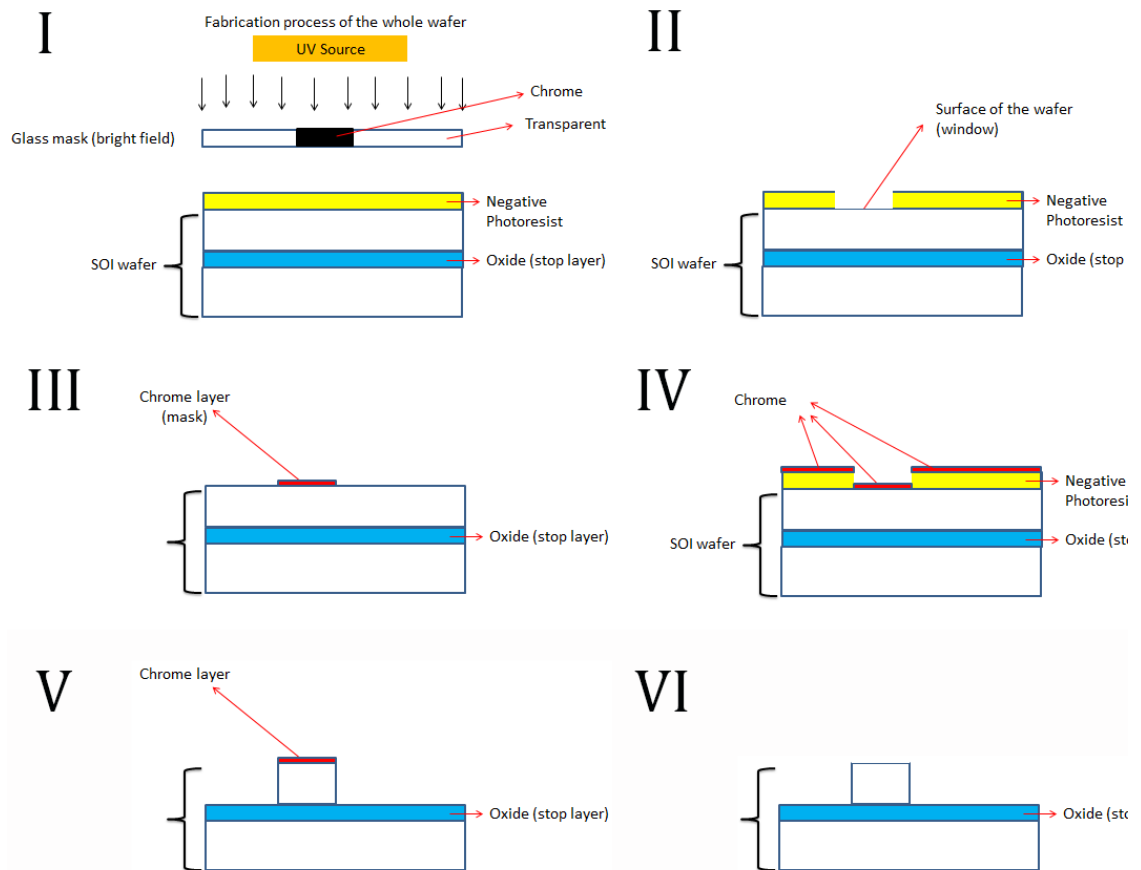


Figure 4.7: The process flow of fabricating the microfluidic stamping device using photolithography on SOI wafer (I) SOI wafer is first coated with SU8 negative photoresist and exposed to UV light (B) The wafer is developed in SU8 developer (III) A thin layer of chrome is coated on the wafer which will be used to protect the underlying silicone-oxide layer. (IV) DRIE was performed in depth of 80µm (V) the thin chromium layer is removed using lift off.

Photolithography on SOI wafers was performed was performed in ANFF-NSW at the University of New South Wales using a Quintel Q6000 Mask Aligner followed by deep reactive ion etching (DRIE) using an STS system.

Photolithography using Q6000 mask aligner

1. Headway spinner (Garland, TX, USA) with rotational speed range of 500-6000 rpm was used for coating the wafer with photoresist. It should be mentioned that for rpm <3000, resist thickness on the wafer will be non-uniform and therefore the thickness should be checked following the coating process.

2. Silicon wafer (UniversityWafer Inc., MA, USA) was removed from the box using gripper and placed on a piece of filter paper and in a petri dish.
3. Negative photoresist (SU-8 2050) stock was and transferred under the hood. It is crucial to note that the bottle containing photoresist should be moved with minimal movement to reduce the risk of production of bubbles.
4. The spin coater was covered with Aluminium foil to collect the splashing photoresist.
5. An appropriate vacuum check was chosen to be put on top of the spinner's vacuum line. The vacuum's function was checked by opening the vacuum pump and closing the vacuum hole with a small piece of silicon.

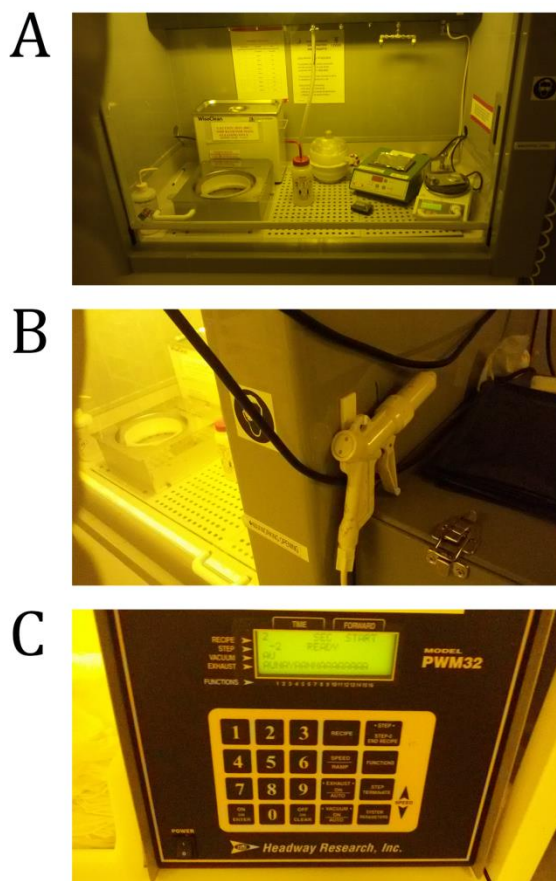


Figure 4.8: Spin coater used for coating photoresist (A) the spin coater is connected to vacuum from a hole at the middle of the sample holder (B) air gun is used for drying the surface of the silicon wafer after cleaning the surface with ethanol and acetone, (C) The spin coater controller.

6. Referring to the photoresist MSDS the corresponding rpm for the desired photoresist thickness was chosen. For SU-8 2050 for 50um thickness the rpm was set to:

- 500 rpm for 10 seconds with acceleration of 100 rpm/second (5 seconds acceleration).
- 3000 rpm for 30 seconds with acceleration of 300 rpm/second (10 seconds acceleration).

For a detailed step of photolithography using Quintel Q6000 mask aligner, please refer to Appendix A.

PDMS soft lithography on SOI moulds

The patterned SOI wafer was silanized carefully using vaporized trichloro (1H, 1H, 2H, 2H-perfluorooctyl) silane (Sigma Aldrich, USA) in a vacuum chamber over night to render the surface hydrophobic for easier release of PDMS (Fig. 4.9). Briefly, 50 μ l of silane was poured into a small container wrapped with aluminium foil which is mounted at the bottom of the vacuum chamber. The wafer was then placed in the chamber and vacuum was made by sucking the air out using Rocker 400 vacuum pump (Kaohsiung City 802, Taiwan). The vacuum in the chamber lowers the evaporation pressure and forces the silane to evaporate. The pump was turned off after 20 minutes following checking the bubbles of silane generated in the container. The chamber was then isolated from the environment by switching the valve connected to the container and kept overnight to give the evaporated silane enough time to settle on the wafer's surface.

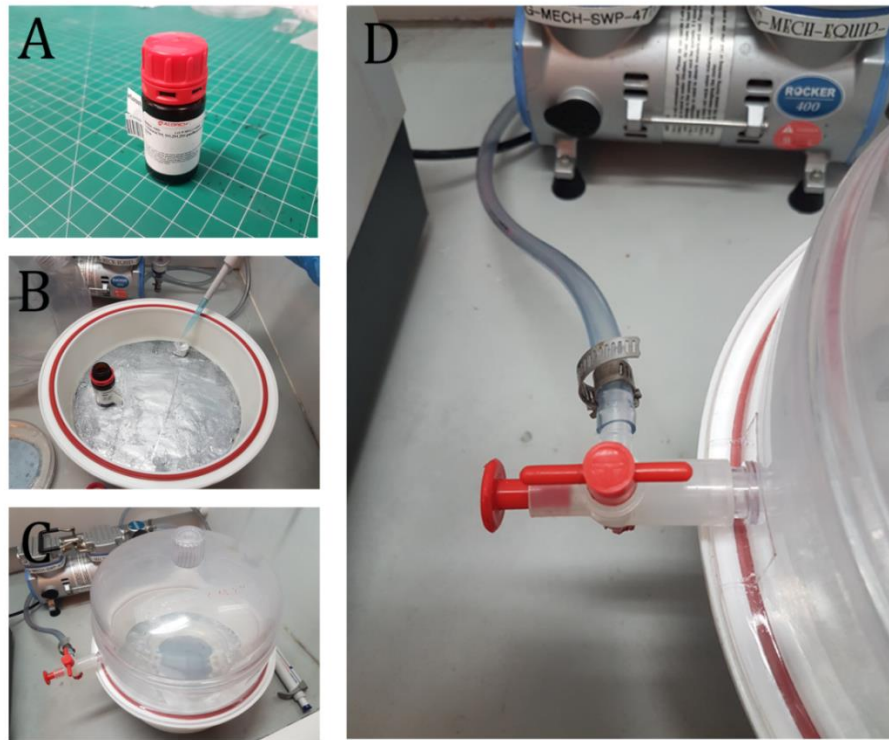


Figure 4.9: The process of silanization: (A) Silane material trichloro (1H, 1H, 2H, 2H-perfluorooctyl) silane, (B) Silane is placed in a small container wrapped with aluminium, (C) The wafer was placed in vacuum chamber and the silane is vaporized (D) check valve to close and release the vacuum.

In order to make PDMS for the moulds, first the required volume of PDMS was calculated. For a 4-inch wafer, and an average chip thickness of 4mm this volume is calculated as follows:

$$V = \frac{\pi D^2}{4} \times h = \frac{\pi(10cm)^2}{4} \times (0.4cm) \cong 31.5 mL$$

Since part of the PDMS polymer sticks to the preparation kit, 33 ml of PDMS pre-polymer was made by mixing a standard 1:10 ratio (Sylgard 184, Dow Corning, USA) of the base and the curing agent. Therefore, the amount of base and curing agent were 30ml and 3ml respectively. The mixture was then degassed in a vacuum chamber for 2 hours to remove any bubbles. PDMS mixture was poured onto the SOI mould and cured at 80 °C for 2 hr inside a conventional oven. The cured PDMS was cut from the mould, and fluidic access holes were punched into the device using a 1.5mm Uni-Core™ Puncher (Sigma-Aldrich

Co, LLC, SG). A complete procedure of soft lithography on SOI mould is shown in Fig. 4.10.

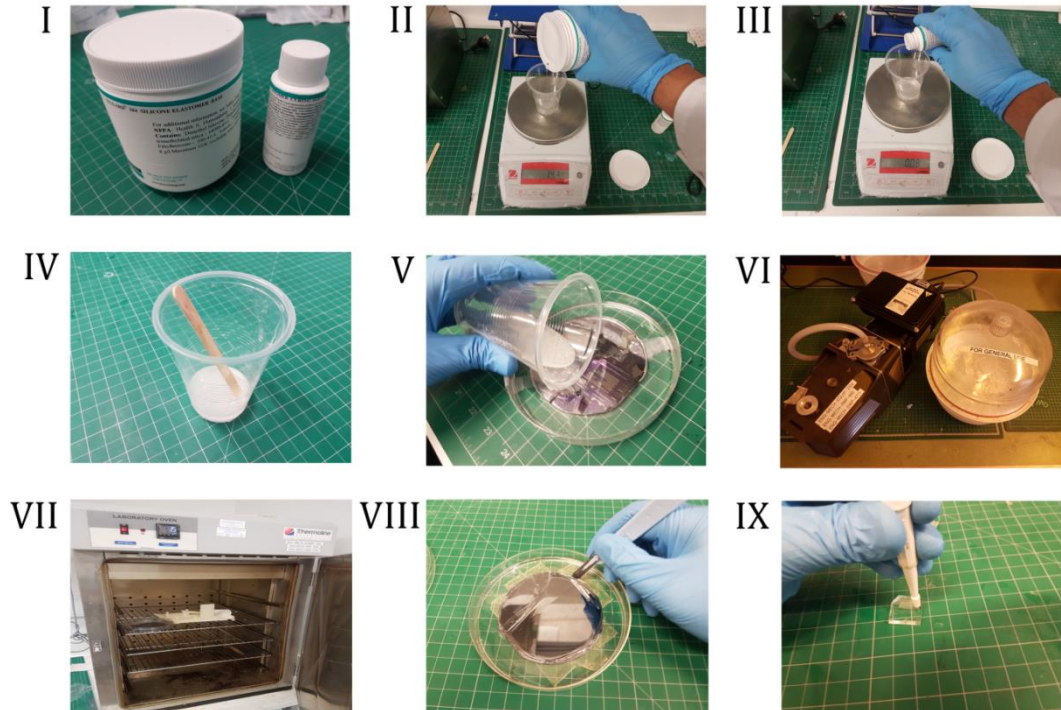


Figure 4.10: The process of soft lithography for making PDMS chips

All the devices were cleaned with isopropanol and Deionized (DI) water and dried using N_2 gas. Prior to use, all the PDMS stamps were autoclaved at ~ 120 °C for 20 min (Fig. 4.11). The fabricated stamps with the desired patterns were brought in conformal contact with the substrate and, if necessary, pressed together to create a seal.

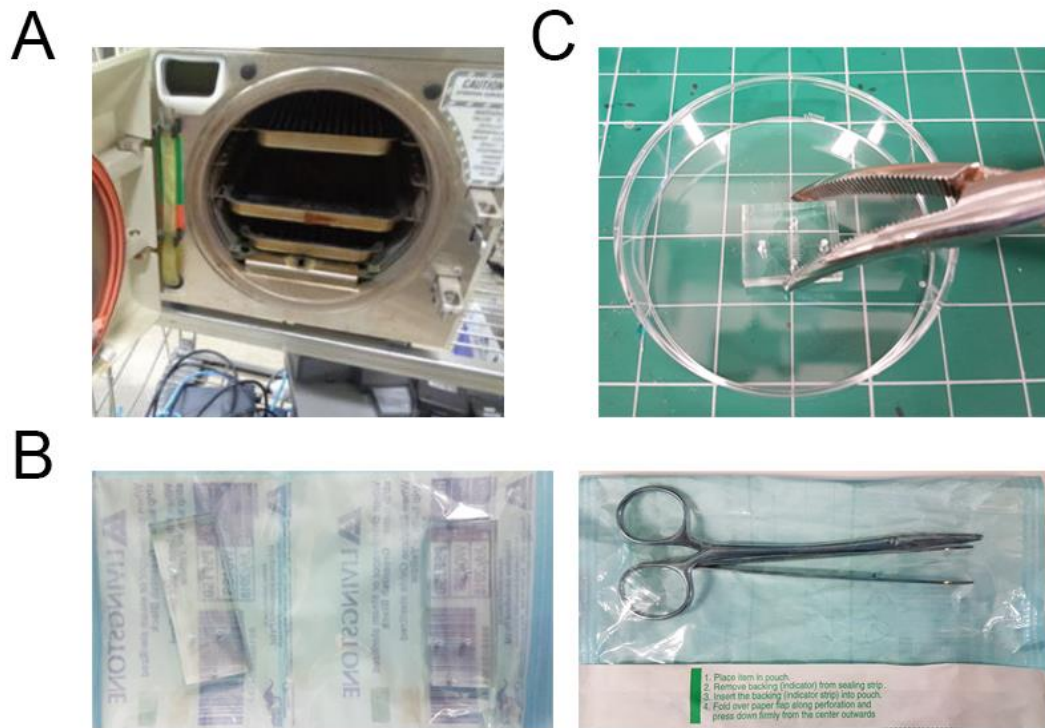


Figure 4.11: (A) The autoclave machine use for sterilizing the devices and the tweezers. (B) The devices and tweezers in the autoclave bags. (C) Tweezers used for mounting the PDMS slab on the petri dish before sample injection.

4.2.3. Cell isolation and culture

Co-culture experiments were conducted with primary cardiac-derived mesenchymal stem cells and mouse aortic vascular endothelial cells with a 1:1 ratio mixture of each cell's specific medium. These cells were chosen as endothelial cells are believed to signal the differentiation of cardiac stem cells [158]. Both cell lines were isolated and expanded by the Victor Chang Cardiac Research Institute (Sydney, Australia). Cardiac-derived mesenchymal stem cells are a rare subset of cells isolated from the interstitial fraction of adult murine heart by FACS using SCA1+/PDGFR α +/PECAM- marker expression [159]. To facilitate live cell imaging using green fluorescent protein expression, cells were isolated from a transgenic mouse that expresses 'enhanced' GFP (EGFP) under the control of the chicken beta-actin promoter [160].

Briefly, mice were sacrificed using cervical dislocation. The adult murine hearts were dissected while avoiding collection of cells from the outflow tract. After mechanical digestion of the hearts, the tissues were suspended in 5ml of 260 U/ml of pre-filtered collagenase Type 2 (w/v) (Worthington, Lakewood, NJ) in PBS and incubated in 37°C water bath. Every 6 min the sample was vigorously agitated. After 12 min the supernatant was collected in 3 mL of heat treated Fetal Bovine Serum (FBS) solution at 4°C. This process was repeated three times until the remaining heart tissue was completely digested and pooled in a 50 mL Falcon tube. The supernatant was then filtered using 40 µm filter strainers (Corning, 352340) and the cells were pelleted by centrifugation for 5 min at 600g. The supernatant was discarded, and the cells were re-suspended in 1 mL of 2% FBS (v/v) in PBS. The cells were pelleted again by centrifugation for 5 min at 600g at 4°C. The supernatant was removed, and remaining cells were re-suspended in the red blood cells (RBC) lysis buffer (MACS), incubated for 10 min and finally centrifuged for 5 min at 600g. After centrifugation, the supernatant was discarded, and the pellets were washed with 2% FCS in PBS. The dead cells from the sample were then removed using the MACS dead cell removal kit according to the manufacturer's guidelines (MACS Miltenyi Biotech, Gladbach, Germany). The collected sample was centrifuged and washed twice, each time pelleting the cells before washing in 2% FCS and discarding the supernatant. The cells were re-suspended in 2% FCS in PBS and separated into 100 µl aliquots. The cells were incubated for 30 minutes with the following antibodies SCA-1, PECAM1, PDGFR α (R&D systems, Minneapolis, MN). Prior to FACS analysis the cells were washed twice with 2% FCS in PBS. The cell population was analysed and sorted by FACS analysis using BD FACS Aria™ Cell Sorter (BD Biosciences), to select the required population based on cell size and surface cell markers. Using compensation samples and

isotype controls, the required population was obtained based on desired expression of cell surface markers and were collected in a 15 mL Falcon tube containing cell culture media. Isolated cells were then plated at a cell density of 5,000 cells in 35 mm culture plates with complete culture medium of α MEM, 20% FBS (v/v), 100 μ g/ml of Penicillin, 250 ng/ml of Streptomycin and 200mM of L-Glutamine. Plated cells were incubated at 37°C under 5% CO₂ in a humidified incubator. Fresh culture medium was changed following the initial day of isolation and on every third to fourth day thereafter. Prior to replenishing the media, the cells were washed twice with sterile PBS to remove non-adherent cells and debris and the cells were treated with TrypLE (Life Technologies, Carlsbad, CA).

Mouse aortic vascular endothelial cells were isolated from the p53-deficient mouse aorta and cultured in M199 medium (Invitrogen) with 5 ng/ml of recombinant vascular endothelial growth factor (VEGF; Sigma-Aldrich), 5ng/ml Hepes (Invitrogen), 10mM heparin sodium (Sigma-Aldrich) and 5% FBS. Mouse aortic vascular endothelial cells from p53-deficient mouse were cultured for over 100 passages as described elsewhere [161]. Fig. 4.12 presents a light microscope image of the cultured endothelial cells and the CFU cardiac stem cells in tissue culture dishes. For the sake of simplicity, hereafter cardiac-derived mesenchymal stem cells are referred to as SC and mouse aortic vascular endothelial cells are referred to as EC.

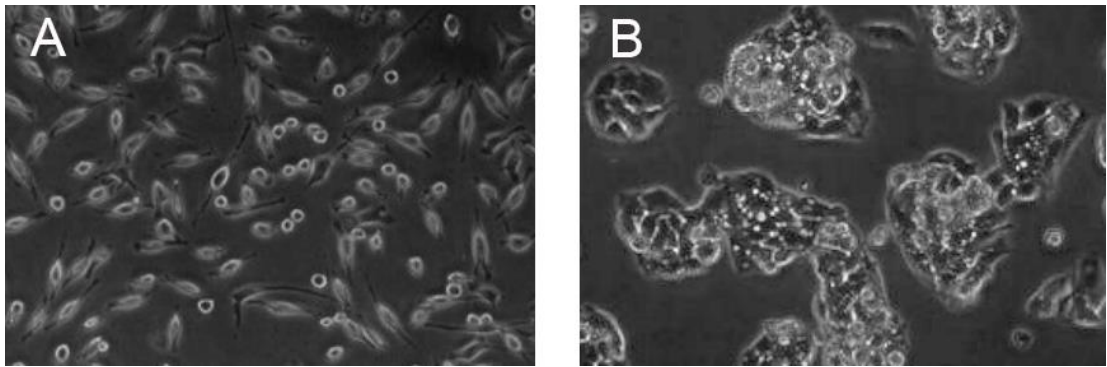


Figure 4.12: Image of Endothelial cells EC (A) and stem cell SC (B) cultures in flasks and under the microscopes.

Fibroblast cell culture

Fibroblast L929 cells (Sigma Aldrich, 04102001-1VL) were cultured using 10% serum, 1% PS in DMEM in a T-75 flask and the medium was changed every 3 days. The cells were passaged at 80% confluency and cultured with a seeding density of 10^4 cells/cm². Briefly, a T-75 flask of fibroblast cells were examined carefully under the normal light microscope (specify the type here) for confluency. Next, all the media is sucked out of the flask and 3ml Trypsin was added to the flask and the flask was tilted several times to ensure trypsin is in contact with cell of the cells. The cells were then placed in incubator for 6 minutes and then examined under the microscope for detachment. The flask was shaken gently to ensure all cells are released from the surface of the flask. 7ml fresh DMEM medium was added to the flask and the cell suspension was aspirated to ensure there is no cell clump. 1 ml of the cell suspension was then added to a new flask with 10ml DMEM medium. The cells were then checked under the microscope and placed inside the incubator (Fig. 4.13).

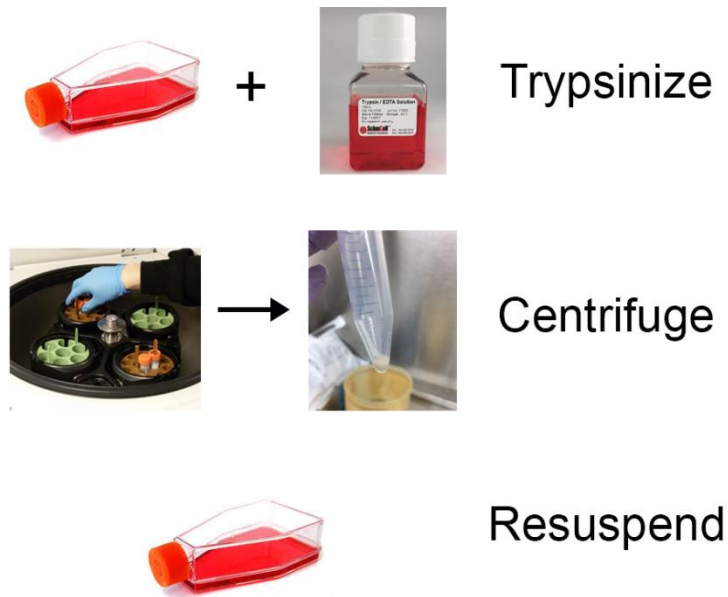


Figure 4.13: Procedure of fibroblast cell culture

4.2.4. Viability assay of the patterned cells

Calcein AM and Propidium Iodide (PI) was used for live and dead staining. Fibroblast cells were injected into the device using hand-held pipettor and were left to attach for 4 hr. The stamp was peeled-off from a 6-well plate and washed once prior to staining. The cells were incubated with 4 μ M Calcein AM and 1 μ M PI for 1 hr followed by medium replacement. Prior to imaging, the staining efficiency was checked using an Olympus IX73 fluorescent microscope.



Figure 4.14: Double live/dead staining kit containing Calcein AM and propidium Iodide solutions (The image is reproduced from Sigmaaldrich website at: <https://www.sigmaaldrich.com/catalog/product/roche/06432379001?lang=en®ion=AU>).

4.2.5. Protein/peptide mixture stamping

Gelatin from Pig Skin, Oregon Green 488 Conjugate (G13186, 5 mg) and Albumin from Bovine Serum (BSA), Texas Red conjugate (A23017, 5mg) were purchased from ThermoFisher scientific. Stock solutions of 1 mg/ml were prepared and stored in refrigeration and were protected from light to minimize photo-bleaching. Before stamping, a solution of Gelatin (0.2 mg/ml) and Albumin (0.4 mg/ml) in DI water were prepared by proper dilution. The microfluidic stamp was placed on a pre-washed glass slide and injected with the diluted solutions. Following an incubation of 1 hr at room temperature to increase protein/peptide mixture adsorption to the glass slides, the stamp was peeled off and the glass slide was washed with DI water, dried with an air gun and fluorescently imaged with an Olympus IX 73 inverted fluorescent microscope.

4.2.6. Microscopy

Fibroblast viability

Imaging of the attached fibroblast L929 cells was performed using the Olympus IX73 inverted microscope. At each time point both phase-contrast and fluorescent channels were captured. For each stamped area three arbitrary sections were tracked over time by marking the well plate bottom. The stamps were carefully peeled off the well plates using sterile (autoclaved) tweezers and covered with fresh medium. The bright field images of the attached cells were captured, while the two remaining plates were transferred back to the incubator (to be stained and imaged after 24 and 48 hr, respectively). Each of the devices was imaged before the staining to account for washed cells. Next, the devices were peeled off and the cells were stained. Following 30 min incubation, the TC plate was imaged using bright-field and fluorescent GFP / TXred channels.

Time lapse microscopy

Time lapse microscopy with an Olympus IX83 equipped with a dedicated CO₂ incubator (37°C) was performed to track cell migration in the SC-EC co-culture experiments as well as assessment of Fibroblast cells proliferation (Fig. 4.18). Microphotographs of a defined region of the device were taken with 20 min intervals for 6 consecutive days. The defined region includes 6 regions each on a separate stamping area where the quality of the images was adjusted individually. To avoid cell drifting, the stage speed was reduced to 1 mm/sec.

4.2.7. Image and data analysis

Collective cell migration analysis using ImageJ

Tracking analysis of time-lapse microphotographs was performed using the manual tracking ImageJ software plug-in (NIH, Bethesda, USA). The generated tracking data were used to graphically plot the trajectories of the SCs and EC and to calculate the motility data. SCs and ECs were counted by segmentation using ImageJ. Phase contrast images were preprocessed with a low pass spatial filter (average of 30×30 pixels) to make image intensity uniform, and then thresholded to segment cells, which have low intensity compared to background. After binary image closure, EC were distinguished from SC by the size and shape of their nuclei using the 'regionprops' function (area and eccentricity); EC have a small dark central region whereas SC with fibroblast morphology were identified by a larger their elongated dark region. Three movies were acquired for each experimental group (See Fig. 4.21). Statistical comparisons of EC and SC in homogeneous culture (EC|EC or SC|SC) or co-culture (EC|SC) were compared using a linear regression models which estimated the slope and intercept for log₂ transform cell numbers (doublings) versus time. The effect of covariates (co-culture or cell type) on the

slope and intercept of growth curves were estimated. MATLAB codes are available in appendix B.

Viability and proliferation analysis

Analysis of viability and proliferation was done by counting the number of cells in specific images using ImageJ software. Figure 4.15 demonstrates different type of images in which the numbers of cells were counted. These images belong to cells attached to the substrate in the device, cells after the peeling, and fluorescent image of the cells respectively.

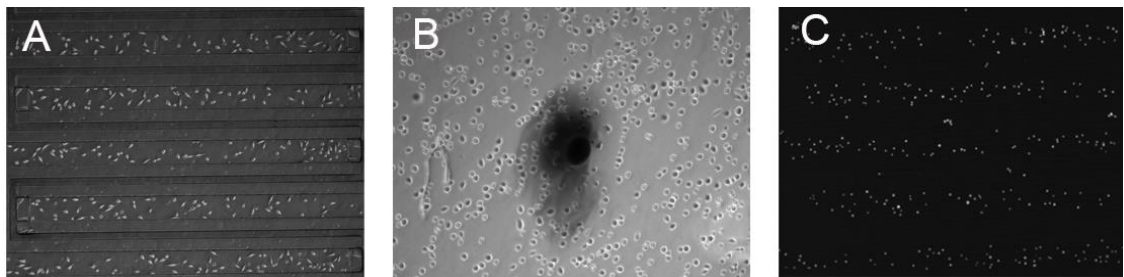


Figure 4.15: Images acquired (A) before peel off (B) after cell doubling after 8 hours and (C) fluorescent image after device peel off.

In order to count the cells in ImageJ initially the threshold was optimised for each image to achieve separated and distinguishable cells with no background noise. The particle analysis tool was used to count the number of cells in each image (Appendix C).

4.2.8. Microfluidic cell culture

Fibroblast L929 microfluidic culture to measure proliferation

Fibroblast L929 cells were cultured in Dulbecco's Modified Eagle Medium (Invitrogen) under humidified condition (5% CO₂ at 37°C) at concentration of 10⁶ cells/ml. The cells were passaged every 3 days at 80% confluency. The PDMS chips were carefully cleaned using distilled water and scotch tape and inspected under a microscope to assure complete

removal of dust particles. All the instruments required for the experiment including the 100 μ l and 1000 μ l pipet tips, the tweezers and 6 PDMS devices were autoclaved and then dried in oven for 2 hr. The devices were then placed inside a 6 well plate using the tweezers and pressed gently to ensure appropriate contact is established between the chip and the substrate. Cell suspension of 4×10^6 cells/ml was prepared using fibroblast L929 cells, harvested from two flasks. For each passage a Vi-CELL cell viability analyser (Beckman Coulter) was used to ensure viability of $> 90\%$. For each injection 20 μ l of cell suspension was aspirated using a pipettor and injected into the device. Next, the cell concentration in all devices was checked under a microscope and 2 ml of DMEM medium was added to each well. The devices were then placed in the time lapse microscope and were tracked for 4 hr to ensure cell attachment. Upon attachment, the time lapse experiment was paused, and the devices were peeled gently under sterile conditions. Subsequently, 1 ml of fresh medium was added to each device to cover the patterned cells, the well plate was placed back to its original position under the microscope and the microscope operation was resumed. Recorded movies before and after device detachment was checked for proper overlapping (Fig. 4.25).

CMSCs-MAEC microfluidic co-culture

For the co-culture experiments, one T-75 confluent flask of SCs and one T-75 confluent flask of EC was used and a cell suspension with concentration of 4×10^6 cells/ml was prepared for each of the cell types. Next, a co-culture device was placed inside a single well of a multi-well plate, while assuring that it is properly sealed against the well's substrate. A 20 μ l of the EC cell suspension was injected into the first inlet of the co-culture device. Next, a 20 μ l of the SC cell suspension was injected to the second device inlet. After an incubation of 4 hr, the cell attachment was verified based on cell morphology changes. Following successful cells attachment, the microscope was paused,

and the devices were peeled using sterile tweezers. A 1 ml mixture of SC and EC medium (1:1 ratio) was added to each well to cover the exposed cell pattern and the plate was placed back to its original position at the microscope stage. The time step and total experimental time were set to 30 min and 7 days, correspondingly.

4.3. Results and discussion

4.3.1. Device operation

Cell Stamping

In a standard micro-contact printing, in order to avoid cross-contamination, proteins are normally stamped on a hydrophobic substrate to prevent non-specific cell attachment. This normally causes an undesirable confinement of the stamped cells to the protein-patterned region, suppresses cell motility and therefore limits cell migration studies. The described co-culture stamping method in this study can overcome this limitation by direct cell seeding on a treatment-free substrate, allowing unrestricted post-stamping cell migration.

The stamp operates in four steps, as shown in Fig. 4.16. Unlike common devices where the PDMS slab is hermetically sealed against the substrate using Oxygen plasma, here the PDMS slab (stamp) is placed against a flat substrate, such as a polystyrene TC dish or a glass slide. In spite of the fact that the sealing is reversible, the stamp flatness ensures that the injected liquid is confined between the channels and does not leak. A cell suspension is injected using a standard lab pipet to the first inlet. The solution flows and fills the channels till the liquid/air interface reaches the end of each channel. There, it encounters a restriction that exhausts air through an air vent while limiting the progression of the liquid due to Laplace's Law. The same procedure is repeated with a second cell suspension, which is injected from an opposing inlet, thus forming an interlaced configuration of alternating solutions. Following rapid cell sedimentation, the

stamp/substrate assembly is incubated for 4 hr until cells adhere to the substrate. Eventually, the stamp can be detached from the substrate and the patterned cells are covered with fresh medium to sustain their viability.

Protein/peptide mixture stamping

When cell migration is less of a concern, hydrophilic protein stamping using micro-contact printing can be used to pattern cells to desired regions on a substrate, by selective cell attachment to hydrophilic protein/peptide regions. Nevertheless, the ability of patterning two different protein/peptide patches in proximity remains challenging due to the difficulty to maintain proper alignment of multiple stamping steps. The presented co-culture stamping method in this study overcomes this problem by injecting two different mixture solutions to the two inlets as shown in Fig. 4.16C followed by a short incubation at room temperature, peeling and washing of the substrate. To demonstrate the feasibility of such a dual-protein/peptide stamping, fluorescently conjugated Gelatin (Oregon Green) and Albumin (Texas Red) were selected. Like the cell stamping, adjustment of the protein/peptide concentration injected to each of the channels allows controlling the number of molecules adsorbed to the substrate.

4.3.2. Device characterization

The restriction at the end of each stamp's channel limits the flow of liquid but allows air to flow out of the device. To improve the stamp's performance the restriction width should be minimized. Although the device can be fabricated with SU8 photoresist, the limited aspect ratio of the resultant restriction would limit the range of operating pressures. DRIE was therefore used to achieve aspect ratio as high as 1:8. Fig. 4.17 shows successful stamp loading. It also demonstrates that the anisotropic RIE fabrication using a standard silicon wafer results in compromised stamp flatness, as shown in the PDMS cross section, which led to leakage of liquid and its accumulation between the PDMS stamp and the substrate.

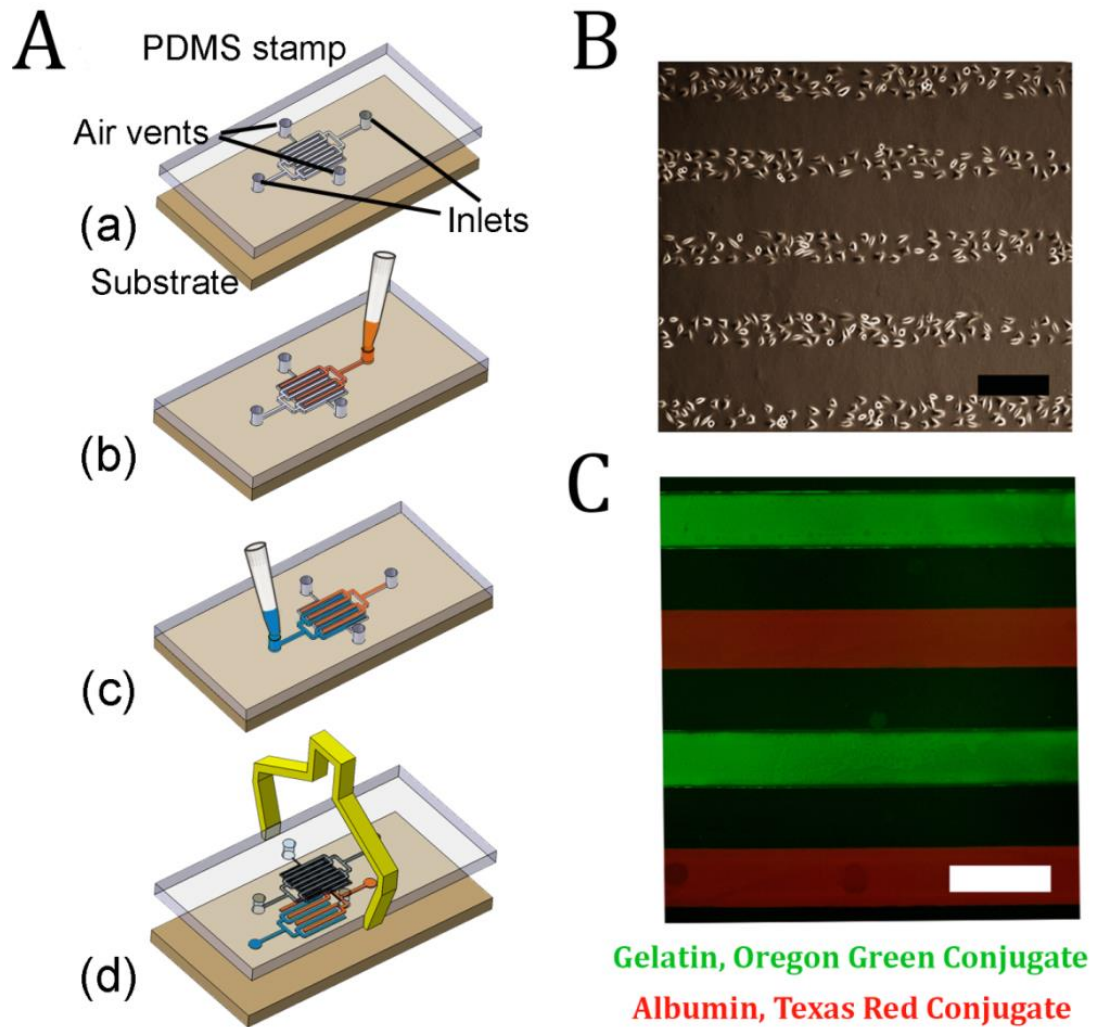


Figure 4.16: Microfluidic stamp structure and patterning. (A) Stamping procedure: (a) The stamp is placed on a flat substrate such as a glass or a tissue-culture dish. (b) Cell suspension is injected to the first inlet using a standard lab pipet. The cell suspension fills the channels while allowing residual air to escape through the air vent. (c) In a similar manner, a second cell suspension is injected from a second inlet. (d) Following cell sedimentation and on-chip incubation, the PDMS stamp is removed while leaving cells attached to the substrate. (B) Fibroblasts L929 patterned on a TC plate. Scale bar 300 μm (C) Fluorescent-conjugated protein/peptide mixture patterning. Scale bar: 500 μm .

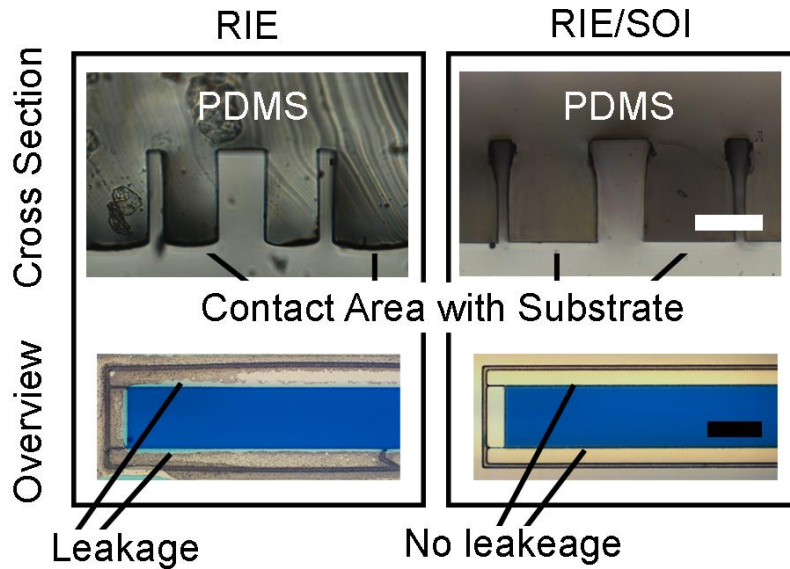


Figure 4.17: Device Characterization: Comparing SOI (Silicone-On-Insulator) vs. Non-SOI wafer fabrication and the resultant leakage-proof performance. Scale bar 50 μm and 100 μm for the top and bottom images respectively.

In order to avoid this leakage, the stamp's contact area with the substrate needs to be flat. To achieve this, together with restrictions of high resolution, a mask was patterned directly on a SOI wafer, followed by DRIE etching through a device thickness of 80 μm until the buried oxide layer was reached. For simplicity, a device thickness of 80 μm was used in all of the experiments. This assured that the restriction's width could be reduced down to 10 μm and it also supports leakage-free operation due to the high degree of stamp flatness. The high tolerance of device thickness also translates to repeatable calculation of the injected liquid and therefore allows the user to control the patterned cell density. The range of operating pressure of the device is provided in Table 4.2.

Table 4.2: Device operating pressure range under various substrates ($n=5$)

Substrate type	P_{low} (kPa)	P_{up} (kPa)
PS cell culture dish	1.032 \pm 0.105	7.763 \pm 0.437
Glass	0.743 \pm 0.365	9.731 \pm 0.815

Cell distribution uniformity

One of the desired characteristics of cell patterning is to achieve a uniform cell distribution (per area). To characterize the cell distribution uniformity along the channels, fibroblasts L929 were injected at three volumetric cell concentrations of 10^6 cells/ml, 2×10^6 cells/ml and 4×10^6 cells/ml. The resulted cell distribution along the channels was measured by counting the number of cells per quadrant, as shown in Fig. 4.18A. Following this approach, the cell distribution in each zone was characterized (Fig. 4.18B) by calculating the number of cells per quadrant normalized by cell suspension concentration (Inoculum concentration; IC) for three injected cell concentrations. To calculate the average number of cells per zone, the normalized number of cells per quadrant is multiplied by the concentration of the cell suspension. As seen from the boxplot, higher cell concentration was found at the distal side of each channel, compared with the proximal zones. To verify this, a single factor ANOVA test was performed and significant difference between the four zones was revealed. Next, a t-test between each two zones were performed and a significant difference was found ($p < 0.05$) between the distribution of cells at zone A and zone B compared to zone C and zone D, as shown in Fig. 4.23B. The difference is the result of rapid sedimentation of cells at the tip of the pipet right before injection. This effect could therefore be reduced by either minimizing the time till injection is initiated, or with design of a longer channel while discarding the channel end. Fig. 4.18C also demonstrates a linear relationship between the average number of cells and the corresponding cell suspension concentration.

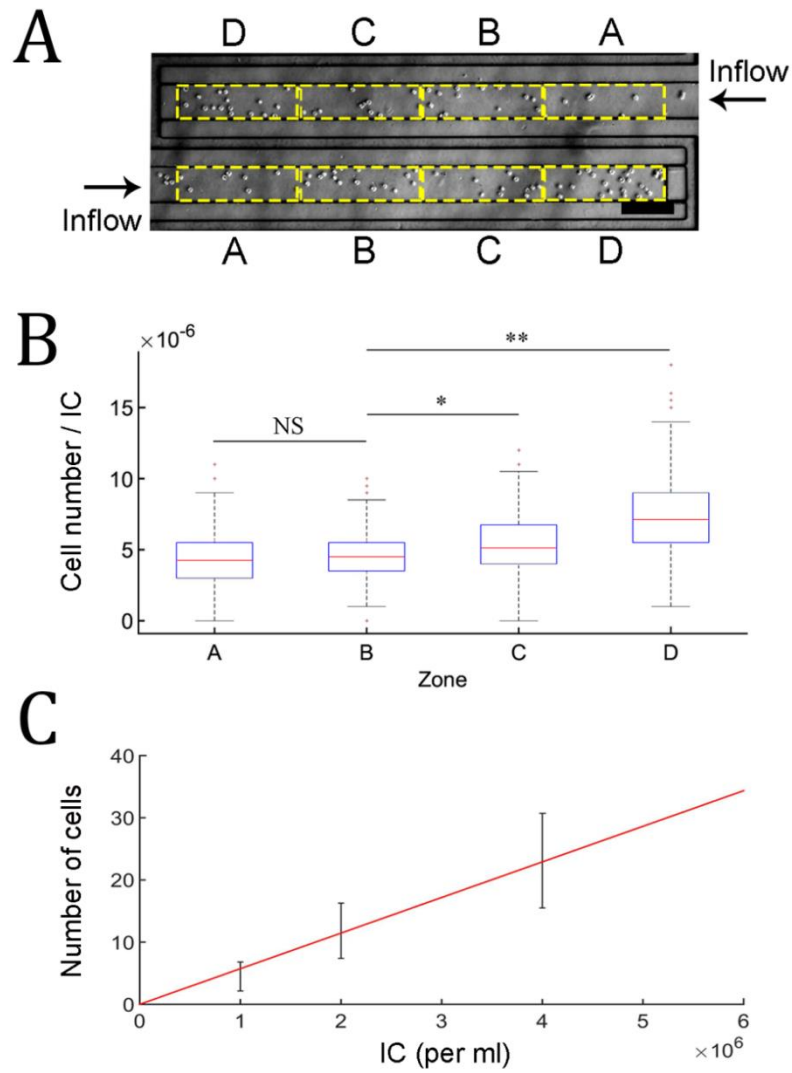


Figure 4.18: Characterization of cell uniformity distribution in the channels by injecting L929 fibroblasts. (A) Each channel was divided to four zones (A, B, C, D) which were indexed based on the directionality of the flow. Scale bar, 200 μm (B) Boxplot of the normalized cell number in each of the zones for the injected bulk cell concentrations of 10^6 cells/ml, 2×10^6 cells/ml and 4×10^6 cells/ml (C) Linear curve fit between average number of cells in each zone and the inoculum concentration (cell suspension concentration).

It was found that near the inlets there is increased cell sedimentation due to flow perturbations. As a result, injection efficiency to the device was lower than 100%, where injection efficiency is defined as the observed cell concentration in the channels divided by the nominal bulk cell concentration before injection. The observed cell concentration was calculated by counting the number of cells in each channel (while excluding sediment cells at the vicinity of the device inlet) and dividing it by the channel's volume (22.8 nl). The bulk cell concentration was measured by Vi-CELL cell viability analyser. It was

found that the average injection efficiency for cell concentration in the range of 1×10^6 cells/ml to 4×10^6 cells/ml was $\xi = 83\% \pm 10\%$. Therefore, the seeded cell density per area is adjusted by calibrating the injected bulk cell suspension concentration, which could further be selected independently for each of the two cell channels. The cell density per area is then given by $D = \xi \cdot \rho \cdot h$ where D is the cell density per area in the channels, ρ is the injected bulk cell density, h is the stamp depth and ξ is the cell injection efficiency. As mentioned before, due to the fabrication method (SOI wafer), the stamp thickness h has a high accuracy of a few micrometers. Using a uniform and accurate stamp thickness therefore results in increased accuracy of the patterned cells density (per area).

Cell viability and proliferation

The post-peeling cell viability is important to assure that the peeling process did not compromise normal cell functionality or inadvertently caused rapid cell death. In addition, it is important to verify that the cell functionality remains unperturbed before and after the cell injection. Ideally, the desired cell proliferation and spreading should not depend on the shape and dimensions of the pattern. There are some challenges associated with cell culturing in microfluidic devices including nutrient depletion and insufficient gas exchange occurring due to their small culturing volume. In the presented device, the cell culture surface and volume are 1.32 mm^2 and 54 nl , respectively for each channel branch (corresponding to surface-to-volume ratio of 24) which is within the recommended range suggested by Halldorsson et al. [162]. To characterize viability and proliferation, Fibroblasts L929 were cultured in the device. Following a 4 hr of incubation, the stamp was peeled off, the cells were covered with fresh medium and were double stained with a dead/live staining kit, as shown in Fig. 4.19A.

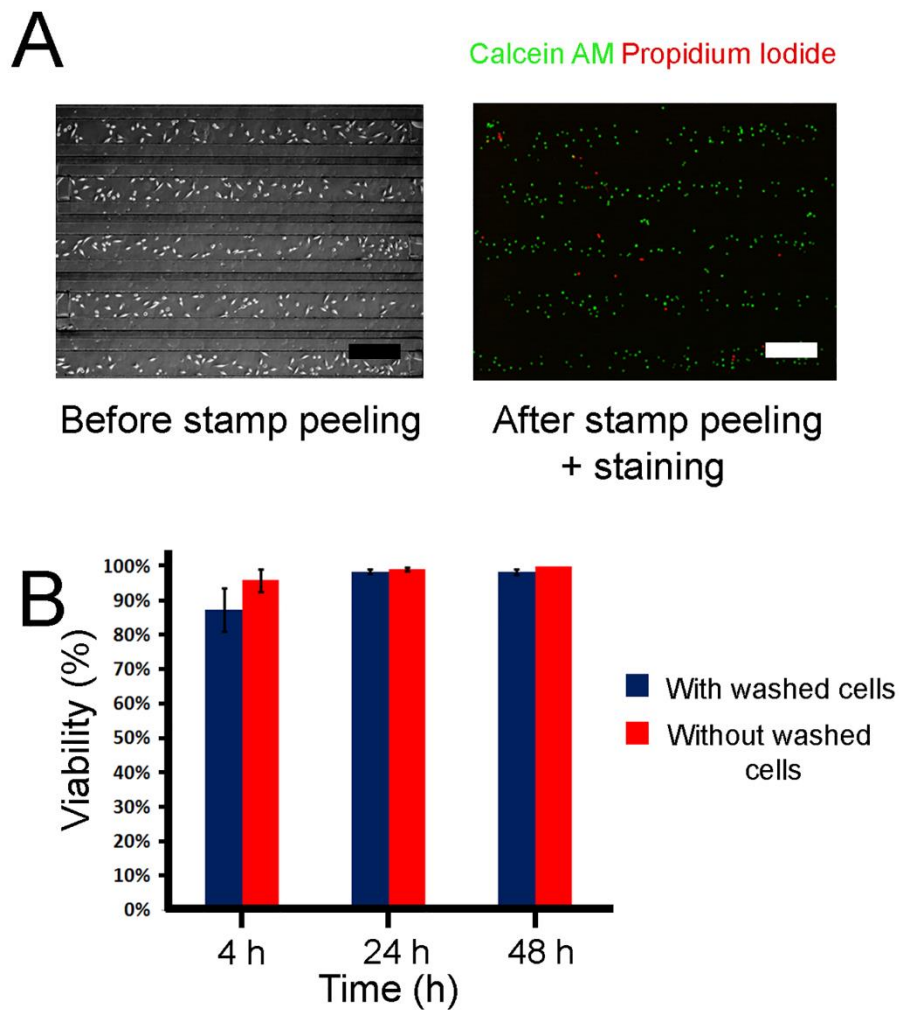


Figure 4.19: Post-stamping cell viability: (A) Image of Fibroblast L929 Cell in stamp and after stamping peeling + Calcein/PI viability staining. (B) Quantification of post-stamp cell viability at $t = 4\text{hr}$, 24 hr and 48 hr . Viability was measured for both the case of counting/ignoring post-peeling washed cells.

During the stamp peeling and medium coverage, a small fraction of the cells was washed. Since the number of washed cells was small it was not possible to estimate their viability using conventional methods. Therefore, the viability was calculated twice. Once while assuming the washed cells as dead and another while ignoring the washed cells, as shown in Fig. 4.19B. It can be seen that cell viability remains $> 85\%$ in all experiments.

The functionality of the cultured cells in terms of proliferation rate was also investigated using time-lapse microscopy. L929 Fibroblasts were patterned and their doubling versus time were counted over a period of 4 days. As shown in Fig. 4.20A and unlike typical protein-based stamps which cause biased cell confinement, in the current stamping

method, the cells freely migrate across the substrate and are not limited to the patterned region. Interestingly, after 24 hr incubation the original cell pattern is barely discerned, confirming the suitability of this technique for long-term cell co-culture.

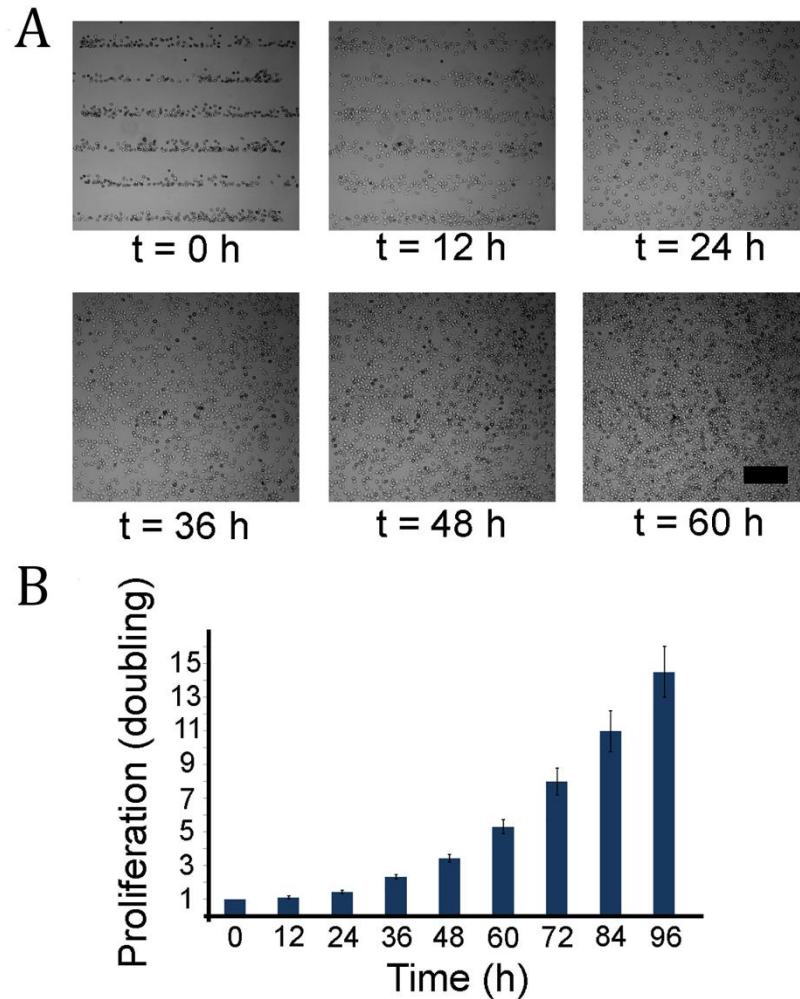


Figure 4.20: Post-stamping cell proliferation: (A) Images of fibroblast proliferation over the course of 60 hours. Here $t=0$ h is the time when the stamp was peeled. (B) Fibroblast proliferation (fold expansion), after stamp is peeled-off ($t=0$ hr) tracked over the course of 96 hours.

To quantify the cell proliferation the cell doubling was tracked over a period of 96 hr, with intervals of 12 hr. As shown in the Fig. 4.20B there is high proliferation rate with a doubling time of ~ 24 hr, comparable with typical cell seeding at these densities.

4.3.3. Interaction of cardiac-derived mesenchymal SC and EC in patterned co-culture

The identification of a specific cell type/population in an *in-vivo* model in real time is a complex task which typically requires sacrificing the animal under study. The co-culture stamping device allows one to isolate and study the interaction between two types of well-defined cell types by using either commercially available or well characterized cell sub-population of choice. Such an *in-vitro* co-culture assay can be used as a prior step towards a more involved *in vivo* experiment. To demonstrate this concept a highly enriched subpopulation of cardiac interstitial cells isolated from adult mouse hearts were harvested by fluorescent activated cell sorting, when grown in tissue culture in high (20%) fetal bovine serum, form colonies with the characteristics of mesenchymal stem cells but with specific *in-vitro* and *in-vivo* properties related to their cardiac origin. It is hypothesised that cardiac-derived mesenchymal SCs secrete growth factors that direct tissue repair after myocardial infarction (MI), including revascularisation of the infarct region after dead cardiomyocytes are removed by phagocytic cells. Sprouting angiogenesis into the infarct zone may be driven by cardiac mesenchymal SCs which reside there, early on after MI. Therefore, the migratory and proliferative behaviour of cardiac mesenchymal SCs and ECs in patterned co-culture was studied by time lapse microscopy.

Fig. 4.21 shows a sequence of images of the co-culture stamping (EC/SC) at three different time points, accompanied by controls that include a single cell culturing of either stem cells (SC) or endothelial cells (EC). As shown in the figure, the stem cells proliferate at a low rate and similarly to fibroblasts, gradually migrate away from their original stamping position.

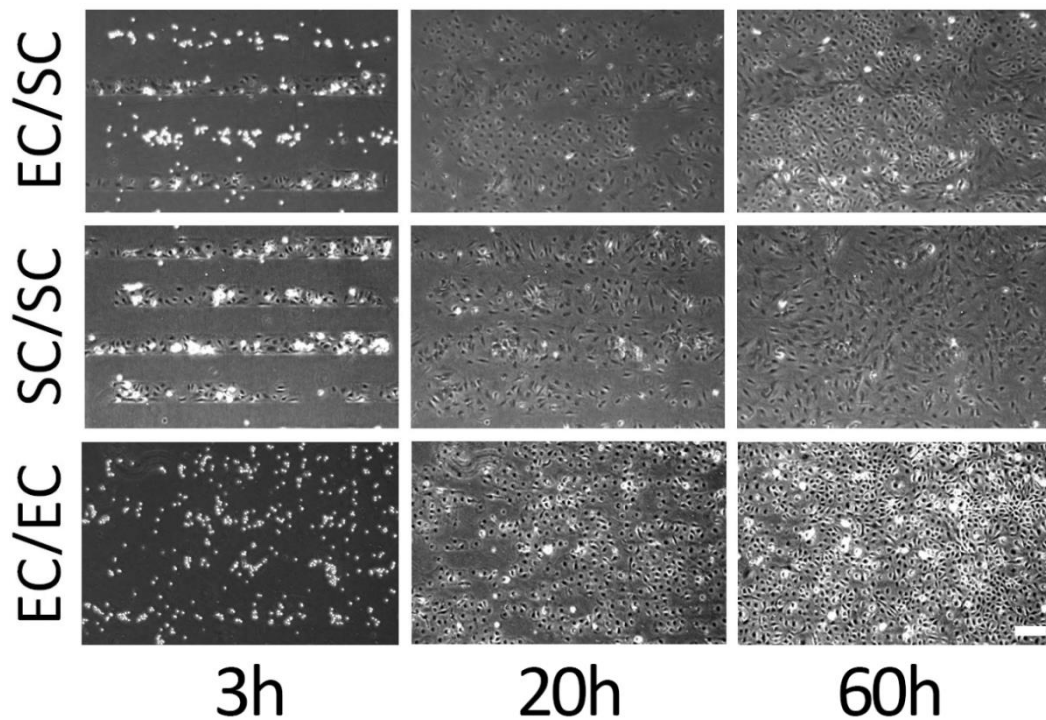


Figure 4.21: Endothelial/Cardiac Stem Cells co-culture. Selected time lapse images of cardiac stem cells (SC) co-cultured with Endothelial Cells (EC) at time $t = 3$ h, 20 h, 60 h and their corresponding single-stamp culture of Endothelial Cells only (EC/EC) and Cardiac Stem Cells only (SC/SC). Scale bar: 200 μm .

In parallel the EC proliferate at a much faster rate and, when they reach the stem cells, they confine them to narrow filaments, as shown in Fig. 4.22. This confinement is observed only in the co-culture experiment and is absent from the two single-culture controls.

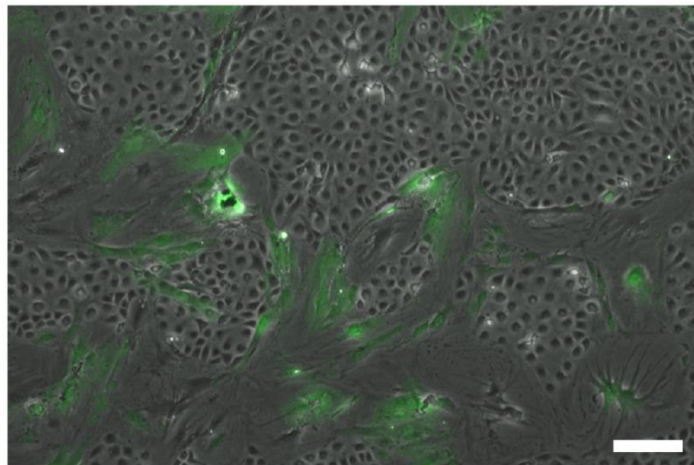


Figure 4.22: Endothelial/Cardiac Stem Cells co-culture. Overgrowth of Cardiac Stem cell clusters by neighboring Endothelial cells in a Co-culture experiment. Scale bar: 200 μm .

To investigate the effect of co-culture on each cell type's growth, proliferation of SC and EC was quantified using MATLAB Image Processing Toolbox. The proliferation rates of SC or EC were estimated by segmenting the number of EC or SC when stamped in co-culture (EC|SC) or in single culture as a control (EC|EC or SC|SC, respectively). The time course of EC and SC proliferation expressed as the number of doublings – \log_2 [cell number] – is shown in Fig. 4.23. A linear regression model was fitted to the data (n=3 movies per condition, Fig. 4.22), showing the effect of co-culture vs single culture and cell type on growth lag (intercept) and growth rate (slope). The doubling times for the single culture of EC (black curve) and single culture of SC (green curve) were 40.0 ± 0.2 hr versus 55.0 ± 0.2 hr, respectively ($p < 0.001$). The growth curve of EC (control) was sigmoidal with a 10 hour growth lag. The growth lag of EC was lost when grown with SC (red curve, $p < 0.001$). Thus, SC provides a microenvironment that increases the initial growth of EC. In contrast, co-culture of SC with EC resulted in growth arrest of SC after 100 hours (blue line, $p < 0.001$).

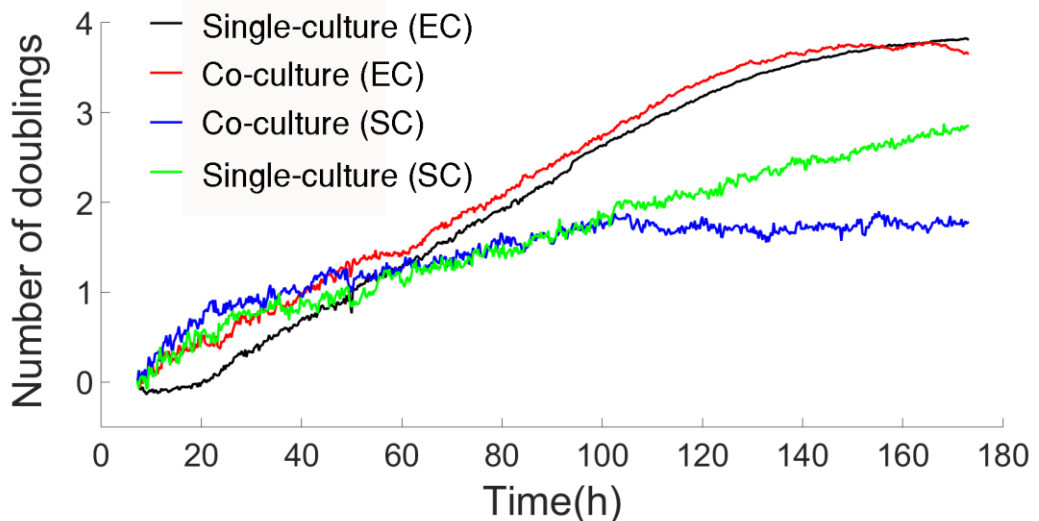


Figure 4.23: (A) Proliferation of Endothelial cells and Stem cells in the single-culture versus co-culture reported as number of doublings versus time.

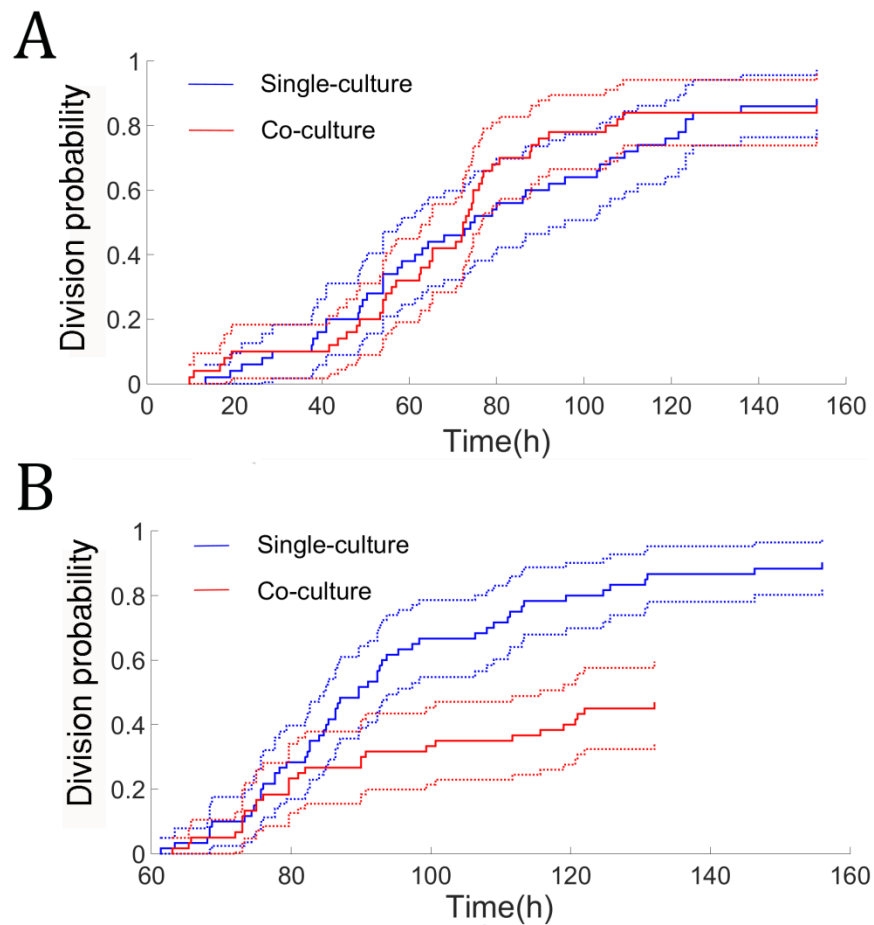


Figure 4.24: Kaplan-Meier and Cox regression analysis of time to division of SC in single-culture (SC/SC) versus co-culture (SC/EC) (A) Probability of division measured from the beginning of the experiment (B) Probability of division starting at $t=60$ hours (risk factor= 0.34 ± 0.09 and $p=5.53\times 10^{-6}$).

Kaplan-Meier and Cox regression analysis was performed to compare the effect of co-culture or single culture on the probability of stem cell division. Cell which did not divide during the course of the study were considered to be right censored. As seen in Fig. 4.24A, there was no effect of co-culture on the probability of stem cell division initially; however, after 60 hours, co-culture reduced the probability of stem cell division (Fig. 4.24B, relative risk= 0.34 ± 0.09 , $p= 5.53\times 10^{-6}$). This means that the relative risk of division of SC in the co-culture is around 1/3 of the risk of division in single culture. These observations are consistent with growth arrest of SC in co-culture at 100 hours (Fig. 4.24, blue curve).

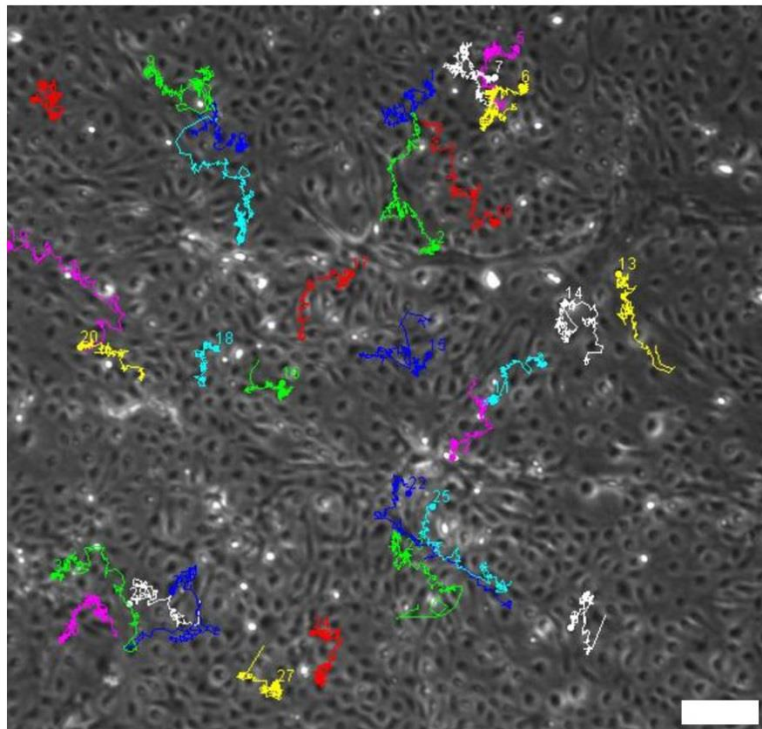


Figure 4.25: Single-cell tracking and collective cell migration analysis; The trajectory of multiple Endothelial Cells (EC) in the co-culture.

To quantify the collective cell migration ImageJ was used to track the trajectory of single cells. Fig. 4.25 shows the colour-indexed tracking of 30 cells along axes normal to the channels. As can be seen, tracked cells show different migratory behaviour. Some of the cells move faster, some of them show migration in a definite direction. Therefore, in order to distinguish between different migratory patterns, “cell type” and “culture conditions” were defined as fixed conditions and “migration speed”, “average migration velocity normal to the channels” and “Forward Migration Index (FMI) normal to the channels” were reported as their function. All statistical significance tests were performed using standard t-test and statistical significance were reported as (** for $p < 0.01$) and (* for $p < 0.05$). Error bars indicate the standard deviation of the data.

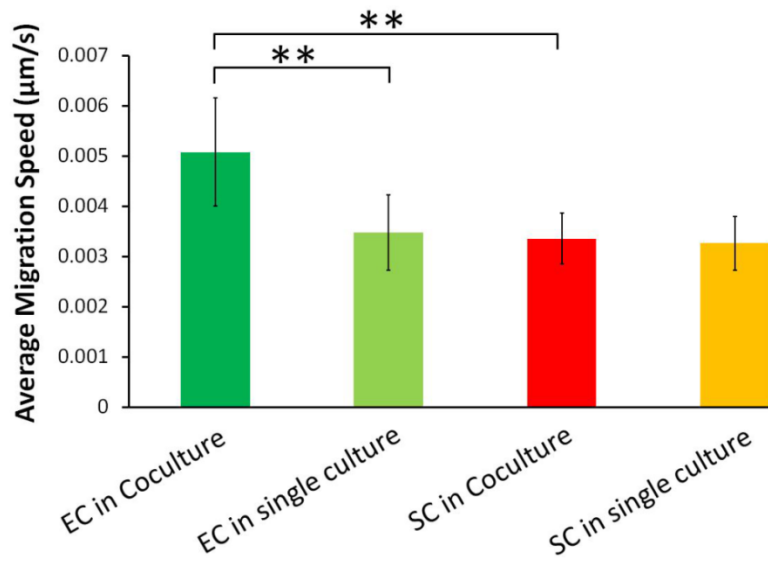


Figure 4.26: Single-cell tracking and collective cell migration analysis (B) Average migration speed of EC and SC in single culture and co-culture (n=30 for each condition) Scale bar: 200 µm.

Fig. 4.26 presents the average migration speed of cells of ECs and SCs under single- or co-culture condition. ECs have higher average speed in comparison to SCs. In addition, average migration speed of ECs was higher in co-culture compared to single culture (p<0.01).

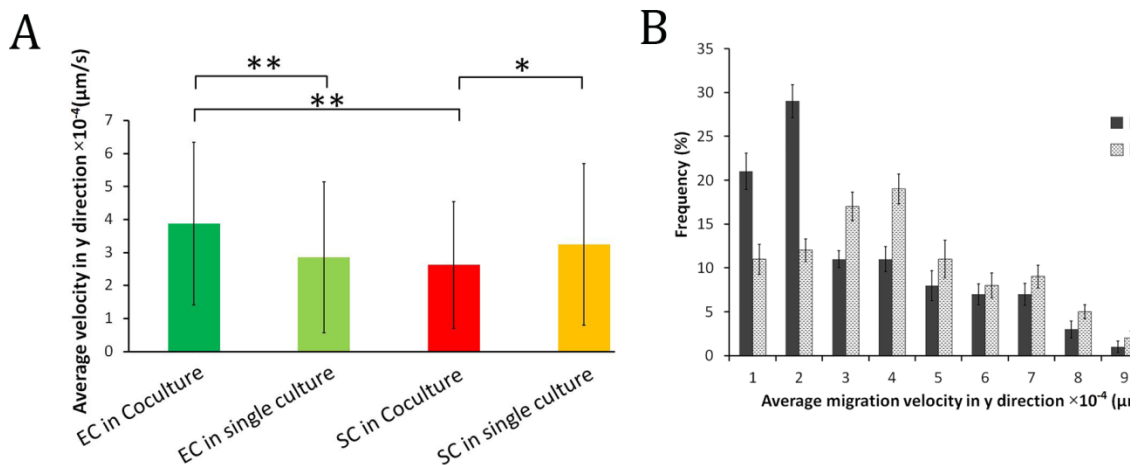


Figure 4.27: Single-cell tracking and collective cell migration analysis (A) Average migration velocity normal to channel direction for EC and SC in single-culture versus co-culture (n=100). (B) Average migration velocity distribution of Endothelial cells in single-culture versus co-culture (n=30).

In order to assess the directional migration of both cell types, the average migration velocity normal to the channels was calculated for 100 cells of each type as shown in Fig.

4.27A and three statistically different groups were found. Interestingly, the average migration velocity of EC in the co-culture (mean value= $3.87 \times 10^{-4} \mu\text{m/s}$) was higher than the single culture (mean value= $2.86 \times 10^{-4} \mu\text{m/s}$, $p < 0.01$) while SC showed higher values in single culture compared to co-culture ($p < 0.05$). This was the result of a difference in collective cell migration of EC and SC and its inhibition as cells encounter adjacent patterns. Fig. 4.27B demonstrates the histogram of average migration velocity of EC normal to channels. As shown in this figure, in the case of single culture, the distribution is skewed to the left with a high frequency of cells with low y-velocity.

In the case of the SC, as observed from Fig. 4.28A, the cells reverse their migration direction when they are in the co-culture, due to EC confinement. To account for this direction, change the distance of SC from the symmetry axis of each stripe was tracked, while each cell is measured relative to the axis of the pattern it originated in. As can be seen from the trajectory of multiple cells in Fig. 4.28A, the SC initially migrates away from the symmetry axis, followed by reversing their direction. This is because EC overgrow SC and displace SC back to the symmetry axis to form the observed elongated bundles. In contrast, in the case of the single culture controls, the cells move away from the symmetry axis of each pattern with symmetric migration rates, without a change in direction.

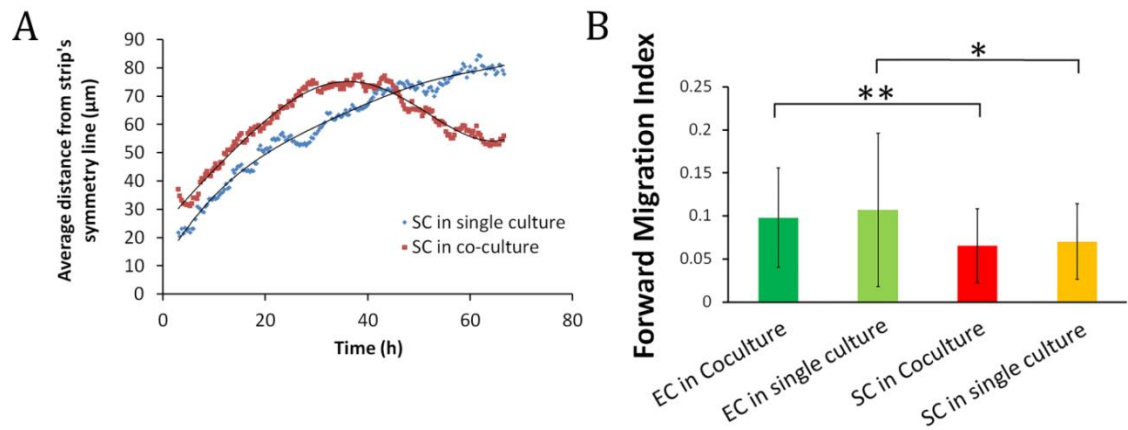


Figure 4.28: Single-cell tracking and collective cell migration analysis (A) Variation of the relative distance of Cardiac Stem Cells from the symmetry line of their corresponding strip with time in the co-culture vs. single-culture, (B) Forward migration index (FMI) in the y-direction for EC and SC in single-culture and co-culture (n=30).

During collective cell migration as well as single cell migration, cells may move in straight lines or move around randomly. Therefore, the behaviour of cells of different types in a specific population can be quantified by defining directional migration of that type. Fig. 4.28B shows the forward migration index (FMI) of EC and SC cells under different culture conditions in y-direction. FMI is defined as the displacement of a cell in a certain direction (e.g. y-direction) divided by the total path length of that cell.[163] As presented in Fig. 4.28B, EC cells show higher FMI compared to SC ($p < 0.05$), in both culture conditions. The FMI plot confirms that the directional migration of cells in the y-direction depends on the cell type, regardless of the culture conditions.

4.4. Conclusions

To explore cell homotypic/heterotypic interaction, a new stamping method was presented to rapidly pattern, in close proximity, two arbitrary adherent cell types in an interlaced configuration of choice. Following the stamp peeling, the two cell types are free to migrate across the stamped substrate and interact to form a tight interlaced 2D complex cell structure. The stamp design is based on a novel in-built valve which restricts the injected liquid flow while allowing residual air to vent out of a shared central channel.

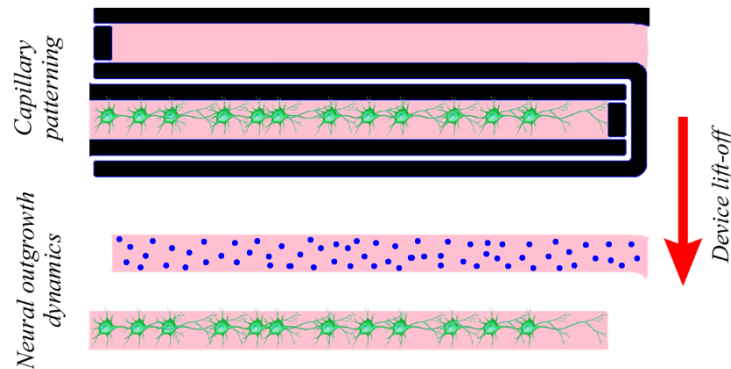
SOI-based RIE etching was used, rather than standard soft lithography, in order to achieve a defined device depth and improved channel cross section uniformity, needed for accurate device characterization. Once a master mould is ready, the number of manufactured stamps is not limited. Furthermore, a single PDMS stamp can be reused multiple times, as long as the inner stamp's surface hydrophobicity is not lost due to protein adsorption.

Using the proposed stamping device, the collective migration of EC/SC was investigated by measuring the average migration speed, average migration velocity in y-direction and cell directionality based on two fixed parameters of cell type and culture type. Statistical analysis of the obtained data revealed that ECs in the co-culture are more motile and migrate faster in the direction normal to channels compared to single culture. Moreover, looking at the migration measurements of EC and SC in the co-culture condition, ECs were more motile and ran faster in the direction normal to the channels compared to SCs. Analysis of the proliferation rate of each cell type revealed that SC provides a microenvironment that increases the initial growth of EC. In contrast, co-culture of SC with EC resulted in growth arrest of SC after 100 hours. The Kaplan-Meier estimate of time to division and Cox regression analysis demonstrated that after 60 hours, the relative risk of division of SC in the co-culture was reduced. Growth arrested SCs differentiated into cells with myofibroblast or spindle shaped morphology (Fig. 4b). Finally, migration of SC away from the symmetric axis of their seeding strip was reversed by EC from the neighbour seeding strip, which had a greater proliferation rate, invading and undermining GFP positive differentiated SC.

To conclude, a novel leakage-free stamping was developed to pattern adherent cell lines and to study the interaction of endothelial and cardiac stem cells by live cell imaging,

quantifying the effect of co-culture on cell proliferation and migration. The stamp is fabricated using RIE etching, does not require dedicated plasma bonding, and is operated with a standard lab pipette. This is the simplest 2D microfluidic co-culture stamping device to date. Therefore, it can be easily adopted by common non-microfluidic cell biology labs for the study of cell-cell modulation and intercellular signalling.

Chapter 5. Microfluidic neuronal patterning for neurite's outgrowth and inhibition assay[†]



Central nervous system (CNS) injury is an environment in which neurons outgrowth is inhibited by the molecules in between the disconnected neurons. The interaction between the neurite and inhibitory cues is therefore a dynamic event in which the neurite's growth cones are either extended over or blocked from entering the inhibition sites. In order to understand this interaction, it is crucial to culture the neurons in accurate spatial locations near the surfaces containing inhibition molecules. This chapter introduces a microfluidic patterning device that enables neurons to be grown adjacent to an inhibitory substrate, Nogo-66. Monitoring the growth cones of the patterned neurons using the microchannel confinement over time reveals that overexpression of a stabilizing molecule Tpm3.1 in the neurons increases the propensity to overcome Nogo-66 inhibition. Using the patterning method proposed here, Tpm3.1 is proposed as a potential target for promoting neurite growth in an inhibitory environment in the central nervous system.

[†] The outcome of this chapter has been published in "A Novel Microfluidic Device-Based Neurite Outgrowth Inhibition Assay Reveals the Neurite Outgrowth-Promoting Activity of Tropomyosin Tpm3.1 in Hippocampal Neurons", Cellular and Molecular Neurobiology 38, 1557-1563.

5.1. Introduction

The advent of microfluidic approaches to mimic live cell's microenvironment has opened a new pathway to precisely and rapidly study the interaction between cells and their surrounding components by providing superior spatiotemporal control and requirement for small amount of reagents. These approaches have been successfully applied in modelling tumour extravasation and metastasis [164, 165], collective cell migration and wound healing assay [166], and stem cell differentiation [167]. One of the areas of research which has been rarely explored is the neuron's microenvironment.

Neuron cells compared to other cell types have quite different structure and function leading to a different kind of interaction with their microenvironment. While basic cells have specific functions and they alone are functional units, neurons interact with each other; i.e. one neuron needs stimulation from other neurons to transmit information. Most importantly, neurons do not replicate which makes severe condition for regeneration following CNS injury.

To study the neuron's microenvironment, different approaches have been developed where most of them are focused on investigating the axon's growth and guidance under the action of attractive and repulsive cues via an appropriate spatiotemporal control [168, 169]. For example, pattern of substrate bound proteins have been generated using stripe assay [170, 171], microcontact printing [172, 173] and laser-assisted patterning [174] leading to significant discoveries regarding cell survival, axon outgrowth and growth cone (GC) turning and branching in response to spatial cues. Other assays include methods for localized release of guidance cues such as micro-pipette based assays [175], optical uncaging of caged molecules [176], and methods for generating diffusible guidance cues like Dunn chamber [177].

Although these methods have successfully been implemented in studying different aspects of the neuronal microenvironment their use is limited by either their operation complexity or their low throughput. In strip assay for example, axons outgrowth and cell motility depends on the type of membrane/protein and its concentration and yet the strip pattern is weak and stripe borders are not sharp [170]. Active patterning methods use external forces to transport cells to a desired spatial position and therefore offer on-demand capability [142, 143]. However, they generally require specialized peripheral equipment such as pumps, lasers and waveform generators and therefore need expert operators to run the experiment. Methods for localized release of guidance cues such as micropipette-based assays are relatively easy to operate but have very low through-put; only one cell at a time can be exposed to gradient. Since stimulation is controlled by pulsating release of guidance cues the method has poor repeatability [178].

Microfluidic devices have solved issues of difficulty in operation, costly experiments and low through-put by providing rapid and precise spatiotemporal control over the neuron's microenvironment. They have been widely used for neural stem cell differentiation [179], and neuropharmacology [180]. Perhaps one of the most promising applications of microfluidics in neuron research is investigating the mechanism of neuronal injury due to physical [181, 182] or chemical stimuli [168, 183] and consequent treatment to study the effect of different factors on neuronal regeneration and repair. However, all of those researches were focused on investigating the effect of extrinsic cues such as inhibitory molecules and growth factors on the neurite outgrowth.

One of the well-known approaches for regeneration of injury microenvironment is the compartmentalized microfluidic chip introduced by Jeon's group where soma and axon parts were separated via volume difference between chambers [184]. Following this

study, circular compartmentalized platforms were developed where soma and axon parts were separated using geometrical confinement [185, 186]. In the above studies, the aim was either to separately treat axons with a biochemical factor or study axon-glia interaction. However, compartmentalization limits axons outgrowth to predefined channel shapes. In addition, since axons outgrowth happens inside the microchannels, studying the effect of substrate-bound cues is not possible.

These issues have been addressed in two sets of devices generating substrate bound coating of inhibitory molecules and permissive/repulsive cues [147, 187]. A modified microfluidic based strip assay has been reported where CNS neurons were placed on top of laminin coated area while axons were allowed to grow and interact with alternating rows of inhibitory substrate. As a proof of concept, chondroitinase-ABC was used as a drug and aggrecan as an inhibitory cue. It was shown that enzymatic treatment promotes axons to cross onto the nerve-inhibitory strips and extend randomly across the pattern [187]. In a new technique, gradients of proteins with complex shapes were fabricated using laminar flows in microchannels [147]. However, this method requires delicate adjustment of spatial gradient, and adsorption of protein onto poly-L-lysine coated substrate questioning the methods reproducibility.

Neuronal regeneration in the injured or diseased central nervous system (CNS) is limited due to a large range of intrinsic and extrinsic factors that inhibit the regrowth of neurites from injured neurons. Reorganization of the neuron's cytoskeleton by interacting with the extracellular molecules enables dynamic extension and exploration of neurites and growth cone, which then form connections with other neurons [188]. Actin-associated protein tropomyosin (Tpm) are a family of proteins that play key roles in regulating the formation of neurites and in neurite branching [189, 190]. For example it is shown that

overexpression of Tpm3.1 results in enlarged growth cones, increase in the number of dendrites and increased axonal branching [191]. In order to understand the effect of Tpm3.1 on the dynamics of neurite outgrowth in the CNS injury environment, it is essential to be able to culture the neurons transfected with this protein in controlled proximity to CNS inhibitory substrates. Here, we describe a new microfluidic device to pattern a microliter sample of primary neuron cells and myelin associated inhibitory molecule NogoA within a certain spatial distance from each other (Fig. 5.1). Using this device, it is shown for the first time that overexpression of hTpm3.1 overcomes the neurite outgrowth inhibition activity of the CNS derived inhibitor Nogo66. The device is fabricated using conventional soft-lithography method and can be simply operated with a standard hand-held pipette and with no previous expertise.

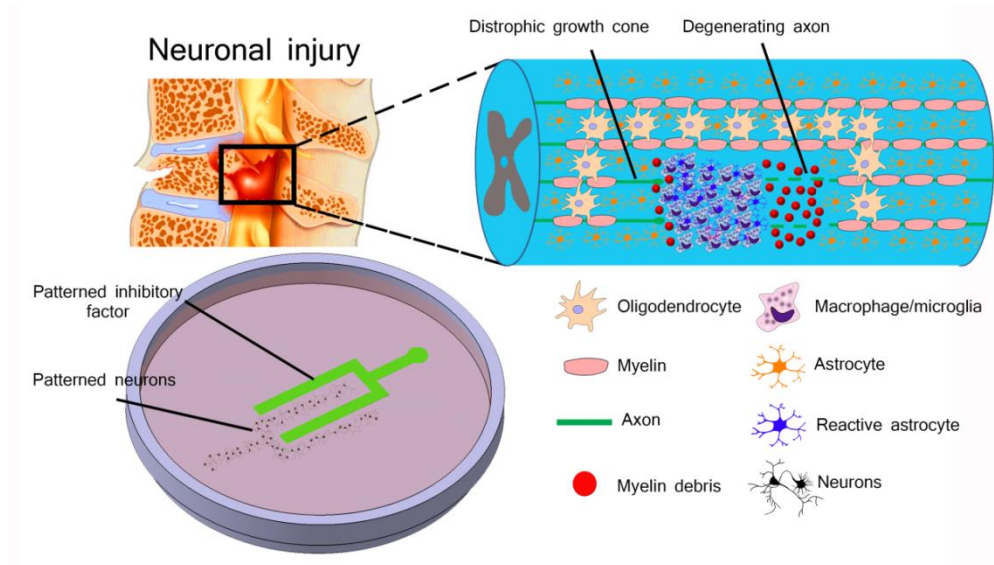


Figure 5.1: The concept of microfluidic neural patterning for generating a model of CNS injury in vitro.

5.2. Material and methods

5.2.1. Device design

In this chapter, a simple method for patterning inhibitory substrate and neuron cells on a tissue culture dish/glass slide is introduced with the aim to understand the neurite

outgrowth dynamics in the neurodegenerative environment. The method is following the principle of operation based on liquid sample confinement using Laplace pressure which is introduced in chapter 3. Therefore, the microfluidic device is acting as a stamp to pattern cells and inhibitory molecules. The relative position of the axon and the inhibitory molecule is a determinant factor in investigating the neurite outgrowth dynamics.

To reproduce the spatial positioning required as Central Nervous System (CNS) injury environment, two categories of devices have been designed. The first category is aimed to trap cortical neurons at the entrance of tiny slots of 10-micron size (Figure 5.2A). The axons will then be allowed to grow into the channels. In this device, the liquid sample, e.g. the medium containing primary neurons is loaded into the top channel through which cells are guided into a bigger culture space known as hatching area. The left and right parts of the hatching area are equipped with dead-end channels with 10 μ m gap. While the liquid fills the hatching area, it pushes the air out of the microfluidic device. Once at the gaps, the liquid will stop due to Laplace pressure while the air passes through the narrow restrictions.

The second design is to pattern cortical neurons in bulk while patterning the inhibitory molecules in an interlaced configuration (Figure 5.2B). In this device, the liquid sample containing cells will be pushed into an array of confining channels equipped with built-in valves. For both devices the inhibitory molecule is injected into the device through a dedicated inlet on the opposite side of the device. The device is designed as a stamp. Therefore, the PDMS device is only temporarily bonded against the substrate and it is removed from the culture substrate following cell seeding and channel coating.

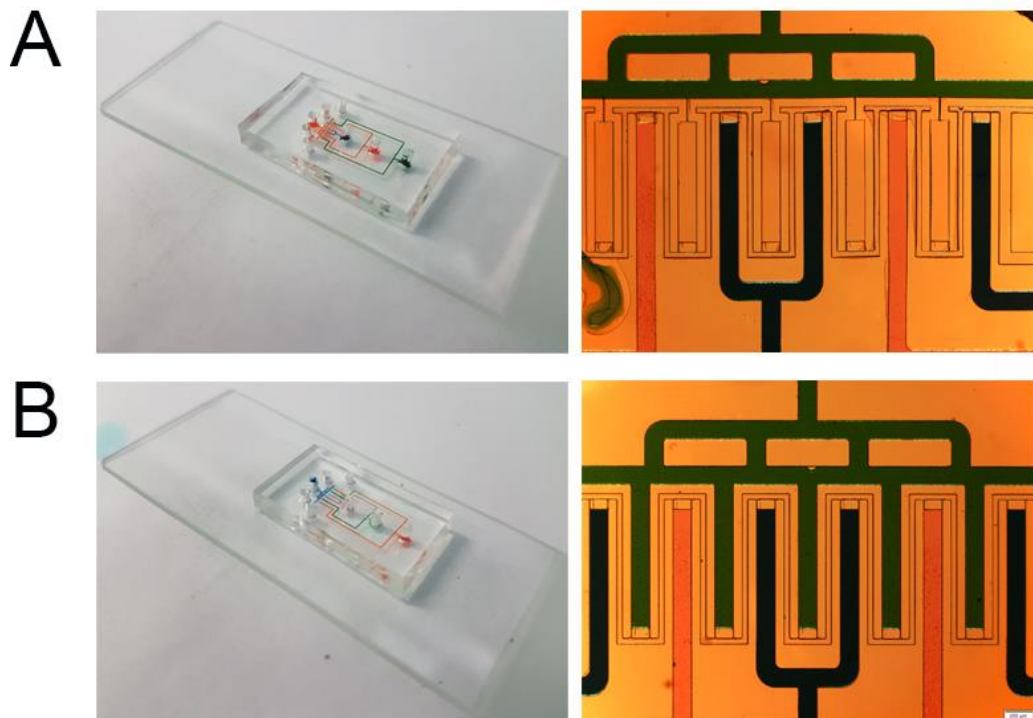


Figure 5.2: Microfluidic neuronal patterning device. (A) Type 1: hatching device; in this device liquid containing cell samples is injected into a hatching area equipped with two in-built valving gaps as wells as narrow slots to trap single neurons (B) Type 2: PDMS device in which channels are visualized by showing image of the device injected with blue, green and orange food colours.

Designing the stamping device for leakage-free operation has been discussed in the previous chapter. Briefly, the filling pressure is determined by Laplace pressure which is caused by the air-liquid interface curvature near the restriction sites. This means that the filling pressure depends on the restriction width. Therefore, different channel size and shapes can be designed as long as the restriction width is within a certain range. As shown in Fig.5.2, two designs have been developed. The first design (Fig. 5.2A) includes an upper hatching area (shown in blue) for trapping single neurons. The second patterning device is an array of microfluidic channels with dead-end traps (Fig. 5.2B).

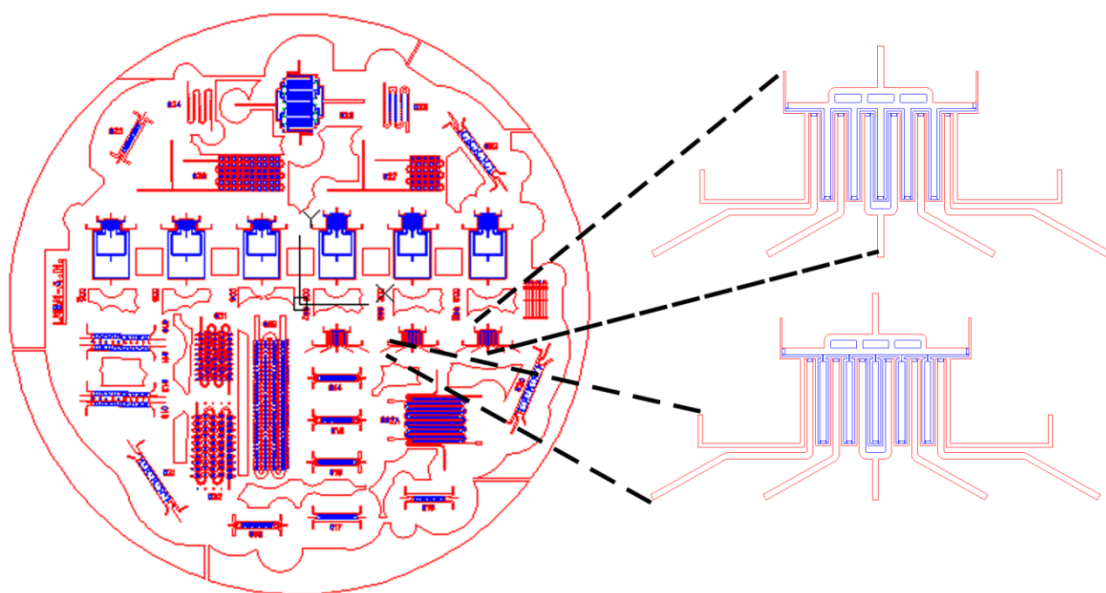


Figure 5.3: Designing the photomask of the neuronal patterning device in AutoCAD software: The photomask design is a 10 inch circle containing different chip designs. Different variations of the patterning device was positioned on a mask to investigate the effect of geometry on device operation. Each device is separated from nearby devices to accommodate punching the access holes, and border lines.

The photomask of the designs was drafted in AutoCAD software (Fig. 5.3). Devices were positioned inside a 4-inch diameter photomask which is a standard dimension for the mask aligner machine. The photomask is bright field (patterns in dark) which is chosen based on the thickness of the photoresist layer. In order to consider the effect of device dimensions on the cell and protein patterning, different sizes of the channels and the slots were chosen to reduce the cost and time of fabrication.

In designing the photomask for the neuronal patterning chips, specific design points were met. First, the volume of the device: this factor determines the number of primary cells required for the culture. The volumes of the devices were designed to be $\sim 1\mu\text{l}$ to minimize the use of primary cell samples. Second the dimensions and area of each microchannel: Cortical neurons have the size of $\sim 20\mu\text{m}$. However, it is possible that they make bigger clumps during the process of cell preparation. The size of the channel was designed to let bigger aggregates move into the device without clogging and the area of the channel was

designed to give a confluent channel following neuron's injection into the device, because neurons do not proliferate. Therefore, to have a sharp neuronal culture, it is essential to have them in an optimized concentration adjusted based on the device culture area. Third, the distance between the nearby designs should be big enough to enable punching the access holes. In this device 1.5mm biopsy punches are used. Moreover, there should be some safe distance for cutting the PDMS slab of nearby devices using cutting blades. The critical geometrical dimensions of the chip are shown in Fig. 5.4.

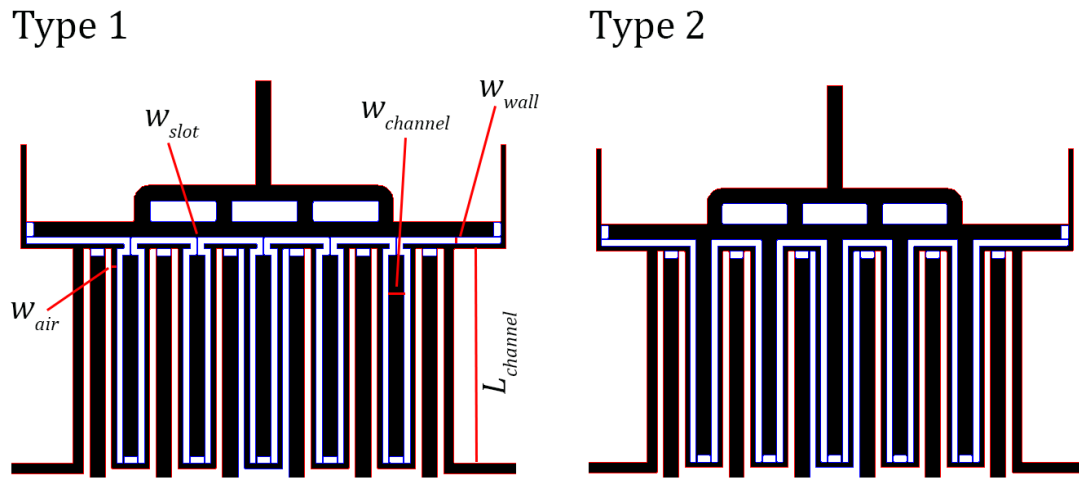


Figure 5.4: Critical dimensions of the neuronal patterning chip; $w_{wall}=62.5\mu\text{m}$, $w_{channel}=150\mu\text{m}$, $w_{gap}=10\mu\text{m}$, $w_{air}=20\mu\text{m}$, $w_{slot}=10\mu\text{m}$.

The mask designed here is a bright-field mask (Fig. 5.5). The area of the channel is dark and the rest of the mask area is transparent. This is a requirement for the microfabrication stage and will depend on the type of photoresist that will be used for fabricating the device.

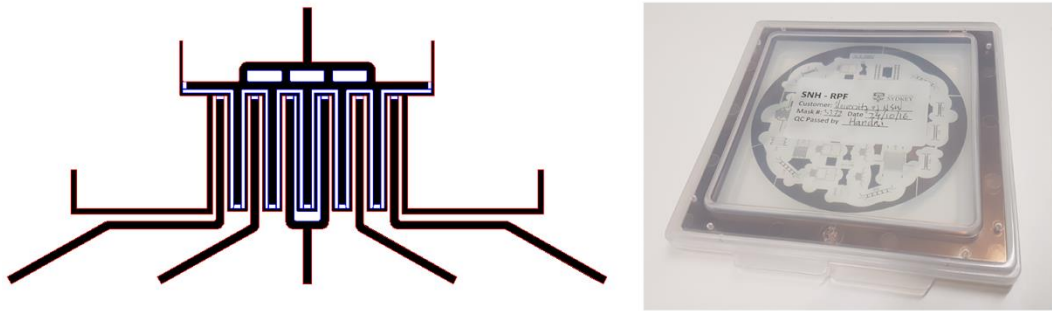


Figure 5.5: (A) Area of the chip design that needs to be dark for fabricating the devices (B) The fabricated mask is a bright-field mask with dark region made out of chrome.

Since the features in this design are quite small (the minimum size of the patterns is $10\mu\text{m}$) and the devices' operation depends on accurate fabrication. Therefore, patterns were made on a glass mask which gives the highest resolution among available photomask materials.

5.2.2. Device fabrication

The fabrication process follows the same procedure of section 4.2.2 of chapter 4. Briefly, deep Reactive Ion Etching (DRIE) on Silicon on Insulator (SOI) wafer was employed to achieve aspect ratios as high as 1:8. The device pattern was designed using the AutoCAD 2015 software (Autodesk®) and printed on a glass mask. The mask was then used to transfer the pattern onto a SU-8-coated SOI wafer (100 mm wafer diameter, $80\pm 1\mu\text{m}$ device layer, $2\mu\text{m}$ buried oxide layer, and $500\pm 15\mu\text{m}$ handle layer), using Karl Suss MA6 Mask Aligner (SUSS MicroTec, Germany), followed by a through-hole DRIE ($80\mu\text{m}$), using the STS system. The patterned SOI wafer was then silanized carefully, using vaporized trichloro (1H, 1H, 2H, 2H-perfluorooctyl) silane (Sigma Aldrich, USA) in a vacuum chamber over night to render the surface hydrophobic for easier release of cured polydimethylsiloxane (PDMS). PDMS (Sylgard 184, Dow Corning, USA) was prepared by mixing elastomer and curing agent in a standard ratio of 10:1 followed by degassing in a vacuum chamber for 1 hour. The mixture was then poured onto the silicon on

insulator (SOI) mould and cured at 80 °C for 2 hours before peeling. Inlet and outlet access holes were made, using 1.5 mm biopsy punch. Prior to use, microfluidic devices were sterilized sequentially in 70% and 100% ethanol for 15 min and allowed to dry completely before use.

5.2.3. Production of recombinant GST-Nogo-66 in *E. coli*

Please refer to Appendix D.

5.2.4. Primary cell preparation

Cortical and hippocampal cells were prepared and plated as co-cultures as previously described (Fath et al. 2009). For this, C57Bl6 wild-type mice were time-mated with heterozygous Tpm3.1/2 transgenic mice, overexpressing the human form of Tpm3.1/2 under the control of the β -actin promoter to generate litters with 50% wild-type and 50% Tpm3.1/2 embryos. The resulting cultures contained equal numbers of both wt and Tpm3.1/2 transgenic cells. In brief, embryos were extracted at E16.5 and brains collectively dissected as shown in fig. 5.6. After exposure to enzymatic reagents, hippocampal and cortical tissues were dissociated via trituration to a single cell suspension. Pelleted hippocampal cells were re-suspended in 10 μ L of DMEM (life Technologies Aust.) supplemented with 2% fetal bovine serum (FBS, life Technologies Aust.) per hippocampus collected, resulting in a high-density cell suspension.

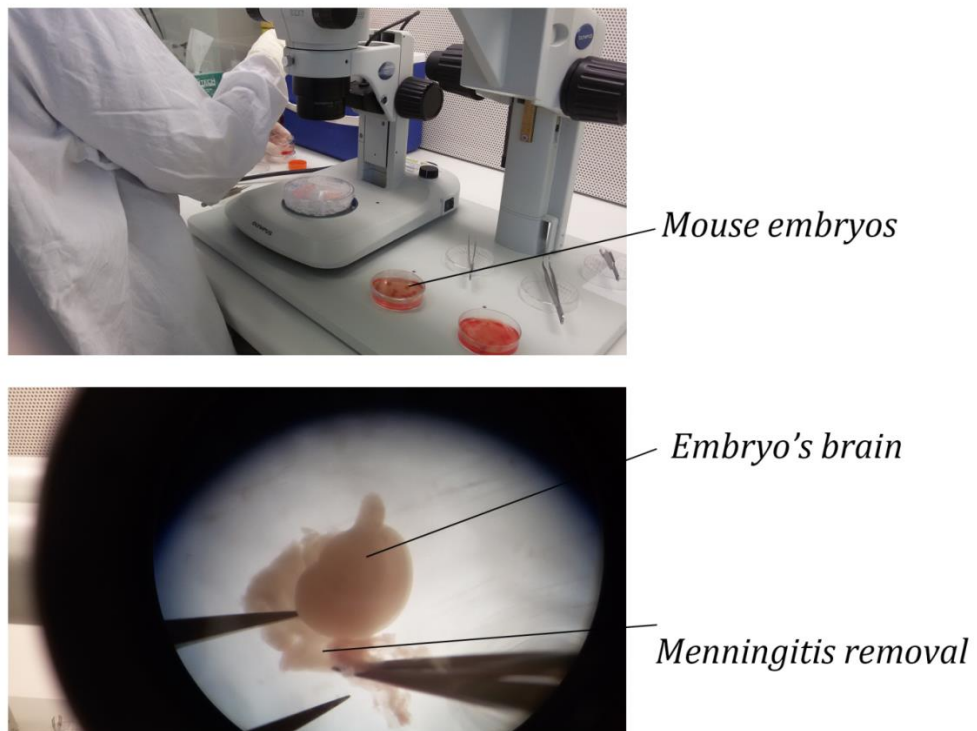


Figure 5.6: Cell extraction from mouse embryo: Embryos from day 16 mouse are obtained by sacrificing the mouse. Embryo's brain was removed and the menningitis was isolated. The hippocampal part of the brain was first chopped into pieces and prepared for further digestion.

5.2.5. Primary cell culture

For the neurite outgrowth assay, cells were seeded onto 18 mm glass coverslips (SDR Scientific) centred within 30 mm culture dishes (Sarstedt) as shown in Fig 5.7. For live imaging, 35 mm dishes containing a no. 1.5 coverslip with a 10 mm glass diameter (MatTek) were used. Coverslips and outer edges inside the dishes (support rings) were coated with 0.1 mg/mL poly-d-lysine (PDL, Sigma-Aldrich).

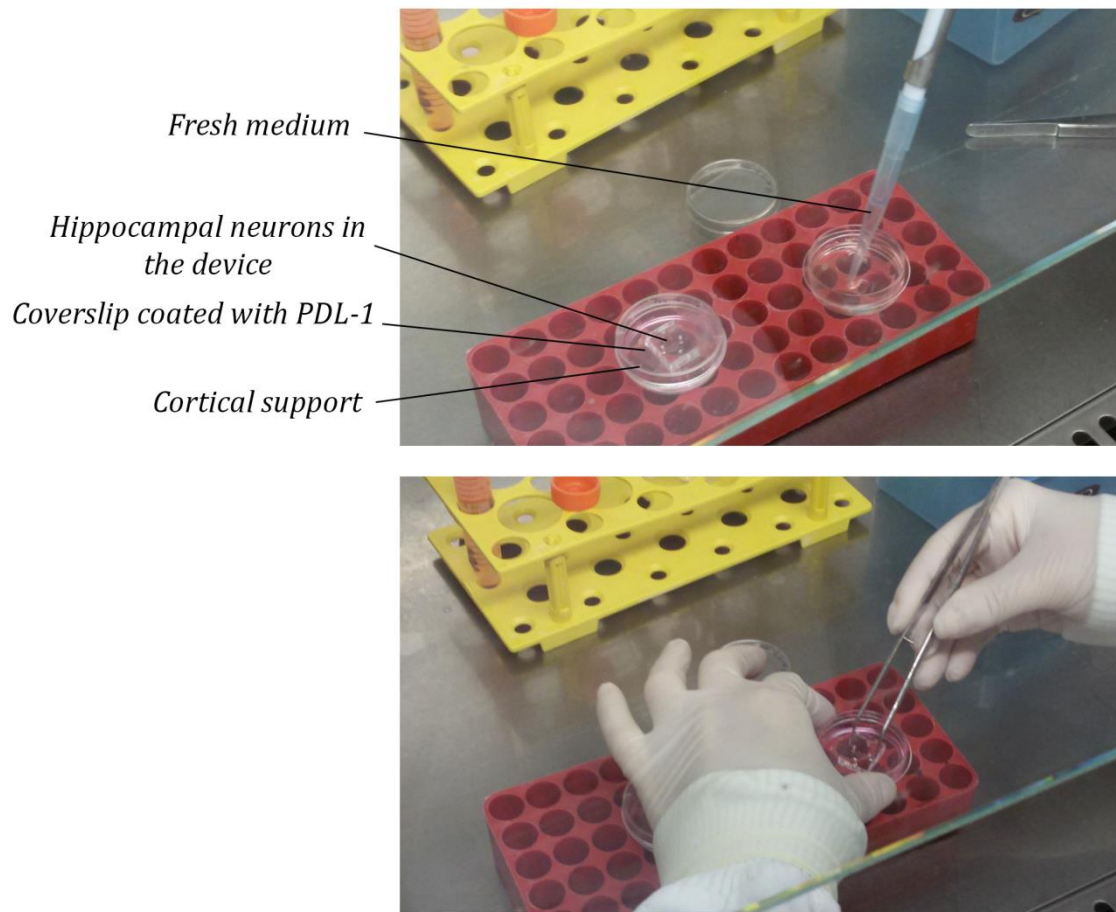


Figure 5.7: Primary cell culture in the neuronal patterning device: Devices are first placed on the coverslip coated with PDL-1. Hippocampal neurons were then injected into the device by adding 2 μ l of cell solution to the inlet followed by pushing the sample into the channel using air blown via 1ml pipette. A cortical support was added to the culture on the tissue culture ring. Following cell attachment, the device was peeled off and fresh medium is added on top of the patterned neurons.

Hippocampal cells were pipetted into the channels opposing the GST-Nogo-66 substrate at a volume of 2 μ l per device. Cortical cells were plated at density of 3×10^5 cells/support ring. 2 h after cell seeding, DMEM from the cortical support rings was aspirated and neurobasal media (NBM) containing 2% B27 (Life Technologies Aust.) and 0.25% Glutamax (Thermofisher) was added, flooding the entire area surrounding the devices. Microfluidic devices were then removed approximately 18h after plating. Cultured neurons were examined both after injection into the device and after peel off to ensure sharp patterns (Fig. 5.8).

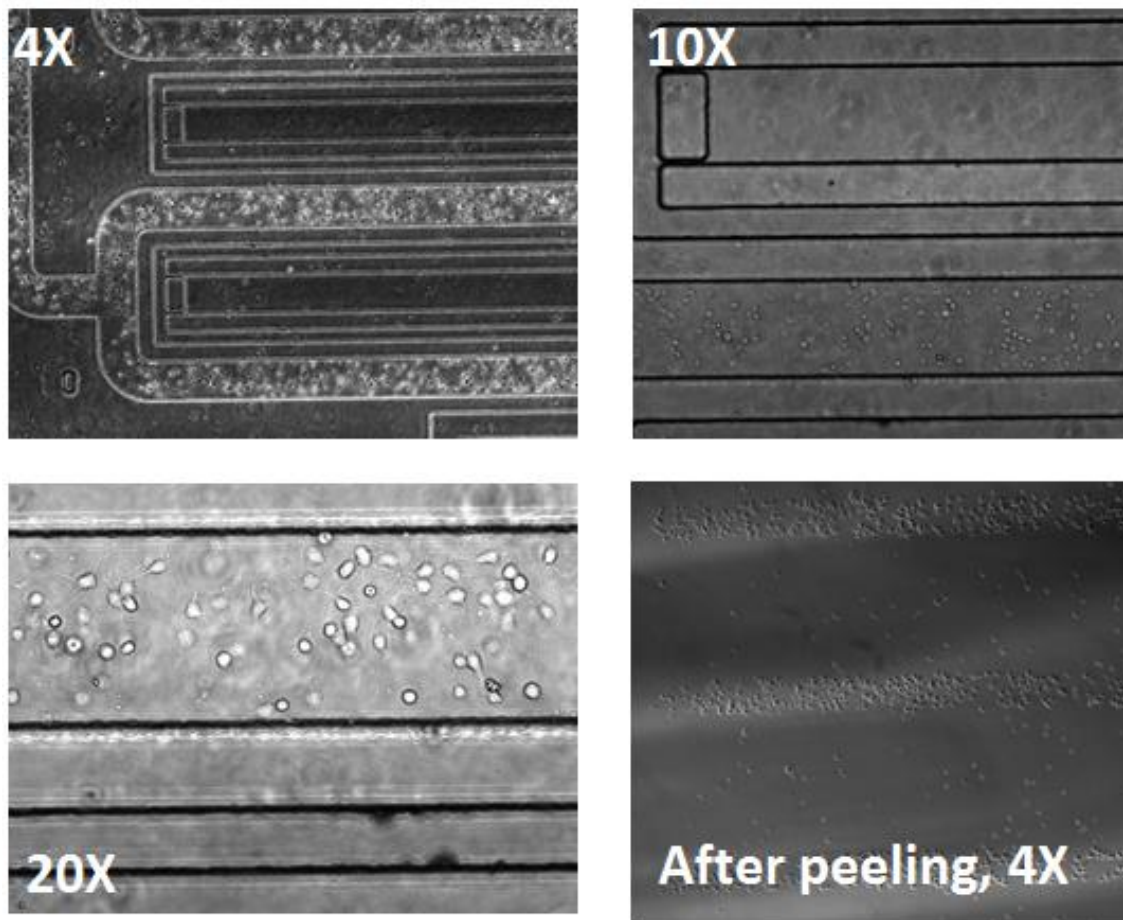


Figure 5.8: Cell culture in the neuronal patterning device before and after peeling.

5.2.6. Live imaging and axon growth rate

Cells were imaged across 24 h from 4 DIV using an Eclipse TiE microscope (Nikon) equipped with Perfect Focus System. Images were acquired at 2 min intervals with a 12 bit Charged Coupled Device camera using a 60 ms exposure and an analogy gain of 2.80 in the NIS Elements V4 software. A Plan Fluor 10x Ph1 NA0.3 objective in phase contrast mode was used. During imaging, cells were maintained at 37 °C with 5% CO₂. Growth rate of the axon was measured in ImageJ using the manual tracking plugin. The length of an axon was manually tracked over a number of frames outside and within GST-Nogo-66-treated regions. Growth rate was calculated by dividing the total length over time. Data was analysed in GraphPad Prism (v.7.02) by one-way ANOVA.

5.2.7. Immunocytochemistry

All immunostaining was carried out as previously described (Patel et al. 2017). Fluorescence images were acquired using either a 10x or 20x objective on an Axioskop40 microscope (Zeiss) with ZEN 2 lite software. For experiments examining the persistence of GST-Nogo-66 over time, coverslips were fixed at 1 DIV and 7 DIV in 4% paraformaldehyde for 15 min and immunostained using α -GST (rbt, 1:500; Abcam Aust.) antibody. Mean fluorescence intensity of the GST-Nogo-66 signal was measured along a 200 μ m length using ImageJ and statistically analysed by unpaired t-tests using Graphpad Prism (v.7.02).

Hippocampal cells from cortical support ring experiments were fixed in 4% paraformaldehyde at 3 DIV and 7 DIV and immunostained using α - β 3-tubulin (chk, 1:500; Merck) and Phalloidin-565 (1:500; Merck). Cell viability was analysed by counting the healthy and dead nuclei of cells as indicated by DAPI staining. One-way t-tests were carried out using GraphPad Prism (v.7.02). For initial outgrowth optimization experiments, cells were fixed at various ages from 2 to 7 DIV and immunostained using α -Map2 (rbt, 1:500; Merck) and α -Tau1 (mse, 1:500; Merck).

Cells used for live imaging were fixed at 5 DIV upon completion of imaging and immunostained using the following antibodies, α -hTpm3.1 (LC1, mse, 1:250; gift from Peter Gunning, Cellular and Genetic Medicine Unit, UNSW, Sydney), α -Nogo-66 (NogoA, rbt, 1:1000; Merck), α - β 3-tubulin (chk, 1:500; Merck). Appropriate Alexa Fluor-labelled secondary antibodies (Life Technologies Aust.) were applied at 1:500 dilutions. Cells plated on removable coverslips were mounted onto glass slides using Prolong Gold anti-fade mounting medium with DAPI (Merck). The details of the antibody staining protocol can be found in Appendix E.

5.2.8. Imaging and data analysis

Live imaging dishes had an 18 mm glass coverslip mounted over the region containing cells, using Prolong Gold mounting media with DAPI. Each microfluidic channel was acquired as a series of images which were stitched together using ImageJ software. Microscope data was then collected and converted into separate image stacks (Fig 5.9).

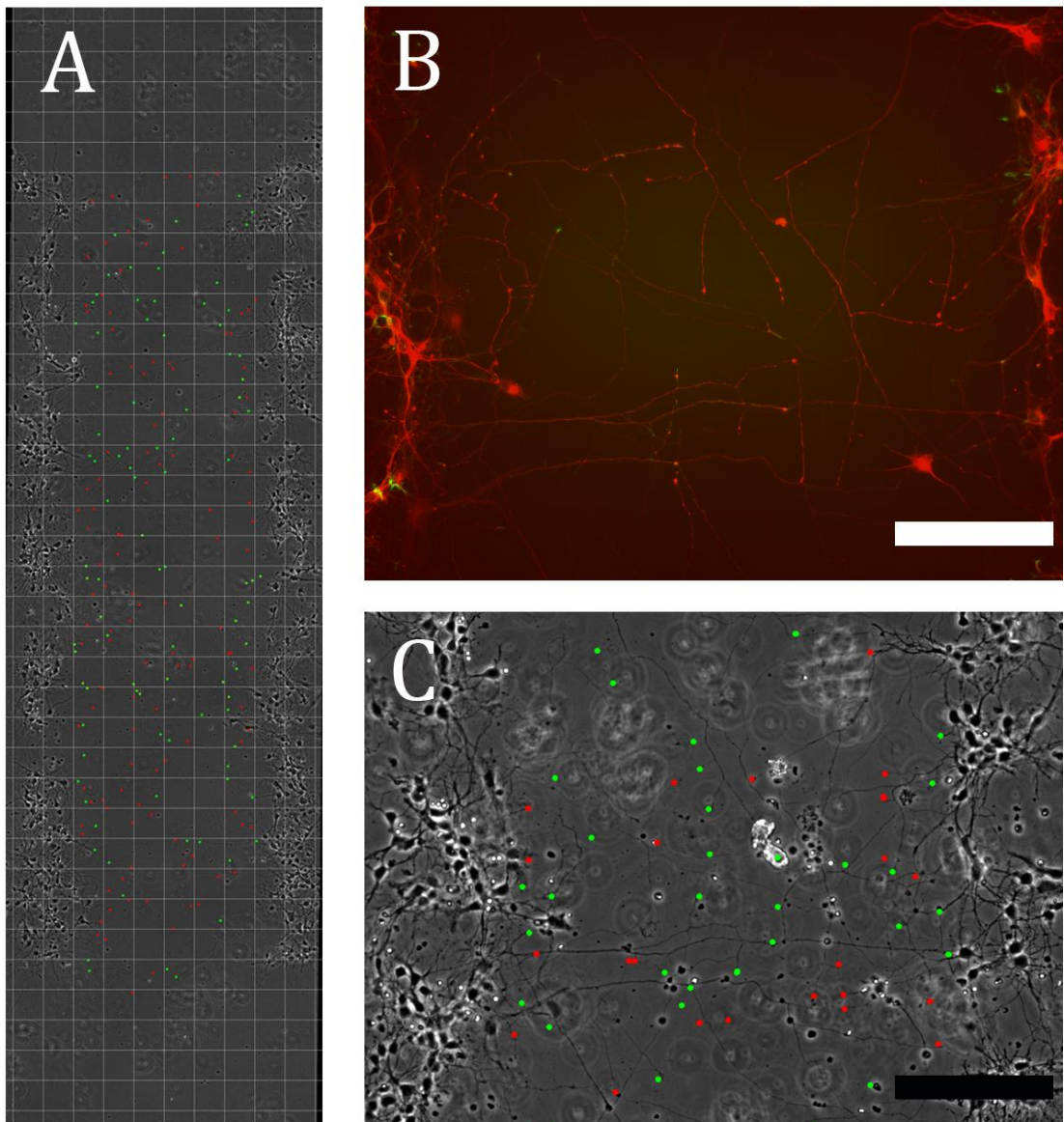


Figure 5.9: (A) Images taken along the patterned substrate was stitched together divided into 6 equal size parts normal to the patterns using ImageJ. (B) Fluorescent image of the neurites and growth cones (C) corresponding analysis of the fluorescent image in which neurites expressing Tp8 are marked with green and the rest of neurites are in red. Scale bar: 150µm.

To measure neurite lengths, the final acquired image from each live-imaging set was matched with its corresponding fluorescent image in ImageJ. In the phase contrast images, the area between the two cell regions was divided into six sections, namely ± 3 , ± 2 and ± 1 , using Grid command. Neurites of hTpm3.1 overexpressing and wt cells were differentiated using the fluorescence image. Growth cones were manually labelled using a green (hTpm3.1) or red (wt) pseudo colored dot on the corresponding phase contrast image. The number of neurite tips in each section of the grid were recorded in Excel and stastically analysed in Graphpad Prism (v.7.02).

5.3. Results and discussion

5.3.1. Neuron and GST-Nogo66 coating

First the patterning devices were characterized for the use of neurons, cultured at low density [192]. A microfluidic device-based assay, which allows rapid and precise patterning of neurons and an inhibitory substrate in an intercalating pattern is established (Fig. 5.10A-C). Neurite outgrowth was determined by measuring a straight line from the outer boundary of the plated cell layer to the tip of the growth cone (Fig. 5.10D). The distance from the edge of the plated cell layer to the GST-Nogo-66-coated region, also shown in (Fig. 5.10D), is 175 μm .

GST-Nogo-66, injected into the device, adhered to the coverslip in the defined channel pattern, and was persistent over a 7-day period, as confirmed by measuring of fluorescence intensity, after immunostaining with an antibody, directed against GST (Fig. 5-11A and B).

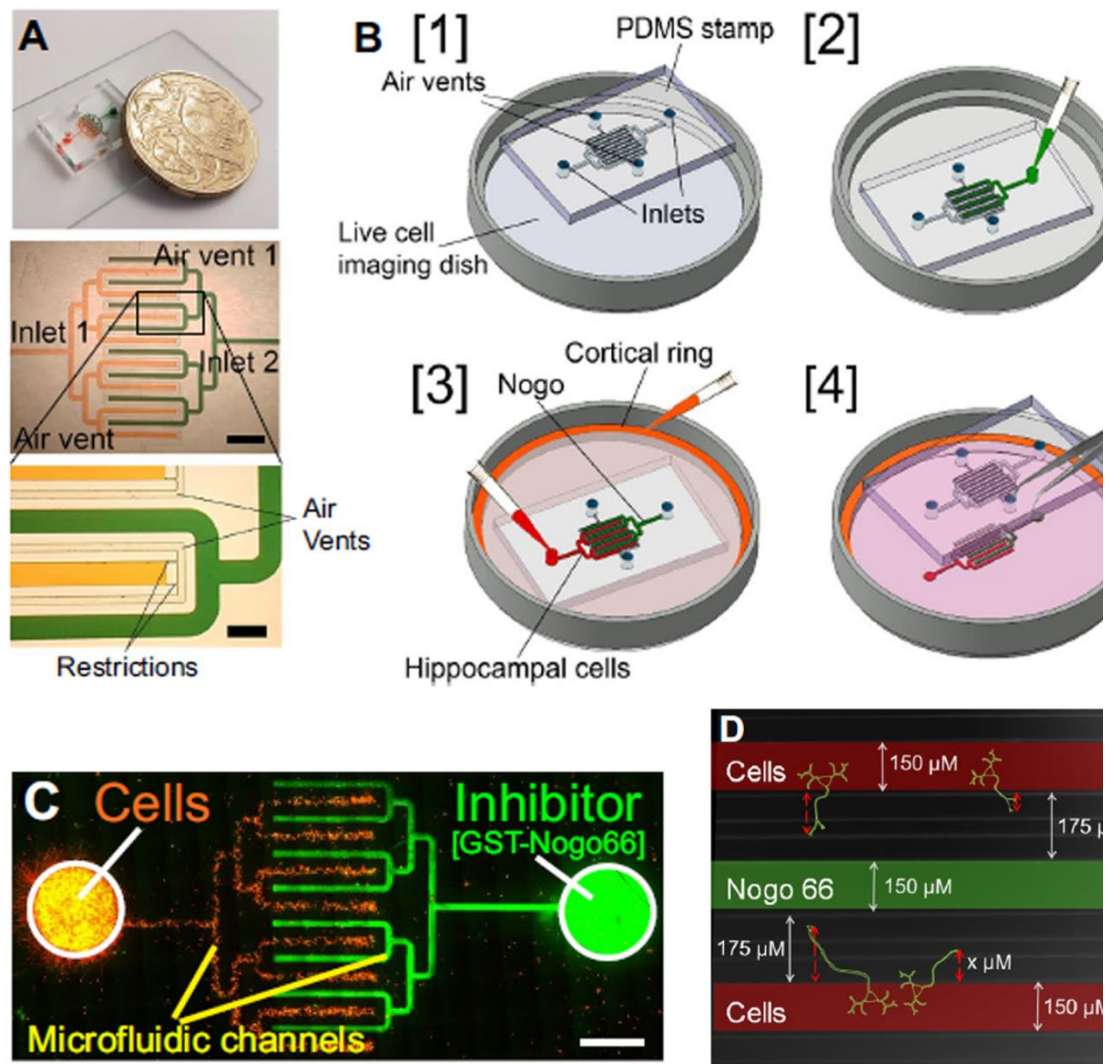


Figure 5.10: Design of microfluidic device. A Photo of microfluidic device for scale (top). Detailed schematic of microfluidic configuration with intercalating channels shown in yellow and green (middle) and enlarged image of area outlined showing device properties (bottom). Scale bars = 1 mm (middle) and 200 μm (bottom). B Schematic showing device being placed into live cell imaging dish B[1], loading of GST-Nogo-66 substrate (green) into channels on the right (B[2]), seeding of hippocampal cells into channels on the left (red) and cortical cells into a support ring (orange)(B[3]) and removal of the microfluidic device once cells are attached (B[4]). C Immunofluorescence image, displaying experimental loading of devices with GSTNogo-66 inhibitory substrate coating on the right (green) and primary hippocampal cells on the left (orange). Scale bar = 1.5 mm. D Brightfield image of microfluidic device (white outline) with a schematic overlay showing channel dimensions and distances between intercalating channels. The schematic demonstrates how the lengths of neurites were measured

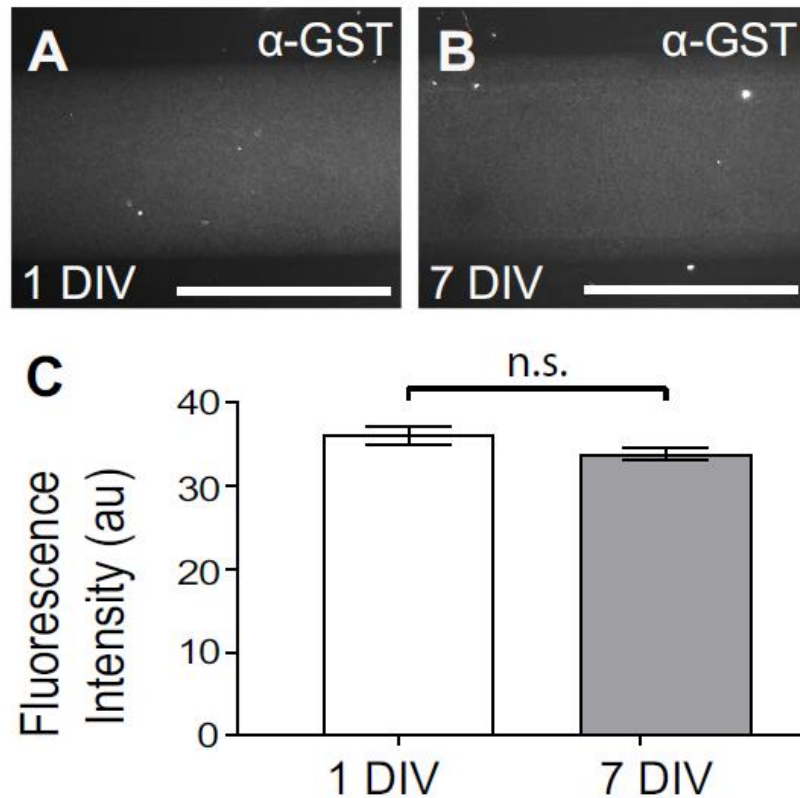


Figure 5.11: Validation of GST Nogo-66 coating: (A-B) Fluorescence images of GST-Nogo-66 coating in channel pattern defined by microfluidic device at 1 day in vitro (DIV) and 7 DIV, scale bars = 150 μ m. (C) Quantification of fluorescence intensity of GST-Nogo-66. Graph shows mean \pm SEM. Unpaired *t* test. *n* = 20.

5.3.2. Neurite outgrowth dynamics

By seeding a cortical support ring around the perimeter of the culture dish, the hippocampal neurons plated onto the centre of the coverslip (in the pattern dictated by the microfluidic device) remain viable, as measured at 3 and 7 DIV (Fig. 5.12 D–L). At 3 DIV, $93.8 \pm 1.1\%$ were alive with support ring versus $43.3 \pm 5.8\%$ without support ring and at 7 DIV, $90.5 \pm 1.7\%$ were alive with support ring versus $34 \pm 10.1\%$ without support ring.

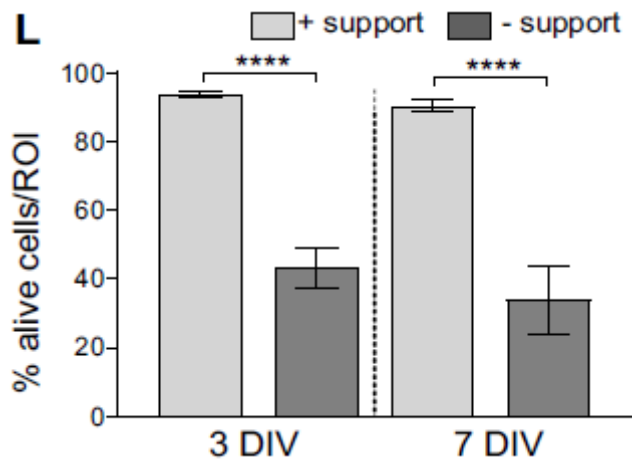
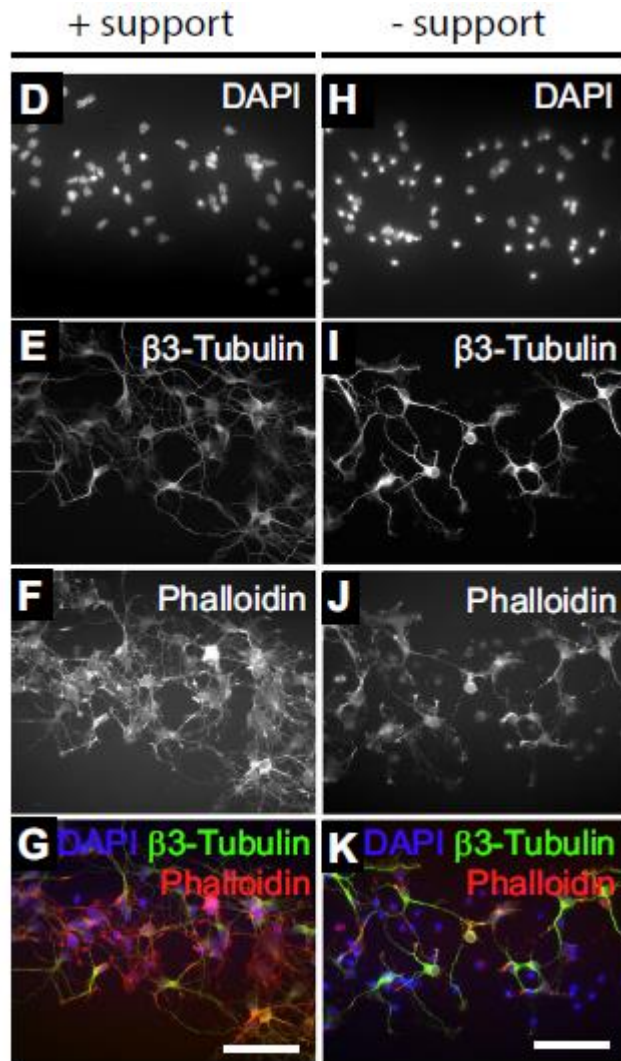


Figure 5.12: (D-K) Fluorescence images of hippocampal neurons at 3 DIV, plated with (D, E, F, G) or without (H, I, J, K) a cortical support ring. Scale bars = 100 μ m. (L) Quantification of cortical support ring experiments at 3 and 7 DIV. Graph depicts the mean percentage of alive cells per region of interest \pm SEM. Unpaired *t* tests. *n* = 10–11. *P* value *****P* < 0.0001.

To determine the optimal time point for analysis of neurite growth behaviour, as neurites encounter the GST-Nogo-66-coated area, neurons were fixed at time points from 2 to 7 days in vitro (DIV) (Fig. 5.13M–S) and measured as mentioned above. Neurite outgrowth was found to reach the GST-Nogo-66 region between 4 DIV and 5 DIV (Fig. 5.13S). Therefore, live-imaging analysis of neurite outgrowth behavior was analyzed over a 24 hrs time period from 4 DIV to 5 DIV.

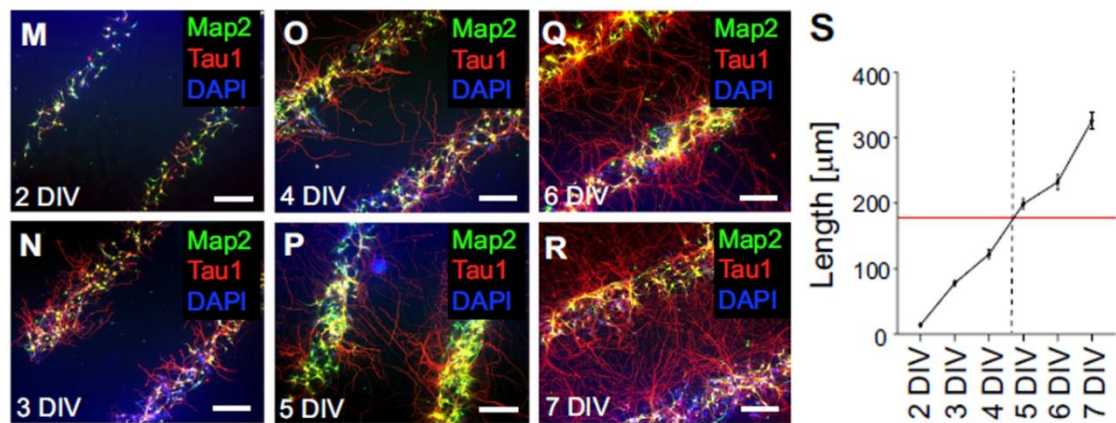


Figure 5.13: (M–R) Immunofluorescence images of neurite outgrowth from 2 DIV to 7 DIV. (S) Quantification of neurite lengths from time points in (M–R). Graph shows mean \pm SEM. The distance between intercalating channels (175 μm) is indicated by the red line. The time point at which neurites reach the GST-Nogo-66-coated substrate is depicted by the black, dashed line. $n = 23$ (2 DIV), 120 (3 DIV), 119 (4 DIV), 125 (5 DIV), 95 (6 DIV), 43 (7 DIV). Scale bars = 200 μm

5.3.3. Neurite inhibition assay

Neurite growth rates of wild-type and Tpm3.1-overexpressing neurons were measured in the growth-permissive area (labelled -2 and -3, Fig. 5.14A) and the GST-Nogo-66 region (labelled -1 and 1, Fig. 5.14A). The obtained data shows that the overexpression of Tpm3.1 significantly slows the rate of neurite outgrowth from 0.85 ± 0.07 to 0.57 ± 0.05 $\mu\text{m}/\text{min}$ (Fig. 5.14B). In fact, overexpression of Tpm3.1 increases stabilization of the actin filament population which consequently leads to reduced growth cone advance and a reduced rate of neurite outgrowth, which is seen in the assay system (Fig. 5.14B).

While neurite growth rate of wild-type neurons slows upon reaching the GST-Nogo-66-coated region (i.e., 0.85 ± 0.07 $\mu\text{m}/\text{min}$ outside GST-Nogo-66 coated region and $0.51 \pm$

0.05 $\mu\text{m}/\text{min}$ within GST-Nogo-66 coated region), neurites of hTpm3.1-overexpressing neurons appear largely insensitive to the inhibitory substrate, showing no significant change in their growth rate upon entering the GST-Nogo-66-coated region.

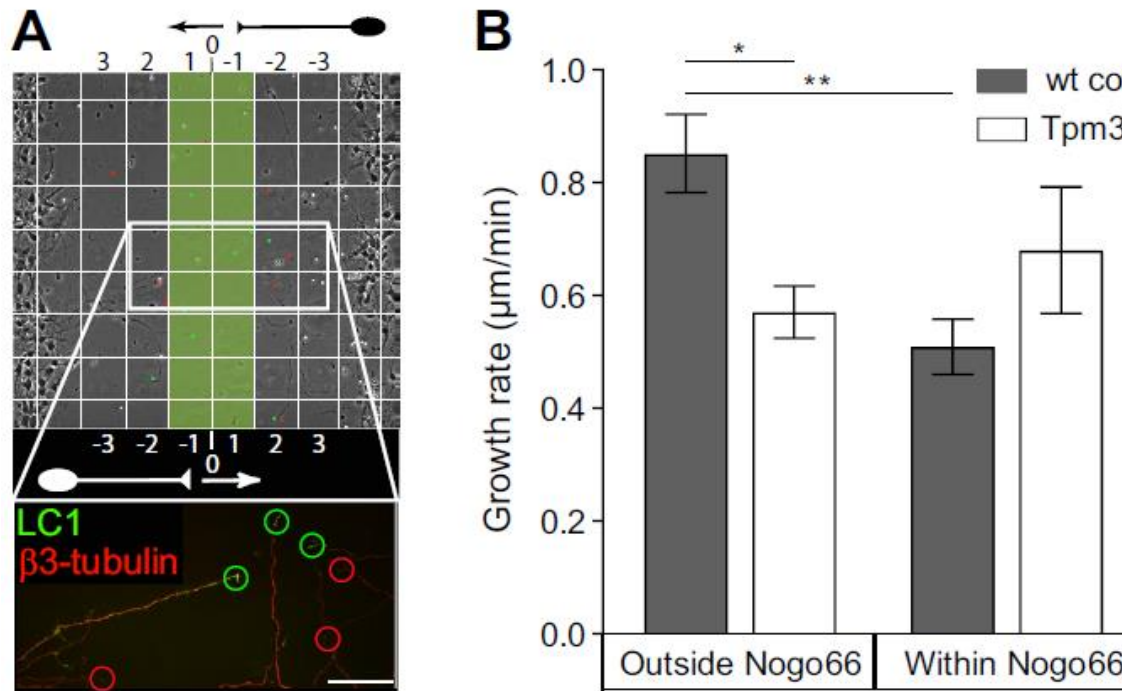


*Figure 5.14: Neurite outgrowth promoting activity of Tpm3.1 in the presence of GST-Nogo-66. (A) Phase contrast image of hippocampal neurons at the completion of live recording. Grid overlay shows the division of cell culture area into regions of interest based on distance from GST-Nogo-66 substrate (pseudo-coloured green). Insert shows magnified region containing hTpm3.1 overexpressing and wt neurites circled in green and red, respectively. Scale bar = 50 μm . (B) Quantification of neurite growth rate within GST-Nogo-66-coated areas and non-coated areas. Tukey's multiple comparisons test. Shown are mean \pm SEM. $n \geq 12$. P value * $P = 0.016$, ** $P < 0.01$.*

Next the proportion of wild-type and hTpm3.1-overexpressing neurons that extend their neurites into the GST-Nogo-66-coated region was determined. A significant difference was found between the ability of wt and hTpm3.1 overexpressing neurons to overcome the GST-Nogo-66 substrate (Fig. 5.15). Compared to wt neurons, neurons overexpressing hTpm3.1 show a much greater propensity to extend into and past the GST-Nogo-66-coated region (Fig. 5.15). This is indicated by a 1.7- and 3.9-fold increase in the number of neurites tips located in (regions -1 and 1) and past (regions 2 and 3) the GST-Nogo-

66-coated area, respectively. No differences in neurite outgrowth were observed between the two groups in the absence of GST-Nogo-66 (Fig. 5.15).

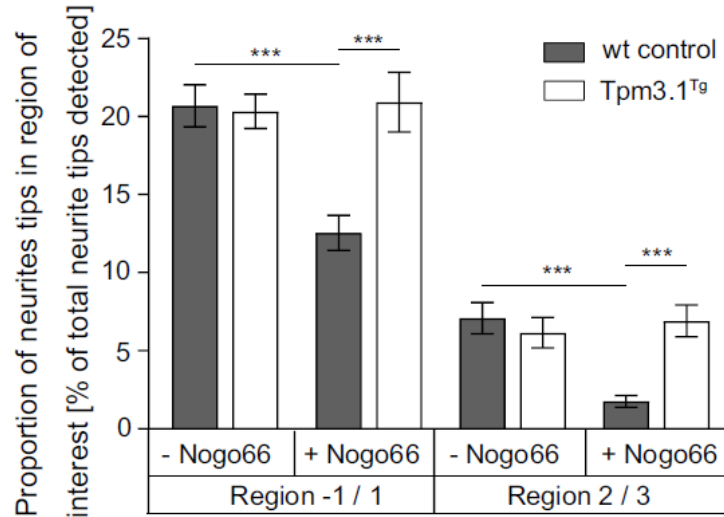
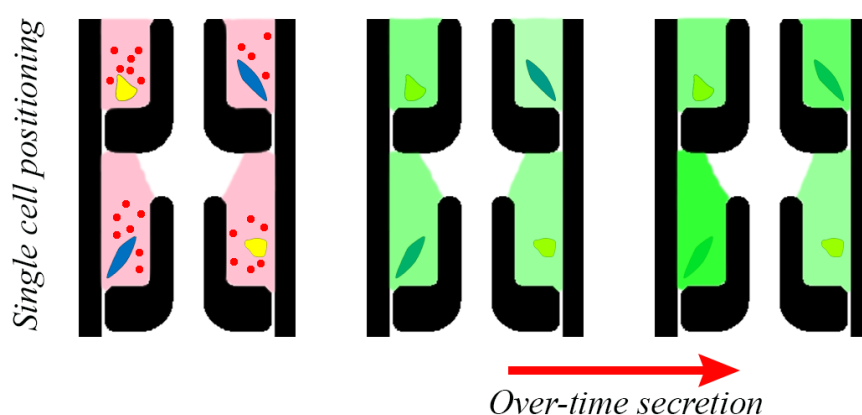


Figure 5.15: Quantification of the proportion of neurite tips within region - 1/1 and region 2/3 in the presence (+Nogo66) or absence (-Nogo66) of GSTNogo- 66. The graph depicts mean of proportions of total number of cells \pm SEM. Bonferroni's multiple comparison test. $n = 20$. P value * $P = 0.0475$, *** $P = 0.0003$, **** $P < 0.0001$

5.4. Conclusion

The new microfluidic device, used in this study, allows for continuous monitoring of the interaction between the growth cones of neurons with inhibitory molecules patterned on substrate of choice. The patterned culture of neurons was achieved by confining the cell/substrate sample inside microchannels using capillary based burst valves. Using this device, we were able to monitor neurite's length, outgrowth rate, and outgrowth direction. We then used the device to create an *in-vitro* model of CNS injury environment by patterning neurons and inhibitory molecules Nogo66. The results led to proving the effect of Tpm3.1 as a protein regulating cytoskeletal stabilization and promoted neurite outgrowth encountering the region coated with inhibitory cues.

Chapter 6. Single cell trapping and secretion assay[‡]



A new sample trapping method is presented to easily and reliably generate an array of hundreds of dispersed nanolitre-volume semi-droplets for single-cells culture and analysis. The liquid segmentation step occurs directly in indexed traps by a tweezer-like mechanism and is stabilized by spatial confinement. Unlike common droplet-based techniques, the semi-droplet wets its surrounding trap walls thus supporting the culturing of both adherent and non-adherent cells. To eliminate cross-droplet cell migration and chemical crosstalk, each semi-droplet is separated from nearby trap by a ~80 pL air plug. The overall setup and injection procedure take less than 10 minutes, is insensitive to fabrication defects and supports cell recovery for downstream analysis. The method offers a new approach to easily capture, image and culture single cells in a chemically isolated microenvironment as a preliminary step towards high-throughput single-cell assays.

[‡] The outcome of this chapter has been published in "Static droplet arrays for culturing single live adherent cells an isolated chemical microenvironment", Lab Chip 18, 2156-2166.

6.1. Introduction

Over the past decade, studying cells at the single cell level has attracted growing interest in cancer research [193, 194], stem cell research [195, 196], immunology [197, 198] and neuroscience [199]. Since measuring the collective behaviour of bulk cell populations only provides the average response, each individual cell acts differently depending on its transcriptional state, biological context, and the microenvironment [12, 29, 200]. Therefore, single cell analysis allows capturing heterogeneity that exists within the cell population at the cellular and molecular (subcellular) level [12, 201]. This transition to single cell analysis entails a broad range from unravelling single cell's genome [202] and transcriptome [203] to studying secreted proteins and biomolecules of each single cell [204, 205].

Despite these inclinations, no effective tool has been proposed until the advent of MEMS technology, as manipulation of single cells and positioning cells in spatially separate locations remained too much of a challenge. Microfluidic devices are capable of handling pico-liter to sub-microliter volumes of liquids and therefore are suitable for manipulating volumes comparable to the volume of single cells. These include microwells [44, 206], micropatterns [52, 207], single cell traps [208], and micropillars [209] all of which are capable of spatially confining single cells for further downstream analysis. The development of each of these devices can be tailored to the specific application and data sought [210].

Flow cytometry is the most widely used technique for high-throughput single-cell analysis and is improved with the introduction of CYTOF[211, 212] (Time of Flight Mass Cytometry, Fluidigm, USA) which enables looking at several biomarkers at a time using transition element isotopes. However, it cannot track single cells over time and therefore

has limited capability to associate cell biomarkers with dynamic cell behaviour. Unlike flow cytometry, time-lapse microscopy can track thousands of cells in parallel while correlating their morphology and dynamic gene expression patterns to selected reporter genes [213, 214]. In spite of these advantages, determining the contribution of single-cell secretion and paracrine signalling to the overall cell response is not possible due to the shared soluble media present in static culture. To accomplish this goal, cells must be kept in separate compartments where their viability and growth can be maintained over extended period of culture. The compartmentalization of individual live cells in pico- to nano-litre volume water-in-oil droplets has complemented these technologies by spatially confining cell-secreted biomolecules to a droplet thus maintaining the single cell chemical signature [215, 216].

In spite of significant progress of droplet-based platforms, the manipulation of single droplets remains challenging. Among these challenges are the ability to control droplet generation on demand, droplet coalescence, re-adjustment of a droplet's volume, and droplet splitting and sorting [217, 218]. Several microfluidic devices have been proposed that use surface properties to manipulate and separate droplets [68] including use of superhydrophobic surfaces [219], surface anisotropy [220], and droplet dispensing on hydrophobic surfaces [221]. However, their use of surface properties and external equipment makes them difficult to operate and may disturb the encapsulated cell's function. Non-microfluidic droplet manipulation techniques [222, 223] can eliminate the need for expertise in liquid handling but their throughput is much lower compared to microfluidic approaches; since droplets are not sheathed, cross-contamination with the outside environment is challenging. Perhaps one of the least addressed manipulation capabilities is droplet immobilization in an indexed array, which is an essential step towards single cell tracking over time scales of hours up to days.

Most of the existing methods for generating stationary droplet arrays rely on the generation of droplets or plugs of dispersed media in a channel primed with oil. In the systems where droplets are made in a continuous oil phase, an array of traps is designed to immobilize the generated droplets [224-227]. Therefore, these methods necessitate delicate production and manipulation of droplets with the volumes of the nanowell/trap size. In addition, the pressure coupling of droplet generation and droplet trapping requires precise adjustment of the loading pressure and therefore rely on complex tubing and automation [228]. Systems introducing plugs of liquid sample into oil are able to produce and capture droplets at the same time but they either rely on multilayer photolithography [102] or computer-controlled microvalving system [229] as well as peripheral equipment like pumps [71].

Since droplets in most of the previous studies are sheathed with oil on all sides, they can only accommodate suspended cells and are not able to support long term incubation of adherent cells [109, 230, 231]. In addition, live cells are prone to anoikis in droplets due to loss of anchorage to a substrate and disruption in cell attachment [232, 233].

A new approach that overcomes these issues with the ability to easily segment the liquid into indexed stationary traps and support live cell culturing was recently presented [115, 234]. The device captures the cells in traps connected to an air vent. Although it successfully outperformed other methods in terms of simplicity, portability and cell recovery it relies on a defect-free fabrication of all traps, which is challenging. Here a new method is presented to easily generate hundreds of stationary semi-droplets in indexed traps for live cell incubation and tracking. The method does not require microfluidic expertise, uses microliter volume of reagents, can be easily tailored to the desired droplet volume, is operated with a standard laboratory pipette and is highly robust.

6.2. Material and methods

6.2.1. Device design

In this work, a novel approach for trapping single cells in an array of nanolitre-size liquid compartments is introduced. Therefore, the motivation was to design a device that can use microliter of cell sample, trap single cells in individual locations; separate cells from each other from any physical or chemical contact and able to maintain the cells over the period of culture. To stop the liquid sample in each compartment, it is essential to have a valving mechanism. The design introduced here uses the principle of Laplace pressure to stop the liquid movement in each trap. Therefore, while liquid is filling the traps, each trap will be occupied by a single cell sample while each neighbouring traps are isolated with a narrow air gap.

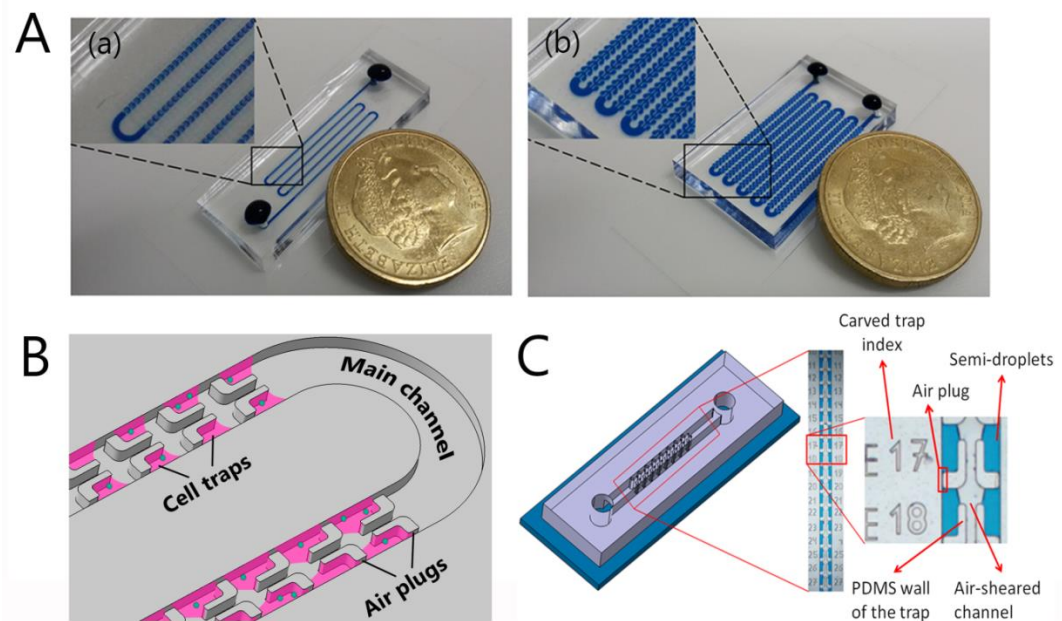


Figure 6.1: Schematic illustration of the high-throughput static droplet device configuration and operation. (A) Image of a chip with (a) 500×2.5nl droplet traps, (b) 600×14nl droplet traps with close-up image of the traps. (B) 3D schematic of the device showing the traps, air plug sites and the main channel. (C) Chip components including traps, semi-droplets, main channel, air plug and trap indices.

A 3D schematic of the static droplet system along with the device filled with blue food colour is shown in Fig. 6.1A-C. It contains two parts; the main channel where the cell

suspension is flowing in and the trapping sites where cells are being captured. The trapping regions of the device are pairs of L-shaped equally distanced obstacles. One of the main concerns in previous microfluidic chamber designs was cell-cell crosstalk between adjacent chambers due to the shared media. In the present device, neighbouring chambers are separated by a narrow gap of air plug which prevents drop-drop signalling and thus maintains each cell's chemical signature (Fig. 6.1B). Indeed, each droplet is a liquid compartment that is both physically and chemically isolated from its neighbouring chamber throughout the experiment.

Chemical isolation: The source of change in each droplet's content can be transport of molecules from one droplet to another or it can be due to bleaching of the fluorescent dye over time. The fact that the droplets fluorescent content has negligible change over time (Fig 6.2) indicates that none of these take place and the droplet content is intact.

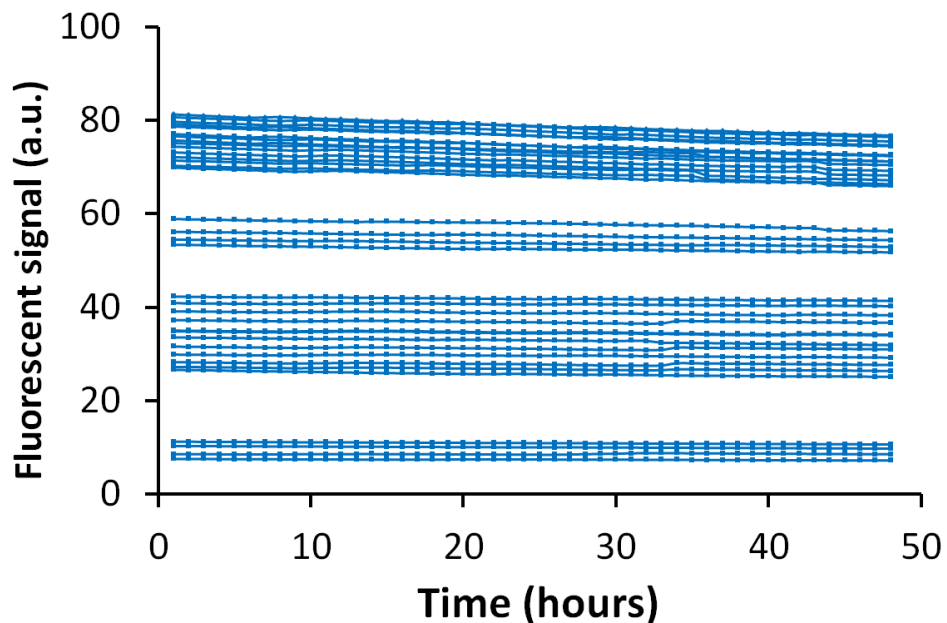


Figure 6.2: Chemical isolation of the droplets throughout the experiment. The device is filled with different concentrations of fluorescein and the fluorescent intensity of droplet was measured over 48 hours experimental period. Each line belongs to a unique droplet.

Physical isolation: After the droplets were formed, the channel was filled with FC oil to sheath the droplets. Looking at each droplet (liquid compartment) following formation

and FC oil injection, no connection was observed between any groups of droplets through the experiments (Fig. 6.1B). Indeed, each droplet is fully isolated from the adjacent droplets by liquid-solid (PDMS walls), liquid-liquid (the FC oil) and liquid-gas (the narrow restriction) interfaces, all of which act as barriers between droplets. This physical isolation ensures that the content of each droplet is fully intact from direct contact with other droplets.

To be able to monitor cell behaviour over time, one needs to be able to precisely locate them. Although marking of the chip near each droplet's location is possible, it is not applicable since the sizes of the chip/chambers are too small. To address this issue, numbers were embedded near each trap (Fig 6.1C)[115]. This way, if for example a cell in trap E17 (Fig. 6.1C) is of interest, it can easily be found and tracked over time.

One of the issues with the current static droplet systems is that they need to produce droplets first and only then trap them in predefined positions. Syncing the number of droplets generated using active systems with the number of available traps is sometimes problematic and needs precise adjustments[226]. The device presented here is capable of simultaneously making droplets and allocating them to traps using only a single pipette injection. Furthermore, one can easily increase the number of traps using a serpentine structure. Using this method, chips with 5 rows of 100 traps (total number of 500 traps) were designed to accommodate as many single cells as possible.

The static droplet system can be permanently or temporarily bonded to a substrate of choice. The case of temporary bonding is a favoured method since it reduces fabrication cost and time. In addition, it can potentially offer the capability to have access to the cultured cells following device peel off. However, temporary sealing of the device may

lead to leakage due to enhanced loading pressure and therefore should be carefully assessed.

Design considerations

In order to be able to design a functional static droplet device and predict the traps filling behavior, the physics of the flow in the channel, as well as its relationship with the geometry of the traps and channel dimensions, should be carefully considered.

Fig. 6.3A presents the geometry of a trap and the corresponding channel width in different locations. In order to ensure that the liquid first enters the trap and only after the trap is fully filled the liquid continues to fill the main channel, it is essential to have $w_{entr.} > w_{channel}$; In this design these values are $100\ \mu\text{m}$ and $70\ \mu\text{m}$ respectively.

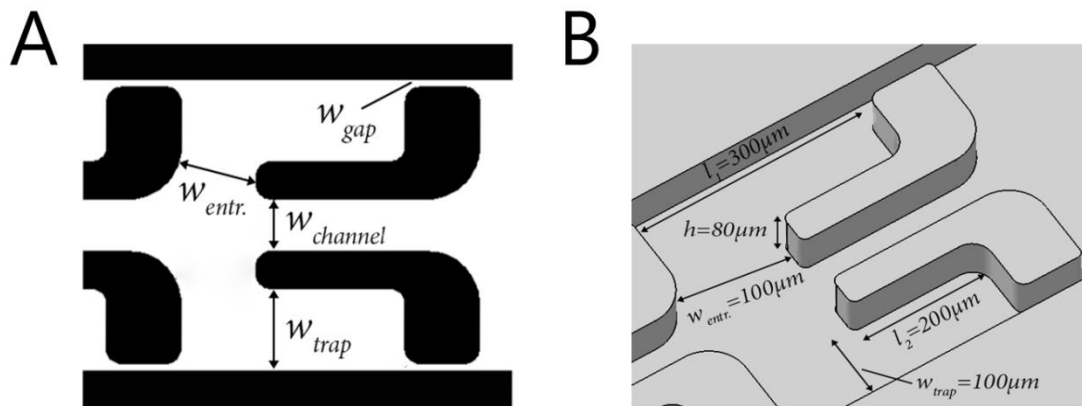


Figure 6.3: (A) Critical dimensions in the static droplet array device (B) Dimensions in the L-shaped traps design.

In order for the flow to move or stop at certain points of its travel into the system, it is crucial to adjust the channel size. In the design, it is ensured that the burst pressure in the main channel is low enough to let the liquid pass with a wide range of filling pressures and is high enough in the restriction to stop the liquid from further movement ($w_{channel} = 70\ \mu\text{m}$ vs $w_{gap} = 10\ \mu\text{m}$). For the device to work, it is crucial that the liquid sample first

fill the trap and then the channel. Therefore, another design point was ($w_{trap} > w_{channel}$). The device dimensions are shown in Fig. 6.3B.

AutoCAD design

Before proceeding with the photolithography, a photomask of the device design was fabricated. The design of the photomask has been implemented in AutoCAD software (Fig. 6.4A). The static droplet array system is composed of repetitive trapping units (Fig. 6.4D). Therefore, first the geometry of the trap including the channel's wall and the trap's wall was drafted following design considerations. In order to use the space for having more number of traps per area, a mirrored image of the trap design was produced. Therefore, each channel of the design has a symmetrical design with two identical traps at the sides of the channel (Fig. 6.4B). A critical design point is the serpentine structure of the channel (Fig. 6.4C). The reason behind this design is to accommodate as much trap as possible and increase the trap density for high throughput assays. The size of the main channel is chosen according to the design considerations to let the liquid-air interface moving in the channel while filling each trap. Each trap in the AutoCAD design has a number close to it (Fig. 6.4B). These numbers help finding each trap easier under the microscope. A standard 4-inch diameter circle was used to include the device designs. The design of the photomask has some parts with irregular shapes (photomask islands) (Fig. 6.4C). The reason these islands are made is to be able to reduce the area coated with chrome which consequently facilitates the process of chrome layer lift off.

In order to investigate the effect of geometry on device operation, two different device designs were included in the AutoCAD file. One with a bigger trap size and a hexagonal structure and the other one is an L-shaped trap with smaller size (Fig. 6.4B). To ensure that there is enough nutrients for single cells to grow in each trap, cell culture surface,

volume and their ratio were calculated in each design. For device A (2.5nl traps), these values are $3.3 \times 10^{-4} \text{ cm}^2$, 2.5 nl, and 12.5 respectively. For device B (14nl traps) these values are $1.79 \times 10^{-3} \text{ cm}^2$, 14 nl and 12.5 respectively. For both designs, the surface to volume ratio is within the recommended range suggested by Halldorsson et al⁶² for effective cell growth and survival.

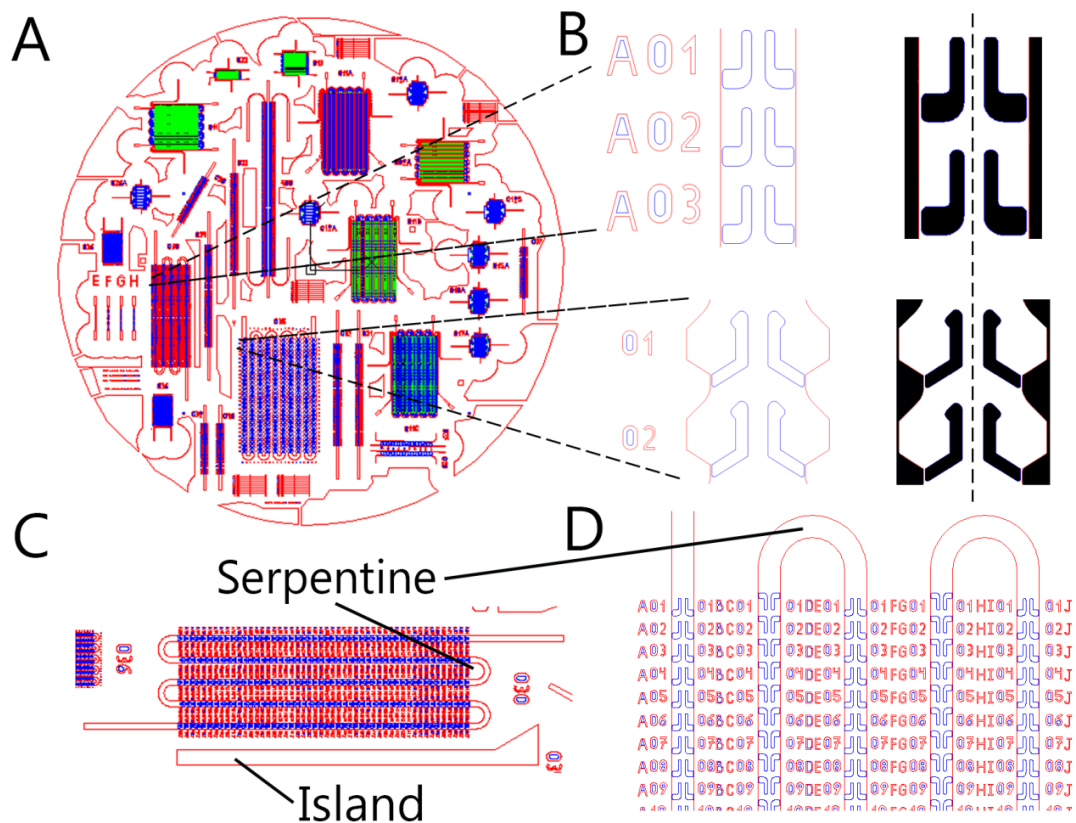


Figure 6.4: Designing the photomask of the static droplet array in AutoCAD software: (A) The photomask design is a 10 inch circle containing different chip designs. Different variations of the patterning device was positioned on a mask to investigate the effect of geometry on device operation (B) Two different geometries of the traps were designed namely the L-shaped device and the hexagonal device. The design is symmetrical. (C) The device has a serpentine structure and each device is separated from the nearby device with an island structure (D) The device design is a repetition of a pair of traps with corresponding numbers.

Fig. 6.5 demonstrates some of the critical dimensions of the static droplet array system. The total volumes of the devices are 2.9652 μl and 16.7545 μl for device A and B respectively. This volume is important when the amount of sample is low (e.g. primary samples). The devices introduced here can be used to trap the cell sample with minimal

waste simply by adjusting the volume of the filling sample to be close to the total volume of the device. The size of each trap plays an important role in trapping single cells. The bigger the trap, the bigger will be the amount of available media for a single cell and the lower will be the required concentration of the cell sample for having single cell trap occupancy. Fig. 6.5A demonstrates the dimensions of traps in both devices. The distance between two neighbouring traps determines whether the liquid segmentation can occur or not. The general rule is that the distance should be small enough to let formation of the droplets and big enough to let the liquid sample fill the trap before filling the main channel. An important design point of the presented device is that the inlet and outlet holes should be far enough from the trapping array (Fig. 6.5B). This design point has two purposes: First reducing the probability of cell clogging. Second, if the traps are placed close to the inlet and outlet, the possibility of droplet evaporation will be increased.

The total area occupied by each chip is shown in Fig. 6.5B. As expected, the array density is much higher in the device with smaller traps, however, it should be mentioned that bigger traps provide a better culture environment for long-term cell culture.

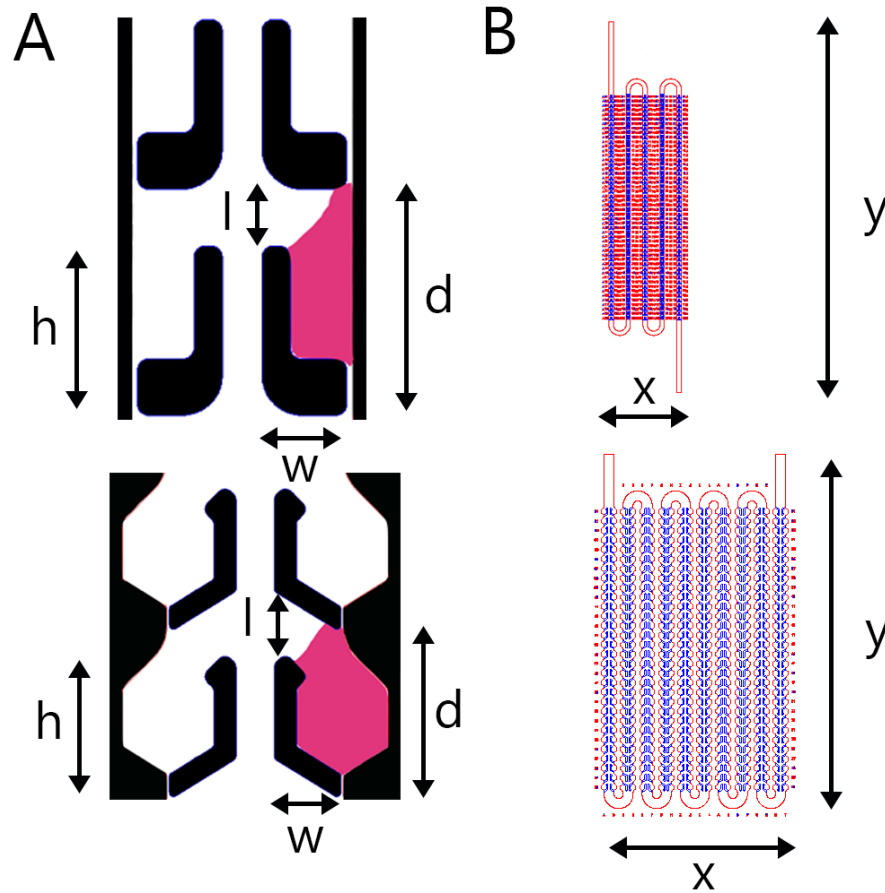


Figure 6.5: (A) Schematic illustration of the geometrical parameters of each trap in which $w=150\mu\text{m}$, $h=300\mu\text{m}$, $l=100\mu\text{m}$, $d=400\mu\text{m}$ for device A and $w=300\mu\text{m}$, $h=620\mu\text{m}$, $l=300\mu\text{m}$, $d=750\mu\text{m}$ for device B. (B) Device dimensions, $x=6.39\text{mm}$, $y=32.8\text{mm}$ for device A and $x=14.29\text{mm}$, $y=27.85\text{mm}$ for device B.

6.2.2. Photomask

The photomask was printed on glass at ANFF University of Sydney. Glass was chosen since the minimal feature size in the designs was $5\mu\text{m}$ which is difficult to be printed on soda-lime or plastic materials. The glass mask provides the highest resolution which is required for defect-free operation of the device and operation of the narrow air gaps at the end of each trap. The bright field polarity was chosen with the negative photoresist. Therefore, areas exposed to UV light were hardened during the exposure. The dark areas in the mask include the area of the channel that will be occupied with either sample or

air. Fig. 6.6A demonstrates the dark and transparent parts on the mask and Fig. 6.6B demonstrates the actual glass mask used for the fabrication process.

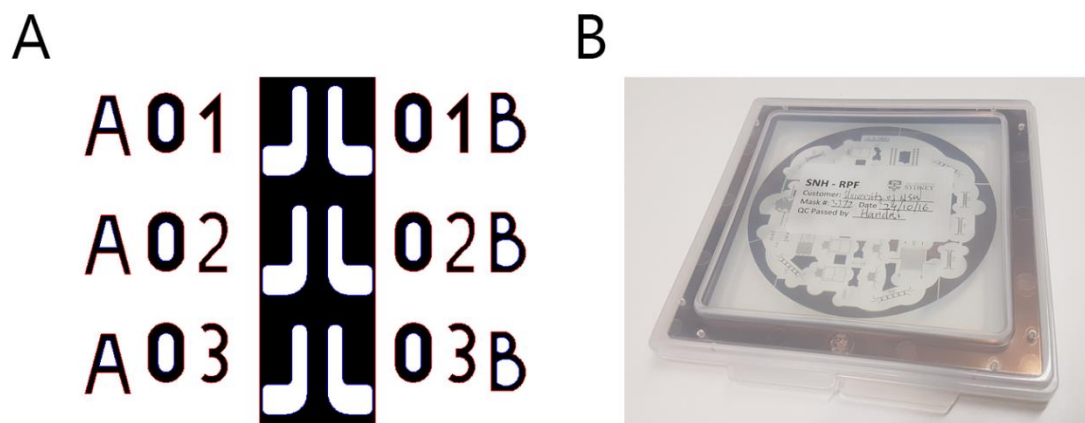


Figure 6.6: (A) Area of the chip design that needs to be dark for fabricating the devices (B) The fabricated mask is a bright-field mask with the dark region made out of chrome.

6.2.2. Device fabrication

Photolithography on standard 4-inch silicon wafer was used to fabricate the mould for PDMS casting. SU-8 permanent epoxy negative photoresist (Microchem, Westborough, MA, USA) was used to coat the silicon wafer. This photoresist can provide film thickness of $0.5\mu\text{m}$ to $200\mu\text{m}$ which makes it a suitable choice for microfluidic applications. In addition, this photoresist can be used for high aspect ratio features and can be dried quickly. The process of fabrication has been performed at the ANFF-NSW cleanroom facility at UNSW. The fabrication steps are provided in Appendix F.

The static droplet array can be fabricated either by bonding the chip to a substrate such as glass/PDMS or by temporarily bonding against a substrate of choice. The latter can be used to have access to single cells following the assay by simple device peel off. However, as mentioned in the previous chapters (chapter 4 and 5), this method required delicate control of the device filling pressure. In fact, the experiments showed that devices made out of photolithography on silicon wafer lead to significant leakage of the sample from

the gap between the chip and the substrate. Fig. 6.7 demonstrates the device fabricated on silicon wafer, the range of filling pressure range in the device made from photolithography on silicon wafer and the leakage which takes place even at low pressures.

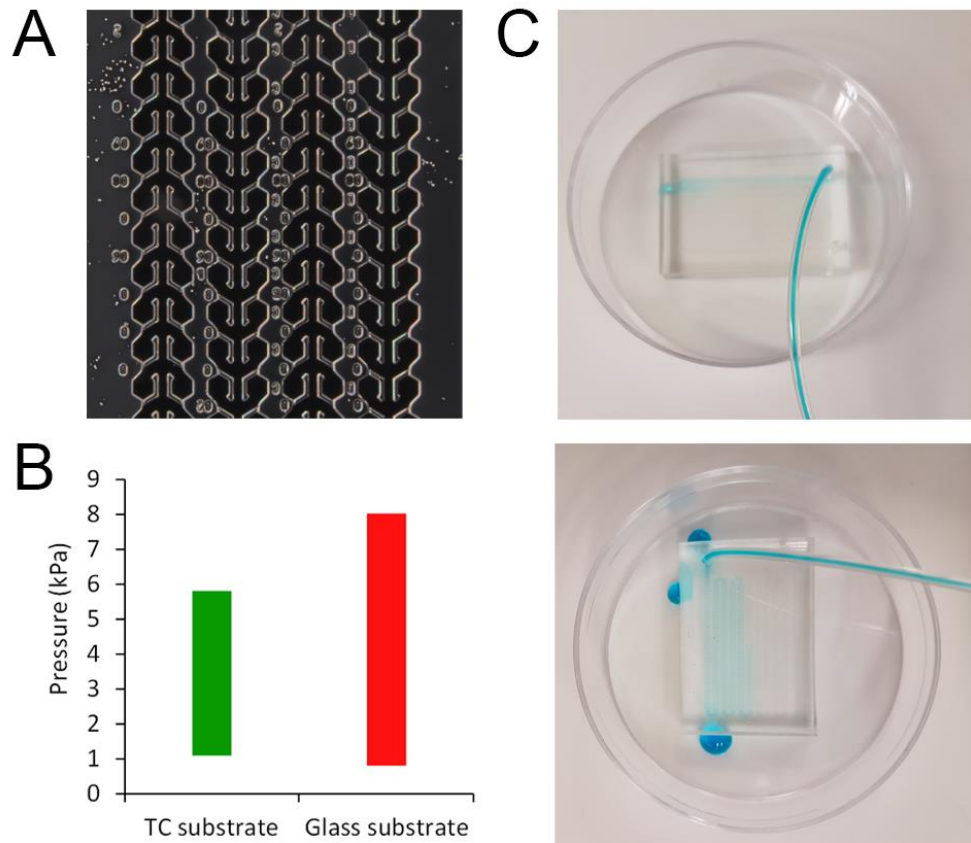


Figure 6.7: Static droplet array device made out of silicon wafer: (A) Micrograph showing the device with the gaps between the traps and the wall is filled causing due to fabrication defects. (B) Range of chip operating pressures of the device for two different substrates (C) Leakage under the chip.

In order to address this issue, Photolithography on SOI wafer was performed. Briefly, deep Reactive Ion Etching (DRIE) on silicon on insulator (SOI) wafer was employed to achieve aspect ratios as high as 1:8. The mask was used to make patterns on a SOI wafer (100mm wafer diameter, $80 \pm 1 \mu\text{m}$ device layer, $2 \mu\text{m}$ buried oxide layer, and $500 \pm 15 \mu\text{m}$ handle layer) coated with SU-8 photoresist using a Karl Suss MA6 Mask Aligner (SUSS MicroTec, Germany) followed by DRIE using a STS system. Fig. 6.8 presents the device

fabricated on SOI wafer and out of PDMS. As can be seen the sharpness and accuracy of the fabrication is significantly improved.

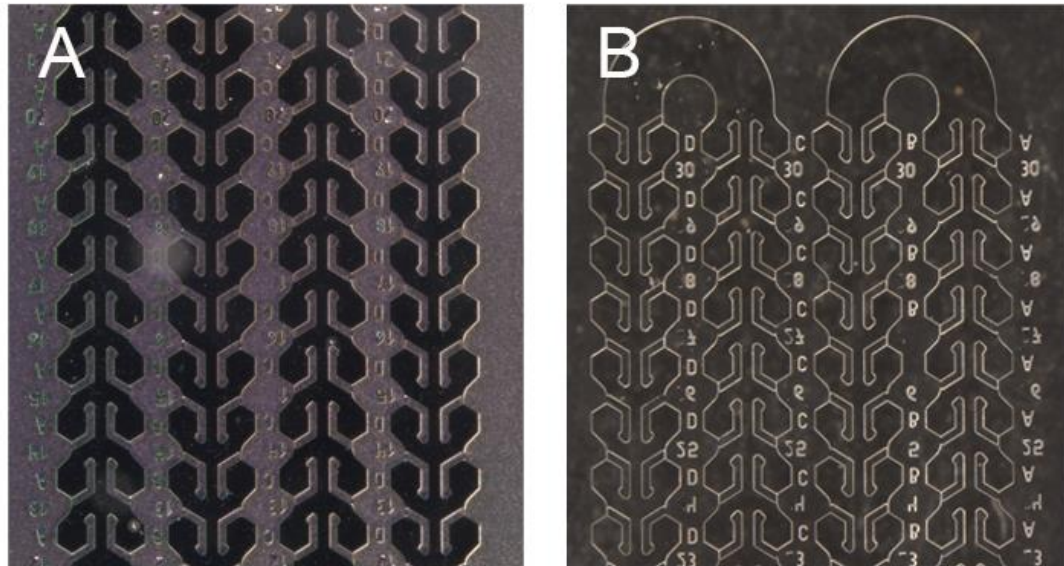


Figure 6.8: Microscope images showing (A) the device pattern on the SOI wafer and (B) after fabrication out of PDMS.

PDMS soft lithography on SOI moulds

The general process of soft lithography and making PDMS devices has been explained in detail in another section (chapter 4- section 4.2.2). Here several points and challenges encountered specifically for fabrication of static droplet system are being discussed.

Since the static droplet array system contains hundreds of small features packed close to each other, pouring PDMS on the wafer leads to the formation of many bubbles especially near the air traps region (Fig. 6.9). Therefore, it was important to make sure that all these bubbles were removed during degassing PDMS on the wafer. This means that degassing this wafer took more than normal.

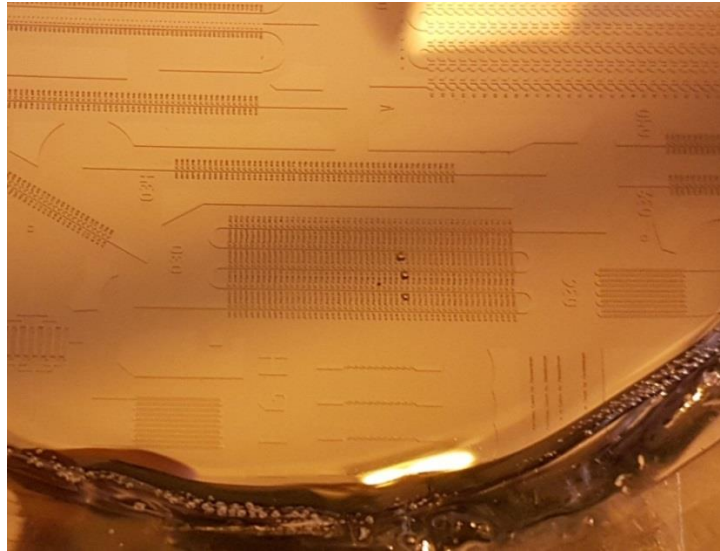


Figure 6.9: Bubbles trapped in the static trapping system during the soft lithography process.

Removing hardened PDMS from the SOI wafer containing the static droplet array device needed to be done carefully and smoothly. The packed array causes a big lift off resistance. As shown in Fig. 6.10 careless removal of PDMS can lead to blockage of some of the air gaps as the PDMS sticks to the wafer and cannot be removed.

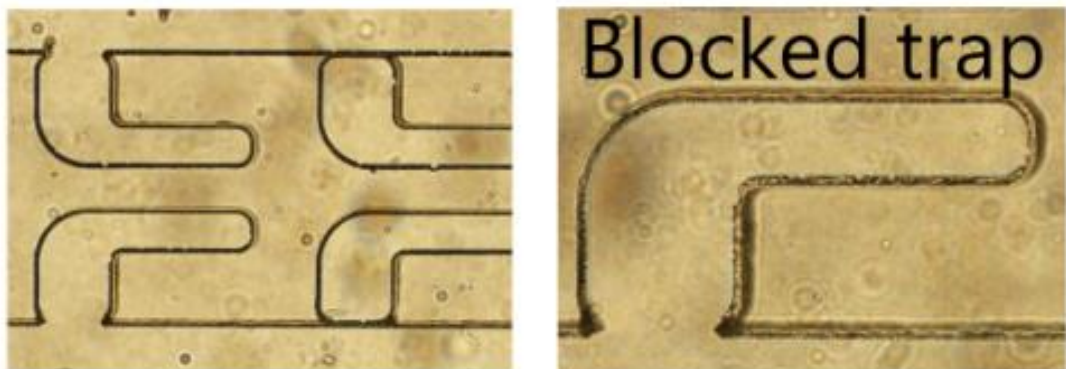


Figure 6.10: Fabrication defect due to rapid PDMS demolding leads to blocked traps impairing the device operation.

The observations showed that high PDMS curing temperatures and high peeling pressures will lead to excessive stress on the SOI wafer which will break the wafer along the stress lines (Fig. 6.11).

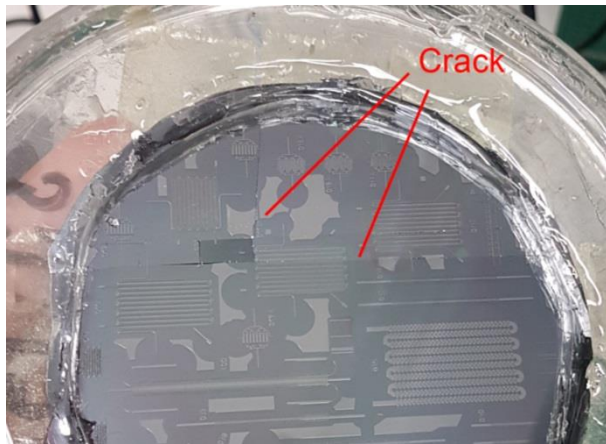


Figure 6.11: Cracks on the surface of the SOI wafer which is caused either due to thermal stress induced by frequent change in temperature between the oven and room or physical stress during the PDMS de-moulding.

Plasma Bonding

Plasma bonding is a process by which the PDMS substrate and the bonding substrate are treated with oxygen plasma which removes organic and hydrocarbon materials through bombardment with oxygen ions. This leads to formation of silanol (SiOH) groups on both surfaces which renders the surface hydrophilic. When two surfaces are brought in contact, strong Si-O-Si bond will be created at the interface of the two surfaces. Fig. 6.12 demonstrates the process as well as the components of the oxygen plasma machine.

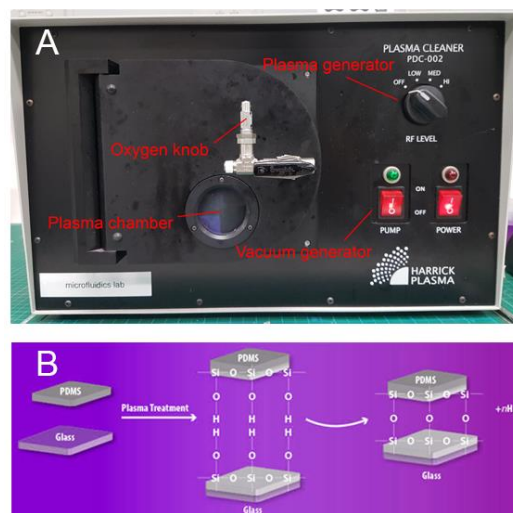


Figure 6.12: (A) Components of the oxygen plasma machine and (B) The chemistry behind plasma bonding.

In order to permanently bond the devices with coverslip substrates, first both the coverslip and the PDMS chip were cleaned using sticky tapes. Next both devices were put in the oxygen plasma machine with their surfaces facing up. The plasma machine was first turned on for 6 minutes to make vacuum inside the plasma chamber. Next, plasma was formed by opening the knob which lets oxygen to move into the chamber in which it was ionized for an optimized period of 3 minutes and 40 seconds. At the end, the plasma was released by opening the gauge. Both the device and coverslip were removed from the chamber and immediately pressed together to make permanent bond (Fig. 6.13). The bonded chips were then placed in an oven for 3 hours before use.

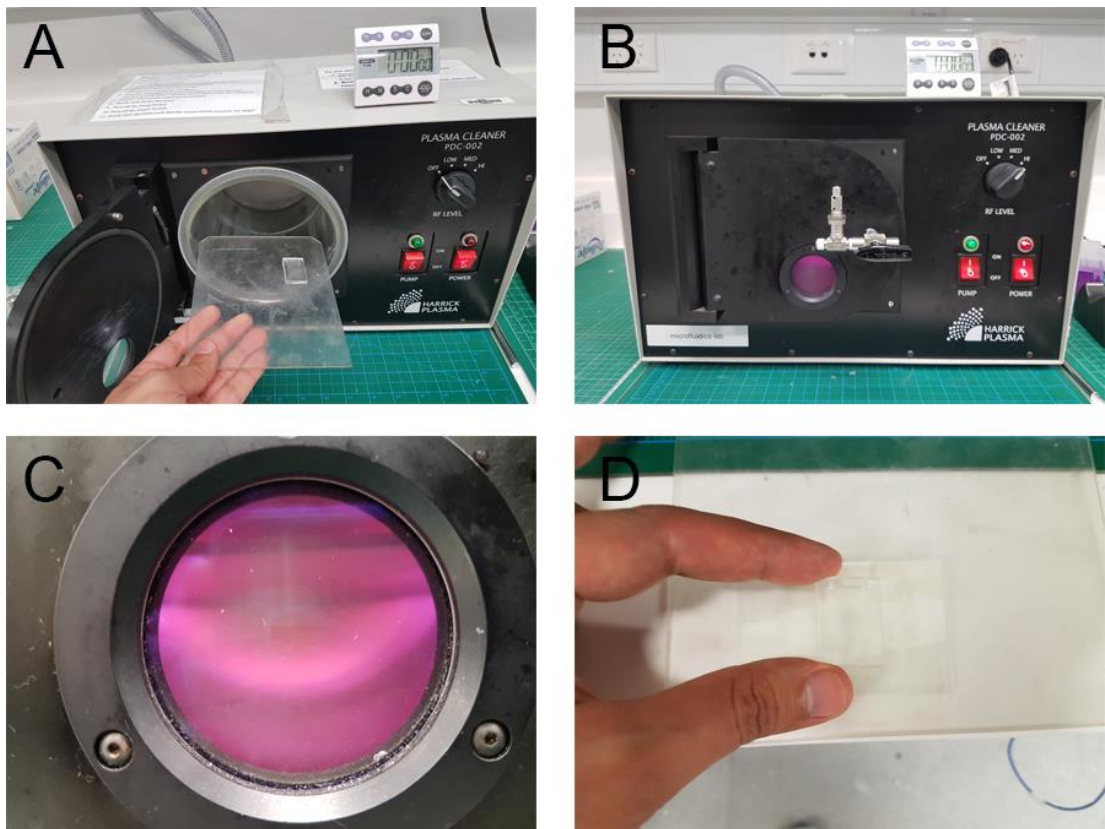


Figure 6.13: The process of permanent bonding of the PDMS chips to coverslips: (A) PDMS chip and the glass slides were cleaned and mounted on the quartz platform facing up, (B, C) plasma formation in the chamber, (D) device and glass slide were removed out of the chamber and pressed together immediately to make permanent bond.

Device preparation

The devices were used in both permanent bonded and temporary sealed modes. For the bonded devices, the channels were flushed with 100 % and 80% ethanol for 20 minutes and rinsed with water before use. For the PDMS slabs with no bonding, the device was soaked in 100% and 80% ethanol for 20 minutes on a laboratory shaker followed by rinsing before use. For both cases, the device was kept under the hood with UV lamps on for 1 hour before the experiments.

6.2.3. Device operation

The static droplet system operates in four steps, as shown in Fig 6.14. A cell suspension is injected into the device using a standard lab pipette/syringe pump. The solution flows and fills both the channel and the traps. When a solution fills one pair of counter traps, the liquid/air interface reaches the narrow restriction which exhausts air while limiting further progress of the liquid. This is due to the opposing surface tension force which is imposed by Laplace pressure at the liquid-gas meniscus (Fig. 6.14-II). When the flow of solution fills the second pair of counter traps, it again pushes air out through the restriction site but simultaneously helps in shaping the air plug between the two adjacent trapping pairs. Following rapid cell sedimentation, the solution in the middle of the channel is blown with air using a standard lab pipette which shears the liquid and leads to the formation of liquid compartments (Fig 6.14-III).

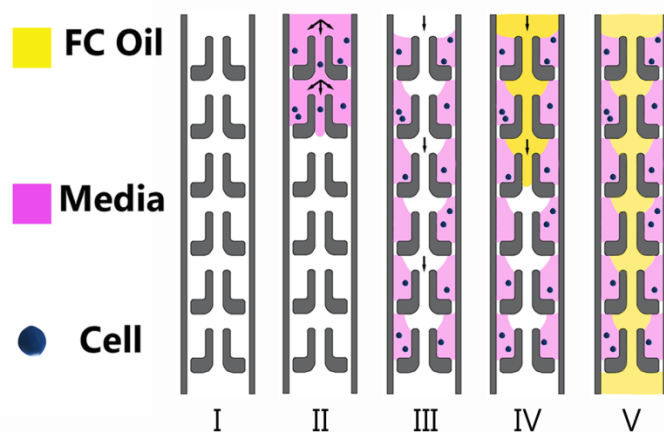


Figure 6.14: Device loading steps: (I) Empty device (II) Cell-containing medium is injected into the channel (III) air pressure shears the continuous liquid into separate semi-droplets (IV and V) Fluorocarbon oil is introduced at the inlet and flows to sheath the stationary semi-droplets.

The residue is collected with sterile filter papers at the outlet. Finally, fluorocarbon oil (Fluorinert FC40) is added to the channel and fills the middle part of the channel (Figure 6.15). Fluorocarbon oil plays two important roles: 1) it prevents extensive evaporation of the nanolitre-sized semi-droplets; 2) it enhances oxygen and CO₂ transfer to/out from the cells.

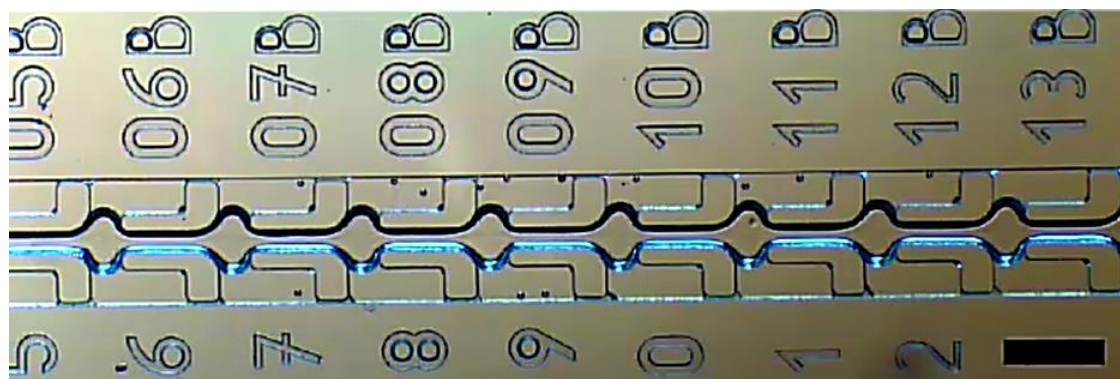


Figure 6.15: Formation of static droplets in SDA device; Particles are trapped in separate chambers, Scale bar=300 μ m.

Fig. 6.16 provides a closer look into the relation between the device geometry and its operation using a green food color liquid sample. As can be seen in Fig. 6.16A, each L-shaped trap is positioned at a distance of 10 μ m from the channel walls forming a narrow air gap. When liquid fills the channels and the traps, the liquid cannot pass these air gaps.

This is clearly shown in the magnified image in Fig. 6.16A in which the air gap is surrounded by the liquid sample on both sides. Fig. 6.16B demonstrates the moment at which the liquid sample is filling the next pair of traps leading to formation of air gaps and droplets isolation. The presence of the narrow restriction is essential in the process of droplet trapping. If the restriction gets blocked (e.g. due to fabrication defect) the liquid cannot move into the traps (Fig. 6.16C). When the liquid tries to fill the blocked the trap, the pressure is built up in the trap preventing the liquid to further move. While the presence of these blocked traps is not affecting the liquid trapping in the other traps, the formation of big bubbles can be extended in the device and transfer the liquid in the whole system.

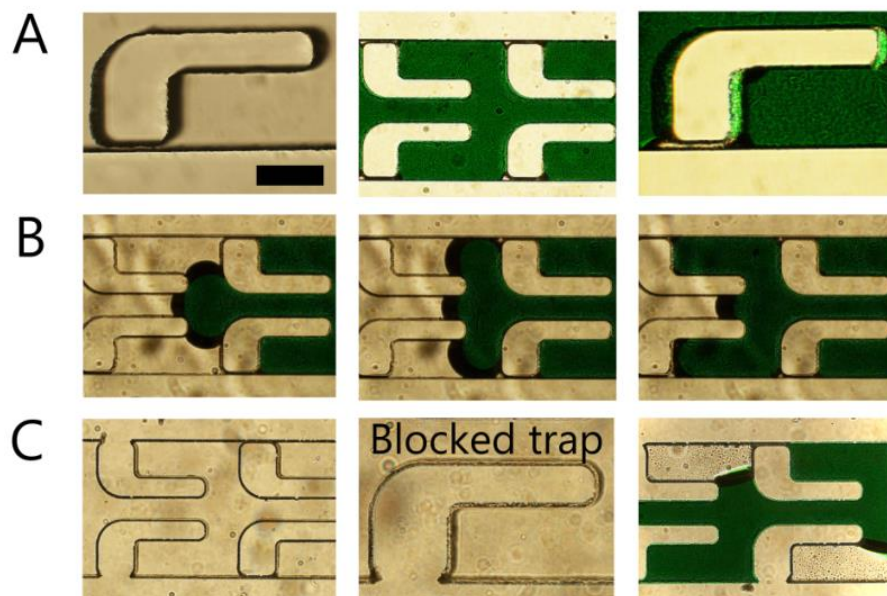


Figure 6.16: A) The geometry of the narrow restriction, B) image sequence showing the liquid-air interface movement in the trap during the sample injection, C) liquid-air interface when moving towards a defective trap with blocked restriction at its end (Scale bar=100 μ m).

Operation set up

The device can be operated in several ways which depends on the type of the assay and availability of resources. The aim during the device operation is to: successfully inject the sample into the channel, use minimum sample volume and achieve high injection

efficiency, trap single cells as much as possible, provide leakage-free operation, observe droplet formation, maintain droplets for longer periods.

Method 1: Syringe pump

The sample can be injected into the device using the syringe pump. In this method, the device should be permanently bonded to the substrate (i.e. coverslip) to avoid sample leakage either during the experiment or when adjusting the inlet and outlet tubing. The set up for this method is shown in Fig. 6.17.

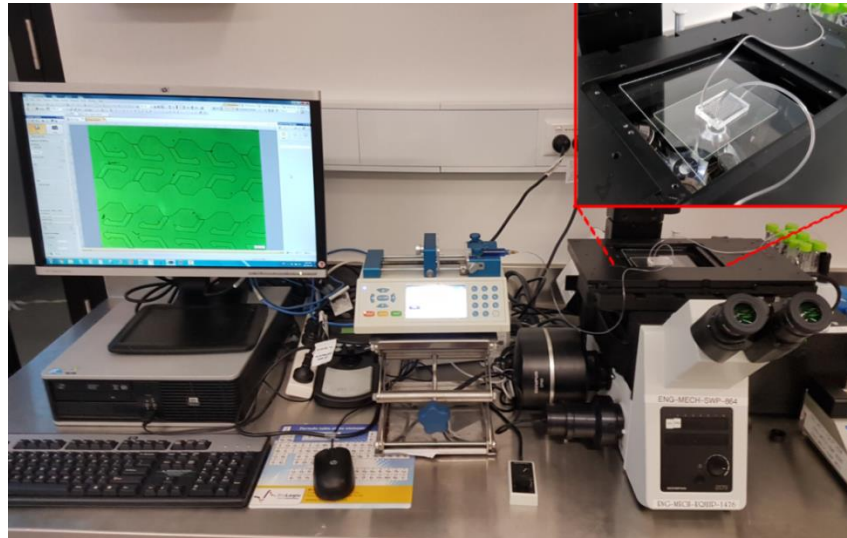


Figure 6.17: Experimental set up of fluidic experiment using syringe pump.

As shown in Fig.6.18, the syringe containing the liquid sample is mounted on a Fusion-720 syringe pump (Chemyx, Stafford, TX, USA) and is connected to the inlet of the device using 1/32" (OD- outer diameter) tubing. The outlet of the device is connected to an empty falcon tube to collect any residual liquid. On the syringe pump, the flow rate can be adjusted by choosing the standard syringe used for the experiment (in this case 5ml BD plastic) and setting the flow rate (Fig. 6.18). The syringe is filled with liquid sample, fixed with pump fixture and is connected to a moving plate that is pushing the syringe when the pump is working.

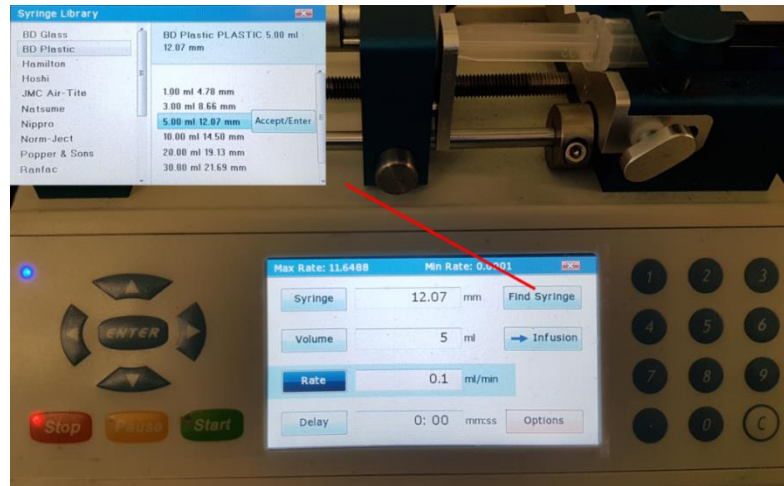


Figure 6.18: Setting up the syringe pump for injecting sample into the static droplet system at constant flow rate.

There are a number of issues associated with this method of operation. First the amount of liquid sample needed for the syringe pump is much higher than the device volume. In case of cells, the volume of the sample is much lower to be operated with a syringe pump. Even if the amount of cell sample is sufficient, most of the sample will be lost. The second issue with this method is the mechanism of operation which is based on flow rate rather than the pressure. Indeed, controlling the filling pressure plays an important role in successful droplet formation in the device as droplet formation is based on the balance between the filling pressure and the capillary pressure. A positive point about this method is the use of the microscope which allows viewing the process and understanding possible problems which may take place during the sample loading/shearing.

Method 2: Pipette injection

Regardless of the state of bonding between the PDMS chip and the substrate, using a pipette to inject the sample into the channels is the simplest and most cost-effective way of device operation. This has been successfully achieved in three ways. In the first method (Fig. 6.19), 5 μ l of the liquid sample was taken, the pipette was then pushed into the inlet hole and the sample was injected by gently pressing the pipette. Once the liquid filled all of the traps, the pipette was carefully removed from the inlet. In the second step and to

form the droplets, a pipette with no sample was set to high sample intake, placed on the device inlet. The air was pushed into the channel by reducing the number on the pipette. The air is blowing the liquid in the main channels and forms the droplets. The residual sample was then collected from the outlet.

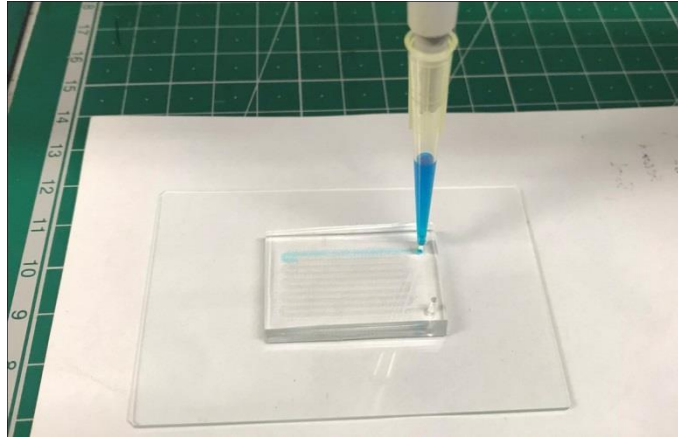


Figure 6.19: Device operation with pipette injection

In the second method with pipette, 5 μ l of the liquid sample was placed in the inlet of the device. Next a pipette with no sample was placed in the outlet and the number on the pipette was increased to suck the liquid from the inlet. This method can be used to both fill the channel and form the droplets (Fig. 6.20).

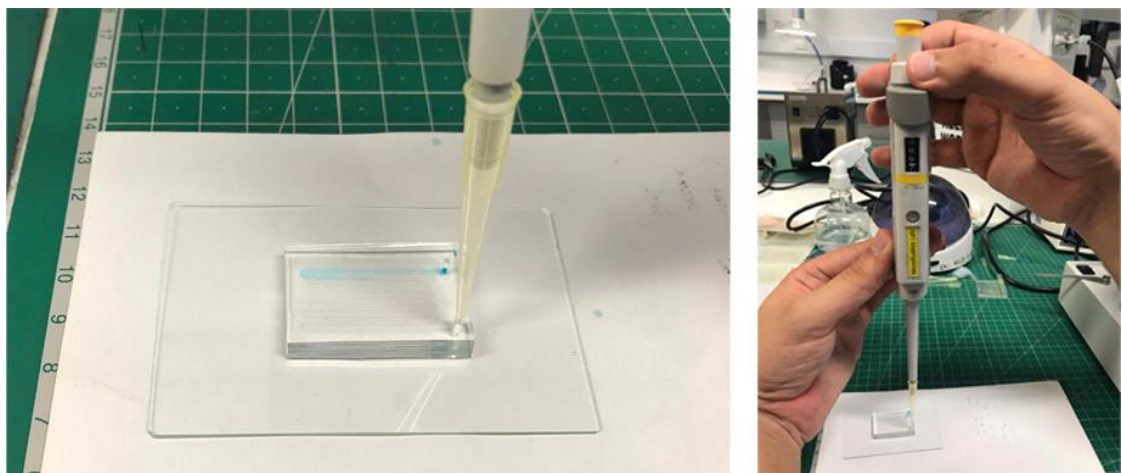


Figure 6.20: Device operation with pipette suction

Finally, in an alternative approach, the device was first placed in the degassing chamber for 20 minutes. Once the device was removed from the chamber a drop of sample was placed on top of the inlet. The pressure difference between the inlet and outlet led the drop to fill the channel.

Bubble generation

One of the major issues associated with the static droplet system is the formation of bubbles in the array which eventually leads to dislocation of the fluorocarbon oil and the content of each droplet. Fig. 6.21A demonstrates a bubble that has occupied the whole volume of a single trap. Since these bubbles can keep high pressures at the interface, they can extend along the array system. Fig. 6.21B demonstrates a sequence of images capturing the growth of a bubble in the system which pushes the oil out of the main channel.

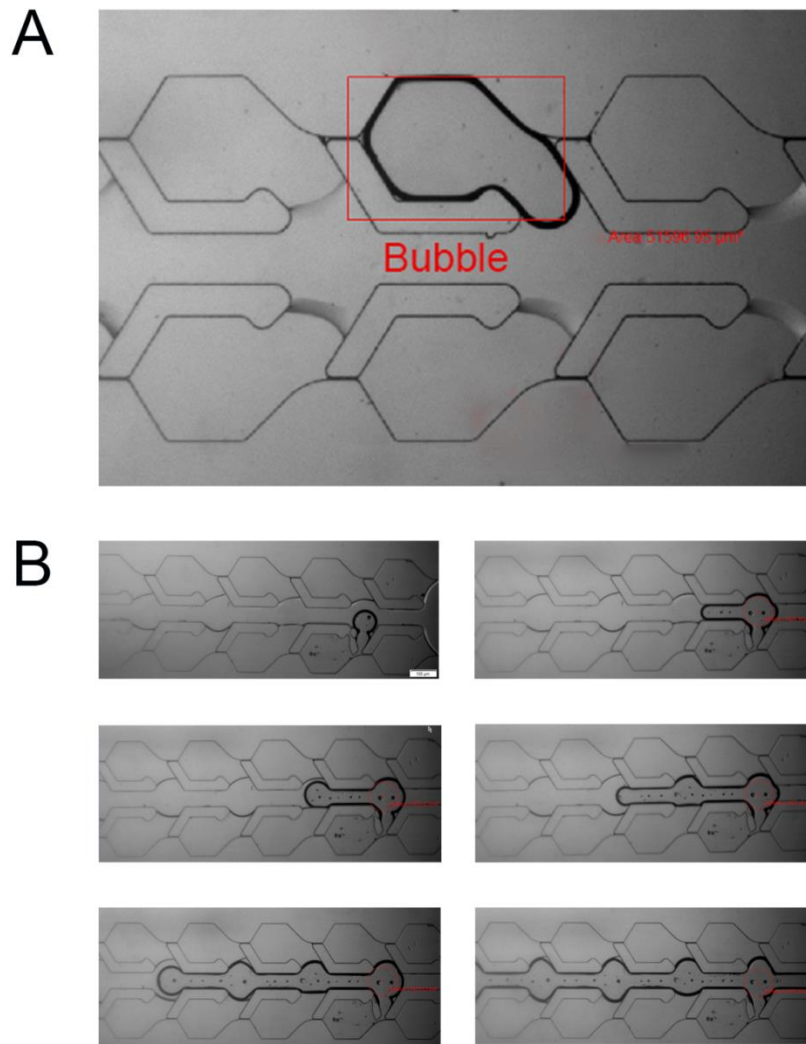


Figure 6.21: Bubble generation in the static droplet array system: (A) A bubble that occupies a trap and is pushing the oil in the main channel, (B) Bubble extension in the system which pushes the FC oil out of the system.

Bubble generation can have a number of sources: The first cause is the geometry of the channel. It is found that when the liquid-air interface reaches a sharp corner, the possibility of liquid detachment from the surface and entrapment of air increases (Fig. 6.22A). The second reason behind the air being trapped in the system is high flow rate. If the liquid sample be injected into the device at higher flow rates, it does not let the existing air enough time to escape (Fig. 6.28B).

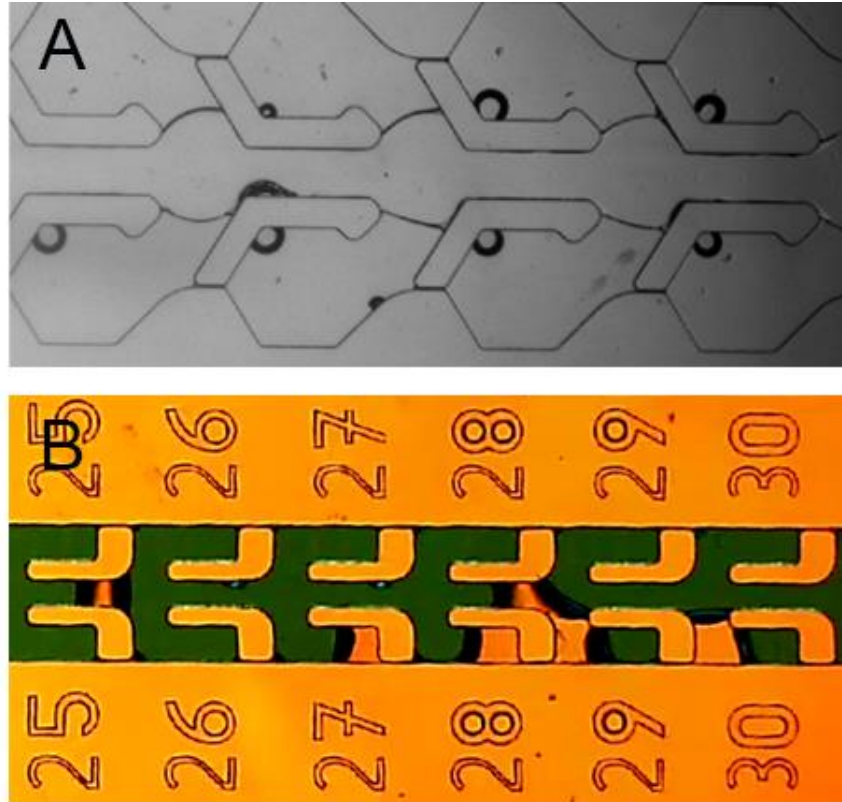


Figure 6.22: Bubble generation in the static droplet array: (A) due to sharp geometry of the trap at the corners, (B) due to high flow rates which prevents the liquid from filling the trap before reaching the next pair of traps.

Each bubble can keep a large amount of pressure inside itself. This pressure depends on the liquid-air interface curvature and can be calculated using the Young-Laplace equation:

$$\Delta P = 4 \frac{\gamma}{r}$$

In which γ is the surface tension (N/m) which is 72 (mN/m) for water-liquid interface at 25°C and r is the bubble radius respectively. r value can change depending on the position in which bubble has been generated. This value of the bubble pressure has been measured during the experiment. Assuming that $r=100\mu\text{m}$, then the pressure difference across the bubble interface will be calculated as,

$$\Delta P = 4 \times 72 \times 10^{-3} \left(\frac{\text{N}}{\text{m}} \right) \times (100 \times 10^{-6})^{-1} = 2.88 \text{ kPa}$$

As can be seen in Fig. 6.22, a typical bubble of 100 μm radius can keep high pressures. This pressure difference across the interface is then pushing the liquid sample back into the main channel and grows along the main channel. This will remove the fluorocarbon oil in the main channel and lead to evaporation of the droplets.

Evaporation

Maintaining the droplets in the static droplet system is a prime challenge due to the small volume of the droplets. The droplets are of 2.5nL or 4 nL size. Evaporation of the droplets can happen at any temperature especially since PDMS is a porous material providing surface contact with air.

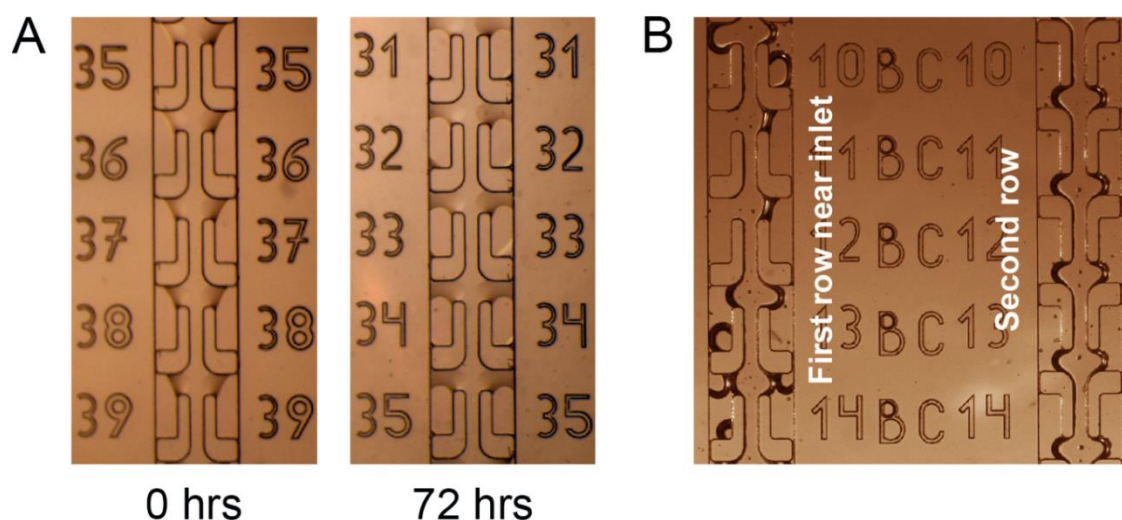


Figure 6.23: Droplet evaporation over time in static droplet array.

Fig. 6.23 demonstrates sample evaporation in the channels. As can be seen here the droplet size decreases over time. In addition, extensive evaporation takes place near the inlet and outlet of the channel as inlets and outlets are the main sources of contact with air at the periphery of the device (Fig. 6.23B). In order to prevent/decrease the droplet evaporation several approaches have been adopted. The first approach was the employment of oil in the main channel. The second approach is soaking the devices in water before using them for the experiments. This way, the pores in the PDMS material

were filled with water blocking the evaporation. Finally, a humidity chamber was tested to investigate the droplet evaporation in the system.

Particle solution preparation

In order to assess the droplet occupancy and obtain an initial evaluation of the trapping efficiency in the devices, different concentrations of particles were made in MACS buffer solution (Miltenyi Biotec, Gladbach, Germany) and injected into the device. Since the size of the cells were between 10 to 20 μm , two sizes of 10.7 μm and 19.2 μm PMMA particles (Magsphere, Pasadena, CA, USA) were used. To make particle solutions with specific concentrations, certain number of particles need to be diluted with MACS buffer (Fig. 6.24). The following parameters are introduced:

C= Number of particles per ml

D= Diameter in microns of the latex particle

ρ = Density of particle in grams per ml (1.05 gr/ml for polystyrene particles)

W= Grams of polymer per ml in latex (0.02 g/ml for 2% solids)

In order to obtain V_2 (ml) of particle with the concentration of C_2 from the stock with concentration of C_1 , the volume of the stock solution required will be:

$$C_1 V_1 = C_2 V_2 \rightarrow V_1 = \frac{C_2 V_2}{C_1} = \frac{C_2 V_2}{\frac{W \left(\frac{\text{gr}}{\text{ml}}\right)}{\rho \left(\frac{\text{gr}}{\text{ml}}\right) \times \frac{1}{6} \pi D^3 (\mu\text{m}^3) \times (10^{-12} \frac{\text{ml}}{\mu\text{m}^3)}}$$

Therefore,

$$V_1 = \frac{C_2 V_2 \times \rho \times \pi \times D^3}{6W \times 10^{12}}$$

In order to make 10ml of 10.7 μ m particles with the concentration of 5 \times 10⁵ particles per ml from the stock solution with 2% solids, the volume of required stock can be calculated as,

$$V_1 = \frac{5 \times 10^5 \times 10(\text{ml}) \times 1.05 \times \pi \times (10.7\mu\text{m})^3}{6 \times 0.02 \times 10^{12}} = \frac{2.0205 \times 10^{10}}{12 \times 10^{10}} = 0.168375 \text{ ml}$$

Therefore 0.168375 ml of the stock solution is diluted in 10 ml MACS buffer solution. The particle stock solution was stirred carefully to make a homogenous solution. In addition, after making the final concentration, the solution was stirred carefully before use.

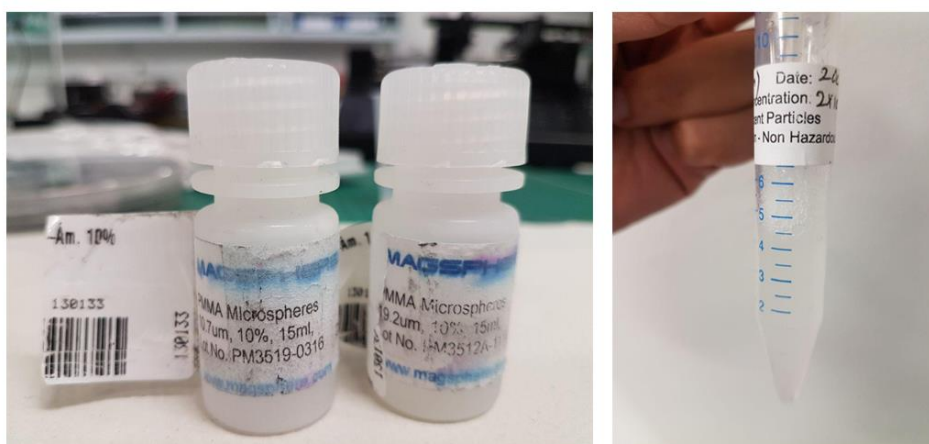


Figure 6.24: PMMA particles stock and diluted solutions used for the trapping assay.

6.2.4. Cell culture

Breast cancer cell line MDA-MB-231(ATCC® HTB-26™) was cultured under standard conditions of 95% humidity and 5% CO₂ in RPMI medium (Gibco, 11875) with 10% FBS, 1% penicillin/streptomycin, and 6% insulin in a T-75 flask and with seeding density of 10⁴ cells/cm² and passaged at 80% confluency (Fig. 6.25B).

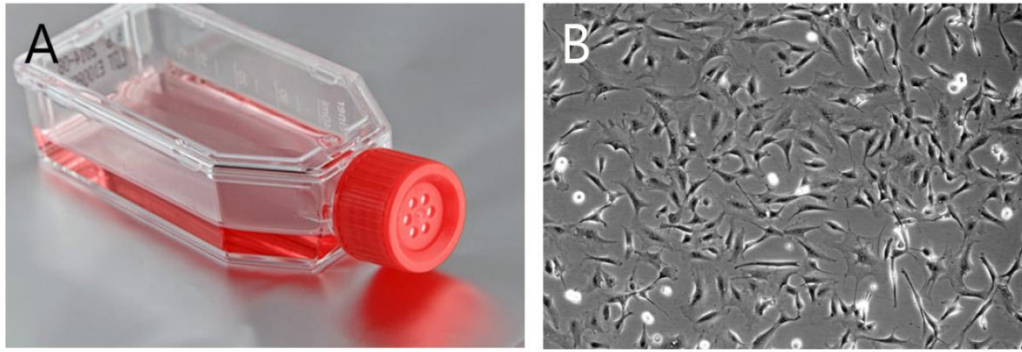


Figure 6.25: (A) Cells cultured in T-75 flask (B) Attached cells under the microscope.

To passage the cells, one confluent flask was first removed, the media was sucked out, and the cell culture surface was washed several times to remove dead cells and small debris. 3ml of Trypsin enzyme was added to the flask to cover the attached cells. The flask was then moved into an incubator and maintained for 6 minutes. Cell detachment was checked under the microscope and if required the flask was hit gently to detach the loosely attached cells. A new flask was filled with 20 ml fresh media, the cell suspension was aspirated to break possible existing cell clumps and 1 ml of the cell suspension was added to the new flask.

6.2.5. Device preparation and set up

Experiments were conducted with pipette injection method and devices were temporarily sealed. Both the devices and the glass slides were sterilized using ethanol wash and UV treatment. The overall set up of the experiment is shown in Fig. 6.26.



Figure 6.26: Experimental set-up of the sample injection under the cell culture hood.

The set-up also required filter papers to absorb sample residual, and a modified humidity chamber. The humidity chamber is designed to reduce droplet evaporation in the system. Sterilized tissue was soaked in water and the devices were put onto the tissues (Fig. 6.27). The whole humidity chamber was then placed in the incubator. The fabricated devices were brought in conformal contact with the substrate and, if necessary, pressed together to create a seal.

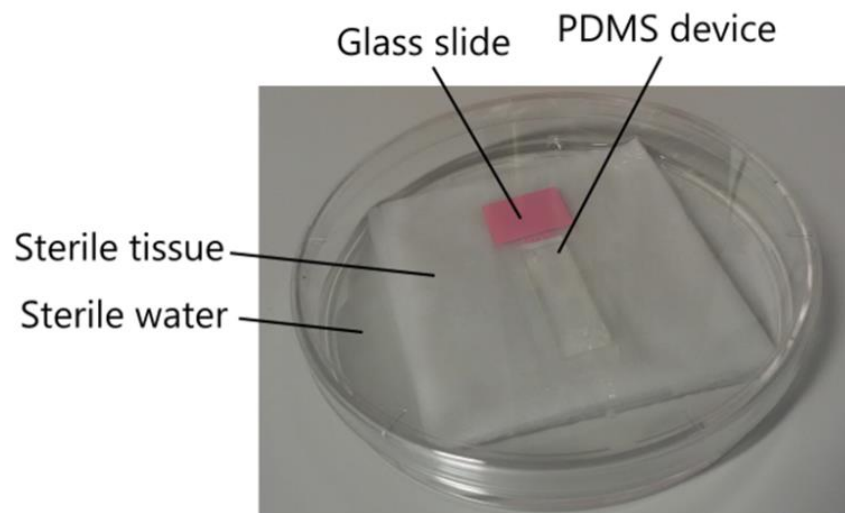


Figure 6.27: Cell culture in the device: Device setup by creating a humidity chamber.

6.2.6. Cell loading and single cell monitoring

To examine the trap occupancy, different cell concentrations were made and tested. One confluent flask of MDA-MB-231 cancer cells was first trypsinized and cells were suspended in appropriate volume of fresh medium. Cells were then counted using countess (Invitrogen) and cell viability of >90% was ensured. Once the cell concentration was achieved, the desired concentration was made by adding appropriate amount of the cell suspension into fresh cell medium. For example, if the cell concentration was 1×10^6 cells per ml, and the desired cell concentration was 2×10^5 cells per ml, 0.2ml of the cell suspension was added to 0.8ml of fresh medium to make 1ml of the desired concentration. For injection into the microfluidic chips, one device was taken with sterile tweezers, sealed against the coverslips and pressed to make a strong bond with the substrate. The cell suspension was mixed well with aspiration using pipette and for each chip 20 μ l (for the device with smaller trap size) and 40 μ l (for the device with bigger trap size) was used. Devices were maintained in a humidity chamber (Fig. 6.27) and were monitored after 6 hours for cell attachment (Fig. 6.28).

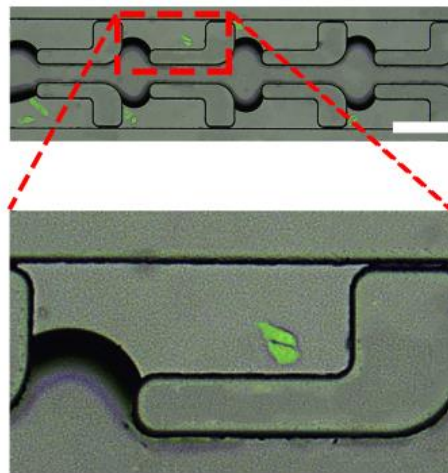


Figure 6.28: Cell attachment to the substrate; here two cells are located just adjacent to each other, Scale bar=200 μ m.

6.2.7. On-chip live/dead staining experiment

Cells were first cultured in the device using pipette injection and incubated for 24 hours. Live/dead double staining kit (Sigma-Aldrich 04511, St. Louis, MO, USA) containing calcein AM and propidium iodide (PI) solutions staining live and dead cells respectively were used. Calcein-AM, is highly lipophilic and can permeate through the cell membrane. It is not a fluorescent molecule, however, the calcein generated from Calcein-AM by esterase in a viable cell generates green fluorescence (excitation: 490 nm, emission: 515 nm). PI can only pass through the membrane of the dead cells and after interaction with the DNA emits red fluorescence (excitation: 535 nm, emission: 617 nm). Since both calcein AM and PI can be excited at 400 nm, the double staining kit can help to image the live and dead cells at the same time. A 4 μ M staining solution was prepared by adding 10 μ l of calcein AM and 5 μ l of PI to 5ml Phosphate-buffered saline (PBS) solution. To stain the cells on chip, 20 μ l of the staining solution was injected into the device and cells were incubated for 1 hr followed by on-chip PBS wash.

6.2.8. Cell viability and proliferation assay

To assess cell viability in the chip, the cell concentration which gives the highest number of single cell traps were used for device loading. Five devices were used for viability measurement at each time points of 12 hrs, 18 hrs, 24 hrs, and 48 hrs (12 experiments in total). At each time point, first a device was removed from the humidity chamber and Trypan blue (Thermofisher, Waltham, MA, USA) was injected into the device. The device was immediately imaged under the microscope. In order to measure proliferation, devices were imaged at three time points of 6 hrs, 24 hrs and 48 hrs. The total number of the cells in the images was counted for each time point.

6.2.9. Matrix metalloproteinase (MMP) assay

Fluorescence resonance energy transfer (FRET)-based polypeptide MMP substrate PEPDAB008 (Biozyme, Apex, NC, USA) can be used to assess activity of enzymes in the MMP family. The excitation and emission wavelengths of this peptide are 485 and 530 nm respectively. The peptide is dissolved in DMSO to make a stock solution of 10 mM concentration. To do this, one vial of the PEPDAB008 substrate containing 1mg was used. The molecular weight of the substrate is 1388.3 g/mol. The amount of DMSO added was then calculated as:

$$C = \frac{n(\text{moles})}{V(\text{liter})} = \frac{\frac{m}{M}}{V} = \frac{m}{M.V} = \frac{1\text{mg}}{1388.3\text{g/mole} \times V(\text{liter})} = 10\text{mM} \rightarrow V(\text{liter}) = \frac{1}{1388.3 \times 10} = 7.2 \times 10^{-5}\text{liter} = 7.2 \times 10^{-2}\text{ml} = 72\mu\text{l}$$

The peptide stock solution was diluted to 40 μM in 50 mM Tris buffer (150mM NaCl, 2mM CaCl_2 , 5 μM ZnSO_4 , and 0.01% Brij-35; PH 7.5). Cell concentration of $7 \times 10^5/\text{ml}$ was prepared and 2.5nl device was used in all experiments. Before injection into the device, cell suspension and MMP substrate were mixed in 1:1 volume ratio. Therefore, the final cell and substrate concentration were $3.5 \times 10^5/\text{ml}$ and 20 μM respectively. Since droplets contain the same concentration of MMP substrate, the amount of fluorescent signal out of each droplet represents the amount of MMP produced by each single cell. Immediately after injection, shearing and sheathing with oil, the device was put under a time-lapse microscope for imaging.

6.2.10. Microscopy

MDA-MB-231 cell distribution, viability and proliferation

For the cell distribution tests, the devices were imaged immediately after injection under a light microscope (Leica DM 4000, Wetzlar, Germany). Imaging of the attached MDA-

MB-231 cells for measuring cell viability was performed using the same microscope (Leica DM 4000).

Fluorescent microscopy

Cell attachment

Following cell attachment on glass substrate after 6 hours in culture, the cells were stained and imaged under Leica DM 5500 fluorescent microscope (Wetzlar, Germany).

On-chip staining

Cells were incubated on-chip for 24 hours after which staining solution was loaded into the main channel of the device. After 1 hour incubation and washing steps, the devices were imaged using Axio Scop.A1 fluorescent microscope (Oberkochen, Germany).

Microscopy for MMP activity of single cancer cells

Leica DMI8 live cell imaging inverted microscope (Figure 6.29) was adjusted to take transmitted and fluorescent images of all semi-droplets by defining the imaging starting point and endpoint. Imaging was performed for a 24-hour time period. The microscope software (LAS X, Leica Microsystems) divided the imaging area into 90 imaging units. Each imaging unit covered 6 semi-droplets. The obtained images were then stitched together by the microscope LAS X software to obtain the final image of the whole device. Four exposure times of 1ms, 200ms, 500ms and 1s were used to make sure that at least one exposure time gives measurable data (Fig. 6.30). Data from the optimum exposure time (500ms) was then used for the data analysis. Fig. 6.31 demonstrates the transmitted, fluorescent and overlapped image of the device at a single time.



Figure 6.29: Leica DMi8 live cell imaging microscope equipped with dedicated incubator and CO₂ and temperature control.

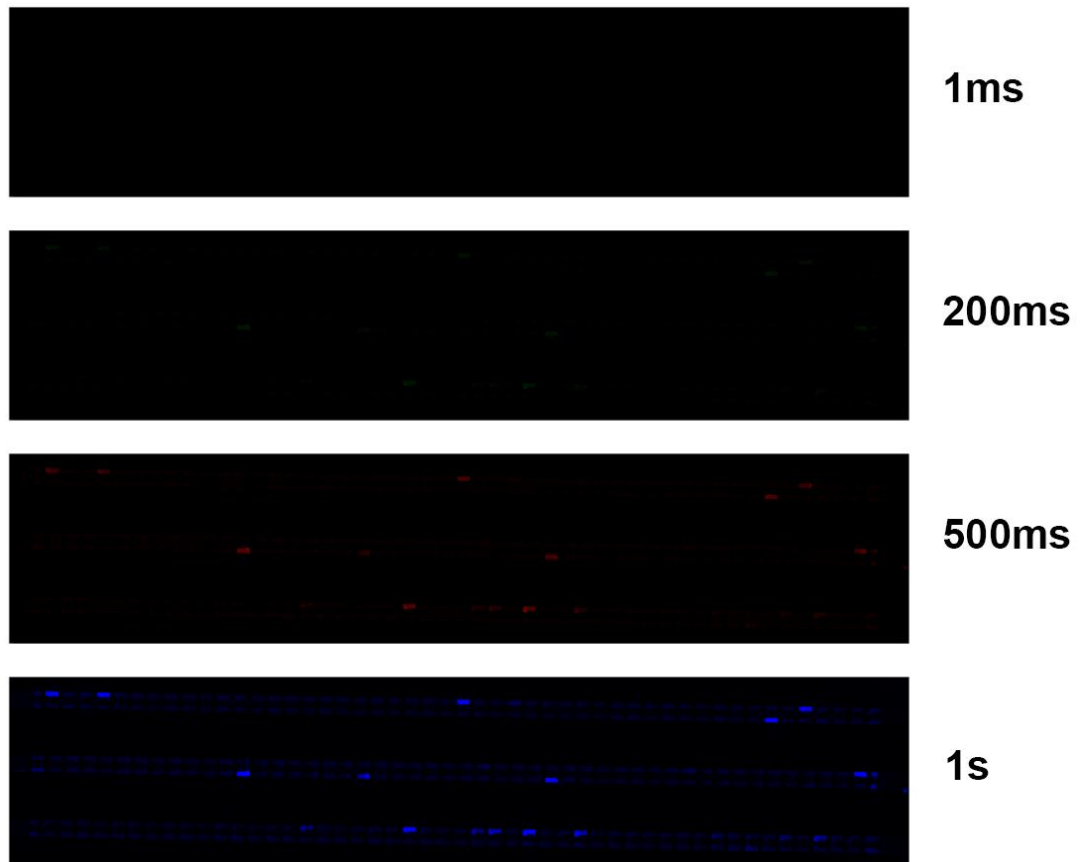


Figure 6.30: Fluorescent image of the MMP activity of single cells in the static droplet array device under different exposure times.

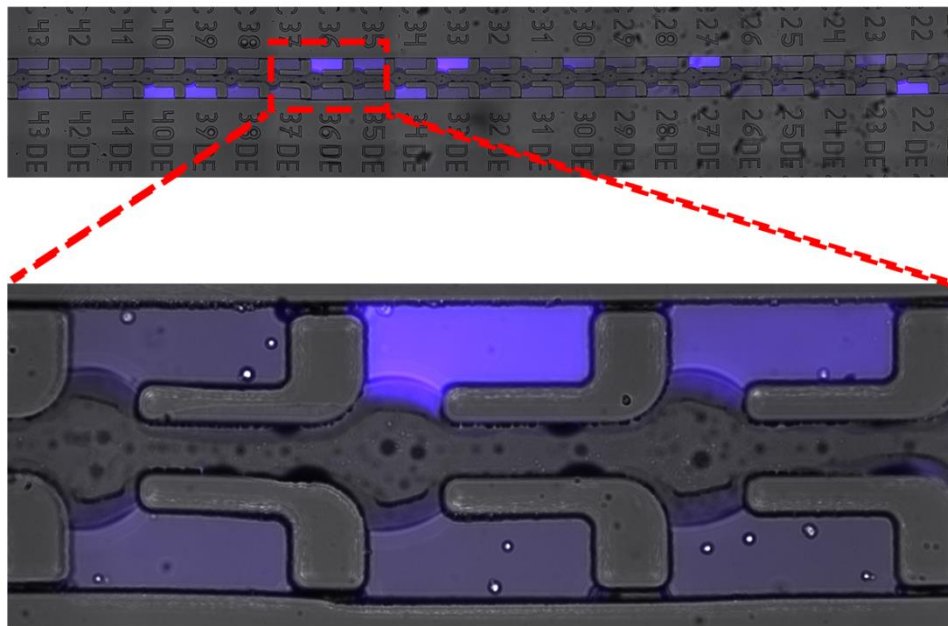


Figure 6.31: Overlapped image of the transmitted and fluorescent microscopy. Magnified image also shows the cells in each droplet.

6.2.11. Image and data analysis

Analysis of distribution, viability and proliferation was done by counting the number of cells in semi-droplets.

To quantify the MMP activity of single MDA-MB-231 cancer cells, fluorescent signals out of each droplet were measured using ImageJ. Since 10 times magnification was used, the device area was divided into 90 image sections. Using LAS X software, the .lif file of the project was separated to folders each containing images of a fixed section over time. On each of the image sequences, the region of interest (ROI) was selected which is the area occupied by each droplet that was defined using the Freehand Selection tool (Fig. 6.32). Then in ROI manager under multi measure, mean grey value was measured for the selected area. Higher fluorescent intensity corresponds to higher enzyme secretion by the cells.

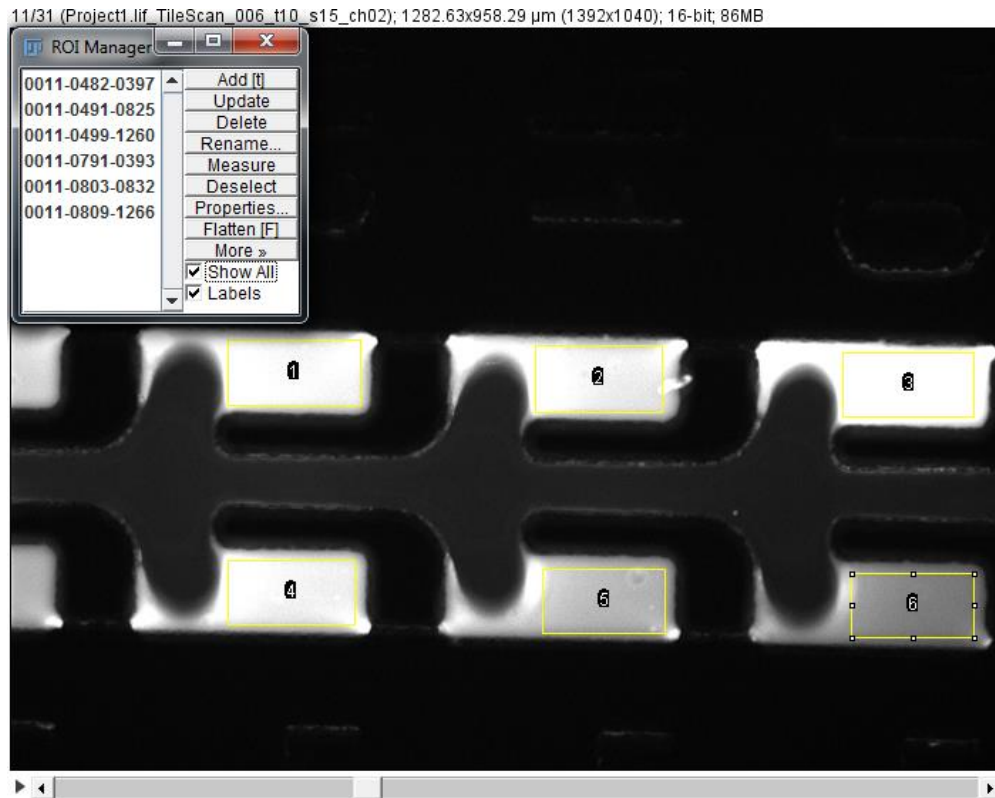


Figure 6.32: Image showing the use of ImageJ for defining ROI and measuring the fluorescent intensity.

6.3. Results and discussion

6.3.1. Device fluidic performance

Capillary pressure opposes the injection pressure, and therefore to make sure that the interface reaches certain locations at certain time points, pressure changes across the liquid-air interface needs to be investigated (Fig. 6.33).

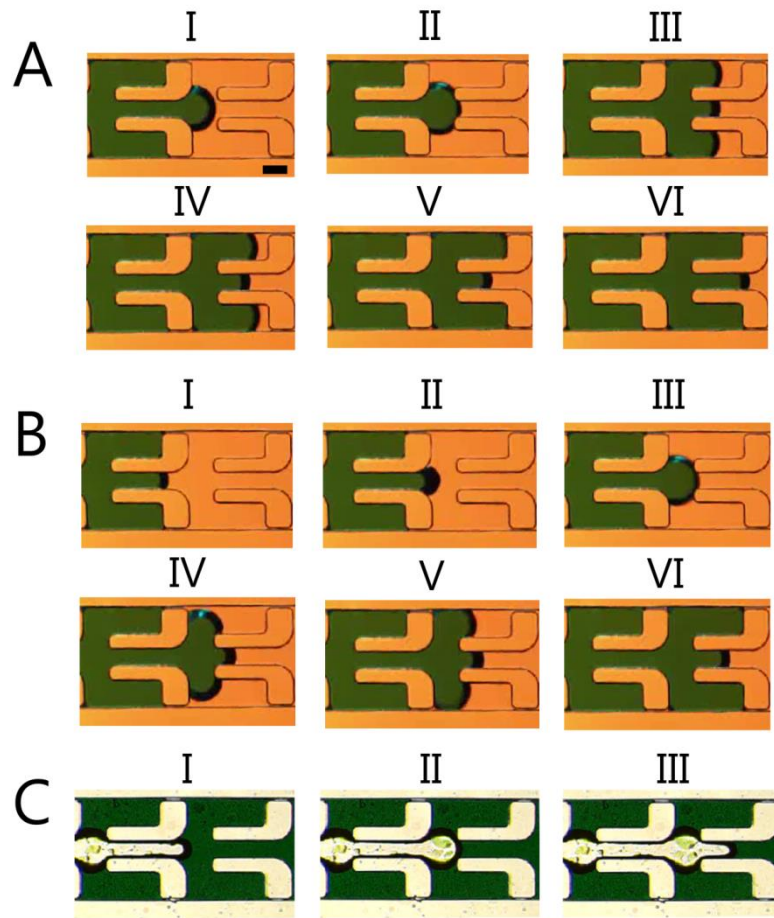


Figure 6.33: Device working mechanism (A) Tracking liquid-air interface in the channel: Time-lapse images of liquid-air interface movement while entering the traps: Liquid filling the previous traps first and then moving toward the next set of traps; Liquid-air interface just before entering the traps demonstrating the entrance length to the traps and the main channel. (B) Liquid stops at the narrow restriction but moves through the main channel; (C) Liquid shearing and droplet compartmentalization; Time-lapse image of liquid shearing in the main channel (Scale bar=100 μm).

Here the interface movement along the channel will be reviewed. Looking at Fig. 6.33A, when liquid-air interface moves from $t=t_1$ to $t= t_1+\Delta t$, the radius of curvature and consequently the value of d (the distance between the channel walls) decreases leading to an increase in the capillary pressure value demanding higher injection pressure to fill the channel. Fig. 6.33A-II demonstrates the moment when the liquid-air interface reaches a trap's entrance. Based on the above explanations, in order to ensure that the liquid first enters the trap and only after it fully filled the trap, it continues to fill the main channel (Fig. 6.33A-VI), it is essential to have $w_{entr.} > w_{channel}$; In this design these values are 100 μm and 70 μm respectively.

The fact that the filling pressure needs to be bigger than the capillary pressure to force the liquid to move in the channel necessitates consideration of any geometrical change that may increase the capillary pressure. Although increased capillary pressure can be balanced with the increased filling pressure, since the device is made to be in a temporary bond with the substrate, the range of the operating pressure is limited. For any given change in the channel geometry, there exists a burst pressure which occurs at the interface's minimum radius of curvature and it is defined as the highest achievable capillary pressure at the liquid interface while moving through that geometry [101]. In the presented design, we have two positions with channel expansion. One when the liquid leaves the main channel and moves toward the traps. And the second one is at the narrow restriction site which functions as a stop valve. It is ensured that the burst pressure in the main channel is low enough to let the liquid pass with a wide range of filling pressures and is high enough in the restriction to stop the liquid from further movement ($w_{channel} = 70 \mu m$ vs $w_{gap} = 10 \mu m$).

The presence of the narrow restriction is essential in the process of droplet trapping. If the restriction gets blocked (e.g. due to fabrication defect), the liquid cannot move into the traps. In addition, from Fig. 6.33B, it is clear that comparing liquid movement in the traps with the main channel, the interface moves faster in the trap which is wider ($w_{trap} > w_{channel}$).

In order to shear the liquid from the main channel and segment the liquid into semi-droplets in separate traps, the principle of surface energy minimization was considered. In chapter 3, it was discussed that such phenomenon takes place in splitting a sessile drop of radius a which is squeezed between parallel plates of distance δ . It is mentioned that if γ_{SL} and γ_{LG} are the surface-liquid and liquid-gas interfacial tensions, the division of the

drop requires an increase in surface energy of $\Delta E/E \approx (\sqrt{2} - 1)/\sqrt{2} \left(1 + \frac{\gamma_{SL} \cdot a}{\gamma_{LG} \cdot \delta}\right)$ [235].

If $a \gg \delta$ and $\gamma_{SL} > \gamma_{LG}$ this equation simplifies to $\Delta E/E \approx \frac{\gamma_{LG} \cdot \delta}{\gamma_{SL} \cdot a}$. This equation shows that to have droplet splitting, the liquid surface contact area should be maximized while liquid-air contact area should be minimized. This means that the trap's length and width should be maximized (the liquid-surface interfacial area) and its height and entrance width ($w_{entr.}$) should be minimized (the liquid-air interfacial area). However, decreasing the device height increases the capillary pressure limiting the range of operational filling pressure. In addition, increasing the trap length may impair device filling during the sample injection step [115]. Fig. 6.33C shows liquid shearing from the main channel over time.

6.3.2. Cell distribution, single cell trapping

In order to evaluate the trapping efficiency (The percentage of traps with only one cell/particle) and to have a rough estimation of the concentration which leads to the highest efficiency (saturation concentration), two sizes of 10.7 μm and 19.2 μm PMMA particles (Magsphere, Pasadena, CA, USA; CAT number: PM010UM and PM020UM) were used. Different concentrations of particles were prepared in MACS buffer solution (Miltenyi Biotec, Gladbach, Germany) and were injected into the device using a lab pipette. In order to be able to compare the effect of particle size, fixed values of concentrations were used (Fig. 6.34). The saturation concentration is $1 \times 10^6/\text{ml}$ for 19.2 μm particles while for 10.7 μm this does not happen even up to $2 \times 10^6/\text{ml}$. This is because bigger particles are able to deviate from the flow streamlines and fill the traps at low concentrations while at high concentrations (above saturation concentration) they have less space to move freely causing clogging at the trap's entrance.

The main goal here was to obtain the maximum number of traps with a single cell. For 10.7 μm particles, the number of traps with single particles increases with increased cell concentration and has a significant increase from $1 \times 10^6/\text{ml}$ to $2 \times 10^6/\text{ml}$. However, for 19.2 μm particles the maximum number of traps with single cells occurs with 1M/ml concentration.

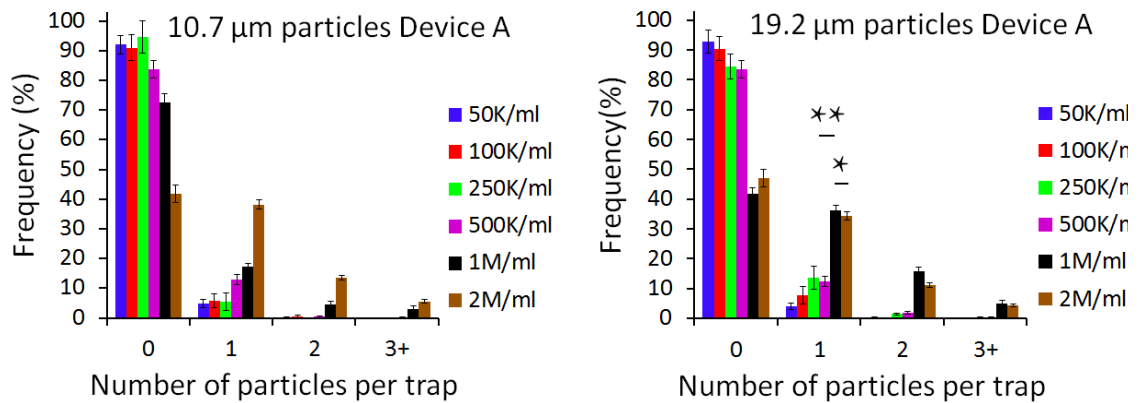


Figure 6.34: Device characterisation: (A) Trapping different concentration of particles inside droplets with regards to the solution concentration and particle size in static droplet arrays ($n=9$, (*): $p<0.05$; (**): $p<0.01$); $N=500$ droplets.

In order to assess cell trapping, two configurations of the device with different trapping size of 2.5nl (device A) and 14nl (device B) were used. Given the fact that the size of MDA-MB-231 cells are in the range of 15-20 μm , cell trapping was performed with the same range of concentrations that were used in the particle trapping experiment to find the saturation concentration. As shown in figure 6.35, as long as the injection flow rate is within the device's operation range (i.e. 0.05-0.35 $\mu\text{l/s}$) any change in trapping efficiency with the injection flow rate is negligible.

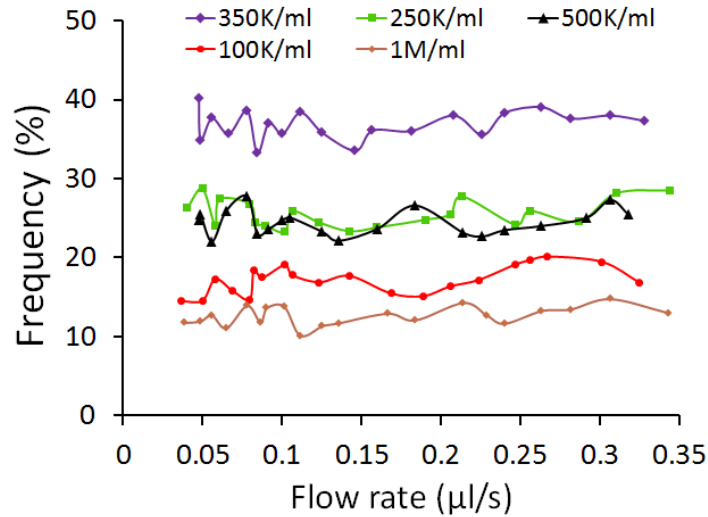


Figure 6.35: single cell trapping efficiency versus flow rate

Fig. 6.36 demonstrates cell occupancy in device A and device B. As can be seen in this figure, the saturation concentration for device A (2.5nl traps) and device B (14nl traps) are $3.5 \times 10^5/\text{ml}$ and $5 \times 10^4/\text{ml}$ respectively leading to highest trapping efficiency of 38.8% and 36.4% for device A and B respectively. Indeed, bigger traps can accommodate more cells and therefore to achieve single cell trapping one should use lower cell concentrations. For both devices, increasing the concentration leads to decreased number of empty traps but increased number of traps containing three and more cells.

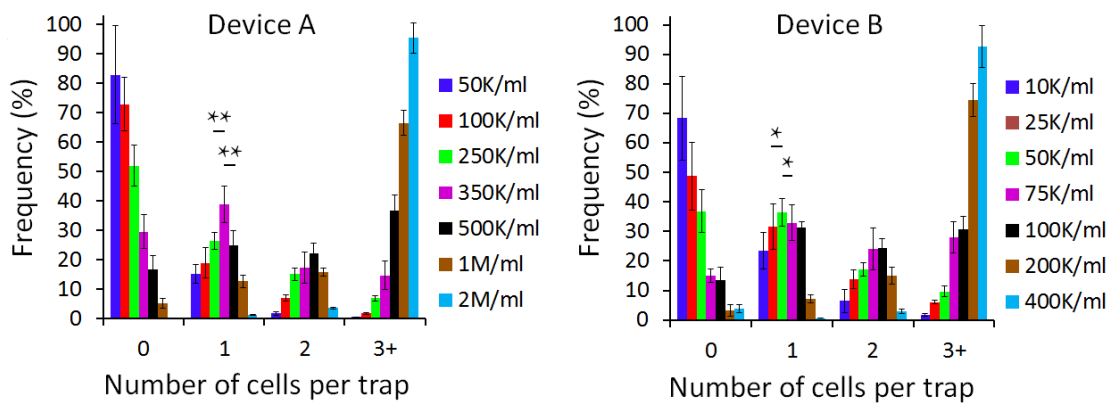


Figure 6.36: Device characterisation: Distribution of MDA-MB-231 breast cancer cells with a wide range of cell concentration in droplet arrays of different size ($n=9$, (*): $p < 0.05$; (**): $p < 0.01$); $N=500$ droplets.

Comparing the distribution of particles and cells in droplets (i.e. Fig. 6.34 and Fig. 6.36), it is found that the results have differences especially at higher concentrations. This was predictable since cells and particles are different in their size distribution (particles are more uniform in size), deformability (cells are more deformable), density (PMMA particles density is around 1.2 gr/ml while cells density is around 1gr/ml), and shape (particles are more homogeneous in shape) [236-238]. Deformability for example was shown to cause lateral migration of cells enabling them to cross the flow streamlines in the channel [239].

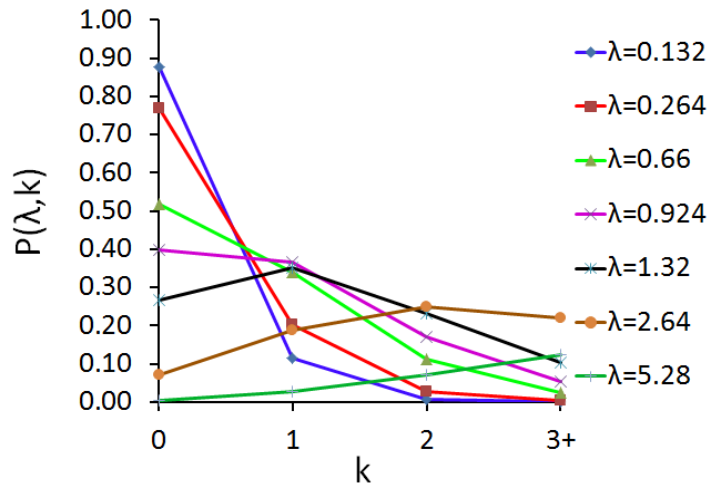


Figure 6.37: Poisson distribution function with λ values corresponding to MDA-MB-231 breast cancer cells with a wide range of cell concentration.

Fig. 6.37 demonstrates the Poisson distribution $p(\lambda, k) = \frac{\lambda^k e^{-\lambda}}{k!}$ which is used to estimate the number of cells per droplet in typical non-deterministic single cell trapping methods [65]. In this equation k is the number of particles in a droplet and λ is the average number of cells per droplet volume and can be defined as the ratio between the volume fraction of cells in the pre-encapsulation solution ϕ_s and that of a droplet containing one cell ϕ_d . (Calculation for λ , ϕ_s and ϕ_d values are as follows. Here, the calculation for cell concentration of $C=1 \times 10^6/\text{ml}$ is presented:

$$V_{\text{single cell}} = \frac{4}{3}\pi r^3 = \frac{1}{6}\pi D^3 = \frac{1}{6}\pi(15)^3 = 1.76 \times 10^3 \mu\text{m}^3$$

For the above cell concentration (i.e. 1×10^6 cells): $V_{\text{cells}} = 1.76 \times 10^9 \mu\text{m}^3$

$$V_{\text{media}} = 1\text{ml} = 10^{12} \mu\text{m}^3$$

$$\phi_s = \frac{V_{\text{cells}}}{V_{\text{media}}} = \frac{1.76 \times 10^9 \mu\text{m}^3}{10^{12} \mu\text{m}^3} = 1.76 \times 10^{-3}$$

$$\phi_d = \frac{V_{\text{single cell}}}{V_{\text{droplet}}} = \frac{1.76 \times 10^3 \mu\text{m}^3}{110 \times 300 \times 80 \mu\text{m}^3} = 6.69 \times 10^{-4}$$

$$\lambda = \frac{\phi_s}{\phi_d} = \frac{1.76 \times 10^{-3}}{6.69 \times 10^{-4}} = 2.64$$

Likewise, λ values were calculated for other concentrations as shown in Table 6.1:

Table 6.1: Calculated values of λ for different cell concentrations

Cell concentration	λ
5×10^4	0.132
1×10^5	0.264
2.5×10^5	0.660
3.5×10^5	0.924
5×10^5	1.320
1×10^6	2.640
2×10^6	5.280

Here $p(\lambda, k)$ is calculated based on the λ values corresponding to different cell concentrations in device A. In theory, the maximum efficiency for trapping single cells takes place when $\lambda = 1$ at 37%. With regard to the Poisson distribution (Fig. 6.37) which is plotted for the same concentrations as of the experiments, it is indicated that the maximum single cell trapping efficiency is 36.67% for $3.5 \times 10^5/\text{ml}$ ($\lambda=0.924$). In the same concentration, the device shows single cell trapping efficiency of 38.8% (percentage error=5.8%).

6.3.3. Device pressure test

As mentioned in the paper, no plasma bonding is performed between the device and the substrate. Instead the device is pressed against the substrate. Since the device bottom is flat (by using photolithography on SOI wafer), a good bonding between the PDMS slab

and the substrate was achieved which allows injection of sample into the device without leakage.

In order to find the device's operation pressure limit, a new experiment was performed using a syringe filled with liquid connected via a pipe to the device's inlet, and raised at various heights (corresponding to an applied pressure of $P=\rho gh$; where ρ is the liquid density, g is the gravitational constant and h is the height difference between the syringe and the device). Fig. 6.44 demonstrates the experimental set up. Before putting the tube into the device's inlet, it was ensured that water is just at the tip of the tube and ready to flow into the channel. The syringe was raised from the device's level. The first pressure recorded was the pressure by which the liquid start filling the channel (P_{min}). When the syringe is raised more, at some point the device starts to leak which shows the upper pressure limit (P_{max}).

Five clean devices were brought into contact to glass/tissue culture substrate and then loaded with a syringe filled with water raised at different heights. As can be seen in Fig. 6.38, when in contact with a glass substrate, the device can maintain leakage-free operation at higher pressures compared to a plastic substrate.

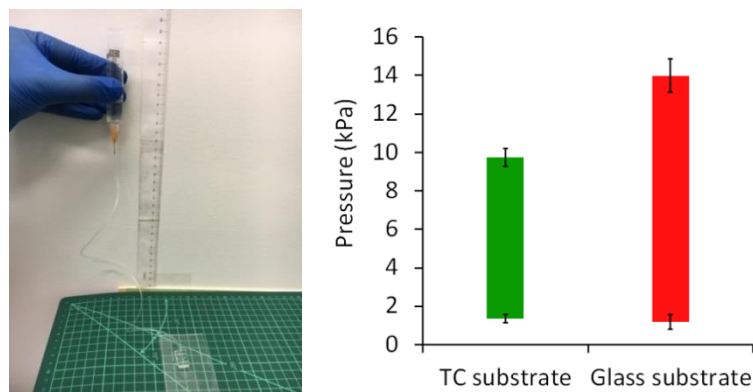


Figure 6.38: Pressure test experimental set up; the pressure range applied at the inlet to drive the liquid into the traps during loading step with no leakage ($n=5$).

A sample of pressure limit calculation is provided below:

For the TC substrate,

$$h_{low}=0.138 \text{ m} \rightarrow P_{low}=\rho gh=998.23\times 9.8\times 0.138=1350.006 \text{ Pa}=1.350 \text{ kPa}$$

$$h_{up}=0.994 \text{ m} \rightarrow P_{up}=\rho gh=998.23\times 9.8\times 0.997=9753.306 \text{ Pa}=9.753 \text{ kPa}$$

6.3.4. Cell culture, viability, proliferation and on-chip staining

Cells were cultured in a device which was temporarily sealed against a TC/glass substrate. To overcome the issue of low-volume droplet evaporation which is shared among droplet-based systems, PDMS devices were soaked in water overnight and at the time of culture a humidity chamber was created. Unlike other droplet methods here each droplet is supported by TC/glass substrate providing cell attachment and preventing anoikis or cell apoptosis [240, 241]. Some of the challenges with long-term cell culturing in single cell devices are droplet evaporation, and nutrient depletion. Therefore, cell viability is important to ensure that culture condition has not compromised cells functionality or inadvertently caused rapid cell death. To ensure that there is enough nutrients for single cells to grow in each trap, cell culture surface, volume and their ratio were calculated in each design. For device A (2.5nl traps), these values are $3.3\times 10^{-4} \text{ cm}^2$, 2.5 nl, and 12.5 respectively. For device B (14nl traps) these values are $1.79\times 10^{-3} \text{ cm}^2$, 14 nl and 12.5 respectively. For both designs, the surface to volume ratio is within the recommended range suggested by Halldorsson et al. [242].

To assess the device capability in maintaining cells function, measured viability and proliferation were measured over 48 hours culture period. MDA-MB-231 cells were prepared at each device's saturation concentration and viability was measured after 12 hours, 18 hours, 24 hours and 48 hours culture using Trypan Blue staining (see Materials and methods) which makes live/dead cells easily distinguishable as shown in Fig. 6.39.

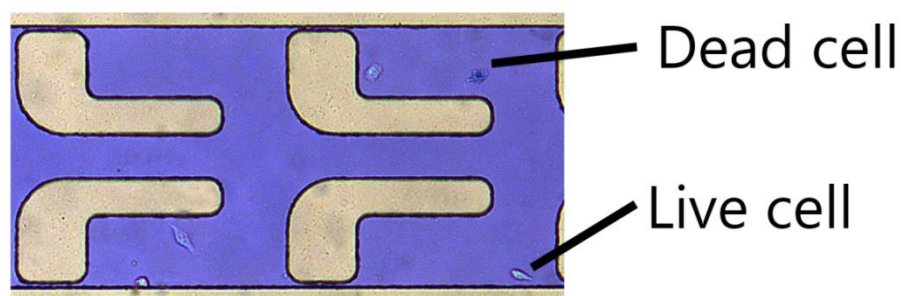


Figure 6.39: Cell and solute treatment in the device. (A) On-chip cell viability assay in each droplet; cells were cultured in the droplets for 12 hrs, 18 hrs, 24 hrs, and 48 hrs after which Trypan blue was injected into the device; Dead cells uptake Trypan blue and can be distinguished from the live cell.

To quantify viability, five chips were imaged at each time point and viability was calculated as the number of live cells to the total number of cells. It can be seen from Fig. 6.40 that cell viability remains $> 85\%$ in most of the experiments. The minimum viability was 81% for device A (2.5nl traps) at 48 hours compared to 87% for device B (14nl traps) ($p < 0.05$, $n = 5$). We therefore conclude that the trap size plays an important role in maintaining cells viability in long-term culture of single cells in droplets. It should be mentioned that despite high cell viability for cancer cells, over time nutrient depletion and build-up of the waste products may reduce the viability of more sensitive cell phenotypes and should be taken into consideration. The functionality of the cultured cells in terms of their proliferation rate was investigated. High proliferation of single cells were observed giving 1.338 and 1.579 times increase in the number of cells in device A and B respectively ($p < 0.05$, $n = 5$). Comparing proliferation of cells in two devices, it can be seen that cells proliferate better in bigger droplets.

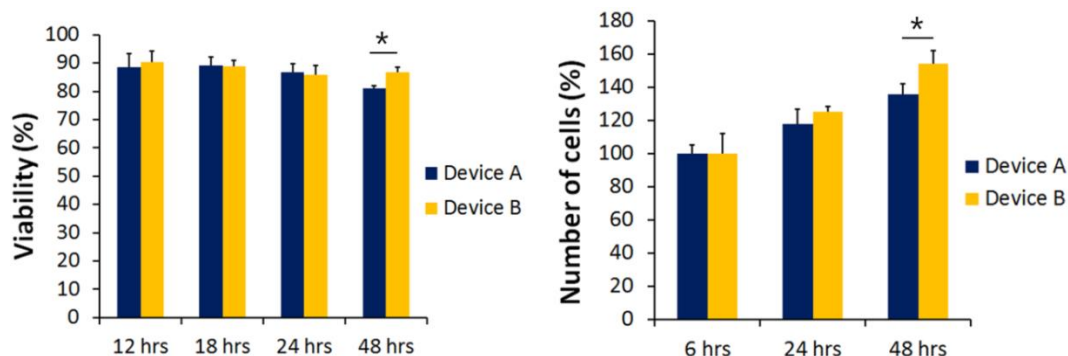


Figure 6.40: Cell and solute treatment in the device. On-chip measurement of cell viability and proliferation over time in device A and B. ($p < 0.05$, $n = 5$); $N = 500$ droplets.

6.3.5. Post peeling cell access

One capability of the device presented here is access to cells following culture owing to the reversible bond between the PDMS device and the culture substrate. This capability can facilitate complicated and time-consuming single cell assays [243, 244]. A pair of tweezers can be used to gently peel the device followed by addition of culture media. To demonstrate this capability, both tissue culture substrate (Corning treated culture dishes, mfr. No. CLS430166, Sigma-Aldrich) and glass substrate were investigated (Fig. 6.41). Autoclaved devices were first placed on top of a substrate and pressed gently to make contact. Following cell injection and device loading, cells were let to attach over a period of 6 hours. For the TC culture substrate, the dish was filled with appropriate volume of culture medium just before reaching the maximum height of the device. Next, the device was carefully peeled off the TC dish using sterile (autoclaved) tweezers. The device area was examined under a light microscope (Leica DMI1 inverted microscope, Wetzlar, Germany) and imaged. For the glass substrate the device was first carefully peeled off using a pair of sterile tweezers and then cells were covered with fresh media and imaged.

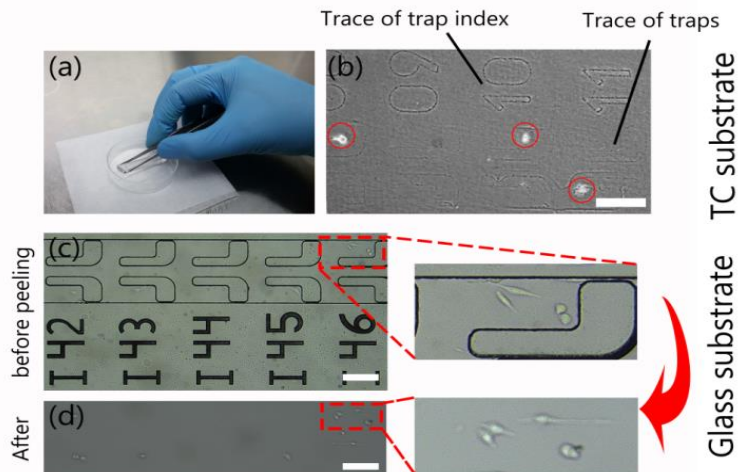


Figure 6.41: Device peel-off: (a) Peeling step using a pair of tweezers. (b) Cell retrieval following peeling from TC-substrate; the trace of traps as well as trap indices are clearly visible enabling cell retrieval and cell addressability with high accuracy. (c) Successful peeling of the device from a glass substrate, Scale bar=200 μ m in all images.

As shown in Fig. 6.41, peeling the device from the TC substrate provides access to individual cells by maintaining the trace of the channel walls as well as the trap indices due to binding of nutrients, protein molecules and dye in phenol red following device peel off and evaporation of droplets. Unlike TC substrate, glass substrate does not preserve the trace of the channel but still provides access to single cells.

Given the ability of the device to trap single cells, the possibility of changing the content of droplets was studied providing a pathway to on-chip access to the cells and droplets chemical composition. This capability was shown before using a variety of methods [227, 231, 245, 246] and can help in miniaturizing high-throughput screening assays [231, 247]. The method introduced here can be used both for droplet dilution or gradient generation and can be done in four simple steps.

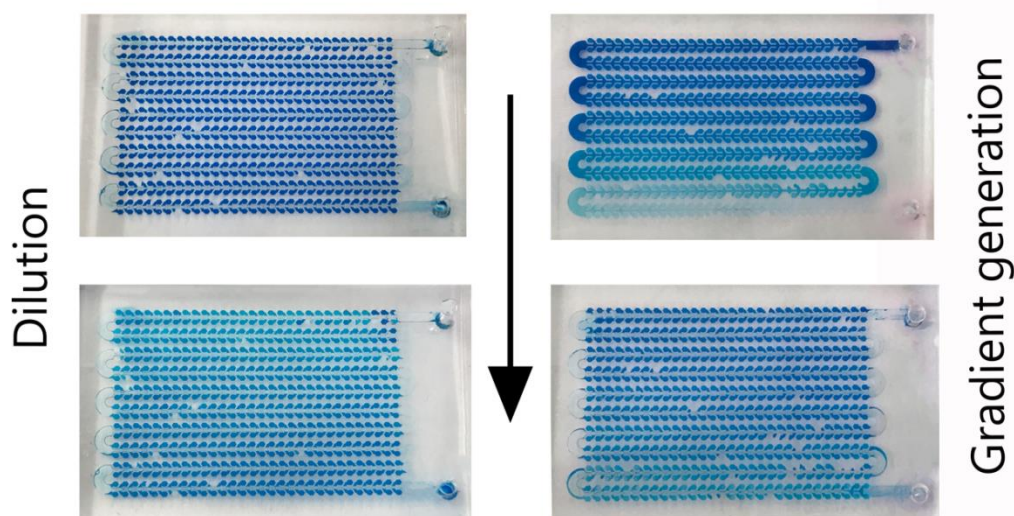


Figure 6.42: Cell and solute treatment in the device. Left: On-chip solute dilution: the device was first filled with blue food dye followed by injection of a water plug. The droplet dilutes the solute in each trap; the size of the droplet defines the dilution factor. Right: Solute gradient formed in droplet array device: The device was first filled with pure water followed by shearing liquid from the main channel and injection of a plug of blue food dye. Shearing the food dye will leave the device with droplets containing gradient of food dye.

Dilution of droplets content starts with injecting the sample into the device and shearing the residual liquid from the main channel (Fig. 6.42-left). Next, the diluting liquid is introduced into the main channel and is sheared. In order to make gradients of solute in static droplets (Fig. 6.42-right), first low concentration solute is injected into the device followed by shearing the excess liquid from the main channel. Next, a plug of high concentration solute (blue food dye) is injected into the device and gradient was achieved by shearing the main channel for the second time. For both dilution and gradient generation, the concentration of the concentrate solute, and the size of the plug determine the dilution factor/the gradient steepness in the droplet array. For example, increasing the size of the water plug will increase the dilution factor (Fig. 6.43). Using multistep sample injection, the device enables generating gradients of two solutes, and changing the gradient steepness (Fig 6.43B and 6.43C).

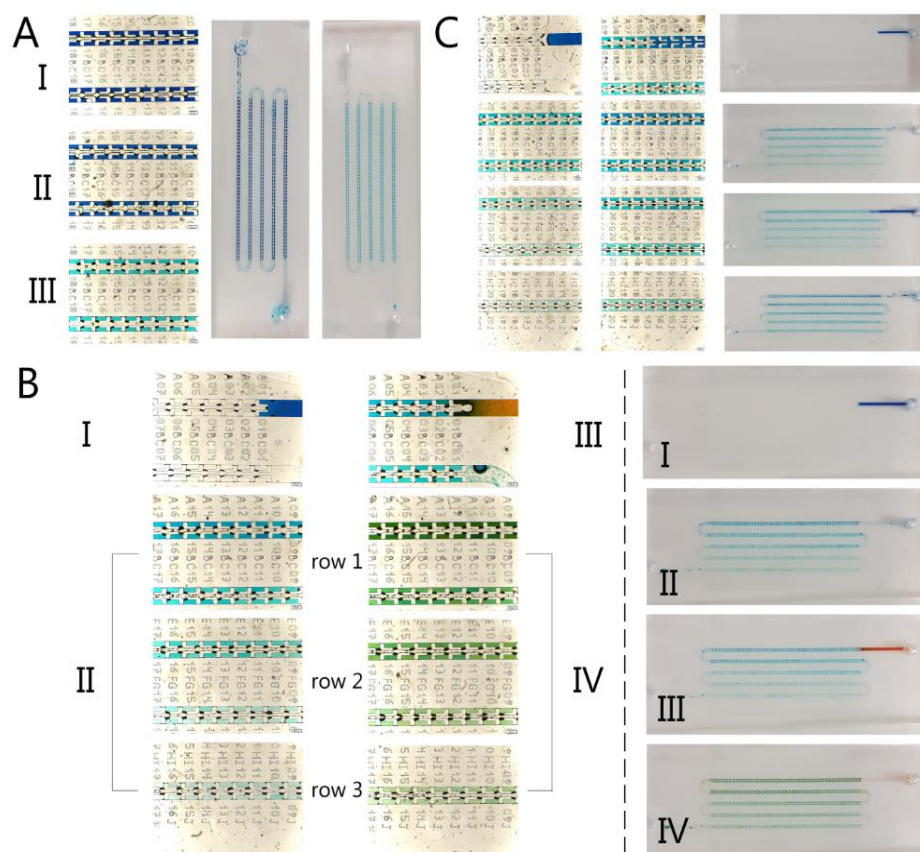


Figure 6.43: Multistep dilution and gradient generation in static droplet arrays A) Multistep dilution B) Two-colour gradient generation with two step addition of a $0.187 \mu\text{l}$ plug of blue and red food colour respectively. C) Gradient generation with two step addition of a $0.187 \mu\text{l}$ plug of blue food colour. (Note: This volume is calculated as the amount of sample filling the channel from the inlet up to the first trap).

In order to show a potential application of sample dilution in the device, cells were cultured in the device over 24 hours. Following oil removal from the main channel, live/dead double staining solution with concentration of $4 \mu\text{M}$ was injected into the device. After 1 hour incubation, the staining solution was removed and cells were washed multiple times by injecting PBS. Fig. 6.44 demonstrates fluorescent image of the stained cells superposing phase contrast, green and red channels revealing cells live/dead status. Live cells uptake calcein AM and will become green while dead cells uptake propidium iodide and are shown in red. Since this dilution can be done several times, sequential reactions on single cell level can be operated with a simple microfluidic device.



Figure 6.44: On-chip staining of cells by adding live/dead staining solution to the droplets content (calcein AM and propidium iodide) after 24 hours culturing period (Scale bar=300 μ m).

6.3.6. Single cancer cell proteolytic assay

Proteolytic degradation of the extracellular matrix (ECM) is known to be a determinant factor in cancer invasion and metastasis. In this process, cancer cells release degrading enzymes that cleave the ECM protein [248]. This highlights the importance of studying proteolytic activity of cells for development of novel protease targeting drugs. An established method for studying such an activity is based on observing the fluorescent intensity out of the reaction between the released enzyme and a protease-sensitive substrate known as fluorescence resonance energy transfer (FRET) substrate [249]. Conventional proteolytic assays measure average activity of the cells masking the fact that cancer invasion due to proteolytic activity is driven by the heterogeneity between cancer cells [250]. In addition, knowing the proteolytic activity of different subclones may lead to more effective treatment strategies [12].

The static droplet system developed in this study enables tracking the proteolytic activity of individual cancer cells over time. Cells were mixed with FRET substrate in 1:1 ratio and trapped in semi-droplets in the device. The frequency of fluorescent traps that have no cells, one cell, two cells or more follows the Poisson distribution (average values are 33.6%, 38.5%, 16.7% and 11.2% respectively).

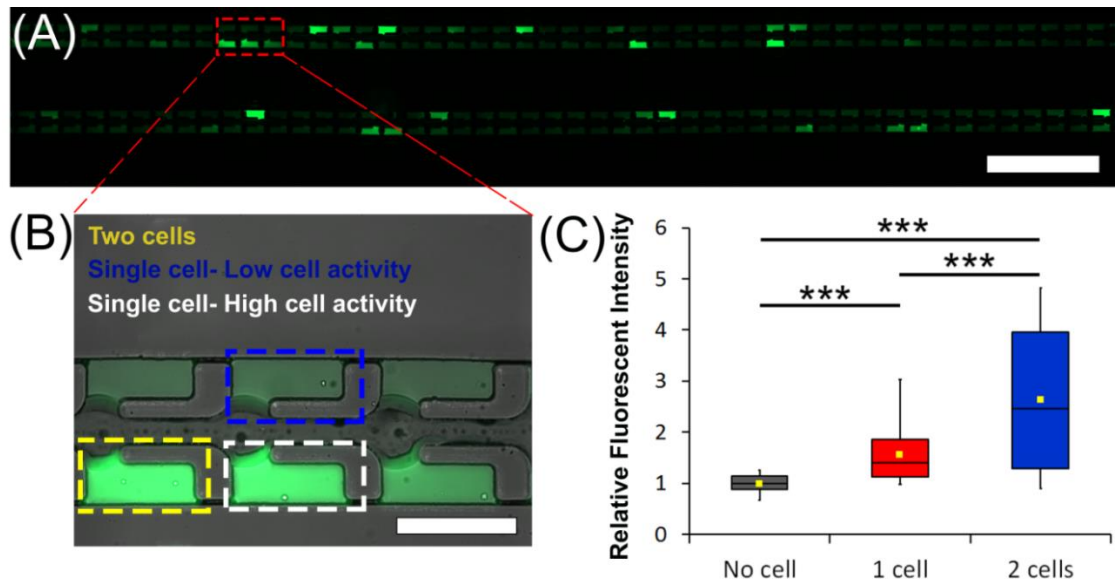


Figure 6.45: MMP assay at the single cell level of MDA-MB-231 cancer cell line. (A) Relative fluorescent intensity in semi-droplets (a) an array showing the fluorescent signal out of different semi-droplets, Scale bar: 1.5mm (b) zoomed view demonstrating droplets with no cell, high activity and low activity single cell with their corresponding fluorescent signal, Scale bar: 300 μ m, (c) A box plot demonstrating the relative fluorescent intensity of each chamber with no cell, one cell or two cells at a certain time point; as expected droplets containing one cell have higher fluorescent signal compared to empty droplets and droplets with two cells are brighter than those containing one cell ($N=102$ for cases with no cell, $N=114$ for cases with one cell and $N=53$ for cases with two cells), $P \leq 0.001$, $n=3$.

Using time-lapse microscopy, dynamic MMP activity of single cells was monitored. Fig. 6.45A demonstrates clear difference between fluorescent intensity of droplets across the device. Fig. 6.45B shows two semi-droplets containing one cell but with different fluorescent signal indicating different level of MMP activity among single cancer cells. Measurement of relative fluorescent intensity (Fig. 6.45C) shows that semi-droplets containing more cells produce stronger signals, i.e., droplets containing two cells are brighter than those containing one cell or no cells ($p < 0.001$).

To demonstrate the capability of the device in measuring cell dynamics behavior, fluorescent intensity of each semi-droplet containing no cells, one cell or two cells were measured over a period of 14 hours and plotted in Fig. 6.46. The MMP activity increases over time. The experimental data is also represented in a heat map showing heterogeneity between MMP activity of single cells and semi-droplets containing different number of cells over time.

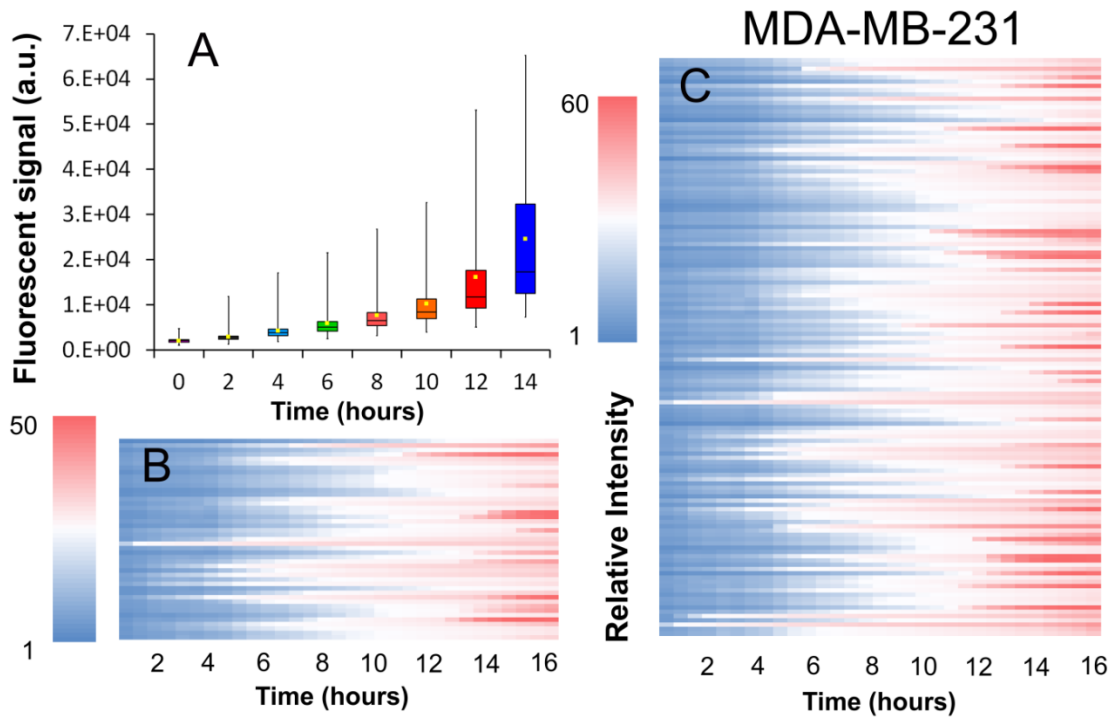


Figure 6.46: MMP assay at the single cell level of MDA-MB-231 cancer cell line. Single cell MMP activity over time (A) fluorescent intensity of droplets over time showing increase in MMP activity in droplets during the course of 14 hours in culture. (B), (C) Cellular heterogeneity and dynamic response; heat map presenting the relative fluorescent intensity in droplets containing one cell in (B) and different number of cells (0, 1, or 2 per droplet) in (C). Red color represents high MMP activity and blue color shows low MMP activity.

Fig. 6.47 presents the relative fluorescent intensity in the droplets with the same number of cells in individual heat maps as well as the number of cells in each trap and their corresponding fluorescent intensity. While traps containing no cell show more or less the same level of signal, the variation of data is getting bigger as the number of cells per trap increases. The green fluorescent signal of Fig. 6.47 also confirms the heterogeneous secretion of traps with the same number of cells.

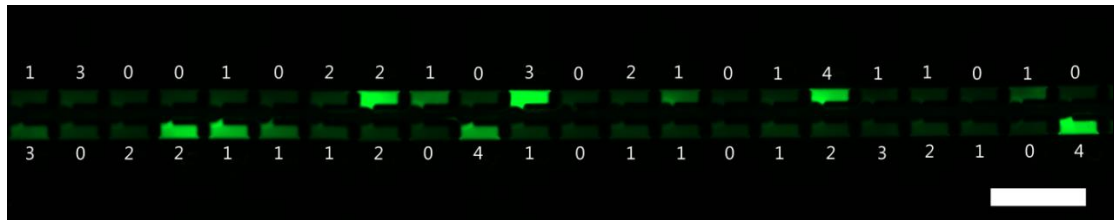
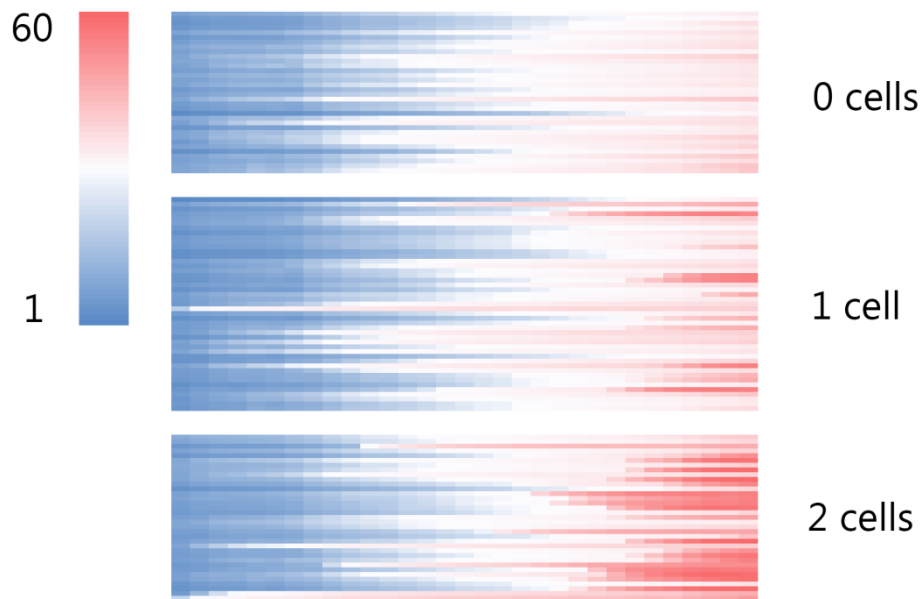


Figure 6.47: Cellular heterogeneity and dynamic response; heat map presenting the relative fluorescent intensity in droplets containing no cell, 1 cell and 2 cells ($n=34$, 45 , and 35 respectively). Red color represents high MMP activity and blue color shows low MMP activity. Bottom: Image of 44 droplets containing different number of cells, Scale bar: $800\ \mu\text{m}$.

6.4. Concluding remarks

In summary, a novel leakage-free static droplet array system with a built-in valving mechanism was introduced, that is able to rapidly and reliably capture single cells in chemically isolated indexed traps and in a high-throughput manner. The presented device enables long-term culture and dynamic monitoring of cells for periods of hours up to days. Maintaining cells viability beyond certain limit and without impairing single cells secretion content can be achieved by a new design in which fresh media can be added to each trap. The device's capability was successfully assessed by capturing the heterogeneity among single cancer cells MMP activity over time. Droplet generation happens in three simple steps of filling, shearing, and sheathing. Critical design considerations of the static droplet array including selection of the width of the channel

in different channel locations were explained and a guideline for analyzing the behavior of liquid-air interface in the device was presented. In addition, two important device capabilities were demonstrated: post-culture access to cells through simple device peel off and on-chip manipulation of droplets content.

The overall setup and injection procedure of this design takes less than 10 minutes, does not require any microfluidic expertise and is operated with standard laboratory pipette which makes it a suitable choice for biologist and other end users. This method may open up new opportunities and lead to fast-tracking single cell discoveries.

Chapter 7. Conclusions

7.1. Key findings

The first aim of this thesis was to investigate the possibility of employing microfluidic capillary effect as a passive and reliable tool of confining cell samples for cell dynamics studies. Theoretical and computational models were utilized to analyse the flow behaviour in microchannels by tracking the liquid-air interface movement through different geometries. While most of the capillary microfluidic devices reported previously have hydrophilic walls to help the liquid to move into the channel, the model used in this thesis proposes uses hydrophobic nature of PDMS as a resistive force to manipulate and stop the flow on demand. Sample confinement (with no surface modification) was made possible by blocking the liquid movement in the system at the desired locations. In order to achieve this, a sudden change in the channel geometry was proposed as it can pin the meniscus of the fluid at the edges and stop the flow. Numerical simulation of the two-phase liquid-air flow showed that for the sudden expansion geometry, the liquid front acts as a barrier in front of the filling flow. This barrier can be decreased by designing a nonlinear expansion area.

To investigate the effect of channel geometry on flow behaviour, an expression was found for the pressure distribution at the liquid-air meniscus advancing in a microchannel of arbitrary shape. Based on this understanding, geometry of a microfluidic junction, as the most general case, was proposed. Analysis of the flow revealed that movement of liquid into each route in the junction depends on the filling pressure as well as the geometry of entrance to each route. Higher filling pressures can induce circulating area at the meniscus near the route's entrance and impede flow from further movement. The microfluidic junction geometry was then modified to consider possibility of liquid compartmentalization. The numerical models showed that if the entrance of a flow route

filled with liquid is parallel to the filling flow, the liquid can be broken up into compartments by applying air pressure.

Using the concept of liquid stop valves, a new microfluidic device was designed and fabricated to confine liquid samples by restricting the injected liquid flow at the end of microchannel while allowing residual air to vent out. The liquid restriction was induced by narrowing down the channel to produce gaps of 10 μm size. The presented device has a number of unique characteristics. First, air escapes through a novel air vent design which connects the end of each trap to the atmosphere. Second, unlike usual microfluidic devices, the PDMS slab of the device is in temporary contact with the substrate, to enable device lift off as a necessary step for creating cell/protein patterns. This requirement imposed issues regarding sample leakage in the system. To solve this problem, a new approach was adopted in which the device fabrication was done using Deep Reactive Ion Etching (DRIE) on Silicon on insulator wafers yielding PDMS slabs with flat surfaces.

Using the proposed stamping device, a patterned co-culture of Endothelial cells and cardiac stem cells were created to investigate cell-cell interaction and collective cell migration during Myocardial Infarction (MI). The collective migration of EC/SC was investigated by measuring the average migration speed, average migration velocity in y-direction and cell directionality based on two fixed parameters of cell type and culture type. Statistical analysis of the obtained data revealed that ECs in the co-culture are more motile and migrate faster in the direction normal to channels compared to single culture. In addition, analysis of the proliferation rate of each cell type revealed that SC provides a microenvironment that increases the initial growth of EC. These findings suggest that cardiac-derived mesenchymal SCs secrete growth factors that direct tissue repair after myocardial infarction (MI), including revascularisation of the infarct region after dead cardiomyocytes are removed by phagocytic cells. Analysis of the proliferation rate of

each cell type revealed that co-culture of SC with EC resulted in growth arrest of SC after 100 hours. Growth arrested SCs differentiated into cells with myofibroblast or spindle shaped morphology.

Using live-cell imaging for tracking cell migration, the presented method can be used as quantifying tool to investigate the effect of co-culture on dynamic cell response. The stamp does not require dedicated plasma bonding and is operated with a standard lab pipette. It can be easily adopted by common non-microfluidic cell biology labs for the study of cell-cell modulation and intercellular signalling.

Capillary based trapping in a microfluidic stamping device can be used for revealing any biophysical event incorporating movement of cells or cell parts. This method was used to successfully pattern primary hippocampal neurons and inhibitory substrate Nogo-66 with accurate spatial resolution as a model system for neural repair following central nervous system (CNS) injury. Using microfluidic stamping device, initially neurons are confined to grow in the microchannels. After 1 day in culture, and following simple device peel off, axons were let to migrate toward the area patterned with inhibitory substrate. By continuously monitoring the neurite's length, outgrowth rate, and outgrowth direction, we were able to monitor the interaction between the neuron's growth cones and the patterned inhibitory molecules Nogo-66. The results led to proving the effect of Tpm3.1 as a protein regulating cytoskeletal stabilization and promoted neurite outgrowth encountering the region coated with inhibitory cues.

Based on the knowledge of the interface movement in the junction geometry, a novel leakage-free static droplet array system with a built-in valving mechanism was introduced that is able to rapidly and reliably generate an array of hundreds to thousands of liquid compartments in three simple steps of filling, shearing, and sheathing. Critical design considerations of the static droplet array including selection of the width of the channel

in different channel locations were explained and an experimental analysis was performed to explain the behaviour of liquid-air interface in the device. In addition, two important device capabilities were demonstrated: post-culture access to cells through simple device peel off and on-chip manipulation of droplets content. This latter capability enabled analysing the cells viability by cell staining using Trypan Blue and live-dead double staining kit. In addition, a method for gradient generation and dilution of the droplets was presented.

Following the Poisson distribution law, the static droplet array device is able to generate an array with ~37% single cell occupancy. It is found that the optimum concentration leading to highest percentage of droplets with single cells depends on the trap size and the initial concentration of cell suspension. Following generation of the static droplets, single cells are chemically and physically isolated in indexed traps by separating the consecutive traps with a small 10 μm air plug. The presented device enables long-term culture and dynamic monitoring of cells for periods of hours up to days.

Since each droplet is chemical isolated, the device opens a great opportunity assays in which the droplet compartments act as individual bioreactors. One such assay was presented in this study to measure the secretion dynamics of single cells over time. Individual MDA-MB-231 breast cancer cells were monitored in droplet over the period of 12 hours. At the droplet level, each single cancer cell produced different amount of matrix metalloproteinase (MMP) enzyme which was then reacted with the fluorogenic substrate encapsulated together with the cells. By measuring the level of fluorescent signal out of each droplet, the device enabled capturing the heterogeneity among single cancer cells MMP activity over time and recognizing the invasiveness of the cell sample.

7.2. Future direction and limitations

Although, the results presented in this thesis explained the role of geometry in manipulation of capillary pressure, further analysis is required to analyse the effect of many other operational/flow factors. For instance, it is important to understand the effect of contact angle and interplay between the geometry and contact angle on the movement of liquid-air interface. This is especially important in microfluidic channels that are made out of multiple materials with different contact angles or those assays which involving coating the surface with several reagents leading to a variable surface chemistry/contact angle during the experiment. An interesting topic would be to analyse the liquid front in three dimensions in channels with different aspect ratios. This would benefit in designing bigger integrated microfluidic device in which the channel dimensions are dictated due to the compatibility with other device components. It should also be mentioned that many of the biological fluids are non-Newtonian. Designing a capillary microfluidic system in these conditions require a separate modelling as these fluids may behave differently in the same geometry.

In order to achieve defined device depth and improved channel cross section uniformity, microfabrication using RIE etching on silicon on insulator (SOI) wafer was used. The procedure of fabrication requires printing mask on glass followed by clean room fabrication which is both time consuming and expensive. The smallest feature on the design is $\sim 10 \mu\text{m}$ which is achievable via photolithography. Further research on using innovative fabrication methods such as high-resolution 3D printing can help in easier fabrication of these devices.

The proposed microfluidic patterning device has a few limitations with regards to its applications. One of these limitations is its incompatibility with a more realistic native 3D cell patterning configuration. Some attempts have been done to pattern thermoset

hydrogels in the device presented here. However, confocal imaging of the patterned hydrogel showed uneven hydrogel patterns. Further analysis can be done to release a perfect pattern of hydrogels by rendering the inner surface of the PDMS channel hydrophilic, using different coating materials. The presented stamping method may open new opportunities to control patterned cells' microenvironment. It is envisioned that the proposed device can be used to generate a hierarchical multilayer protein layers by repeated stamping steps, where each layer can harbor two different protein types/concentrations. This bottom-up effect can further be complemented by a top-down effect, where the patterned cells are incubated with various biomolecules such as growth factors, cytokines, drugs or a combination of their concentrations. The freedom to engineer the cells' microenvironment, together with the preservation of their motile capability can offer valuable information on multi-cellular migration behaviour under external stimuli.

The patterning method described in this thesis can be used to engineer more complex cell patterning configurations by adding new channels in a triple (or more) interlaced configuration, subject to geometric limitations that allow air to be vented out during the liquid filling stage. Therefore, there is no limitation on the number of patterned cells in the device. Furthermore, the presented stamping method can be considered as a candidate for a new approach towards complex three-dimensional organ printing. This could be achieved by repeated stacked stamping of gel-encapsulated cells. Using such a printing strategy could lead to the design of complex interlaced 3D sheets or semi-tubular geometries. A layer-by-layer cell printing, in contrast to pixel-by-pixel cell printing could offer higher throughput and the elimination of an in-plane printing misalignment.

One of the major issues associated with the static droplet system is formation of bubble in the array which eventually leads to dislocation of the fluorocarbon oil and the content

of each droplet. Since these bubbles can keep high pressures at the interface, they can extend along the array system and impair the device's operation. Bubble generation can have a number of sources including sharp corners in the geometry and high liquid filling flow rates. The effect of these factors on the device operation should be the top priority during the device design process. Another prime challenge in the static droplet system is droplet evaporation. Since droplets have nanolitre volume, evaporation of the droplets can happen at any temperature especially since PDMS is a porous material providing considerable contact with air. This limits the variety of assays that are sensitive to droplet's volume or require capturing phenomena such as cell proliferation over extended periods of weeks or months. Future development of this device should focus on development of a reliable method for blocking droplet evaporation.

The static droplet array device can be improved in a few ways that may significantly increase its application. First, since the device is only temporarily bonded on a substrate, the technique allows cell recovery following culture for any type of downstream analysis (gene expression analysis, PCR, etc). However, reliable and repetitive harvesting of the cells with high efficiency was not investigated. One of the main future improvements of this device can therefore be finding methods for retrieving the cells. One of the possible methods can be using micropipette tips to detach and remove the cell from the substrate. Alternatively, methods can be used to push the static droplets out of the system. Another limitation of the presented device is nutrient depletion in the droplet over time. Although media renewal can be achieved by adding fresh media from the inlet, the droplets content would possibly be washed away, and their chemical signature will be lost. An improved design can consider changing the design so that addition of new materials can be done separately and in parallel to all of the traps. Finally, the static droplet array device can be used for myriad of applications that has not been explored. These include single cell co-

culture assays, droplet PCR, and T-cell activation via surface modification. Cells can also be mixed with a pre-gelling hydrogel solution, trapped inside the droplets and then let the process of gelation to take place. For example, a thermoset hydrogel can be maintained at low temperatures (e.g. room temperature), immediately mixed with the cells and then injected in the device. Once cells are trapped the temperature can be increased to initiate the gelation.

Appendix A. UV exposure using mask aligner

The exposure was performed in three parts: Part A, B and C.

PART A

- Lamp Power supply was turned ON.
- Mode switch was set at **CP (constant power)** position, and Intensity/Power Meter was set at **WATT** position.
- **LAMP START switch** was pressed and hold till lamps turns on (rise in current value on the meter).



Figure A.1: Turning the UV source on the mask aligner.

PART B:

- Turn ON Mask Aligner.
- Lamp intensity and exposure time was checked following below process:
 - a) Press **EXPOSE TEST**
 - b) Switch **MODE to C.I.** (constant intensity).
 - c) Change Intensity/Power Meter to **mW/cm²**.
 - d) Press **Shutter** to open, intensity reading should be 10mW/cm², press Shutter again to close it.

- The exposure time was set and while UV glass was put on **Pulse** was pressed to verify it.

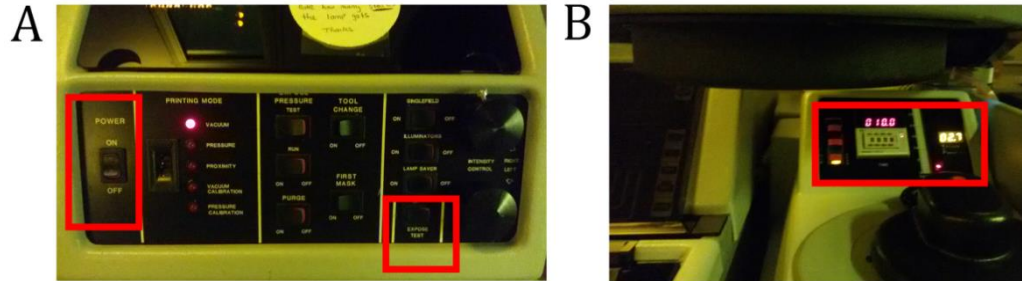


Figure A.2: Turning on the mask aligner and setting the exposure time.

*** Exposure time: According to MSDS for 45-80 micron thickness the exposure energy should be **150-215 MJ/cm²**. Because our lamp energy is **10 MW/cm²** so the exposure time will be: **150/10=15-20 seconds**.

.....

PART C:

The steps of loading the silicon wafer on the mask aligner are presented in Fig. C.3 and are brought in details below:

- Press **Mask Load** to move the microscope head into load position, place the mask plate (**mask face down**) and press **mask Vacuum** to hold it.
- Choose correct wafer chuck and press **Load Wafer**. Make sure **Chip Load** is ON.
- Wait for **ALIGN light** to light up.
- Press **Mask Load** to bring microscope head into Align position.
- Align wafer to pattern on the mask, using X, Y, and θ joysticks. During alignment watch limits to X,Y, and θ . If any light comes on above the microscope eyepieces, stop and go back.
- When alignment is ready, press **Contact**.

- Check that timer is set and to the correct time, then press **Expose**.
- Wafer unloads itself.
- Press **Mask Load**, and **Mask Vacuum** to remove the mask plate, and then **Mask Load** again to return the microscope head to its normal position.
- Turn the Mask **Aligner OFF**.
- Turn the Lamp **Power OFF**.

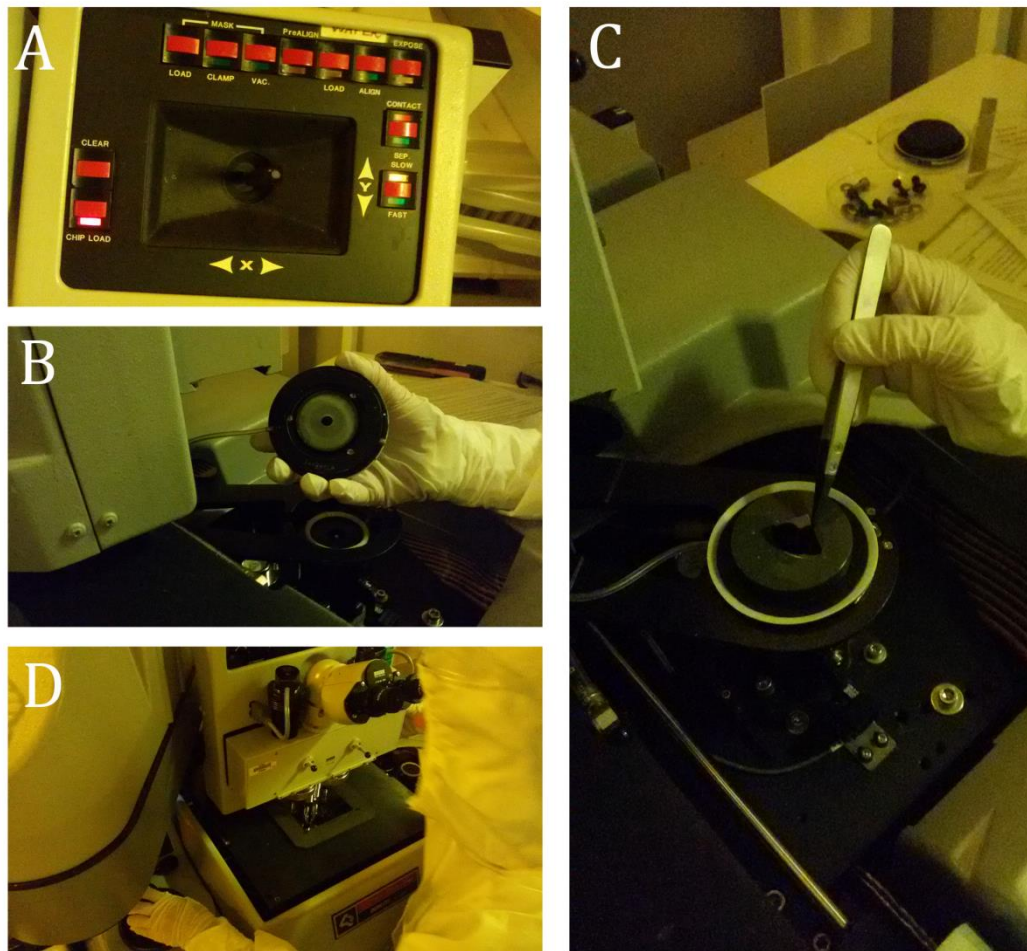


Figure A.3: Loading the mask and the silicon wafer coated with SU8 negative photoresist onto the chuck of the mask aligner and checking the correct alignment and contact between the mask and the wafer using the microscope.

Appendix B. MATLAB codes for analysing cell migration and proliferation

KM analysis censored:

```
%% data
y1=time_monoculture;
y2=time_coculture;
T = 230;
cens1 = (y1>T);
cens2 = (y2>T);
[f1,x1,flo1,fup1] = ecdf(y1,'censoring',cens1);
[f2,x2,flo2,fup2] = ecdf(y2,'censoring',cens2);
% plot empirical cumulative distribution function
stairs(x1,f1,'-b');
hold on;
stairs(x1,flo1,':b');
stairs(x1,fup1,':b');

stairs(x2,f2,'-r');
stairs(x2,flo2,':r');
stairs(x2,fup2,':r');

xlabel('hours');
ylabel('division probablity');

T=[y1;y2];
X=[zeros(size(y1));ones(size(y2))];
[b,logl,H,stats] = coxphfit(X,T);
```

Get background:

```
function [bw]=getBackground(im)
% segments background
% setup=1 reserved for seting background
SE=strel('disk',4);
[bw,thresh]=edge(im,'canny');
bw=imclose(bw,SE);
bw=imfill(bw,'holes');
bw=~bw;
im(bw)=0;
end
```

Get Nucleus:

```
function [count,data]=getNucleus(im,foreground,thresh)
% thresh=40;
SE=strel('disk',4);
% get threshold for nuclei
x=double(im(foreground));
background_thresh=median(x);
bw=(foreground&(im<background_thresh));
bw=imopen(bw,SE);
cc=bwconncomp(bw);
stats=regionprops(cc,{'Area','Centroid','Eccentricity'});
data.Area=[stats.Area];
data.Eccentricity=[stats.Eccentricity];
Centroid=[stats.Centroid];
Centroid=reshape(Centroid(:),2,length(Centroid)/2);
data.Centroid=Centroid';
```

```

data.intensity=zeros(length(cc),1);
for i=1:length(stats)
    data.intensity(i)=mean(im(cc.PixelIdxList{i}));
end

selected_ndx=(data.Area<thresh.Area(2)) & (data.Area>thresh.Area(1)) ...

& (data.Eccentricity<thresh.Eccentricity(2)) & (data.Eccentricity>thresh.
Eccentricity(1)) ...

& (data.intensity<thresh.Nucleus(2)) & (data.intensity>thresh.Nucleus(1))
;
    count=sum(selected_ndx);
    data.selected_ndx=selected_ndx;
end

```

SegmentScript:

```

load('H:\Data\Amin Hasanzadeh\Google Drive\Image
stacks\1\s4\PHC\data.mat');
subplot(2,1,1);
n=length(EndoCount);
t=0.25:0.25:0.25*n;
plot(t,ContactArea,'-k',t,GFPArea,'-g');
legend('Total cell Area','GFP+ cell area');
subplot(2,1,2);
plot(t,EndoCount,'-k');
legend('Endothelial cell count');

load('H:\Data\Amin Hasanzadeh\Google Drive\Image
stacks\1\s5\PHC\data.mat');
subplot(2,1,1);
hold on;
n=length(EndoCount);
t=0.25:0.25:0.25*n;
plot(t,ContactArea,'-k',t,GFPArea,'-g');
subplot(2,1,2);
hold on;
plot(t,EndoCount,'-k');

load('H:\Data\Amin Hasanzadeh\Google Drive\Image
stacks\1\s6\PHC\data.mat');
subplot(2,1,1);
n=length(EndoCount);
t=0.25:0.25:0.25*n;
plot(t,ContactArea,'-k',t,GFPArea,'-g');
subplot(2,1,2);
plot(t,EndoCount,'-k');

```

SegmentStack:

```

function [EndoCount,ContactArea,GFPArea]=SegmentStack(isTest)
    close all;
    if nargin<1
        isTest=false;
    end

```

```

[FileName,PathName,~] = uigetfile('*.tif','Get phase contrast
image stack','MultiSelect','on');
olddir=cd;
cd(PathName);
[GFPFileName,GFPPathName,~] = uigetfile('*.tif','Get GFP image
stack','MultiSelect','on');
cd(olddir);
if length(GFPFileName)~=length(FileName)
    error('Different number of GFP and Phase contrast files');
end

n=length(FileName);
EndoCount=zeros(n,1);
ContactArea=zeros(n,1);
GFPArea=zeros(n,1);
mkdir([PathName 'Segmented nuclei']);
thresh.Area=[50,500];
thresh.Eccentricity=[0,0.96];
thresh.Nucleus=[0,34];
GFPThresh=0;
for i=1:n
    im=imread([PathName FileName{i}]);
    imGFP=imread([GFPPathName GFPFileName{i}]);
    GFP_Pos=imGFP>GFPThresh;
    [background]=getBackground(im);
    background=~((~background)|GFP_Pos);% remove GFP positive
retions
    temp_im=[];
    temp_im(:,:,1)=mat2gray(im);
    temp_im(background)=0;
    temp_im(:,:,2)=temp_im(:,:,1);
    temp_im(:,:,3)=temp_im(:,:,1);
    green_channel=squeeze(temp_im(:,:,2));
    green_channel(GFP_Pos)=green_channel(GFP_Pos)+0.5;
    temp_im(:,:,2)=green_channel;% enhance GFP region
    imshow(temp_im,[]);
    hold on;
    foreground=~background;
    ContactArea(i)=sum(foreground(:));
    GFPArea(i)=sum(GFP_Pos(:));

[EndoCount(i),data]=getNucleus(im,foreground&(~GFP_Pos),thresh);

plot(data.Centroid(data.selected_ndx,1),data.Centroid(data.selected_nd
x,2),'xr');% selected cell green
    if isTest

plot(data.Centroid(~data.selected_ndx,1),data.Centroid(~data.selected_
ndx,2),'or');% not selected red
        for j=1:size(data.Centroid,1)
            str=[' ', '(' , num2str(data.Area(j)), ', ', ...

num2str(data.Eccentricity(j),2), ', ', num2str(data.intensity(j),2), ') '
];
            text(data.Centroid(j,1),data.Centroid(j,2),...
                str,'Color','y');
        end
    end
    hold off;
    display(['Image ' num2str(i) ' of ' num2str(n)]);
    F=getframe(gcf);

```

```
        imwrite(F.cdata,[PathName 'Segmented nuclei\' FileName{i}]);  
    end  
    save([PathName 'data.mat'], 'EndoCount', 'ContactArea', 'GFPArea');  
end
```

Appendix C. Cell counting in ImageJ

Following running ImageJ and opening the image:

Step 1: Image>Duplicate

Step 2: Image>type>8 bit

Step 3: Image>adjust>threshold>Dark background: adjust the slides to have cells as separate circles

Step 4: analyze>analyze particles> in 'show' choose outlines. Check in 'display results'.

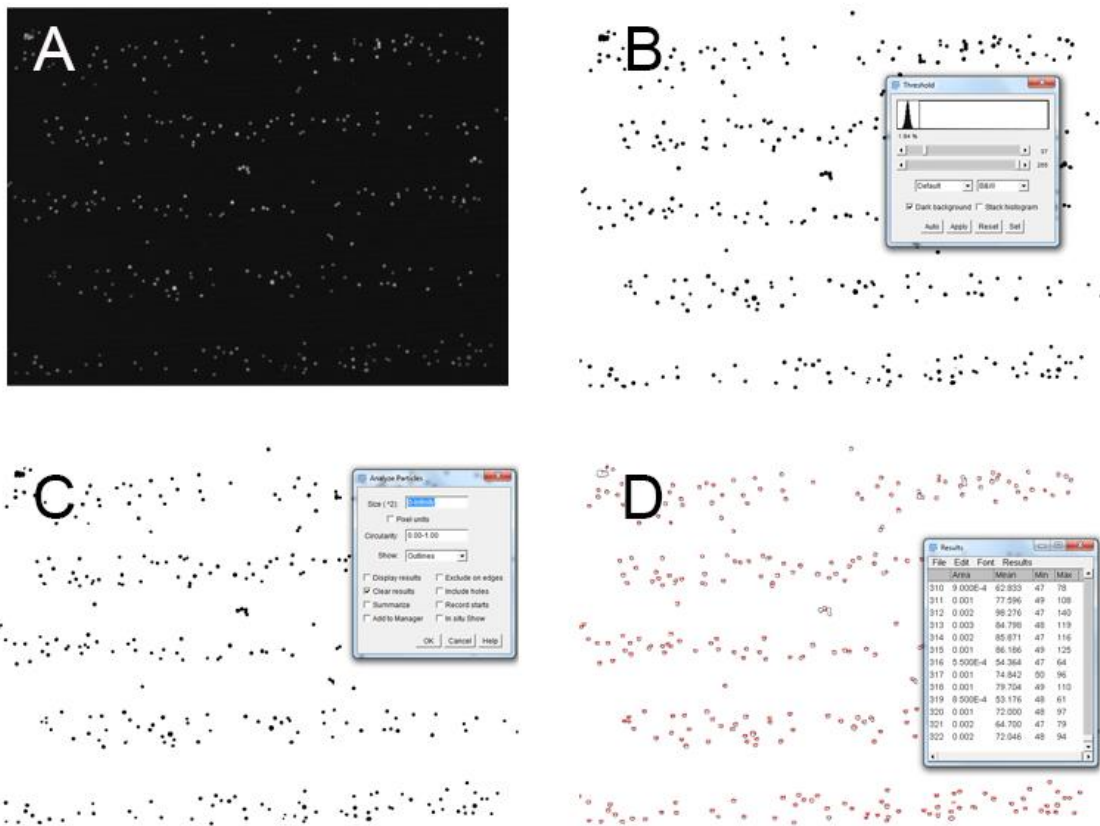


Figure C.1: Sequence of image analysis in ImageJ. (A) Crude image from the microscope (B) Adjusting the image threshold to distinguish individual cells. (C) Counting the number of cells by making an outline around each cell. (D) The counting results showing the number of cells.

**Appendix D. Production of
recombinant GST-Nogo-66 in *E.*
*coli***

Expression vector pGEX2T, encoding human Nogo-66 was kindly donated by Professor Pei-hua Lu at School of Medicine of Shanghai Jiaotong University. pGEX2T-Nogo-66 was PCR sequenced to verify the Nogo-66 gene prior to protein production. pGEX2T-Nogo-66 plasmid was transformed into E. coli expression strain (DE3) for GST-Nogo-66 recombinant protein expression. Bacterially expressed protein was purified via GSH agarose beads as recombinant GST-Nogo-66 derived from cytoplasm. Proteins were further purified by reverse phase high pressure liquid chromatography 600S HPLC (Waters Corporation, MA, USA) on a C8 column (Sigma, MO, USA). Prior to experimental use, purified GST-Nogo-66 was diluted in neurobasal medium (Life Technologies) not containing supplements to a final concentration of 0.5 $\mu\text{g}/\mu\text{l}$. It was then injected into one side of the microfluidic device and incubated for approximately 18 h overnight at 37 °C the day prior to cell seeding. Following incubation, remaining soluble GST-Nogo-66 was removed and channels were flushed with 1x PBS to remove any residual substrate. Control dishes contained cells only.

Appendix E. Neurons antibody staining protocol

Fixing

1. Aspirate media and add 2ml 4% PFA to each well. (PFA in PBS)
2. Incubate for 15 min at RT.
3. Rinse 2x with 1x PBS.
4. Continue with the following steps for staining, or store at 4° C with 1ml 1x PBS/well and parafilm plate.

Permeabilisation (0.1% tritonX100 in PBS-sterile filtered)

1. Aspirate off PBS and add 2ml of Perm. Soln to each well.
2. Incubate for 5 min at RT.
3. Rinse twice with 2ml 1xPBS.

Note: This step can be done by removing Cover Slips (CS) from each well and using 200ul of Perm. Soln and 200ul of 1xPBS for rinsing.

Removal of CSs

1. Using two sets of fine forceps carefully remove CSs from wells and place on parafilm.
2. Gently press down on either side of CS to ensure it stuck down.
3. Immediately pipette 100ul of 1xPBS onto CS to ensure cells do not dry out (have this pipette of PBS ready before removing CS from well)
4. Remove until all CSs are removed from wells and on tray with PBS.

Blocking (2% FBS in PBS- sterile filtered)

1. Aspirate PBS and add 200ul of blocking soln to each CS.
2. Incubate for 30 min at RT (during this time prepare the primary antibody complex)

Primary antibody preparation

- a) Dilute in blocking solution (150 ul/CS)
- b) Remove antibody from fridge and put on ice

- c) Hold antibody tube by lid to avoid warming
 - d) Add blocking solution to Eppendorf tube first and then add antibody
 - e) Vortex then spin down
-

Example: We want to stain the cells with primary and secondary antibodies as listed below:

- LC1 with dilution 1:250 in blocking soln. stains the growth tips of neurons (Mouse)
- NOGO A with dilution of 1:1000 in blocking soln. stains the Tpm cells (Rabbit)
- β 3 tubulin with the dilution of 1:250 stains for the tubulin (Chicken)

Assuming that we have three coverslips 150 μ L of the staining solution will be used for each CS. So, in total we will need 450 μ L.

LC1: 1:250 \rightarrow $(1/250) * 450 = 1.8 \mu$ L

NOGO A: 1:1000 \rightarrow $(1/1000) * 450 = 0.45 \mu$ L

β 3 tubulin: 1:250 \rightarrow $(1/250) * 450 = 1.8 \mu$ L

The final staining solution is prepared by adding the above amount to 450ul of blocking solution.

Note 1: For all of the above stains we have both primary and secondary. Only for Phalloidin we have one step staining.

Note 2: The three primary stains will be mixed and then the complex will be used as the primary staining step.

Note 3: The stains used for primary staining should be from different sources. Otherwise it will not work. For example, looking at the primary stains above they are from mouse, rabbit and chicken.

Note 4: The secondary antibody will be anti-mouse, anti-rabbit and anti-chicken which targets each specific primary antibody.

Note 5: The reason we did 1:1000 for Nogo is because based on our experience it is too strong.

Primary antibody

1. Aspirate PBS and add 50ul of primary antibody/blocking soln complex
2. Incubate for 1 hr at RT, or at 4° C overnight.

Secondary antibody preparation

- a) 1:500 dilution
- b) Remove secondary antibody from fridge and put on ice in dimly lit area in enclosed esky
- c) Hold tube by lid to avoid warming the tube
- d) Add blocking solution to Eppendorf tube first then add secondary antibody
- e) Vortex and spin down

Secondary antibody

1. Aspirate primary antibody and rinse 5x with 1x PBS
2. Add 50ul of secondary antibody/blocking solution complex
3. Incubate in the dark for 30 min at RT (during this time, label the glass slides for mounting)
4. Rinse 5x with PBS then mount coverslips onto labelled glass slides.

Mounting

1. Add mounting media to an Eppendorf tube and cover with foil to avoid light exposure.
2. Prepare a 50 ml falcon tube with MilliQ water and place a kimwipe nearby to absorb excess water.
3. Place a 10 ul dot of mounting onto the slide where the coverslip will be placed.

4. Using two pairs of fine forceps carefully pick up the coverslip and submerge in the milliQ water.
5. Gently dab the edge of the coverslip onto the kimwipe to remove any excess water.
6. Carefully place the coverslip cell side down onto the mounting media dot
 - a. Have the coverslip at 45° angle to the slide.
 - b. Make contact with the mounting media first on one side of the coverslip.
 - c. Using the forceps gently lower the coverslip so that the mounting media slowly spreads under the whole coverslip
 - d. Try to ensure that no bubbles are allowed to form under the coverslip
7. Repeat for all coverslips.
8. Allow coverslips and mounting media to dry in the dark (drawer/cupboard).
9. Once dry, seal edges of the coverslips with clear nail varnish.
10. Once the varnish has dried, image or store at 4° C in slide box.

Appendix F. Cleanroom photolithography

Step1: Substrate preparation

Although the fabrication is held in cleanroom, having micron size particles on the surface of the silicon wafer was probable. This is especially important considering the fine features of $\sim 5\mu\text{m}$ in the design. Therefore, at the first step, the substrate was cleaned in two steps. At the first step, the substrate was cleaned using piranha wet etch and rinsed with DI water. Next the wafer was placed inside an oxygen plasma machine to remove any organic compound on silicon substrate. The wafer was then placed on the spin coater. Before running the spin coater, it was ensured that the suction hole generates the negative pressure required to hold the wafer during spinning period. The spinning rotational speed was then set to 500 rpm. To clean the wafer before resist coating, acetone and isopropanol were applied respectively to clean the substrate and dried using an air gun. The setup of the process is shown in Fig. F.1.

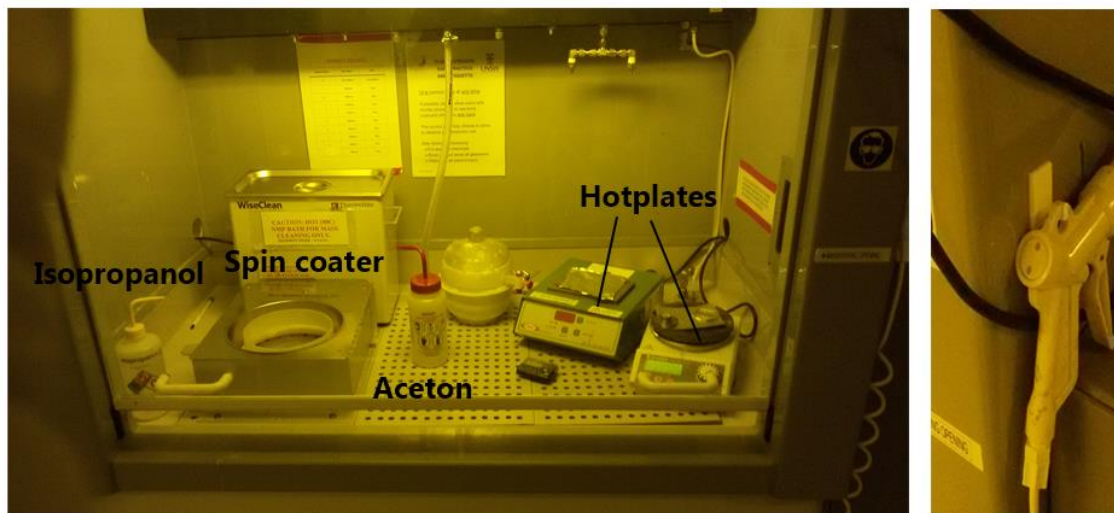


Figure F.1: Substrate preparation before photoresist coating. The procedure involves using spin coater to spin the silicon wafer while isopropanol and acetone are used to clean the surface of the wafer. Air gun is used to dry the surface.

Step 2: Coating

Coating of the silicon wafer should be done by selecting the appropriate SU-8 2000 photoresist based on the thickness and the relation between the rotational speed and the resist thickness. This relation is provided by Microchem (Fig. F.2):

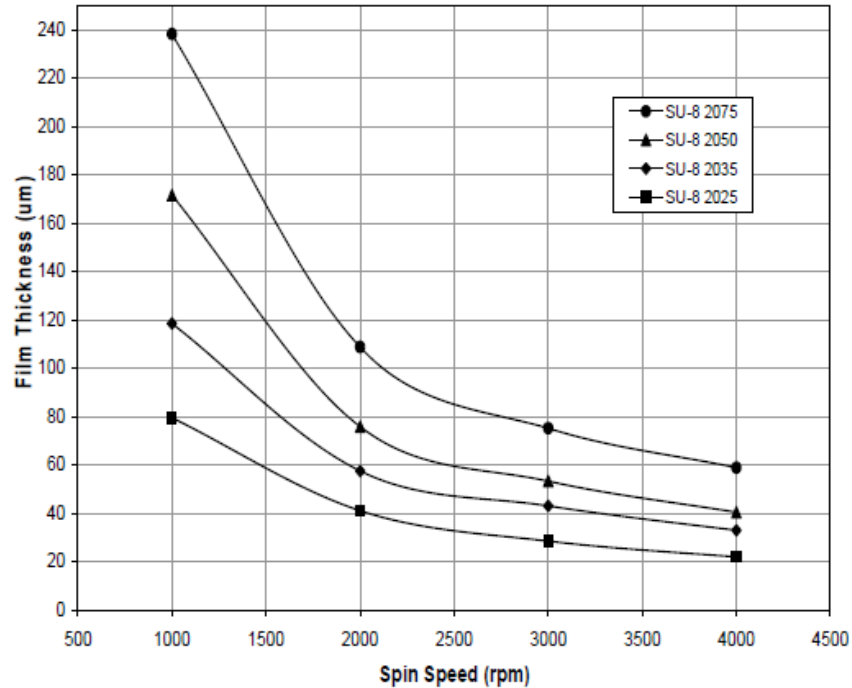


Figure F.2: Selecting the correct photoresist for spin coating in photolithography process: SU-8 2000 Spin Speed versus Thickness. Clearly as the spin speed increases, the film thickness decreases. The film thickness also depends on the viscosity of the photoresist.

Based on Fig. F.2, and the fact that the device height is $80\mu\text{m}$, SU-8 2050 photoresist at spin speed of 1900 rpm was chosen. The spin coater was covered with aluminum to absorb any residual photoresist that may splash out from the surface of the wafer. In the next step, the spin coater was programmed. For the thickness of $80\mu\text{m}$, the following program was used:

- 500 rpm for 10 seconds with acceleration of 100 rpm/second (5 seconds acceleration).

- 1900 rpm for 30 seconds with acceleration of 300 rpm/second (10 seconds acceleration).



Figure F.3: Programming the spin coater: The spinning process takes place in two steps: and initial step of 500rpm to distribute the photoresist on the surface of the wafer and a final step of 1900 rpm to make an even coating with 80 μ m thickness.

For each inch of the wafer diameter, 1ml of photoresist was dispensed on the wafer. Careful attention was made to make sure there is no bubble generated while dispensing the photoresist on the wafer (Fig. F.4). If bubble is seen on the wafer after the coating process, then any design that falls under that bubble will be defective and out of order. The uniformity of the coated resist was checked before proceeding with further steps. Before starting the spin coating, the hotplate was turned on for the soft-baking process which placed after the spin coating.



Fig. F.4: Dispensing the photoresist on silicon wafer. The bubbles generate should be avoided.

Step 3: Soft bake

The purpose of soft baking is to dry the photoresist film. To achieve this, two levelled hotplates were chosen. Looking at Table F.1 (Microchem corp.) for 80µm film thickness, the soft bake time should be 0-3 minutes at 65°C followed by 6-9 minutes at 95°C. Therefore, one hotplate was set to 65°C and the other at 95°C (Table F.1). Following soft bake, the wafer was removed from the hotplate and was set to cool down to the room temperature.

Table F.1: The recommended soft bake temperatures and times at selected film thicknesses

Thickness (µm)	Soft Bake times (minutes)	
	At 65°C	At 95°C
25-40	0-3	5-6
54-80	0-3	6-9
85-110	5	10-20
115-150	5	20-30
160-225	7	30-45

** Values advised by Microchem Corp.*

Step 4: Exposure

Karl Suss MA6 Mask Aligner (SUSS MicroTec, Germany) was used to perform the exposure step. The UV lamp power intensity on this machine is 10mW/cm². The exposure time was chosen according to the instructions by Microchem (Table F.2). For the film thickness of 80µm, the range of exposure energy is 150-215MJ/cm². Therefore, the exposure time can be found simply by dividing the exposure energy to the lamp power intensity:

$$t = \frac{150}{10} = 15 \text{ seconds} \text{ or } t = \frac{215}{10} = 21.5 \text{ seconds}$$

The exposure time of 18 seconds was therefore chosen. The photomask and the coated wafer were mounted onto the mask holder and the wafer chuck respectively (Fig. F.5). The photomask was held tight by applying vacuum. Next, the photomask was brought in full contact with the surface of the wafer. The use of contact mode was important as any distance between the UV source and the surface of the mask could lead to inaccurate channel dimensions as light is deflecting across the gap between the mask and the wafer.

Table F.2: Exposure energy according to the photoresist film thickness

Thickness (μm)	Exposure energy (mJ/cm^2)
25-40	150-160
45-80	150-215
85-110	215-240
115-150	240-260
160-225	260-350

** Values advised by Microchem Corp.*

Step 5: Post-exposure bake

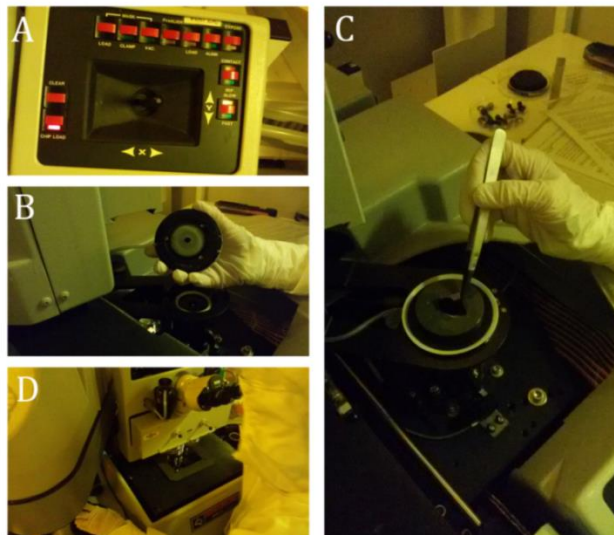


Figure F.5: Loading the mask and the silicon wafer coated with SU8 negative photoresist onto the chuck of the mask aligner and checking the correct alignment and contact between the mask and the wafer using the microscope.

Immediately after exposure, the exposed wafer is placed on hotplates following Table B.3. The correct implementation of the exposure (correct timing and intensity) was checked, as the image of the channel designs were visible after placing the wafer on the hotplate. According to Table F.3, the post-bake time for 80 μ m film thickness is 1-2 minutes at 65°C followed by 6-7 minutes at 95°C.

*Table F.3: Post-exposure baking time**

Thickness (μ m)	Post-exposure bake time at 65°C (minutes)	Post-exposure bake time at 95°C (minutes)
25-40	1	5-6
45-80	1-2	6-7
85-110	2-5	8-10
115-150	5	10-12
160-225	5	12-15

* Values advised by Microchem Corp.

Step 6: Development and hard-bake

Development is a process by which the unexposed regions of the SU-8 film are being washed away. This has been done by immersing the wafer in the SU-8 developer while agitating the container for 6 minutes followed by rinsing with IPA and drying. The rinsing step in some experiments showed white film which shows underdevelopment of the unexposed photoresist. At these conditions, the wafer was immersed in SU-8 developer for another 20 seconds to complete the development process. Hard bake was done by placing the wafer at 150°C -250°C for 5-30 minutes. The overview of the fabrication steps are shown in Fig. F.6.

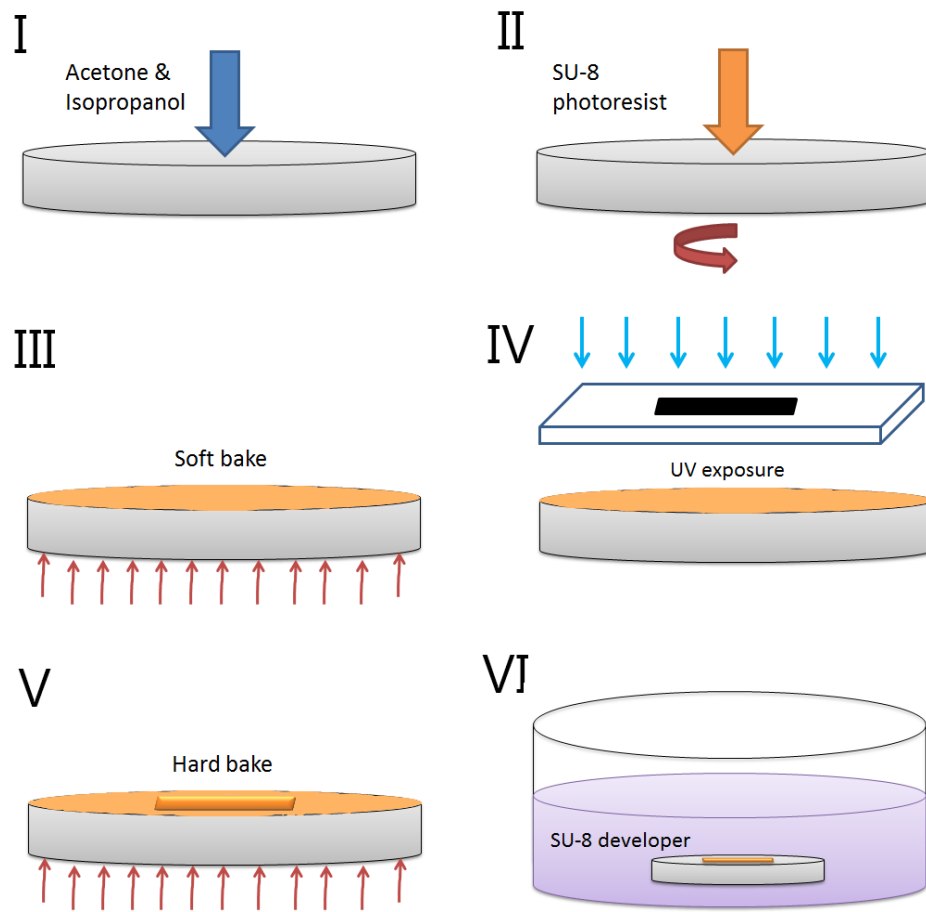


Figure F.6: Overview of the steps for fabrication of the static droplet array system using photolithography process.

References

1. Shi, J., et al., *Acoustic tweezers: patterning cells and microparticles using standing surface acoustic waves (SSAW)*. Lab on a Chip, 2009. **9**(20): p. 2890-2895.
2. Ho, C.-T., et al., *Rapid heterogeneous liver-cell on-chip patterning via the enhanced field-induced dielectrophoresis trap*. Lab on a Chip, 2006. **6**(6): p. 724-734.
3. Zhang, H. and K.-K. Liu, *Optical tweezers for single cells*. Journal of the Royal Society, Interface, 2008. **5**(24): p. 671-690.
4. Cooper, G.M., *The Cell: A Molecular Approach*. 2000: ASM Press.
5. Ruijtenberg, S. and S. van den Heuvel, *Coordinating cell proliferation and differentiation: Antagonism between cell cycle regulators and cell type-specific gene expression*. Cell cycle (Georgetown, Tex.), 2016. **15**(2): p. 196-212.
6. Scarpa, E. and R. Mayor, *Collective cell migration in development*. The Journal of Cell Biology, 2016. **212**(2): p. 143.
7. Aman, A. and T. Piotrowski, *Cell migration during morphogenesis*. Developmental Biology, 2010. **341**(1): p. 20-33.
8. Lim, Y.Z. and A.P. South, *Tumour–stroma crosstalk in the development of squamous cell carcinoma*. The International Journal of Biochemistry & Cell Biology, 2014. **53**: p. 450-458.
9. McKenna, W.L., et al., *Tbr1 and Fezf2 Regulate Alternate Corticofugal Neuronal Identities during Neocortical Development*. The Journal of Neuroscience, 2011. **31**(2): p. 549.
10. Xie, A.W., et al., *Controlled Self-assembly of Stem Cell Aggregates Instructs Pluripotency and Lineage Bias*. Scientific Reports, 2017. **7**(1): p. 14070.
11. Burrell, R.A., et al., *The causes and consequences of genetic heterogeneity in cancer evolution*. Nature, 2013. **501**: p. 338.
12. Altschuler, S.J. and L.F. Wu, *Cellular Heterogeneity: Do Differences Make a Difference?* Cell, 2010. **141**(4): p. 559-563.
13. Pierschbacher, M.D. and E. Ruoslahti, *Cell attachment activity of fibronectin can be duplicated by small synthetic fragments of the molecule*. Nature, 1984. **309**(5963): p. 30-33.
14. Kane, R.S., et al., *Patterning proteins and cells using soft lithography*. Biomaterials, 1999. **20**(23): p. 2363-2376.
15. Mrksich, M., *A surface chemistry approach to studying cell adhesion*. Chemical Society Reviews, 2000. **29**(4): p. 267-273.
16. Rodriguez, N.M., et al., *Micropatterned Multicolor Dynamically Adhesive Substrates to Control Cell Adhesion and Multicellular Organization*. Langmuir, 2014. **30**(5): p. 1327-1335.
17. Dickinson, L.E., et al., *Patterning microscale extracellular matrices to study endothelial and cancer cell interactions in vitro*. Lab on a Chip, 2012. **12**(21): p. 4244-4248.
18. Stumpf, F., et al., *Single-cell PCR of genomic DNA enabled by automated single-cell printing for cell isolation*. Biosensors and Bioelectronics, 2015. **69**: p. 301-306.
19. Gross, A., et al., *Single-Cell Printer: Automated, On Demand, and Label Free*. Journal of Laboratory Automation, 2013. **18**(6): p. 504-518.
20. Ino, K., et al., *Cell culture arrays using magnetic force-based cell patterning for dynamic single cell analysis*. Lab on a Chip, 2008. **8**(1): p. 134-142.
21. Agresti, J.J., et al., *Ultrahigh-throughput screening in drop-based microfluidics for directed evolution*. Proceedings of the National Academy of Sciences, 2010. **107**(9): p. 4004.
22. Wiklund, M., *Acoustofluidics 12: Biocompatibility and cell viability in microfluidic acoustic resonators*. Lab on a Chip, 2012. **12**(11): p. 2018-2028.

23. Yang, L., et al., *Effects of Dielectrophoresis on Growth, Viability and Immunoreactivity of Listeria monocytogenes*. Journal of Biological Engineering, 2008. **2**(1): p. 6.
24. Rasmussen, M.B., L.B. Oddershede, and H. Siegumfeldt, *Optical tweezers cause physiological damage to Escherichia coli and Listeria bacteria*. Applied and environmental microbiology, 2008. **74**(8): p. 2441-2446.
25. Guo, F., et al., *Three-dimensional manipulation of single cells using surface acoustic waves*. Proceedings of the National Academy of Sciences, 2016. **113**(6): p. 1522.
26. Radel, S., et al., *Breakdown of immobilisation/separation and morphology changes of yeast suspended in water-rich ethanol mixtures exposed to ultrasonic plane standing waves*. Bioseparation, 2000. **9**(6): p. 369-377.
27. Tung, Y.-C., et al., *High-throughput 3D spheroid culture and drug testing using a 384 hanging drop array*. Analyst, 2011. **136**(3): p. 473-478.
28. Kobel, S., et al., *Optimization of microfluidic single cell trapping for long-term on-chip culture*. Lab on a Chip, 2010. **10**(7): p. 857-863.
29. Hassanzadeh-Barforoushi, A., et al., *A rapid co-culture stamping device for studying intercellular communication*. Scientific Reports, 2016. **6**: p. 35618.
30. Stefen, H., et al., *A Novel Microfluidic Device-Based Neurite Outgrowth Inhibition Assay Reveals the Neurite Outgrowth-Promoting Activity of Tropomyosin Tpm3.1 in Hippocampal Neurons*. Cellular and Molecular Neurobiology, 2018. **38**(8): p. 1557-1563.
31. Hassanzadeh-Barforoushi, A., et al., *Static droplet array for culturing single live adherent cells in an isolated chemical microenvironment*. Lab on a Chip, 2018. **18**(15): p. 2156-2166.
32. Bhatia, S.N., M.L. Yarmush, and M. Toner, *Controlling cell interactions by micropatterning in co-cultures: Hepatocytes and 3T3 fibroblasts*. Journal of Biomedical Materials Research: An Official Journal of The Society for Biomaterials and The Japanese Society for Biomaterials, 1997. **34**(2): p. 189-199.
33. Bourkoula, A., et al., *Guided cell adhesion, orientation, morphology and differentiation on silicon substrates photolithographically micropatterned with a cell-repellent cross-linked poly (vinyl alcohol) film*. Biomedical Materials, 2018. **14**(1): p. 014101.
34. Théry, M. and M. Piel, *Adhesive micropatterns for cells: a microcontact printing protocol*. Cold Spring Harbor Protocols, 2009. **2009**(7): p. pdb. prot5255.
35. Tsuda, Y., et al., *Heterotypic cell interactions on a dually patterned surface*. Biochemical and Biophysical Research Communications, 2006. **348**(3): p. 937-944.
36. Li, S., et al., *Standing Surface Acoustic Wave Based Cell Coculture*. Analytical Chemistry, 2014. **86**(19): p. 9853-9859.
37. Ruiz, S.A. and C.S. Chen, *Microcontact printing: A tool to pattern*. Soft Matter, 2007. **3**(2): p. 168-177.
38. Tien, J., C.M. Nelson, and C.S. Chen, *Fabrication of aligned microstructures with a single elastomeric stamp*. Proceedings of the National Academy of Sciences, 2002. **99**(4): p. 1758-1762.
39. Wu, C., et al., *Lift-off cell lithography for cell patterning with clean background*. Lab on a Chip, 2018. **18**(20): p. 3074-3078.
40. Frimat, J.-P., et al., *Plasma stencilling methods for cell patterning*. Analytical and bioanalytical chemistry, 2009. **395**(3): p. 601-609.
41. Yousaf, M.N., B.T. Houseman, and M. Mrksich, *Turning On Cell Migration with Electroactive Substrates*. Angewandte Chemie, 2001. **113**(6): p. 1127-1130.
42. Kaji, H., et al., *In Situ Control of Cellular Growth and Migration on Substrates Using Microelectrodes*. Journal of the American Chemical Society, 2004. **126**(46): p. 15026-15027.
43. Akiyama, H., et al., *Fabrication of complex three-dimensional tissue architectures using a magnetic force-based cell patterning technique*. Biomedical Microdevices, 2009. **11**(4): p. 713-721.

44. Yuan, J. and P.A. Sims, *An Automated Microwell Platform for Large-Scale Single Cell RNA-Seq*. Scientific Reports, 2016. **6**: p. 33883.
45. Abali, F., et al., *Isolation of single cells for protein therapeutics using microwell selection and Surface Plasmon Resonance imaging*. Analytical Biochemistry, 2017. **531**: p. 45-47.
46. Astolfi, M., et al., *Micro-dissected tumor tissues on chip: an ex vivo method for drug testing and personalized therapy*. Lab on a Chip, 2016. **16**(2): p. 312-325.
47. Patra, B., et al., *Drug testing and flow cytometry analysis on a large number of uniform sized tumor spheroids using a microfluidic device*. Scientific reports, 2016. **6**: p. 21061-21061.
48. Kim, S.H., et al., *Electroactive Microwell Arrays for Highly Efficient Single-Cell Trapping and Analysis*. Small, 2011. **7**(22): p. 3239-3247.
49. Ameri, S.K., P.K. Singh, and S. Sonkusale, *Utilization of graphene electrode in transparent microwell arrays for high throughput cell trapping and lysis*. Biosensors and Bioelectronics, 2014. **61**: p. 625-630.
50. Bocchi, M., et al., *Inverted open microwells for cell trapping, cell aggregate formation and parallel recovery of live cells*. Lab on a Chip, 2012. **12**(17): p. 3168-3176.
51. Ruppen, J., et al., *A microfluidic platform for chemoresistive testing of multicellular pleural cancer spheroids*. Lab on a Chip, 2014. **14**(6): p. 1198-1205.
52. Collins, D.J., et al., *Two-dimensional single-cell patterning with one cell per well driven by surface acoustic waves*. Nature Communications, 2015. **6**: p. 8686.
53. Jing, T., et al., *Jetting microfluidics with size-sorting capability for single-cell protease detection*. Biosensors and Bioelectronics, 2015. **66**: p. 19-23.
54. Occhetta, P., et al., *Design of a microfluidic strategy for trapping and screening single cells*. Medical Engineering & Physics, 2016. **38**(1): p. 33-40.
55. Chung, K., et al., *A microfluidic array for large-scale ordering and orientation of embryos*. Nature Methods, 2010. **8**: p. 171.
56. Frimat, J.-P., et al., *A microfluidic array with cellular valving for single cell co-culture*. Lab on a Chip, 2011. **11**(2): p. 231-237.
57. Grist, S.M., et al., *On-chip clearing of arrays of 3-D cell cultures and micro-tissues*. Biomicrofluidics, 2016. **10**(4): p. 044107.
58. Lee, J. and M.A. Burns, *Asymmetric traps array for particle transport*. RSC Advances, 2015. **5**(5): p. 3358-3364.
59. Liberale, C., et al., *Integrated microfluidic device for single-cell trapping and spectroscopy*. Scientific reports, 2013. **3**: p. 1258-1258.
60. Huang, N.-T., Y.-J. Hwong, and R.L. Lai, *A microfluidic microwell device for immunomagnetic single-cell trapping*. Microfluidics and Nanofluidics, 2018. **22**(2): p. 16.
61. Kim, M.G., et al., *Label-free analysis of the characteristics of a single cell trapped by acoustic tweezers*. Scientific Reports, 2017. **7**(1): p. 14092.
62. Teh, S.-Y., et al., *Droplet microfluidics*. Lab on a Chip, 2008. **8**(2): p. 198-220.
63. Leman, M., et al., *Droplet-based microfluidics at the femtolitre scale*. Lab on a Chip, 2015. **15**(3): p. 753-765.
64. Fu, H., W. Zeng, and S. Li, *Quantitative study of the production rate of droplets in a T-junction microdroplet generator*. Journal of Micromechanics and Microengineering, 2017. **27**(12): p. 125020.
65. Collins, D.J., et al., *The Poisson distribution and beyond: methods for microfluidic droplet production and single cell encapsulation*. Lab on a Chip, 2015. **15**(17): p. 3439-3459.
66. Holtze, C., A.S. Weisse, and M. Vranceanu, *Commercial Value and Challenges of Drop-Based Microfluidic Screening Platforms—An Opinion*. Micromachines, 2017. **8**(6).
67. Kaminski, T.S. and P. Garstecki, *Controlled droplet microfluidic systems for multistep chemical and biological assays*. Chemical Society Reviews, 2017. **46**(20): p. 6210-6226.

68. Simon, M.G. and A.P. Lee, *Microfluidic Droplet Manipulations and Their Applications*, in *Microdroplet Technology: Principles and Emerging Applications in Biology and Chemistry*, P. Day, A. Manz, and Y. Zhang, Editors. 2012, Springer New York: New York, NY. p. 23-50.
69. Wang, J., et al., *Fluid mixing in droplet-based microfluidics with a serpentine microchannel*. RSC Advances, 2015. **5**(126): p. 104138-104144.
70. Sgro, A.E. and D.T. Chiu, *Droplet freezing, docking, and the exchange of immiscible phase and surfactant around frozen droplets*. Lab on a chip, 2010. **10**(14): p. 1873-1877.
71. Sun, M., S.S. Bithi, and S.A. Vanapalli, *Microfluidic static droplet arrays with tuneable gradients in material composition*. Lab on a Chip, 2011. **11**(23): p. 3949-3952.
72. Safavieh, R. and D. Juncker, *Capillarics: pre-programmed, self-powered microfluidic circuits built from capillary elements*. Lab on a Chip, 2013. **13**(21): p. 4180-4189.
73. Maria, M.S., et al., *Capillary flow-driven microfluidic device with wettability gradient and sedimentation effects for blood plasma separation*. Scientific Reports, 2017. **7**: p. 43457.
74. Epifania, R., et al., *Capillary-driven microfluidic device with integrated nanoporous microbeads for ultrarapid biosensing assays*. Sensors and Actuators B: Chemical, 2018. **265**: p. 452-458.
75. de Boer, A.R., et al., *A microfluidic-based enzymatic assay for bioactivity screening combined with capillary liquid chromatography and mass spectrometry*. Lab on a Chip, 2005. **5**(11): p. 1286-1292.
76. Reis, N.M., et al., *Lab on a stick: multi-analyte cellular assays in a microfluidic dipstick*. Lab on a Chip, 2016. **16**(15): p. 2891-2899.
77. Walker, G.M. and D.J. Beebe, *A passive pumping method for microfluidic devices*. Lab on a Chip, 2002. **2**(3): p. 131-134.
78. Berthier, E. and D.J. Beebe, *Flow rate analysis of a surface tension driven passive micropump*. Lab on a Chip, 2007. **7**(11): p. 1475-1478.
79. Toepke, M.W., V.V. Abhyankar, and D.J. Beebe, *Microfluidic logic gates and timers*. Lab on a Chip, 2007. **7**(11): p. 1449-1453.
80. Eijkel, J.C.T. and A. van den Berg, *Water in micro- and nanofluidics systems described using the water potential*. Lab on a Chip, 2005. **5**(11): p. 1202-1209.
81. Lynn, N.S. and D.S. Dandy, *Passive microfluidic pumping using coupled capillary/evaporation effects*. Lab on a chip, 2009. **9**(23): p. 3422-3429.
82. Zimmermann, M., et al., *Capillary pumps for autonomous capillary systems*. Lab on a Chip, 2007. **7**(1): p. 119-125.
83. Safavieh, R., A. Tamayol, and D. Juncker, *Serpentine and leading-edge capillary pumps for microfluidic capillary systems*. Microfluidics and Nanofluidics, 2015. **18**(3): p. 357-366.
84. Juncker, D., et al., *Autonomous Microfluidic Capillary System*. Analytical Chemistry, 2002. **74**(24): p. 6139-6144.
85. Wolf, M., et al., *Simultaneous detection of C-reactive protein and other cardiac markers in human plasma using micromosaic immunoassays and self-regulating microfluidic networks*. Biosensors and Bioelectronics, 2004. **19**(10): p. 1193-1202.
86. Olanrewaju, A.O., et al., *Microfluidic Capillary Circuit for Rapid and Facile Bacteria Detection*. Analytical Chemistry, 2017. **89**(12): p. 6846-6853.
87. Casavant, B.P., et al., *Suspended microfluidics*. Proceedings of the National Academy of Sciences, 2013. **110**(25): p. 10111.
88. Berthier, J., et al., *On the halt of spontaneous capillary flows in diverging open channels*. Medical Engineering & Physics, 2017. **48**: p. 75-80.
89. Handique, K., et al., *Nanoliter Liquid Metering in Microchannels Using Hydrophobic Patterns*. Analytical Chemistry, 2000. **72**(17): p. 4100-4109.

90. Thio, T.H.G., et al., *Theoretical development and critical analysis of burst frequency equations for passive valves on centrifugal microfluidic platforms*. Medical & biological engineering & computing, 2013. **51**(5): p. 525-535.
91. Cho, H., et al., *How the capillary burst microvalve works*. Journal of Colloid and Interface Science, 2007. **306**(2): p. 379-385.
92. Kazemzadeh, A., et al., *The effect of contact angles and capillary dimensions on the burst frequency of super hydrophilic and hydrophilic centrifugal microfluidic platforms, a CFD study*. PloS one, 2013. **8**(9): p. e73002-e73002.
93. Choi, J., et al., *Thin, Soft, Skin-Mounted Microfluidic Networks with Capillary Bursting Valves for Chrono-Sampling of Sweat*. Advanced Healthcare Materials, 2017. **6**(5): p. 1601355.
94. Glière, A. and C. Delattre, *Modeling and fabrication of capillary stop valves for planar microfluidic systems*. Sensors and Actuators A: Physical, 2006. **130-131**: p. 601-608.
95. Papadimitriou, V.A., et al., *3D capillary stop valves for versatile patterning inside microfluidic chips*. Analytica Chimica Acta, 2018. **1000**: p. 232-238.
96. Taher, A., et al., *Analytical, numerical and experimental study on capillary flow in a microchannel traversing a backward facing step*. International Journal of Multiphase Flow, 2018. **107**: p. 221-229.
97. Hitzbleck, M., et al., *Capillary soft valves for microfluidics*. Lab on a Chip, 2012. **12**(11): p. 1972-1978.
98. Hitzbleck, M. and E. Delamarche, *Advanced Capillary Soft Valves for Flow Control in Self-Driven Microfluidics*. Vol. 4. 2013. 1-8.
99. Melin, J., et al., *A liquid-triggered liquid microvalve for on-chip flow control*. Sensors and Actuators B: Chemical, 2004. **100**(3): p. 463-468.
100. Zimmermann, M., P. Hunziker, and E. Delamarche, *Valves for autonomous capillary systems*. Microfluidics and Nanofluidics, 2008. **5**(3): p. 395-402.
101. Hagemeyer, B., F. Zechall, and M. Stelzle, *Towards plug and play filling of microfluidic devices by utilizing networks of capillary stop valves*. Biomicrofluidics, 2014. **8**(5): p. 056501-056501.
102. Cohen, D.E., et al., *Self-digitization of sample volumes*. Analytical chemistry, 2010. **82**(13): p. 5707-5717.
103. Gumuscu, B., et al., *Large scale patterning of hydrogel microarrays using capillary pinning*. Lab on a Chip, 2015. **15**(3): p. 664-667.
104. Schneider, T., et al., *Self-Digitization of Samples into a High-Density Microfluidic Bottom-Well Array*. Analytical Chemistry, 2013. **85**(21): p. 10417-10423.
105. Xu, Y., et al., *A fully sealed plastic chip for multiplex PCR and its application in bacteria identification*. Lab on a Chip, 2015. **15**(13): p. 2826-2834.
106. Sposito, A.J. and D.L. DeVoe, *Staggered trap arrays for robust microfluidic sample digitization*. Lab on a Chip, 2017. **17**(23): p. 4105-4112.
107. Boukellal, H., et al., *Simple, robust storage of drops and fluids in a microfluidic device*. Lab on a Chip, 2009. **9**(2): p. 331-338.
108. Sun, M. and S.A. Vanapalli, *Generation of Chemical Concentration Gradients in Mobile Droplet Arrays via Fragmentation of Long Immiscible Diluting Plugs*. Analytical Chemistry, 2013. **85**(4): p. 2044-2048.
109. Dewan, A., et al., *Growth kinetics of microalgae in microfluidic static droplet arrays*. Biotechnology and Bioengineering, 2012. **109**(12): p. 2987-2996.
110. Gumuscu, B., et al., *Compartmentalized 3D Tissue Culture Arrays under Controlled Microfluidic Delivery*. Scientific Reports, 2017. **7**(1): p. 3381.
111. Zervantonakis, I.K., et al., *Three-dimensional microfluidic model for tumor cell intravasation and endothelial barrier function*. Proceedings of the National Academy of Sciences of the United States of America, 2012. **109**(34): p. 13515-13520.
112. Yu, Y.J., et al., *Hydrogel-incorporating unit in a well: 3D cell culture for high-throughput analysis*. Lab on a Chip, 2018. **18**(17): p. 2604-2613.

113. Polacheck, W.J., J.L. Charest, and R.D. Kamm, *Interstitial flow influences direction of tumor cell migration through competing mechanisms*. Proceedings of the National Academy of Sciences of the United States of America, 2011. **108**(27): p. 11115-11120.
114. Lee, S.H., et al., *Capillary Based Patterning of Cellular Communities in Laterally Open Channels*. Analytical Chemistry, 2010. **82**(7): p. 2900-2906.
115. Shemesh, J., et al., *Stationary nanoliter droplet array with a substrate of choice for single adherent/nonadherent cell incubation and analysis*. Proceedings of the National Academy of Sciences, 2014. **111**(31): p. 11293.
116. Avesar, J., et al., *Nanoliter Cell Culture Array with Tunable Chemical Gradients*. Analytical Chemistry, 2018. **90**(12): p. 7480-7488.
117. Avesar, J., et al., *Rapid phenotypic antimicrobial susceptibility testing using nanoliter arrays*. Proceedings of the National Academy of Sciences, 2017. **114**(29): p. E5787.
118. Lee, Y., et al., *Microfluidics within a well: an injection-molded plastic array 3D culture platform*. Lab on a Chip, 2018. **18**(16): p. 2433-2440.
119. Virumbrales-Muñoz, M., et al., *Multiwell capillarity-based microfluidic device for the study of 3D tumour tissue-2D endothelium interactions and drug screening in co-culture models*. Scientific Reports, 2017. **7**(1): p. 11998.
120. Parlato, S., et al., *3D Microfluidic model for evaluating immunotherapy efficacy by tracking dendritic cell behaviour toward tumor cells*. Scientific Reports, 2017. **7**(1): p. 1093.
121. Yang, K., et al., *A dual-docking microfluidic cell migration assay (D(2)-Chip) for testing neutrophil chemotaxis and the memory effect*. Integrative biology : quantitative biosciences from nano to macro, 2017. **9**(4): p. 303-312.
122. Zhang, M., et al., *A simple microfluidic strategy for cell migration assay in an in vitro wound-healing model*. Wound Repair and Regeneration, 2013. **21**(6): p. 897-903.
123. Menon, N.V., et al., *Microfluidic Assay To Study the Combinatorial Impact of Substrate Properties on Mesenchymal Stem Cell Migration*. ACS Applied Materials & Interfaces, 2015. **7**(31): p. 17095-17103.
124. Gladkov, A., et al., *Design of Cultured Neuron Networks in vitro with Predefined Connectivity Using Asymmetric Microfluidic Channels*. Scientific Reports, 2017. **7**(1): p. 15625.
125. Honegger, T., et al., *Microfluidic neurite guidance to study structure-function relationships in topologically-complex population-based neural networks*. Scientific reports, 2016. **6**: p. 28384-28384.
126. Shi, P., et al., *Combined microfluidics/protein patterning platform for pharmacological interrogation of axon pathfinding*. Lab on a chip, 2010. **10**(8): p. 1005-1010.
127. Gu, L., et al., *Microfluidic control of axonal guidance*. Scientific Reports, 2014. **4**: p. 6457.
128. Nédelec, S., et al., *Concentration-dependent requirement for local protein synthesis in motor neuron subtype-specific response to axon guidance cues*. The Journal of neuroscience : the official journal of the Society for Neuroscience, 2012. **32**(4): p. 1496-1506.
129. Konry, T., et al., *Droplet-based microfluidic platforms for single T cell secretion analysis of IL-10 cytokine*. Biosensors & bioelectronics, 2011. **26**(5): p. 2707-2710.
130. Ismail, A.E., et al., *Interfacial Structure and Dynamics of Siloxane Systems: PDMS-Vapor and PDMS-Water*. Macromolecules, 2009. **42**(8): p. 3186-3194.
131. Berthier, J., *Chapter 2 - Theory of Wetting**, in *Micro-Drops and Digital Microfluidics (Second Edition)*. 2013, William Andrew Publishing. p. 7-73.
132. Muldur, S.K., et al., *Modulation of surface bio-functionality by using gold nanostructures on protein repellent surfaces*. RSC Advances, 2015. **5**(101): p. 83187-83196.
133. Roccio, M., S. Gobaa, and M.P. Lutolf, *High-throughput clonal analysis of neural stem cells in microarrayed artificial niches*. Integrative Biology, 2012. **4**(4): p. 391-400.

134. Wang, X., et al., *Regulating the stemness of mesenchymal stem cells by tuning micropattern features*. Journal of Materials Chemistry B, 2016. **4**(1): p. 37-45.
135. Kundu, A., et al., *Superimposed topographic and chemical cues synergistically guide neurite outgrowth*. Lab on a Chip, 2013. **13**(15): p. 3070-3081.
136. Pan, Z., et al., *Control of cell nucleus shapes via micropillar patterns*. Biomaterials, 2012. **33**(6): p. 1730-1735.
137. Scadden, D.T., *The stem-cell niche as an entity of action*. Nature, 2006. **441**(7097): p. 1075-1079.
138. Yeon, J.H., et al., *In vitro formation and characterization of a perfusable three-dimensional tubular capillary network in microfluidic devices*. Lab on a Chip, 2012. **12**(16): p. 2815-2822.
139. Bhowmick, N.A., E.G. Neilson, and H.L. Moses, *Stromal fibroblasts in cancer initiation and progression*. Nature, 2004. **432**(7015): p. 332-337.
140. Calvo, F., et al., *Mechanotransduction and YAP-dependent matrix remodelling is required for the generation and maintenance of cancer-associated fibroblasts*. Nat Cell Biol, 2013. **15**(6): p. 637-646.
141. Erez, N., et al., *Cancer-Associated Fibroblasts Are Activated in Incipient Neoplasia to Orchestrate Tumor-Promoting Inflammation in an NF- κ B-Dependent Manner*. Cancer Cell, 2010. **17**(2): p. 135-147.
142. Xie, Y., et al., *Optoacoustic tweezers: a programmable, localized cell concentrator based on opto-thermally generated, acoustically activated, surface bubbles*. Lab on a Chip, 2013. **13**(9): p. 1772-1779.
143. Ding, X., et al., *Tunable patterning of microparticles and cells using standing surface acoustic waves*. Lab on a Chip, 2012. **12**(14): p. 2491-2497.
144. Wood, C.D., et al., *Alignment of particles in microfluidic systems using standing surface acoustic waves*. Applied Physics Letters, 2008. **92**(4): p. 044104.
145. Takayama, S., et al., *Patterning cells and their environments using multiple laminar fluid flows in capillary networks*. Proceedings of the National Academy of Sciences, 1999. **96**(10): p. 5545-5548.
146. Jiang, X., et al., *A General Method for Patterning Gradients of Biomolecules on Surfaces Using Microfluidic Networks*. Analytical Chemistry, 2005. **77**(8): p. 2338-2347.
147. Dertinger, S.K.W., et al., *Gradients of substrate-bound laminin orient axonal specification of neurons*. Proceedings of the National Academy of Sciences, 2002. **99**(20): p. 12542.
148. Chen, Q., et al., *Targeted isolation and analysis of single tumor cells with aptamer-encoded microwell array on microfluidic device*. Lab on a Chip, 2012. **12**(24): p. 5180-5185.
149. Mrksich, M., et al., *Using Microcontact Printing to Pattern the Attachment of Mammalian Cells to Self-Assembled Monolayers of Alkanethiolates on Transparent Films of Gold and Silver*. Experimental Cell Research, 1997. **235**(2): p. 305-313.
150. Folch, A. and M. Toner, *Cellular Micropatterns on Biocompatible Materials*. Biotechnology Progress, 1998. **14**(3): p. 388-392.
151. Petrelli, A., et al., *Nano-volume drop patterning for rapid on-chip neuronal connectivity assays*. Lab on a Chip, 2013. **13**(22): p. 4419-4429.
152. Folch, A., et al., *Microfabricated elastomeric stencils for micropatterning cell cultures*. Journal of Biomedical Materials Research, 2000. **52**(2): p. 346-353.
153. Wright, D., et al., *Reusable, reversibly sealable parylene membranes for cell and protein patterning*. Journal of Biomedical Materials Research Part A, 2008. **85A**(2): p. 530-538.
154. Ostuni, E., et al., *Patterning Mammalian Cells Using Elastomeric Membranes*. Langmuir, 2000. **16**(20): p. 7811-7819.

155. Yousaf, M.N., B.T. Houseman, and M. Mrksich, *Using electroactive substrates to pattern the attachment of two different cell populations*. Proceedings of the National Academy of Sciences, 2001. **98**(11): p. 5992-5996.
156. Yamato, M., et al., *Thermally responsive polymer-grafted surfaces facilitate patterned cell seeding and co-culture*. Biomaterials, 2002. **23**(2): p. 561-567.
157. Chiu, D.T., et al., *Patterned deposition of cells and proteins onto surfaces by using three-dimensional microfluidic systems*. Proceedings of the National Academy of Sciences, 2000. **97**(6): p. 2408-2413.
158. Mathison, M. and T.K. Rosengart, *Heart regeneration: The endothelial cell comes first*. The Journal of thoracic and cardiovascular surgery, 2018. **155**(3): p. 1128-1129.
159. Chong, James J.H., et al., *Adult Cardiac-Resident MSC-like Stem Cells with a Proepicardial Origin*. Cell Stem Cell, 2011. **9**(6): p. 527-540.
160. Okabe, M., et al., *'Green mice' as a source of ubiquitous green cells*. FEBS Letters, 1997. **407**(3): p. 313-319.
161. Nishiyama, T., et al., *Functional Analysis of an Established Mouse Vascular Endothelial Cell Line*. Journal of Vascular Research, 2007. **44**(2): p. 138-148.
162. Halldorsson, S., et al., *Advantages and challenges of microfluidic cell culture in polydimethylsiloxane devices*. Biosensors and Bioelectronics, 2015. **63**: p. 218-231.
163. Foxman, E.F., E.J. Kunkel, and E.C. Butcher, *Integrating Conflicting Chemotactic Signals: The Role of Memory in Leukocyte Navigation*. The Journal of Cell Biology, 1999. **147**(3): p. 577-588.
164. Bersini, S., et al., *A microfluidic 3D in vitro model for specificity of breast cancer metastasis to bone*. Biomaterials, 2014. **35**(8): p. 2454-2461.
165. Young, E.W.K., *Cells, tissues, and organs on chips: challenges and opportunities for the cancer tumor microenvironment*. Integrative Biology, 2013. **5**(9): p. 1096-1109.
166. Sticker, D., et al., *Microfluidic Migration and Wound Healing Assay Based on Mechanically Induced Injuries of Defined and Highly Reproducible Areas*. Analytical Chemistry, 2017. **89**(4): p. 2326-2333.
167. Allazetta, S. and M.P. Lutolf, *Stem cell niche engineering through droplet microfluidics*. Current Opinion in Biotechnology, 2015. **35**: p. 86-93.
168. Li, L., et al., *Spatiotemporally Controlled and Multifactor Involved Assay of Neuronal Compartment Regeneration after Chemical Injury in an Integrated Microfluidics*. Analytical Chemistry, 2012. **84**(15): p. 6444-6453.
169. Millet, L.J. and M.U. Gillette, *New perspectives on neuronal development via microfluidic environments*. Trends in Neurosciences, 2012. **35**(12): p. 752-761.
170. Knöll, B., et al., *Stripe assay to examine axonal guidance and cell migration*. Nature Protocols, 2007. **2**: p. 1216.
171. Monnier, P.P., et al., *The Rho/ROCK pathway mediates neurite growth-inhibitory activity associated with the chondroitin sulfate proteoglycans of the CNS glial scar*. Molecular and Cellular Neuroscience, 2003. **22**(3): p. 319-330.
172. Offenhäusser, A., et al., *Microcontact printing of proteins for neuronal cell guidance*. Soft Matter, 2007. **3**(3): p. 290-298.
173. Vogt, A.K., et al., *Impact of micropatterned surfaces on neuronal polarity*. Journal of Neuroscience Methods, 2004. **134**(2): p. 191-198.
174. Scott, M.A., Z.D. Wissner-Gross, and M.F. Yanik, *Ultra-rapid laser protein micropatterning: screening for directed polarization of single neurons*. Lab on a Chip, 2012. **12**(12): p. 2265-2276.
175. Pujic, Z., et al., *Analysis of the growth cone turning assay for studying axon guidance*. Journal of Neuroscience Methods, 2008. **170**(2): p. 220-228.
176. Pinato, G., et al., *Less than 5 Netrin-1 molecules initiate attraction but 200 Sema3A molecules are necessary for repulsion*. Scientific Reports, 2012. **2**: p. 675.
177. Dudanova, I., et al., *Genetic Evidence for a Contribution of EphA:EphrinA Reverse Signaling to Motor Axon Guidance*. The Journal of Neuroscience, 2012. **32**(15): p. 5209.

178. Dupin, I., M. Dahan, and V. Studer, *Investigating Axonal Guidance with Microdevice-Based Approaches*. The Journal of Neuroscience, 2013. **33**(45): p. 17647.
179. Kang, W., et al., *Microfluidic device for stem cell differentiation and localized electroporation of postmitotic neurons*. Lab on a Chip, 2014. **14**(23): p. 4486-4495.
180. Marom, A., et al., *Microfluidic Chip for Site-Specific Neuropharmacological Treatment and Activity Probing of 3D Neuronal "Optonet" Cultures*. Advanced Healthcare Materials, 2015. **4**(10): p. 1478-1483.
181. Hosmane, S., et al., *Valve-based microfluidic compression platform: single axon injury and regrowth*. Lab on a Chip, 2011. **11**(22): p. 3888-3895.
182. Hellman, A.N., et al., *Examination of axonal injury and regeneration in micropatterned neuronal culture using pulsed laser microbeam dissection*. Lab on a Chip, 2010. **10**(16): p. 2083-2092.
183. Yang, I.H., et al., *Compartmentalized microfluidic culture platform to study mechanism of paclitaxel-induced axonal degeneration*. Experimental Neurology, 2009. **218**(1): p. 124-128.
184. Taylor, A.M., et al., *A microfluidic culture platform for CNS axonal injury, regeneration and transport*. Nature Methods, 2005. **2**: p. 599.
185. Park, J., et al., *Microfluidic compartmentalized co-culture platform for CNS axon myelination research*. Biomedical Microdevices, 2009. **11**(6): p. 1145.
186. Hosmane, S., et al., *Circular compartmentalized microfluidic platform: Study of axon–glia interactions*. Lab on a Chip, 2010. **10**(6): p. 741-747.
187. Vahidi, B., et al., *Microfluidic-based strip assay for testing the effects of various surface-bound inhibitors in spinal cord injury*. Journal of Neuroscience Methods, 2008. **170**(2): p. 188-196.
188. Acebes, A. and A. Ferrús, *Cellular and molecular features of axon collaterals and dendrites*. Trends in Neurosciences, 2000. **23**(11): p. 557-565.
189. Curthoys, N.M., et al., *Tropomyosins induce neuritogenesis and determine neurite branching patterns in B35 neuroblastoma cells*. Molecular and Cellular Neuroscience, 2014. **58**: p. 11-21.
190. Fath, T., et al., *New aspects of tropomyosin-regulated neuritogenesis revealed by the deletion of Tm5NM1 and 2*. European Journal of Cell Biology, 2010. **89**(7): p. 489-498.
191. Schevzov, G., et al., *Specific features of neuronal size and shape are regulated by tropomyosin isoforms*. Molecular biology of the cell, 2005. **16**(7): p. 3425-3437.
192. Fath, T., et al., *Primary support cultures of hippocampal and substantia nigra neurons*. Nature Protocols, 2008. **4**: p. 78.
193. Saadatpour, A., et al., *Single-cell analysis in cancer genomics*. Trends in genetics : TIG, 2015. **31**(10): p. 576-586.
194. Navin, N.E., *The first five years of single-cell cancer genomics and beyond*. Genome Research, 2015. **25**(10): p. 1499-1507.
195. Wen, L. and F. Tang, *Single-cell sequencing in stem cell biology*. Genome Biology, 2016. **17**(1): p. 71.
196. Kobel, S.A., et al., *Automated analysis of single stem cells in microfluidic traps*. Lab on a Chip, 2012. **12**(16): p. 2843-2849.
197. Chattopadhyay, P.K., et al., *Single-cell technologies for monitoring immune systems*. Nature Immunology, 2014. **15**: p. 128.
198. Ma, C., et al., *A clinical microchip for evaluation of single immune cells reveals high functional heterogeneity in phenotypically similar T cells*. Nature Medicine, 2011. **17**: p. 738.
199. Zeisel, A., et al., *Cell types in the mouse cortex and hippocampus revealed by single-cell RNA-seq*. Science, 2015. **347**(6226): p. 1138.
200. Marusyk, A. and K. Polyak, *Tumor heterogeneity: Causes and consequences*. Biochimica et Biophysica Acta (BBA) - Reviews on Cancer, 2010. **1805**(1): p. 105-117.
201. Dueck, H., J. Eberwine, and J. Kim, *Variation is function: Are single cell differences functionally important?* BioEssays, 2016. **38**(2): p. 172-180.

202. Gawad, C., W. Koh, and S.R. Quake, *Single-cell genome sequencing: current state of the science*. Nature Reviews Genetics, 2016. **17**: p. 175.
203. Kanter, I. and T. Kalisky, *Single Cell Transcriptomics: Methods and Applications*. Frontiers in Oncology, 2015. **5**(53).
204. Hughes, A.J., et al., *Single-cell western blotting*. Nature Methods, 2014. **11**: p. 749.
205. Son, K.J., et al., *Microfluidic compartments with sensing microbeads for dynamic monitoring of cytokine and exosome release from single cells*. Analyst, 2016. **141**(2): p. 679-688.
206. Rettig, J.R. and A. Folch, *Large-Scale Single-Cell Trapping And Imaging Using Microwell Arrays*. Analytical Chemistry, 2005. **77**(17): p. 5628-5634.
207. Chen, C.S., et al., *Micropatterned Surfaces for Control of Cell Shape, Position, and Function*. Biotechnology Progress, 1998. **14**(3): p. 356-363.
208. Chen, H., et al., *High-throughput, deterministic single cell trapping and long-term clonal cell culture in microfluidic devices*. Lab on a Chip, 2015. **15**(4): p. 1072-1083.
209. Park, K.J., et al., *Micropillar arrays enabling single microbial cell encapsulation in hydrogels*. Lab on a Chip, 2014. **14**(11): p. 1873-1879.
210. Armbrrecht, L. and P.S. Dittrich, *Recent Advances in the Analysis of Single Cells*. Analytical Chemistry, 2017. **89**(1): p. 2-21.
211. Bjornson, Z.B., G.P. Nolan, and W.J. Fantl, *Single-cell mass cytometry for analysis of immune system functional states*. Current Opinion in Immunology, 2013. **25**(4): p. 484-494.
212. Cheung, R.K. and P.J. Utz, *CytoTOF—the next generation of cell detection*. Nature Reviews Rheumatology, 2011. **7**: p. 502.
213. Muzzey, D. and A. van Oudenaarden, *Quantitative Time-Lapse Fluorescence Microscopy in Single Cells*. Annual Review of Cell and Developmental Biology, 2009. **25**(1): p. 301-327.
214. Young, J.W., et al., *Measuring single-cell gene expression dynamics in bacteria using fluorescence time-lapse microscopy*. Nature Protocols, 2011. **7**: p. 80.
215. Mazutis, L., et al., *Single-cell analysis and sorting using droplet-based microfluidics*. Nature protocols, 2013. **8**(5): p. 870-891.
216. Joensson, H.N. and H. Andersson Svahn, *Droplet Microfluidics—A Tool for Single-Cell Analysis*. Angewandte Chemie International Edition, 2012. **51**(49): p. 12176-12192.
217. Holtze, C., S. Weisse, and M. Vranceanu, *Commercial Value and Challenges of Drop-Based Microfluidic Screening Platforms—An Opinion*. Micromachines, 2017. **8**(6): p. 193.
218. Yang, C.-G., Z.-R. Xu, and J.-H. Wang, *Manipulation of droplets in microfluidic systems*. TrAC Trends in Analytical Chemistry, 2010. **29**(2): p. 141-157.
219. Draper, M.C., et al., *Superhydrophobic Surfaces as an On-Chip Microfluidic Toolkit for Total Droplet Control*. Analytical Chemistry, 2013. **85**(11): p. 5405-5410.
220. Holmes, H.R. and K.F. Böhringer, *Transporting droplets through surface anisotropy*. Microsystems & Nanoengineering, 2015. **1**: p. 15022.
221. Küster, S.K., et al., *Interfacing Droplet Microfluidics with Matrix-Assisted Laser Desorption/Ionization Mass Spectrometry: Label-Free Content Analysis of Single Droplets*. Analytical Chemistry, 2013. **85**(3): p. 1285-1289.
222. Garcia-Cordero, J.L. and Z.H. Fan, *Sessile droplets for chemical and biological assays*. Lab on a Chip, 2017. **17**(13): p. 2150-2166.
223. Sun, Y., X. Zhou, and Y. Yu, *A novel picoliter droplet array for parallel real-time polymerase chain reaction based on double-inkjet printing*. Lab on a Chip, 2014. **14**(18): p. 3603-3610.
224. Schmitz, C.H.J., et al., *Dropspots: a picoliter array in a microfluidic device*. Lab on a Chip, 2009. **9**(1): p. 44-49.
225. Huebner, A., et al., *Static microdroplet arrays: a microfluidic device for droplet trapping, incubation and release for enzymatic and cell-based assays*. Lab on a Chip, 2009. **9**(5): p. 692-698.

226. Sarkar, S., et al., *Phenotypic drug profiling in droplet microfluidics for better targeting of drug-resistant tumors*. Lab on a Chip, 2015. **15**(23): p. 4441-4450.
227. Fradet, E., et al., *Combining rails and anchors with laser forcing for selective manipulation within 2D droplet arrays*. Lab on a Chip, 2011. **11**(24): p. 4228-4234.
228. Junkin, M., et al., *High-Content Quantification of Single-Cell Immune Dynamics*. Cell Reports, 2016. **15**(2): p. 411-422.
229. Jeong, H.-H., et al., *A highly addressable static droplet array enabling digital control of a single droplet at pico-volume resolution*. Lab on a Chip, 2016. **16**(9): p. 1698-1707.
230. Leung, K., et al., *A programmable droplet-based microfluidic device applied to multiparameter analysis of single microbes and microbial communities*. Proceedings of the National Academy of Sciences, 2012. **109**(20): p. 7665-7670.
231. Jeong, H.-H., et al., *Microfluidic static droplet array for analyzing microbial communication on a population gradient*. Lab on a Chip, 2015. **15**(3): p. 889-899.
232. Mehlen, P. and A. Puisieux, *Metastasis: a question of life or death*. Nature Reviews Cancer, 2006. **6**: p. 449.
233. Bithi, S.S. and S.A. Vanapalli, *Microfluidic cell isolation technology for drug testing of single tumor cells and their clusters*. Scientific Reports, 2017. **7**: p. 41707.
234. Avesar, J., et al., *Rapid phenotypic antimicrobial susceptibility testing using nanoliter arrays*. Proceedings of the National Academy of Sciences, 2017. **114**(29): p. E5787-E5795.
235. Berthier, J., *Chapter 5 - EWOD Microsystems**, in *Micro-Drops and Digital Microfluidics (Second Edition)*. 2013, William Andrew Publishing. p. 225-301.
236. Beech, J.P., et al., *Sorting cells by size, shape and deformability*. Lab on a Chip, 2012. **12**(6): p. 1048-1051.
237. Karimi, A., S. Yazdi, and A.M. Ardekani, *Hydrodynamic mechanisms of cell and particle trapping in microfluidics*. Biomicrofluidics, 2013. **7**(2): p. 021501.
238. Zhang, Z., et al., *Behavior of rigid and deformable particles in deterministic lateral displacement devices with different post shapes*. The Journal of Chemical Physics, 2015. **143**(24): p. 243145.
239. Doddi, S.K. and P. Bagchi, *Lateral migration of a capsule in a plane Poiseuille flow in a channel*. International Journal of Multiphase Flow, 2008. **34**(10): p. 966-986.
240. Frisch, S.M. and R.A. Sreaton, *Anoikis mechanisms*. Current Opinion in Cell Biology, 2001. **13**(5): p. 555-562.
241. Chen, Y.-C., et al., *Paired single cell co-culture microenvironments isolated by two-phase flow with continuous nutrient renewal*. Lab on a Chip, 2014. **14**(16): p. 2941-2947.
242. Halldorsson, S., et al., *Advantages and challenges of microfluidic cell culture in polydimethylsiloxane devices*. Biosensors and Bioelectronics, 2015. **63**(Supplement C): p. 218-231.
243. Macosko, Evan Z., et al., *Highly Parallel Genome-wide Expression Profiling of Individual Cells Using Nanoliter Droplets*. Cell, 2015. **161**(5): p. 1202-1214.
244. Shalek, A.K., et al., *Single-cell RNA-seq reveals dynamic paracrine control of cellular variation*. Nature, 2014. **510**: p. 363.
245. Hu, S.-W., et al., *Versatile Microfluidic Droplets Array for Bioanalysis*. ACS Applied Materials & Interfaces, 2015. **7**(1): p. 935-940.
246. Bithi, S.S., et al., *Coalescing drops in microfluidic parking networks: A multifunctional platform for drop-based microfluidics*. Biomicrofluidics, 2014. **8**(3): p. 034118.
247. Davenport, M., et al., *New and developing diagnostic technologies for urinary tract infections*. Nature Reviews Urology, 2017. **14**: p. 296.
248. Das, A., et al., *MMP proteolytic activity regulates cancer invasiveness by modulating integrins*. Scientific Reports, 2017. **7**(1): p. 14219.
249. Fields, G.B., *Using Fluorogenic Peptide Substrates to Assay Matrix Metalloproteinases*, in *Matrix Metalloproteinase Protocols*, I.M. Clark, Editor. 2010, Humana Press: Totowa, NJ. p. 393-433.

250. Chapman, A., et al., *Heterogeneous Tumor Subpopulations Cooperate to Drive Invasion*. Cell Reports, 2014. **8**(3): p. 688-695.